

MODELLING SUSPENDED SAND TRANSPORT UNDER BREAKING WAVES

Gabriel Lim

u1142499

**A thesis submitted in partial fulfilment of the requirements of the University of East
London for the degree of Doctor of Philosophy**

24 March 2021

Director of Studies: Dr. Ravindra Jayaratne

Second Supervisor: Dr. Ali Abbas

Internal Examiner: Dr. John Walsh (UEL)

External Examiner: Professor Harshinie Karunaratna (Swansea University)

Original Submission Date: 06 December 2019

PhD Viva Date: 06 March 2020

Resubmission Date: 24 March 2021

Contents

| | |
|--|-----|
| Contents | 3 |
| List of Figures | 5 |
| List of Tables | 6 |
| List of Symbols/Notations | 7 |
| List of Research Output | 10 |
| Abstract | 11 |
| Chapter 1 - Introduction | 12 |
| 1.1. Research Context & Motivation | 12 |
| 1.1.1. Background | 12 |
| 1.1.2. Need for Improvement | 17 |
| 1.1.3. Aim, Research Questions and Objectives | 19 |
| 1.2. Thesis Structure and Approach | 20 |
| Chapter 2 – Suspended Sand Concentration Models for Breaking Wave Conditions | 23 |
| 2.1. Introduction | 23 |
| 2.2. Existing Models | 25 |
| 2.2.1. Reference Concentration – C_0 | 25 |
| 2.2.2. Concentration Profile and Mixing Parameter | 32 |
| 2.3. Proposed model – Lim et al. (2020) – L19 | 37 |
| 2.3.1. L19 Reference Concentration Model | 37 |
| 2.3.2. L19 Concentration Profile and Mixing Parameter | 46 |
| Chapter 3 – Validation of Reference Concentration and Concentration Profile Models | 47 |
| 3.1. Introduction | 47 |
| 3.2. Overview of Experimental Datasets | 47 |
| LIP Experiments – Roelvink & Reniers (1995) | 48 |
| CROSSTEX Experiments – Yoon & Cox (2010) | 52 |
| SandT-Pro Experiments – Ribberink et al. (2014) | 56 |
| SINBAD Experiments – van der Zanden et al. (2016) | 59 |
| 3.3. Validation of Models | 62 |
| 3.3.1 Reference Concentration (C_0) and Vertical Mixing (M) | 62 |
| 3.3.2. Concentration Profile ($C[z]$) | 85 |
| 3.4. Chapter Summary & Overview of Key Findings | 107 |
| Chapter 4 – Validation for Cross-shore Suspended Transport Rates | 111 |
| 4.1. Introduction | 111 |

| | |
|--|-----|
| 4.2. Methodology and Formulae..... | 114 |
| 4.3. Validation..... | 117 |
| 4.3.1. Current-related suspended transport (q_{sc})..... | 117 |
| 4.3.2. Wave-related suspended transport (q_{sw})..... | 144 |
| Chapter 5 – Discussion | 145 |
| 5.1. Limitations and Improvements to Suspended Sand Concentration Models | 146 |
| REFERENCE CONCENTRATION..... | 146 |
| CONCENTRATION PROFILE AND TRANSPORT RATES..... | 161 |
| 5.2. Limitations of Datasets Used..... | 170 |
| 5.2.1. Availability and limitations of data..... | 170 |
| 5.2.2. Instruments used and implications..... | 171 |
| Chapter 6 – Conclusions and Recommendations for Further Study | 174 |
| 6.1. Conclusions..... | 174 |
| 6.2. Recommendations for Further Study | 181 |
| Acknowledgements..... | 184 |
| References..... | 185 |
| Appendix A..... | 198 |

List of Figures

| | |
|---|-----|
| Figure 1 - Cross-shore profile evolution of LIP Experiments (Erosive case). a) shows whole cross-shore profile, b) shows zoom in of breaking zone | 51 |
| Figure 2 - Cross-shore profile evolution of LIP Experiments (Accretive case). a) shows whole cross-shore profile, b) shows zoom in of breaking zone | 51 |
| Figure 3 - Cross-shore profile evolution of CROSSTEX Experiments. a) shows erosive case, b) shows accretive case | 55 |
| Figure 4 - Cross-shore profile evolution of SandT-Pro Experiments | 58 |
| Figure 5 – Cross-shore profile evolution of SINBAD Experiments | 61 |
| Figure 6 – Measured vs. Computed reference concentration: derived using the model of MS92. | 64 |
| Figure 7 - Cross-shore distributions of mixing parameter (top panels), measured and computed reference concentration (middle panels) and bed profile evolution (lower panels). | 67 |
| Figure 8 - Measured vs. Computed reference concentration – derived using the model of SR93. | 69 |
| Figure 9 - Cross-shore distributions of mixing parameter (top panels), measured and computed reference concentration (middle panels) and bed profile (lower panels). | 70 |
| Figure 10 - Measured vs. Computed reference concentration – derived using model of SP04. | 72 |
| Figure 11 - Cross-shore distributions of mixing parameter (top panels), measured and computed reference concentration (middle panels) and bed profile (lower panels). | 73 |
| Figure 12 - Cross-shore distributions of local wave height (H), breaker height (H_b), local water depth (d), and inverse water depth ($1/d$) compared against cross-shore distribution of measured reference concentration (C_0) | 74 |
| Figure 13 - Measured vs. Computed reference concentration – derived using the model of JS07. | 75 |
| Figure 14 - Cross-shore distributions of mixing parameter (top panels), measured and computed reference concentration (middle panels) and bed profile (lower panels). | 77 |
| Figure 15 - Measured vs. Computed reference concentration – derived using the model of VR07. ... | 79 |
| Figure 16 - Cross-shore distributions of mixing parameter (top panels), measured and computed reference concentration (middle panels) and bed profile (lower panels). | 79 |
| Figure 17 - Measured vs. Computed reference concentration – derived using the model of vdZ17. ... | 81 |
| Figure 18 - Cross-shore distributions of mixing parameter (top panels), measured and computed reference concentration (middle panels) and bed profile (lower panels). | 81 |
| Figure 19 - Measured vs. Computed reference concentration – derived using the model of L19. | 82 |
| Figure 20 - Cross-shore distributions of mixing parameter (top panels), measured and computed reference concentration (middle panels) and bed profile (lower panels). | 83 |
| Figure 21 - Concentration profile ($C[z]$) of Measured (red circles) vs. computed (R39, black circles) concentration. | 90 |
| Figure 22 - Concentration profile ($C[z]$) of Measured (red circles) vs. computed (SR93, green circles) concentration. | 92 |
| Figure 23 - Concentration profile ($C[z]$) of Measured (red circles) vs. computed (LK01, orange circles) concentration. | 97 |
| Figure 24 - Concentration profile ($C[z]$) of Measured (red circles) vs. computed (JS07, blue circles) concentration. | 99 |
| Figure 25 - Concentration profile ($C[z]$) of Measured (red circles) vs. computed (W12, light blue circles) concentration. | 101 |
| Figure 26 - Concentration profile ($C[z]$) of Measured vs. computed (SR93, green circles on left plots) vs. computed (L19, purple circles on right plots) concentration. | 102 |
| Figure 27 - Concentration profile ($C[z]$) of Measured vs. computed (L19) concentration with new constant $B = 3.3$; Eq.(33). | 105 |

| | |
|--|-----|
| Figure 28 - Concentration profile ($C[z]$) of Measured (red circles) vs. computed (L19, purple circles; W12 grey squares). | 107 |
| Figure 29 – Vertical profiles of computed $u[z]$, $C[z]$ and $uC[z]$ – L19 vs. VR93 vs. VR07. | 121 |
| Figure 30 - Cross-shore distribution of measured volumetric q_{sc} | 122 |
| Figure 31 - Cross-shore distribution of q_{sc} : Computed (VR93, VR07) vs. Measured | 124 |
| Figure 32 - computed vs. measured q_{sc} (scalars) – (kg/m/s)..... | 124 |
| Figure 33 – depth-averaged \bar{u} , $C[z]$, $uC[z]$ and q_{sc} for SR93 in plots a-d) respectively..... | 130 |
| Figure 34 - depth-averaged \bar{u} , $C[z]$, $uC[z]$ and q_{sc} for W12 in plots a-d) respectively. | 132 |
| Figure 35 - depth-averaged \bar{u} , $C[z]$, $uC[z]$ and q_{sc} for L19 in plots a-d) respectively. | 134 |
| Figure 36 - q_{sc} for L19 vs. measured in plot a), q_{sc} for SR93 vs. W12 vs. measured in plots b). Plot c) shows the measured bed profile. | 136 |
| Figure 37 - depth-averaged \bar{u} , $C[z]$, $uC[z]$ and q_{sc} for VR93 in plots a-d) respectively. | 139 |
| Figure 38 – depth-averaged \bar{u} , $C[z]$, $uC[z]$ and q_{sc} for VR07 in plots a-d) respectively..... | 141 |
| Figure 39 - q_{sc} for L19 vs. measured in plot a), q_{sc} for VR93 vs. VR07 vs. measured in plots b). Plot c) shows the measured bed profile. | 143 |
| Figure 40 – Vertical profile of Froude-scaled TKE at 1cm above the bed from the SINBAD and CROSSTEX datasets. | 148 |
| Figure 41 - Delft3D-FLOW model domain: grid and bathymetry for Perranporth Beach, UK..... | 156 |

List of Tables

| | |
|---|-----|
| Table 1 – Experiment data cases used from SINBAD dataset in calibration of Omega constant..... | 45 |
| Table 2 - Experiment data cases used from LIP dataset in calibration of Omega constant | 45 |
| Table 3 - Summary of experimental conditions for the LIP Experiments..... | 49 |
| Table 4 - Overview of Test 1B conditions used..... | 49 |
| Table 5 - Overview of Test 1C conditions used..... | 50 |
| Table 6 - Summary of experimental conditions for the CROSSTEX Experiments | 53 |
| Table 7 - Overview of Erosive Test conditions..... | 54 |
| Table 8 - Overview of Accretive Test conditions | 55 |
| Table 9 - Summary of experimental conditions for the SandT-Pro Experiments | 57 |
| Table 10 - Overview of Test RB1 conditions..... | 58 |
| Table 11 - Summary of experimental conditions for SINBAD Experiments..... | 60 |
| Table 12 - Overview of all Runs from $t=30-45$ mins | 61 |
| Table 13 - Summary of RMSE for all reference concentration models tested against measured data. 85 | |
| Table 14 - Brief summary of LSTF dataset (c.f. Wang et al. 2002)..... | 94 |
| Table 15 - RMSE for individual test cases of $C[z]$ models (kg/m ³)..... | 103 |
| Table 16 - RMSE for each model over all cross-shore regions for each dataset (kg/m ³)..... | 104 |
| Table 17 - R^2 and RMSE values between computed and measured q_{sc} | 123 |
| Table 18 - Combinations of C_0 and $C[z]$ formulae used for Part B.1..... | 126 |
| Table 19 - Part B.1. RMSE for depth-averaged $C[z]$, depth-averaged $uC[z]$ and q_{sc} | 135 |
| Table 20 - Combination of C_0 and $C[z]$ formulae used for Part B.2 | 137 |
| Table 21 - Part B.2. RMSE for depth-averaged $C[z]$, depth-averaged $uC[z]$ and q_{sc} | 142 |

List of Symbols/Notations

| | |
|---------------------------------|---|
| A | = roller area (m ²) |
| a | = reference level (m) - (for van Rijn, 1984; 1993; 2007; vdZ et al., 2017c) |
| A _b | = amplitude of orbital excursion near bed (m) |
| B | = dimensionless calibration constant for L19 concentration profile formula (-) |
| \hat{A}_δ | = near bed peak orbital excursion based on significant wave height (m) |
| c | = wave celerity (m/s) |
| \tilde{C} | = oscillating component of suspended sand concentration (kg/m ³) |
| C ₀ | = reference concentration (kg/m ³) |
| C[z] | = time-averaged concentration profile (kg/m ³) |
| c _μ | = constant = 0.09 (-) |
| d | = local water depth (m) |
| d _b | = depth at breaking (m) |
| D _B | = wave energy dissipation due to wave breaking (kg/m ⁶) |
| D ₅₀ | = average grain diameter (m) |
| D* | = dimensionless particle diameter (-) |
| D _r | = roller dissipation rate (kg/s ³) |
| E _r | = roller energy (kg/s ²) |
| f | = constant related to breaker type (Thornton & Guza, 1983) (-) |
| f _w | = dimensionless grain roughness friction factor (-) |
| g | = gravitational acceleration (m/s ²) |
| H | = wave height (m) |
| H _b | = breaker height (m) |
| H _s | = significant wave height (m) |
| K | = proportionality constant for MS92 reference concentration formula (s/m ²) |
| k | = wave number (m ⁻¹) |
| k _b | = (total) near-bed TKE = k* + k _{br} (m ² /s ²) |
| k _{br} | = external breaking generated TKE (m ² /s ²) |
| k _d | = dimensionless empirical coefficient (-) |
| k _{wb} | = wave number at breaking point (m ⁻¹) |
| k* | = bed shear TKE (m ² /s ²) |
| k ₁ , k ₂ | = constants (-) (used by SR93 and JS07) |
| L | = wavelength (m) |

| | |
|------------------|--|
| L_b | = breaker length (m) |
| L_s | = mixing length (m) |
| M | = dimensionless mixing parameter (-) (Rouse number) |
| P | = equilibrium profile shape parameter (-) (LK01 concentration profile formula) |
| q_s | = total (cross-shore) suspended sand transport rate (kg/m/s) |
| q_{sc} | = current-related suspended sand transport rate (kg/m/s) |
| q_{sw} | = wave-related suspended sand transport rate (kg/m/s) |
| s | = specific gravity (-) |
| T | = wave period (s) |
| T_Φ | = dimensionless transport parameter (-) |
| u_b | = maximum orbital velocity (m/s) |
| $uC[z]$ | = time-averaged horizontal suspended sand flux (kg/m ² s) |
| \hat{u}_b | = near-bottom velocity at breaking point (m/s) |
| \tilde{u} | = oscillating component of flow velocity (m/s) |
| u' | = cross-shore fluid velocity (m/s) |
| u^* | = bed shear velocity (m/s) |
| u^*_{cr} | = the critical bed shear velocity (m/s) |
| u^*_{kb} | = adapted bed shear velocity (m/s) |
| u^*_{wc} | = shear velocity under wave-current coexistent field (m/s) |
| $u[z]$ | = time-averaged horizontal fluid velocity profile (m/s) |
| \hat{U}_δ | = is the near-bed peak orbital velocity (m/s) |
| v' | = alongshore fluid velocity (m/s) |
| w_s | = grain settling velocity (m/s) |
| w' | = vertical fluid velocity (m/s) |
| x | = cross-shore coordinate (m) |
| z_0 | = reference level (m) - (for SR93, JS07, L19) |
| z | = elevation above bed (m) |
| α_c | = dimensionless term from Spielmann et al. (2004) (-) |
| α_{cw} | = wave-current interaction coefficient (-) |
| β | = coefficient related to wave steepness (-) |
| γ | = dimensionless constant for L19 C_0 model (-) |
| γ_b | = breaker index (-) |

| | |
|-----------------|---|
| Δ_r | = ripple height (cm) |
| ε_b | = diffusion coefficient under breaking waves (-) |
| ε_s | = sediment diffusivity term or simply the diffusion coefficient |
| ε_v | = eddy viscosity (m^2/s) |
| θ | = Shields parameter (-) |
| κ | = von Karmen constant (-) |
| ν | = kinematic viscosity (m^2/s) |
| ρ_s | = density of sediment (kg/m^3) |
| ρ_w | = density of water (kg/m^3) |
| τ | = dimensional shear stress (N/m^2) |
| τ_s | = surface shear stress (N/m^2) |
| $\tau'_{b,c}$ | = current related bed shear stress (N/m^2) |
| $\tau'_{b,cr}$ | = Shields critical bed shear stress (N/m^2) |
| $\tau'_{b,cw}$ | = current and wave related bed shear stress = $\tau'_{b,c} + \tau'_{b,w}$ (N/m^2) |
| $\tau'_{b,w}$ | = wave related bed shear stress (N/m^2) |
| ψ_b | = modified Shields parameter (used by SR93) (-) |
| ω | = wave angular frequency (s^{-1}) |
| Ω | = calibration constant related to cross-shore region (for L19 C_0 formula) (-) |

List of Research Output

- **Lim, G.,** and Jayaratne, R. (unsubmitted): *Modelling Cross-shore Suspended Sand Transport Rates under Breaking Waves*. Prepared for submission to Coastal Engineering, Elsevier. **(Journal paper – based on findings from Chapter 4)**
- **Lim, G.,** and Jayaratne, R. (unsubmitted): *Modelling the Suspended Sand Concentration Profile under Breaking Waves*. Prepared for submission to Coastal Engineering, Elsevier. **(Journal paper – based on findings from Chapter 3.3.2.)**
- **Lim, G.,** and Jayaratne, R. (2020): *New Suspended Sand Concentration Model for Breaking Waves*. 37th International Conference on Coastal Engineering, ASCE. **(Oral Presentation)**
- **Lim, G.,** Jayaratne, R. and Shibayama, T. (2020): *Suspended Sand Concentration Models under Breaking Waves: New and Existing Formulations*. Marine Geology, Elsevier. **(Journal paper – based on findings from Chapter 3.3.1.)**
- **Lim, G.,** Jayaratne, R., Shibayama, T. (2018): *An Evaluation of Suspended Sediment Concentration Models under Breaking Waves*, 36th International Conference on Coastal Engineering, ASCE, Maryland, USA. (Extension of the work presented at SedNet '17). **(Oral presentation)**
- **Lim, G.,** Jayaratne, R., Shibayama, T. (2017): *An Evaluation of Suspended Sediment Concentration Models under Breaking Waves*, 10th International SedNet Conference (SedNet 2017), Genoa, Italy. **(Poster presentation)**

Abstract

The modelling of coastal morphodynamics has often been hindered by the lack of robustness/accuracy of constituent formulae, especially sediment transport formulae in the breaking and swash zones. Consequently, modellers are often forced to rely on crude calibration efforts and practical models consisting of empirical tuning-constants, to obtain favourable model results. Such methods are often unavoidable however due to theoretical limitations of existing models. The aim of this thesis is therefore to improve accuracy and applicability of suspended sand transport models for breaking wave conditions, for implementation into morphodynamic modelling studies.

Several existing suspended sand transport models (6 reference concentration C_0 + 5 concentration profile $C[z]$) models were evaluated quantitatively and qualitatively against one another, and against state-of-the-art high-resolution datasets which were collected under large-scale breaking wave conditions. Numerous limitations were observed in existing models, with the most common of these being their inability to accurately replicate suspended transport patterns in multiple cross-shore regions. This was due to various issues, such as not adequately accounting for the effects of breaking-induced turbulent kinetic energy on resulting sand transport. This resulted in large discrepancies between computed and measured transport particularly in the highly turbulent breaking zone. Such poor performance in computing C_0 and $C[z]$ had residual effects on the resulting suspended flux ($uC[z]$) and current-related transport rate (q_{sc}) computations also, which are essential to the accurate modelling of morphodynamics, particularly in the medium- to long-term.

A novel set of suspended sand transport (C_0 + $C[z]$) models (“L19”) were developed for breaking wave conditions and evaluated against the aforementioned existing models and datasets. The L19 formulae showed significantly greater performance than all existing models, indicating excellent agreement with measured data in all tested cross-shore regions. These improvements led to considerably better estimations of $uC[z]$ and q_{sc} , which have promising implications for future morphodynamic modelling.

Chapter 1 - Introduction

1.1. Research Context & Motivation

1.1.1. Background

The modelling of coastal morphodynamics has been the subject of interest of numerous comprehensive research projects over the last century. Such modelling endeavours are however often hindered by the lack of robustness and accuracy of constituent formulae, particularly constituent sediment transport formulae. Consequently, modellers are often forced to rely on arduous and time-consuming calibration efforts and practical models, which consist of (numerous) empirical tuning constants, to obtain favourable model results. Such methods are quite crude and inefficient but often unavoidable due to theoretical limitations of existing models. An essential first step in improving morphodynamic modelling capabilities is the development of more robust sediment transport formulae that are accurate, widely applicable (to a range of different conditions) and computationally efficient. The aim of this thesis is therefore to evaluate the performance of existing suspended sand transport formulae, identifying key limitations and developing an improved set of suspended sand transport models that are applicable for use in morphodynamic models.

Coastal Morphodynamics

Coastal morphodynamics is a product of small- and large-scale processes that occur over long, often decadal to centennial, time scales. As these processes occur over large areas (in the 10^1 to 10^2 km) over many years (10^1 to 10^2 years), they are difficult to predict. Naturally occurring processes and systems are non-linear, and therefore long-term morphodynamic behaviour may be considered inherently ‘unpredictable’. Though this is not entirely true, the prediction of medium- to long-term morphodynamics is no trivial task. Reliability of model simulations not only depend on the robustness of constituent formulations, but also on the quality (as well as consistency and availability) of the data used for input conditions and model calibration/validation. Effective means in gaining valuable insights into such complex processes include carefully designed, controlled laboratory and field experimental studies (or measurement/monitoring campaigns for large-scale processes) supported by thorough analysis and computational (and other) modelling efforts.

A vast range of different modelling techniques have been adopted in the endeavour to understand the morphological behaviour of coastal areas, ranging from data-driven or reduced-physics modelling techniques in recent years (e.g. Karunarathna et al., 2011; 2012; 2016) to more traditional one-line or n-line (e.g. Dabees & Kamphuis, 1998; Hanson & Kraus, 2004; Barbaro et al., 2010), or two-dimensional and (quasi) three-dimensional (Q3D/3D) process-based numerical modelling techniques (e.g. Lesser et al., 2004; Dronen & Deigaard, 2007; Li et al., 2007; Jayaratne et al., 2012; Putzar & Malcherek, 2014; Wang et al., 2014; Sanchez et al., 2015; Klonaris et al., 2018; Luijendijk et al., 2019). Coastal area modelling suites such as Delft3D (Deltares), MIKE21 (Danish Hydraulics Institute) and Telemac (Laboratoire National d'Hydraulique et Environnement) are powerful process-based modelling suites that couple hydrodynamic modules (waves and currents) with sediment transport and morphodynamic modules to simulate complex coastal environments. Such modelling suites (as well as other process-based models) were once thought to be inefficient and unsuitable for predicting morphological changes for the long-term, but in recent years practical developments (e.g. 'morfac' and input reduction techniques; refer to Appendix A) have enabled modellers to push conventional temporal boundaries, effectively using process-based models to simulate detailed morphological changes for the medium- (e.g. Lesser et al., 2004; Elias et al., 2015) and long-term (e.g. Wang et al., 2014; van der Wegen & Roelvink, 2008; Dastgheib, 2012; Sanchez et al., 2015; Dam et al., 2016; Luijendijk et al., 2019).

Despite numerous reported studies indicating good results in medium- to long-term morphodynamic modelling using morfac and input reduction techniques, efforts are still often heavily dependent on arduous calibration efforts due to a lack of robustness of constituent sediment transport formulae (theoretical limitations). Even state-of-the-art coastal area models such as Delft3D, MIKE21 and Telemac are comprised of relatively simple physics, relying instead on numerous (semi-)empirical parameterisations, which are often not very well-founded in measured data nor on fundamental understanding of key hydrodynamic and sediment transport processes (van der Werf et al., 2015). Of the models that are thoroughly validated against experimental data, many are only validated for their ability to predict bed changes, rather than individual bedload and suspended load components (van der Zanden et al., 2017a; henceforth abbreviated to vdZ et al.) and their relative contributions to net transport. There is therefore a need for the development of more improved (practical and process-based) sediment transport formulae that are well-validated against data from field and laboratory experiments (van Rijn et al., 2013). This is especially the case for the breaking and swash zones

where previous attempts at accurately modelling sediment transport has been most challenging due to the complex interaction between highly turbulent hydrodynamic processes and transported sediments that occur in these regions (c.f. vdZ, 2016).

Modes of Sand Transport

Though the aforementioned morphodynamic models are often used to simulate large-scale spatial domains (10^1 to 10^2 km), they often rely on parameterisations of underlying small-scale processes (vdZ, 2016), particularly in the case of process-based models. Of the numerous processes and factors that drive coastal morphodynamics, sediment transport plays a fundamental role. Sediment is constantly transported by waves, (wave-induced) currents and tides, both in the cross-shore (on- and off-shore) and alongshore directions. Although aeolian processes are also known to be responsible for transport of finer sediments, having considerable effects on some morphological processes such as dune evolution, this thesis will only focus on the sediment (sand) transported by hydrodynamic processes in the cross-shore direction.

Sediment transport driven by hydrodynamic processes are generally broken down into three categories: bedload, suspended load and wash load, with the effects of wash load often being considered negligible in morphodynamic studies involving sand transport. The mode by which sediment is transported is a function of the balance between gravitational and drag (or fluid lift) forces acting on the sediment grains. Gravitational forces act on the grains to keep them in contact with the bed, whilst drag (and fluid lift) forces attempt to dislodge and transport the grains. Depending on whether or not the sediments are cohesive, resulting transport mechanisms vary, however this study will be focused on the transport of non-cohesive sediments (sand), and the word ‘sediment’ herein will be used interchangeably with the word ‘sand’. Sediment particles with grain diameter ranging between 62-2000 μm are usually referred to as sand (van Rijn, 1993).

When the dislodging drag or lift forces are prevalent over grounding forces, there is sediment motion. The balance of the forces acting on the grains also determine the mechanism of transport. When drag forces (induced by bottom currents) exceed the gravitational (and friction) forces, the grains slide or roll – this mode of transport is known as ‘bedload’. When the fluid lift forces (induced by turbulent events, e.g. wave breaking) are greater than the gravitational forces (or more practically: when the bed-shear velocity is greater than the settling velocity),

sediment is entrained (sediment pick-up) and this mode is known as ‘suspension’ or ‘suspended load’. In reality, there is no explicit layer that separates the bedload from the suspended load. However, for practical reasons the two layers are separated by a ‘reference level’, with all sediment transport below the reference level being referred to as ‘bedload’ and transport above the reference level ‘suspended load’. Though both modes of transport play important roles in net sediment transport and in resulting morphological changes, accurately modelling the suspended load has been relatively more difficult in the past than modelling the bedload. This is largely due to the complex hydrodynamic processes that occur under the turbulent events that induce sediment suspension (e.g. wave breaking in the breaking zone; the region in which waves break is called the ‘breaking zone’). The focus of this thesis therefore is in improving suspended sand transport models for the purpose of integrating them into morphodynamic models to enhance their performance.

Suspended Sand Transport in the Surf Zone

Suspended load is commonly attributed to three physical phenomena: 1) vortices generated by sand ripples, 2) movement of the bottom layer with high bed shear stresses (sheet flow) and 3) turbulence generated by wave breaking (e.g. Shibayama & Rattanapitikon, 1993; Jayaratne & Shibayama, 2007). The first two mechanisms are found to occur in and outside the surf zone, whereas wave breaking predominantly occurs in the surf zone. As waves approach the shore and propagate into shallower water, shoaling occurs (this occurs in the shoaling zone). Shoaling causes wave height and steepness to increase, and also the fluid velocity at the wave crest to exceed the wave speed, resulting in kinematic instability within the wave, and consequently wave breaking (Thornton & Guza, 1983). As the waves break, wave energy is dissipated as potential energy is converted to turbulent kinetic energy, heat, sound, bubbles/sea-spray and more. They also generate currents in the longshore and cross-shore directions which produce turbulence and induce/enhance sediment transport.

Over the years, experimental studies have reported that the magnitude of sediment suspension (e.g. Kana 1978, 1979; Shibayama & Rattanapitikon, 1993; Beach & Sternberg, 1996; Voulgaris & Collins, 2000), turbulence production and dissipation rates (Thornton & Guza, 1983) and transport mechanisms (Ting & Kirby, 1994; vdZ et al., 2016) found within the surf zone are a function of the wave type. Under non-breaking wave conditions, the suspended sediment concentration is largely confined to the thin layer above the bottom, known as the

wave bottom boundary layer (referred to as WBBL or WBL in existing literature) where bed-shear is the prominent cause of sediment pickup. This however is not the case under breaking conditions, where the sediment is suspended over the whole water column. Considerable differences can also be observed in the concentration profile and turbulence structure (Brinkkemper et al., 2016) depending on the breaker types.

Yoon & Cox (2010) reported that the timescale of turbulence propagation was relatively longer under spilling breakers, with corresponding turbulence intensities being relatively constant at any given time due to advection of residual turbulence from previous breakers. This is consistent with the observations of Brinkkemper et al. (2016) who found that the amount of turbulence measured was homogenous over the whole wave cycle under spilling breakers. Aagaard et al. (2018) reported that near-bed turbulence under spilling breakers peaked much later in the wave cycle, suggesting slower penetration of surface-generated turbulent kinetic energy (TKE) into the water column. It is speculated that this may be a result of turbulence in spilling breakers being largely confined in the upper water column due to relatively small eddies present under these conditions (c.f. Thornton & Guza, 1983; Brinkkemper et al., 2016).

On the contrary, TKE under plunging breakers is generated almost immediately after the wave has broken (Ting & Kirby, 1995; vdZ et al., 2019). A large amount of the breaking-generated TKE is dissipated in the form of bores above the water surface, and the remainder is injected into the water column (vdZ et al., 2016). As the waves plunge, a jet (Shibayama & Rattanapitikon, 1993; Otsuka et al., 2017) of highly pressurised (Mocke & Smith, 1992) and aerated water (Voulgaris and Collins, 2000; Yoon and Cox, 2010) is thrust into the water column at the plunging point. This plunging process enhancing bed shear stresses (Cox & Kobayashi, 2000; Sumer et al., 2013; vdZ et al., 2017a) and generates strong turbulent vortices/eddies (vdZ et al. 2018; 2019; Aagaard et al., 2018) that rotate about the horizontal axis (Aagaard & Hughes, 2010) and induce an upward-directed pressure gradient force (Sumer et al., 2013). These vortices travel rapidly (vdZ et al., 2017a) and obliquely downward towards the bed (Nadaoka et al., 1989; Brinkkemper et al., 2016; Otsuka et al., 2017; De Serio & Mossa, 2019; Hsu et al., 2019) and shoreward in the direction of wave propagation (Peregrine & Svendsen, 1978). Turbulent kinetic energy is dissipated as it travels down the water column, from the surface to the bed, with dissipation rates and depth of TKE penetration depending on the strength and size of the generated vortices (Thornton & Guza, 1983). Despite the turbulence dissipation throughout the water column, varying amounts of TKE can still reach the bed (Thornton & Guza, 1983; Grasso et al., 2012), transported by the large-scale eddies (Ting &

Kirby, 1995). Especially in regions where the water depth is shallow, the externally injected TKE can contribute significantly to the near-bed TKE (Scott et al., 2005; vdZ et al. 2016). As the turbulent eddies reach the bed, the external turbulence adds to the locally produced TKE induced by bed shear (Sumer et al., 2013) in the WBBL. Though not the dominant source of TKE in the surf zone, turbulence induced by bed shear can also contribute importantly to near-bed TKE (Brinkkemper et al., 2016; vdZ et al., 2016).

As mentioned above, the highly turbulent large-scale vortices invade the WBBL and enhance bed-shear stresses and upward-directed pressure gradient forces which entrain large amounts of sediment from the bed (Aagaard & Hughes, 2010; Otsuka et al., 2017; vdZ et al., 2017a) in the form of dense clouds (Sato et al., 1990, Shibayama & Rattanapitikon, 1993). The breaking generated TKE does not only travel vertically (injection, dissipation, vertical advection and diffusion), but is also advected horizontally in the offshore direction (vdZ et al., 2016). The dense clouds of sediment can also be advected away from the breaking/plunging point and contribute to net sediment transport (Aagaard & Hughes, 2010) and increase concentration in adjacent cross-shore regions. Over barred bed conditions, this breaking-induced turbulence often does not decay entirely within one wave cycle and can linger in the breaker bar trough region as ‘residual turbulence’ (Fernandez-Mora et al., 2016; vdZ et al., 2016; 2019; van der A et al., 2017). Trapped air bubbles from the plunger also rise towards the surface (Ting & Kirby, 1995; Mori et al., 2007; Jayaratne & Shibayama, 2007) generating large upwards-localised velocities (Voulgaris & Collins, 2000), which carry suspended sediment into the upper water column. The combination of the rising air bubbles and the highly turbulent vortices enhances strong vertical sediment mixing in the breaking region (Nielsen, 1984; Ogston & Sternberg, 2002; Aagaard & Hughes, 2010; Aagaard & Jensen, 2013; Yoon et al., 2015; Pang et al., 2020). The vertical profile of suspended sediment concentration is often used in conjunction with horizontal fluid velocities to compute the cross-shore suspended sediment transport rate, which in turn is used in the modelling of coastal morphodynamics (this is further elaborated in Chapter 4). Thus, the accurate prediction of the suspended sediment concentration is directly linked to the accuracy of morphodynamic modelling.

1.1.2. Need for Improvement

In particular, a lack of knowledge of sediment transport processes and how they relate to hydrodynamics makes the application of short-term process-based transport models to long-

term coastal evolution challenging (Karunarathna et al., 2009). This is in agreement with Hanson et al., (2003) who reported that process-based models seemed to perform reasonably for first-order processes, but morphological changes such as bed profile evolution were driven by higher order processes (such as sediment transport and hydrodynamic forces). Small inaccuracies in the computation of such higher order processes can accumulate to produce unrealistic predictions of coastal morphodynamics, particularly in the long-term. The improvement of sediment transport models could therefore serve as a stepping-stone in the bridging of knowledge gaps that currently hinder the more effective use of process-based morphodynamic models in long-term simulations.

At present, morphodynamic models use advection/diffusion models to compute the suspended sediment transport and concentration profile, where the advection term represents the current-related transport and the diffusion term represents turbulence-related horizontal and vertical sediment fluxes (vdZ, 2016). Horizontal bed-shear driven sediment pick-up rate or reference concentration formulae are commonly used to model the vertical exchange of sediment between the suspension and bedload layers (as briefly described in Chapter 1.1.1. and further detailed in Chapters 2.2.1. and 3.3.1.). Such formulations (e.g. van Rijn, 1993; 2007) have been found to be successful in modelling concentration under non-breaking conditions but are unable to adeptly capture the high levels of sediment entrainment induced by breaking wave conditions (this is further discussed and demonstrated in Chapter 3.3.1. of this thesis). Existing sediment transport formulae could be enhanced by incorporating recent insights regarding the complex breaking-related hydrodynamics and resulting sediment transport processes, as well as quantitative and qualitative trends/relationships relating the sediment transport to breaking-induced forces, local wave climate and bathymetry.

High-resolution large-scale datasets consisting of sediment concentration measurements (with co-located hydrodynamic and morphological data) carried out in numerous cross-shore locations were not widely available until recent years. As a result, many of the existing SSC models were only validated under a limited number of measured cases in the breaking and shoaling zones, and often did not consider the effects of wave breaking at all (van Rijn et al., 2013; vdZ, 2016). In other cases, the models were largely validated using data from small-scale wave flumes (e.g. Sato et al., 1990), where the extent of hydrodynamic forces/processes found under field-scale breaking waves could not be fully replicated. Hence, many of the existing formulations were derived and validated based on incomplete insights and limited

measurements of the complex hydrodynamic forces found under breaking waves. This lack of process understanding resulting from a deficiency in detailed measurements is reflected in the performance of existing suspended load models. With rapid technological advancements in recent years, instruments and facilities used in the measuring of accurate hydrodynamic (e.g. orbital, turbulent and settling velocities), sediment transport (suspended sediment concentration, rates and fluxes) and morphological (bar migration and bed changes) data have been improved considerably. Such developments have helped to shed novel insights into once poorly understood phenomena such as wave breaking and resulting sediment transport processes, both in laboratory (e.g. Scott et al., 2005; Yoon & Cox, 2010; Wang et al., 2012; Brinkkemper et al., 2016; vdZ et al., 2016; 2017a,b; 2018; van der A et al., 2017; Fromant et al., 2019) and field experiments (e.g. Aagaard et al., 2018; Christensen et al., 2019; Brand et al., 2019; 2020). This calls for the developing of more accurate sediment transport formulations that are thoroughly validated against high-resolution measured data.

1.1.3. Aim, Research Questions and Objectives

The aim of this thesis is therefore *to improve accuracy and applicability of suspended sand transport models for breaking wave conditions, for implementation into morphodynamic modelling studies*. This aim is addressed by answering the following research questions and by the fulfilment of subsequent objectives:

RQ1) What are the key limitations of existing suspended sand transport formulae for breaking wave conditions?

RQ2) How can these limitations be addressed to produce more robust and accurate transport formulae for future use in morphodynamic modelling studies?

RQ3) To what extent do improvements to reference concentration and concentration profile models affect resulting computations of horizontal suspended flux and cross-shore transport rates?

This thesis attempts to address the aim and research questions by completing a series of objectives:

-OB1: To identify key limitations of existing reference concentration and concentration profile models by qualitatively and quantitatively evaluating their performance against state-of-the-art measured datasets and latest process insights.

-OB2: To derive a new practical model that accurately predicts suspended sand transport patterns under breaking waves, and to validate it against existing models and measured data.

-OB3: To evaluate the applicability of the new and existing transport models to morphodynamic models and suggest methods of improvement.

-OB4: To investigate the extent to which the improvements to reference concentration and concentration profile models affect the prediction of cross-shore suspended sand transport rates.

Objective 1 corresponds to Research Question 1, Objective 2 & 3 to Research Question 2 and Objective 4 to Research Question 3.

1.2. Thesis Structure and Approach

Chapter 2 gives an overview of the numerous suspended sand concentration models that are evaluated in this thesis. Chapter 2.1 provides a short introduction to suspended sand concentration modelling. Chapter 2.2. covers details on the formulae as well as key assumptions and parameters incorporated into existing suspended sand concentration formulae. Chapter 2.2.1. and Chapter 2.2.2. cover the key assumptions and parameters of 6 existing reference concentration models and 5 existing concentration profile models respectively. Chapter 2.3.1. details the development process of the newly proposed L19 reference concentration model, with some qualitative comparison with the existing models. It should be noted that though the development of the new L19 model (Objective 2) was carried out after the evaluation study presented in Chapter 3 (Objective 1), it is presented in Chapter 2 for the reader's convenience; to allow the reader to compare the underlying assumptions and model formulation of both existing and new concentration models within the same chapter. Discussion on differences in key parameters, modelling approaches and some strengths/weaknesses of the respective approaches are also documented in this section. The findings from the analysis of key parameters and strengths/weaknesses of existing models are then incorporated into the

development of the new L19 model, and details regarding the modelling philosophy and initial calibration of tuning constants are also provided.

The findings presented in Chapter 3 address the second objective of this thesis and are partly based on a model validation study documented in a journal paper (Chapter 3.3.1.) that was published in *Marine Geology*, Elsevier (Lim et al., 2020). This chapter presents the findings from an evaluation study of seven reference concentration (C_0) and 5 concentration profile ($C[z]$) formulae that were derived for breaking wave conditions (models covered in Chapter 2). These models were evaluated for performance against 4 recently published, high-resolution datasets collected under the LIP (refer to Roelvink & Reniers, 1995), CROSSTEX (refer to Yoon & Cox, 2010), SandT-Pro (refer to Ribberink et al., 2014) and SINBAD (refer to van der Zanden et al., 2016) projects, which are covered in detail in Chapter 3.2. The datasets included measurements from different cross-shore regions, regular and irregular waves and both spilling and plunging breaking waves. Chapter 3.3. presents the quantitative and qualitative validation of the existing and newly proposed reference concentration models (Chapter 3.3.1.) and concentration profile models (Chapter 3.3.2.) as mentioned above. The performance of the models was measured quantitatively by computing the root mean square error (RMSE) between the measured and computed reference concentration, and also qualitatively by studying patterns and trends in comparison plots.

As cross-shore suspended sediment transport rates are a function of the concentration profile ($C[z]$), they are also an indirect function of the reference concentration. It was predicted that poor performance of reference concentration and concentration profile models would have residual effects on the resulting sediment transport rates, making them unreliable and leading to unrealistic predictions morphological changes. In order to test this hypothesis, the performance of the newly proposed SSC formulae from Chapter 2 are evaluated for performance in predicting the current-related cross-shore suspended sediment transport rates (q_{sc}) – addressing the fourth and final objective of this thesis in Chapter 4. The predicted transport rates are validated against field-scale laboratory measured data, as well as two sets of commonly used sediment transport formulae, including the Delft3D default transport formulae (van Rijn, 1993). The extent to which improvements to reference concentration and concentration profile models had on resulting transport rates is also covered in Chapter 4.

Chapter 5 covers an in-depth discussion regarding the research objectives presented in Chapter 1.1.3., as well as the limitations of the datasets used throughout this thesis. Finally, Chapter 6

summarises the main conclusions from all sections of this thesis and gives some recommendations for further research.

Chapter 2 – Reference Concentration and Concentration Profile Models

2.1. Introduction

In recent years, various experimental and numerical studies have enhanced our understanding of fundamental processes, providing valuable insights into physical phenomena such as wave breaking and the complex interactions between the resulting hydrodynamics and local sediment. However, even with novel insights, describing the complex sediment movement within the surf zone is still difficult, as it is influenced by vertical (vdZ et al., 2019) and cross-shore (van Rijn et al., 2013; vdZ et al. 2017b) hydrodynamic non-uniformity, breaking induced turbulence and asymmetric oscillatory motion under shallow water waves (Sato et al., 1990).

Many of the sediment transport formulae widely used in numerical modelling suites are based on the convection-diffusion equation (neglecting horizontal convection and diffusion), which essentially describe the vertical balance between upward mixing of sediments forced by turbulent motion and downward settling forced by gravity.

$$C(z)\omega_s + \varepsilon_s \frac{dc(z)}{dz} = 0 \quad (1)$$

where $C[z]$ is the time-averaged vertical concentration profile – also known as SSC with respect to the elevation above the bed (z); ε_s is the sediment diffusivity term or simply the diffusion coefficient.

In solving the convection-diffusion equation, the concentration at a reference level is often used as a boundary condition (Shibayama & Rattanapitikon, 1993). A considerable number of studies have endeavoured to model the suspended sand concentration (SSC) at the near-bottom reference level, i.e. the reference concentration (C_0). Some have related the reference concentration to the bed shear stress or bed shear velocity, or the dimensionless bed shear stress – i.e. Shields Parameter (e.g. Van Rijn, 1984, 2007; Shibayama & Rattanapitikon 1993; Camenen & Larson, 2008), others to local wave height, water depth or relative wave height (e.g. Mocke & Smith, 1992) or the wave height at the breaking point (e.g. Jayaratne & Shibayama, 2007), energy dissipation of the surface roller (e.g. Smith & Mocke, 1993; Spielmann et al., 2004) and inclusion of near-bed TKE to increase bed shear stress (e.g. Hsu &

Liu, 2004; Okayasu et al., 2010; vdZ et al. 2017c). Various formulae used to determine C_0 are described in Chapters 2.2.1. and 2.3.1. and validated in Chapter 3.3.1. of this thesis.

The estimation of C_0 is then used in computing the vertical concentration profile, generally by using either a set of exponential (e.g. Larson & Kraus, 2001; Wang et al., 2012) or power function (Rouse, 1939; Shibayama & Rattanapitikon, 1993; Jayaratne & Shibayama, 2007) formulae. In Eq. 1, the upward mixing forces (which occur either through diffusion or convection) are represented by the sediment diffusivity term (ϵ_s) and the countering, downward settling force acting on suspended sand particles is represented by the settling velocity (w_s). Correctly predicting the balance between the upward entraining and downward settling forces is essential in determining how much sediment is in suspension, and for modelling the concentration profile accurately.

Concentration profile formulae generally consist of a mixing parameter which is usually a function of the sediment diffusivity term and the settling velocity - representing the aforementioned upward entraining and downward settling forces. Different formulations of the mixing parameter have been developed over the last few decades, with numerous formulations of the sediment diffusivity term (refer to Chapter 2.2.2. for examples), each producing different results. No single set of formulae has gained universal acceptance as the default. The accurate modelling of the concentration profile is further complicated by the effects of breaking waves (Ogston & Sternberg, 2002) which generate turbulent eddies that enhance sediment pickup and mixing (as described in Chapter 1.1.1.). This means that mixing parameters developed for non-breaking conditions would not be very well suited to conditions with strong plunging breakers where breaking-induced turbulence levels are considerable. The different formulae used to model $C[z]$ under breaking wave conditions are detailed in Chapters 2.2.2. and 2.3.2. and validated in Chapter 3.3.2.

Some of these major contributions to suspended sand concentration modelling (reference concentration and concentration profile) are described in Chapter 2.2., covering key assumptions and parameters incorporated into the model development. A newly proposed model is then described in Chapter 2.3., providing details of the model development, assumptions, derivation of parameters and tuning constants.

2.2. Existing Models

2.2.1. Reference Concentration (C_0)

It should be noted that in this section commonly used parameters such as the wave climate (e.g. wave height, length, period), local water depth and any other parameters used in multiple formulae are the same for all formulations unless specified otherwise. As such, any parameters that are defined in earlier formulae are not repeated for each new set of formulae unless there are variations in their definitions.

2.2.1.1. Mocke & Smith (1992) – MS92

The reference concentration formula of Mocke & Smith (1992) was comprised of three main terms: the relative wave height term (which was a measure of breaking intensity and depth penetration), a turbulence dissipation term (based on periodic bores) and a TKE term (which incorporated TKE from mean bed shear). The complementing relative wave height term, which represents the injection of TKE into the water column, is combined with the turbulence dissipation term and the Shields parameter to account for local TKE.

Mocke & Smith (1992) proposed the following equation to compute the bottom reference concentration (C_0) in kg/m^3 :

$$C_0 = \rho_s K^{-0.92} \left(\frac{H}{d}\right)^{3.32} \left(\frac{H^3}{dT}\right)^{-0.92} \theta^{0.37} \quad (2)$$

where

ρ_s is the density of sand = 2650 kg/m^3

$K = 1.51 \times 10^3 \text{ s/m}^2$ is a proportionality constant related to the turbulence dissipation term

H is local wave height

d is local water depth

T is the wave period

θ is the Shields Parameter

The Shields Parameter was defined by the following:

$$\theta = \frac{\tau}{[\rho_w(s-1)gD_{50}]} \quad (3)$$

where τ is the dimensional shear stress = $0.5\rho_w f_w u_*^2$

ρ_w = density of seawater = 1025 kg/m^3

s is the specific gravity = ρ_s/ρ_w

f_w is the dimensionless grain roughness friction factor = $\exp(5.213*[(r)/(A_b)^{0.194}]-5.977)$:
based on Swart, (1974).

A_b is the amplitude of orbital excursion at bed and $r = 2.5D_{50}$ is the hydraulic roughness
(Nielsen, 1986)

u_* = bed shear velocity

g = gravitational acceleration = 9.81 m/s^2

D_{50} is the average grain diameter

2.2.1.2. Shibayama & Rattanapitikon (1993) – SR93

SR93 proposed a simple set of formulae to predict the reference concentration under breaking wave and non-breaking wave conditions. They assumed that the reference concentration was a function of the maximum bed shear, sediment diameter and in the case of non-breaking waves, also ripple-height. For breaking wave conditions, SR93 proposed two different formulations of the Shields Parameter: one for plunging waves and one for all other breaker types. The formulations of Shields Parameter used by SR93 are defined as:

$$\psi_b = \frac{\left\{ u_* + 0.01 [H^3 g(4Td)]^{\frac{1}{3}} \right\}^2}{[(s-1)gD_{50}]} \quad \text{for plunging breakers} \quad (4a)$$

$$\psi_b = \psi = \frac{0.5f_w u_b^2}{(s-1)gD_{50}} \quad \text{for other breaker types} \quad (4b)$$

where

$H^3g(4Td)$ is the rate of wave energy dissipation due to wave breaking

u_b is the maximum orbital velocity.

Shear velocity or maximum shear velocity is one of the key driving parameters in the reference concentration formulation of SR93. For cases where the maximum shear velocity cannot be obtained using measurements, SR93 defined maximum shear velocity as:

$$u_* = \sqrt{(0.5f_w u_b^2)} \quad (5)$$

The maximum orbital velocity is also an important parameter in the formulation of SR93. As the reference level is typically in the WBBL, it is assumed in this thesis that the maximum orbital velocity (u_b) can be equated to the near-bottom velocity at the breaking point (\hat{u}_b).

$$u_b \approx \hat{u}_b \quad (6)$$

where \hat{u}_b can be found from Eq.12. Alternatively, the orbital velocity can be computed from the linear wave theory. Based on the computed Shields Parameter and experimental observations of sediment and fluid characteristics, the following formula was derived for the reference concentration (C_0) in g/l:

$$C_0 = \frac{10}{3} \frac{[(\psi_b - 0.05)v]}{\{\sqrt{[(s-1)g D_{50}]100D_{50}}\}} \quad (7)$$

where

reference level $z_0 = 100D_{50}$

ν = kinematic viscosity = $1.17 \times 10^{-6} \text{ m}^2/\text{s}$, and 0.05 is the critical value of Shields Parameter for threshold general movement of sand.

Note: as the units g/l are equal to kg/m^3 (i.e. $1 \text{ g/l} = 1 \text{ kg}/\text{m}^3$), the reference concentration computed using the formulae of SR93 and also JS07 (described in Chapter 2.2.1.4.) are displayed in kg/m^3 for uniformity of units in the analysis presented in Chapters 3 and 4.

2.2.1.3. Spielmann et al. (2004) – SP04

Spielmann et al. (2004) reported that in the surf zone, wave breaking caused a downward horizontal transfer in momentum from the fluid above the wave trough, which in turn contributed to the driving force for mean flow. Spielmann et al. (2004) took this effect into consideration by incorporating shear stress at the water surface. This surface shear stress (τ_s) was related to the roller dissipation rate (D_r) by Deigaard & Fredsoe (1989):

$$\tau_s = \frac{D_r}{c} \quad (8)$$

where c = wave celerity = $\sqrt{(g \cdot d)}$

The parameterisation of Nairn et al. (1990) was used to model the roller dissipation rate as follows:

$$D_r = 2\beta g \frac{E_r}{c} \quad (9)$$

where

β = coefficient related to the wave steepness = 0.1

One of the key parameters used in determining the roller dissipation rate is the roller energy E_r . This parameter can be computed using different methods, but in this thesis the formulation of Svendsen (1984) has been implemented due to its computational efficiency:

$$E_r = \rho_w \frac{Ac^2}{2L} \quad (10)$$

where

A = roller area = estimated empirically as $0.9H^2$ by Svendsen (1984).

L = wavelength was estimated using linear wave theory.

SP04 emphasised the effect the breaking roller had on surf zone hydrodynamics, particularly in the vicinity of breaker bars. For this reason, it was deemed important to include the surface shear stress induced by the breaking roller and in turn, to propose a parameterisation that is dependent on the Shields Parameter. Instead of the standard bed shear stress used in the Shields Parameter, SP04 used the sea-surface shear stress induced by the breaking roller (τ_s). Based on the modified Shields Parameter, the following reference concentration formulation was proposed in kg/m^3 :

$$C_0 = \alpha_c \rho_s \left[\frac{D_r}{(\rho_s - \rho_w) g D_{50} c} \right]^3 \quad (11)$$

where:

α_c = dimensionless term = 1×10^{-6}

2.2.1.4. Jayaratne & Shibayama (2007) – JS07

The reference concentration (C_0) formula of Jayaratne & Shibayama (2007) was derived from the time-averaged suspended sediment transport rate. The formulation was driven mainly by the wave climate (wave height, wavelength, celerity, etc.) and to a lesser extent, the sediment characteristics/interaction (average grain diameter, settling velocity, etc.). One of the key drivers in the JS07 model is based on the relationship between the near-bottom velocity at the breaking point (\hat{u}_b) and the particle settling velocity (w_s). Jayaratne & Shibayama (2007) considered \hat{u}_b to represent the intensity of near-bottom turbulence at the breaking point, which would in theory entrain the sediment from the bed. The settling velocity (w_s) would represent the magnitude of the opposite force that causes entrained sediment to settle again. It was proposed that the relationship between the two parameters would be effective in modelling the SSC under breaking wave conditions. The near-bottom velocity at the breaking point (\hat{u}_b) is derived as follows:

$$\hat{u}_b = \frac{\pi H_b}{T \sinh(k_{wb} d_b)} \quad (12)$$

where the subscript b denotes at the breaking point, k_{wb} is the wave number at the breaking point = $2\pi/L_b$.

The relationship proposed by Jayaratne & Shibayama (2007) for computing reference concentration in g/l at the reference level of $100D_{50}$ was defined as:

$$C_0 = 1.22 * 10^{-6} \text{ gT} \frac{\hat{u}_b^{2.3}}{w_s^{3.3}} \quad (13)$$

where

w_s = particle settling velocity

Note: Jayaratne & Shibayama (2007) reported $1.22 * 10^{-9}$ instead of $* 10^{-6}$. This is because the units used in JS07 were centimetres, whereas herein metres are used.

Though the above formulation was derived for breaking conditions only, for the purpose of testing its applicability to adjacent cross-shore zones also, the local wave height (H) was used in place of the breaker height (H_b) in this thesis. This was also done with the wavelength (L) being used instead of breaker length (L_b) and local water depth (d) instead of breaker depth (d_b). This is further discussed in Chapter 5.2.

2.2.1.5. Van Rijn (2007) – VR07

Van Rijn (1984) reported that some of the main driving hydraulic parameters of suspended load were the particle settling velocity and the sediment diffusion coefficient. It was assumed, in particular, that the reference concentration at the bed was determined by particle diameter (D_*) and the transport parameter T_Φ .

$$D_* = D_{50} \left[\frac{(s-1)g}{\nu^2} \right]^{\frac{1}{3}} \quad (14)$$

The particle diameter, also referred to as the dimensionless grain size, is a function of the average grain diameter and also hydraulic parameters such as the kinematic viscosity (ν). The transport parameter is a dimensionless bed shear stress term that considers the induced bed shear velocity and the critical bed shear velocity, with the assumption that sediment movement occurs when the critical velocity is exceeded. The transport parameter T_Φ was modified in van Rijn (2007) to incorporate the current and wave related bed shear stress ($\tau'_{b,cw}$) and the Shields critical bed shear stress ($\tau'_{b,cr}$) instead of the bed shear velocity.

$$T_\Phi = (\tau'_{b,cw} - \tau'_{b,cr}) / \tau'_{b,cr} \quad (15)$$

$\tau'_{b,cr}$ = Shields critical bed shear stress

$\tau'_{b,cw}$ = current and wave related bed shear stress = $\tau'_{b,c} + \tau'_{b,w}$

$\tau'_{b,c}$ = current related bed shear stress and $\tau'_{b,w}$ = wave related bed shear stress

See van Rijn (2007) for details on how to derive the bed shear stresses.

For instantaneous volumetric reference concentration for suspended load, the following formula was proposed:

$$C_0 = 0.015 * \frac{D_{50}}{a} * \frac{T_\Phi^{1.5}}{D_*^{0.3}} \quad (16)$$

$a = z_0$ = the reference level, with minimum value of 0.01m. See van Rijn (2007) for details on deriving a . The minimum value of $a = 0.01m$ is used in this thesis. Note: Equation 16 gives the volumetric concentration and should therefore be multiplied by $\rho_s = 2650 \text{ kg/m}^3$ to obtain C_0 in kg/m^3 . Also, the model of van Rijn (2007) was only validated against the SINBAD and CROSSTEX datasets in Chapter 3.3.1. The reason for this is the measured wave orbital velocity (computed from measured root-mean-square [rms] wave orbital velocity) was not collected in

the SandT-Pro experiments, and the time-averaged current velocity was not measured in the LIP experiments – both of these measurements are required as input parameters for VR07.

2.2.1.6. Van der Zanden et al. (2017c) – VDZ17

The reference concentration C_0 equation is the same as that of van Rijn (1984; 2007), as is the reference level. The fundamental difference between the vdZ17 model and the van Rijn (2007) model is the inclusion of external breaking generated TKE into the transport parameter (T_Φ) of van Rijn (1984). The original transport parameter of van Rijn (1984) was proportionate to the sediment pick-up rate and represented the difference between exerted and critical bed shear. The transport parameter of van Rijn (1984) was as follows:

$$T_\Phi = \frac{u_*^2 - u_{*cr}^2}{u_{*cr}^2} \quad (17)$$

where u_* is the bed shear velocity and u_{*cr} is the critical bed shear velocity $= 4w_s/D^*$.

Van Rijn (1984) proposed that sediment pick-up occurred when bed shear velocity (u_*) exceeded the critical bed shear velocity (u_{*cr}); i.e. sediment pick-up is equal to zero when $u_{*cr} > u_*$. This was based on the assumption that the turbulence that drives the sediment pickup rate is entirely generated locally by bed-friction (vdZ et al., 2017c; c.f. Chapter 2.3.1.1.).

The transport parameter of van Rijn (1984) was reformulated to include external breaking generated TKE, making the near-bed TKE (k_b) the main driver for the new formulation as follows:

$$T_\Phi = \frac{u_{*kb}^2 - u_{*cr}^2}{u_{*cr}^2} \quad (18)$$

$$u_{*kb} = c\mu^{1/4} \sqrt{k_b} \quad (19)$$

where u_{*kb} = adapted bed shear velocity, $c\mu$ = constant = 0.09, k_b = (total) near-bed TKE = the sum of the locally produced bed shear TKE (k^*) and external breaking generated TKE (k_{br}).

When there is no external breaking generated TKE (i.e. $k_{br} = 0$), $k_b = k^*$ and sediment entrainment is entirely driven by the locally produced bed shear. Note: the model of vdZ17 was only validated against the SINBAD and CROSSTEX experiments in Chapter 3.3.1., as the

cross-shore (u'), alongshore (v') and vertical (w') fluid velocities were not collected under the SandT-Pro and LIP experiments.

2.2.2. Concentration Profile and Mixing Parameter

This section briefly describes the various formulations used to model the concentration profile and vertical mixing parameters throughout this thesis. There are some existing concentration profile models that implicitly assume that the vertical distribution of sediment concentration is only affected by bottom shear stress and wave orbital motion (e.g. Nielsen, 1986; van Rijn, 1993). Such models were largely developed/tested for non-breaking wave conditions and were demonstrated to be unsuitable for use under breaking wave conditions in studies such as Wang et al. (2012). Thus, these models will not be included in the present study which is focused on suspended sand concentration modelling under breaking waves.

2.2.2.1. Rouse (1939) – R39:

One of the most widely used concentration profile formulae are either variations of, or based on the simple power function referred to as the ‘Rouse profile’ equation, which can be expressed as (e.g. van Rijn, 2007):

$$C(z) = C_0 \left\{ \left[\frac{(d-z)}{z} \right] \left[\frac{a}{(d-a)} \right] \right\}^M \quad (20)$$

where M is the dimensionless mixing parameter, based on the widely known Rouse number:

$$M = \frac{w_s}{\kappa u_*} \quad (21)$$

where w_s is the settling velocity, κ is the von Karmen constant (=0.4) and u_* is the bed-shear velocity.

Rouse (1939) considered the effects of the water depth, grain size and settling velocity, combining it with the reference concentration to make a universal equation for computing the concentration profile. In particular, the Rouse number controls the shape of the resulting concentration profile, with different studies providing guidelines that can be used to anticipate

the suspension conditions and the importance of the suspended load. An example of such guidelines was provided by van Rijn (2007) as follows:

- M=5: suspended sediment in near-bed layer ($z < 0.1d$)
- M=2: suspended sediment up to mid of water depth ($z < 0.5d$)
- M=1: suspended sediment up to water surface ($z < d$)
- M=0.1: suspended sediment almost uniformly distributed over water depth.

The Rouse number parameter can also be used to determine how quickly the concentration profile gradient declines with distance from the bed – where the larger this number is, the more abruptly concentration declines from the bed.

A limitation of the Rouse equation that is addressed in recent literature (e.g. Liu et al., 2014; Sun et al., 2020) is that it assumes that the SSC approaches zero as elevation above bed (z) reaches the local water depth (d), and that SSC approaches infinity as z approaches the bed, resulting in a reverse ‘s’ shape vertical concentration profile. This of course is unrealistic. As such, Liu et al. (2014) suggested that preconditions such as $d > z > 0\text{cm}$ or $0.8d > z > 20\text{cm}$ must be met for the Rouse equation to be used. All evaluation carried out in this thesis uses measurements that adhere to the essential preconditions ($d > z > 0\text{cm}$), and therefore should not cause the equation to be unusable in this respect.

2.2.2.2. Shibayama & Rattanapitikon (1993) – SR93:

For non-breaking conditions, Shibayama & Rattanapitikon (1993) proposed an exponential formula derived from the steady diffusion equation to predict the time-averaged concentration profile. They predicted however that an exponential concentration profile or uniform value of the diffusion coefficient would not be suitable for breaking wave conditions. Based on experimental data and the assumption that the diffusion coefficient is proportional to the eddy viscosity of flow, Shibayama & Rattanapitikon (1993) adopted the concept of Okayasu (1989) who suggested that a linear distribution of the eddy viscosity (ϵ_v) was proportionate to the rate of wave energy dissipation due to wave breaking (D_B).

The rate of wave energy dissipation by wave breaking was estimated by Thornton & Guza (1983) as follows:

$$\frac{D_B}{\rho} = \frac{fH^3g}{4Td} \quad (22)$$

where f is a constant related to the breaker type.

The incorporating of the rate of wave energy dissipation by wave breaking (D_B) is commonly used in modelling the diffusion coefficient under breaking waves. The effect of shear due to normal alternating flows under waves was introduced into the diffusion coefficient under breaking waves to produce the following:

$$\varepsilon_b = \left[k_1 \cdot u_* + k_2 \left(\frac{D_B}{\rho} \right)^{\frac{1}{3}} \right] \quad (23)$$

where k_1 and k_2 are constants: $k_1 = 0.04$ for all breaker types; $k_2 = 0.450$ for plunging, 0.114 for spilling breakers and 0.216 for transitional breakers.

The main limitation of the Rouse profile equation mentioned in Chapter 2.2.2.1. ($SSC \rightarrow 0$ as $z \rightarrow d$) was overcome by the introduction of a simplified equation, which is also a commonly used power function formula for modelling the concentration profile (e.g. Aagard & Jensen, 2013):

$$C(z) = C_0 \left(\frac{z_0}{z} \right)^M \quad (24)$$

This equation is however best suited for cases where the elevation z is considerably smaller than the local water depth (Liu et al., 2014).

The mixing parameter of the SR93 formula was modified from the original Rouse number to incorporate the diffusion coefficient as follows:

$$M = \frac{w_s}{\varepsilon_b} \quad (25)$$

For irregular waves, the significant wave height and peak period may be used for the evaluation of parameter M (SR93).

2.2.2.3. Larson & Kraus (2001) – LK01:

Larson & Kraus (2001) assumed that, under breaking waves, the time-averaged turbulence intensity was homogenous throughout the water column and that the vertical distribution of suspended sediment concentration ($C[z]$) was proportional to $\exp[-(w_s/\varepsilon_s)z]$, where the ε_s is the sediment-mixing or diffusion coefficient. This is similar to the concept used in the mixing

parameter M shown in Eq. 25. Larson & Kraus (2001) estimated the diffusion coefficient by incorporating the rate of wave energy dissipation produced by wave breaking as follows:

$$\varepsilon_s = k_d \left(\frac{D_B}{\rho} \right)^{\frac{1}{3}} d \quad (26)$$

Where k_d is an empirical coefficient.

Numerous empirical and numerical models have been developed to estimate the wave energy dissipation rate (D_B), e.g. (Dean, 1977; Thornton & Guza, 1983; Dally et al., 1985; Kriebel et al., 1991; Rattanapitikon & Shibayama, 1998). Larson & Kraus (2001) used the formulation of Dean (1977) to estimate the rate of wave energy dissipation:

$$\frac{D_B}{\rho} = \frac{5}{24} g^{\frac{3}{2}} \gamma_b^2 P^{\frac{3}{2}} d \quad (27)$$

where γ_b = breaker index (=0.8), P = equilibrium profile shape parameter, estimated by Kriebel et al. (1991) as follows:

$$P = \frac{9}{4} \left(\frac{w_s^2}{g} \right)^{\frac{1}{3}} \quad (28)$$

Combining equations 26 and 27 with $\exp[-(w_s/\varepsilon_s)z]$, Larson & Kraus (2001) proposed the following equation for the vertical concentration profile:

$$c(z) = c_0 \cdot \exp \left(- \frac{w_s}{k_d \left(\frac{D_B}{\rho} \right)^{1/3}} \cdot \frac{z}{d} \right) \quad (29)$$

where k_d is a dimensionless empirical coefficient independent of grain size (≈ 0.03).

2.2.2.4. Jayaratne & Shibayama (2007) – JS07:

JS07 accounted for local TKE by including the shear velocity under the wave-current co-existent field (u_{*wc}) and included the breaking energy dissipation model of Rattanapitikon & Shibayama (1998) to represent the external breaking generated TKE. Though elements of turbulent velocities induced by both waves (e.g. orbital velocity) and currents (e.g. shear

velocity) have been incorporated into the formulation, the high flow velocities induced by breaking-generated vortices are not explicitly accounted for.

The concentration profile and mixing parameter were computed using Eqs. 24 & 25, but a different diffusion coefficient was used as follows:

$$\varepsilon_b = k_1 \cdot u_{*wc} + k_2 \left(\frac{D_B}{\rho} \right)^{1/3} \quad (30)$$

where k_1 and k_2 are constants: $k_1 = 0.08$ for all breaking types and $k_2 = 0.480$ for plunging and 0.225 for spilling breakers.

u_{*wc} = shear velocity under wave-current coexistent field

$$\frac{D_B}{\rho} = \frac{0.15 \cdot c \cdot g}{8d \left\{ H^2 - \left[d \cdot \exp\left(-0.36 - 1.25 \frac{d}{\sqrt{L \cdot H}}\right) \right]^2 \right\}} \quad (31)$$

D_B = average rate of wave energy dissipation due to wave breaking computed from the empirical relationships in Rattanapitikon & Shibayama (1998).

2.2.2.5. Wang et al. (2012) – W12:

Having carried out some comprehensive analysis of the performance of the Larson & Kraus (2001, henceforth referred to as LK01) concentration profile model and that of Nielsen (1986), Wang et al. (2012) proposed that the existing LK01 model could be improved by incorporating the effects of wave orbital motion and bottom shear stress (as done by Nielsen, 1986 - henceforth referred to as N86) into a combined formula. This was because each of the existing models (LK01 and N86) incorporated different processes that induced sediment entrainment and vertical mixing. The LK01 model assumed that the wave breaking-induced turbulence and associated wave-energy dissipation was the sole cause of sediment suspension and the primary factor influencing the suspension patterns (Wang et al., 2012). Wang et al. (2012) argued that although breaking-induced TKE is the dominant cause of sediment pickup and mixing in the surf zone, effects of near-bottom shear and wave orbital velocities do still contribute to the concentration profile, and therefore should be incorporated into $C[z]$ models for breaking wave conditions.

As a result, Wang et al. (2012) combined the existing model of Nielsen (1986), which only incorporated intensity and length of wave orbital motion (for non-breaking conditions), with the model of Larson & Kraus (2001), which only incorporated the turbulence generated by wave breaking (through the wave-energy dissipation rate parameter). The combined model is as follows:

$$c(z) = c_0 \exp \left(-z \cdot \frac{w_s}{k_d \left(\frac{D_B}{\rho} \right)^{1/3}} \cdot \frac{1}{d} + \frac{1}{L_s} \right) \quad (32)$$

Where L_s is the mixing length:

$$L_s = \frac{0.075 \Delta_r \omega \hat{A}_\delta}{w_s} \quad \text{for } \frac{\omega \hat{A}_\delta}{w_s} \leq 15 \quad (33a)$$

$$L_s = 1.4 \Delta_r \quad \text{for } \frac{\omega \hat{A}_\delta}{w_s} > 15 \quad (33b)$$

where $\omega = 2\pi/T$, is the wave angular frequency, Δ_r is the ripple height (representative values of 1cm and 1.2cm used for spilling and plunging breakers respectively; Wang et al., 2012), and \hat{A}_δ is the near bed peak orbital excursion determined based on significant wave height (H_s) and peak wave period (T_p) as:

$$\hat{A}_\delta = \frac{T}{2\pi} \hat{u}_b \quad (34)$$

\hat{u}_b is the near-bed peak orbital velocity, computed using Eq.12.

This model was referred to as the Larson-Kraus-Nielsen model by Wang et al. (2012) but will simply be referred to the model of Wang et al. (2012), abbreviated to W12 herein for brevity.

2.3. Proposed model – Lim et al. (2020) – L19

2.3.1. L19 Reference Concentration Model

2.3.1.1. Modelling Philosophy

In attempting to develop improved SSC models, one has the choice to take existing models and modify them, or to develop a new model entirely. Regardless of whether existing models are developed, or new models derived, there are some key issues that must be considered in the development of SSC models, some of which are covered in this chapter.

All sediment transport is affected by 1) the body of water (e.g. wave climate, fluid density and viscosity), 2) the sediment properties (e.g. cohesive/non-cohesive, grain diameter and grain density) and 3) the local bathymetry (e.g. breaking bars or ripples) and the complex interactions between each of these ‘interfaces’. For example:

- 1) The body of water can influence the magnitude of sediment entrainment through wave propagation, the transporting of the suspended sediment through currents, and the fluid density and/or viscosity can have effects on the settling velocity of suspended sediments.
- 2) The sediment properties, such as the grain diameter or density, can influence the amount of sediment that is transported, the mechanism by which it is transported (e.g. bedload or suspended load) and if picked-up then how long grains remain in suspension.
- 3) The bottom bathymetry can influence the wave heights, lengths, celerity and processes such as shoaling and breaking which are directly linked with sediment suspension mechanisms. Such processes can also help to differentiate between the different cross-shore regions, e.g. shoaling, breaking and swash zones.

These are just some of the ways these different interfaces influence sediment transport and more specifically in the context of this thesis, the suspended sand concentration. As such, it is clearly essential to incorporate key parameters related to these interfaces in the modelling of suspended sand transport. Derived from the aforementioned interfaces and interactions between them, it is suggested that three core issues need to be addressed in order to develop robust and widely applicable SSC models: A) applicability of the SSC model to multiple cross-shore zones, B) identifying the predominant sources/causes of sediment suspension in the cross-shore zones of interest and how to incorporate them into the SSC formulae, C) not only incorporating the sediment entraining forces, but also the grain settling forces.

It is essential for SSC formulae used in morphodynamic models to be able to account for different cross-shore zones because a concentration model that is only applicable to one cross-shore zone (e.g. the shoaling zone) has very limited uses from a practical viewpoint. This is also particularly important under breaking wave conditions where variations in turbulent kinetic energy (TKE) and resulting SSC vary greatly between the different cross-shore regions. Developing models to account for the different nearshore regions however is one of the more challenging issues that must be addressed, as the prevalent sand suspension mechanisms in each of the cross-shore zones differ from zone to zone – e.g. suspension due to wave breaking agitation is predominant in the breaker zone, but suspension due to bed-shear is prevalent in

the shoaling zone. As such, developing a single model that can adeptly account for the range of physical processes and suspension mechanisms found in the nearshore regions is not straightforward.

Aside from the main entraining forces found in the different cross-shore regions, it is also important to adequately represent the relationship between the sediment entraining forces (and upward diffusion) and grain settling forces in order to predict how much sand is in suspension at any given time. A commonly used approach for determining the suspended sediment concentration is the use of the Shields Parameter or sediment pickup rate (e.g. *Mocke & Smith, 1992; Shibayama & Rattanapitikon, 1993; van Rijn, 2007; c.f. Chapter 2.2.1.*). This approach assumes that sediment entrainment occurs when the exerted bed shear exceeds the critical bed shear, and that bed shear is the sole or dominant cause of sediment pickup. Though this assumption is applicable under non-breaking conditions, or in regions (e.g. shoaling zone) that are unaffected by breaking-induced TKE, under breaking conditions and in particular the breaking zone, this assumption is no longer applicable (*vdZ et al., 2017c; Aagaard et al., 2018; Lim et al., 2020*).

As described in Chapter 1.1.1., wave breaking injects external TKE into the water column which travels downwards towards the bed and agitates sediment into suspension. When this occurs, the TKE generated by bed shear is no longer the dominant cause of sediment pickup under breaking waves, where breaking-generated TKE is considerably larger. I.e. in the shoaling zone pre-breaking, the locally produced TKE (bed shear turbulence) is dominant, but in the breaking and inner-surf zones, externally produced TKE (breaking-generated turbulence) is dominant (*vdZ et al., 2019*). Many existing SSC models do not (adeptly) account for this externally generated TKE, only considering the effects of locally generated (by bed shear) TKE on SSC. Consequently, the high levels of SSC found in the breaking zone under strong plunging breakers cannot be well represented by models driven by the Shields Parameter or sediment pickup rate alone (this is demonstrated in Chapter 3.3.1). Further discussion on the applicability of models to multiple cross-shore zones and the use of the sediment pickup rate (Shields parameter) in concentration formulae is further discussed throughout Chapter 3 and in Chapter 5, following the validation and analysis of model performance.

The range of parameters used to represent the grain settling forces in concentration models is considerably smaller, with many studies incorporating parameters such as gravitational acceleration (e.g. *Mocke & Smith, 1992; Shibayama & Rattanapitikon, 1993; Spielmann et al.,*

2004) or the settling velocity or even a combination of both (e.g. Jayaratne & Shibayama, 2007) to represent grain settling/grounding forces. Other factors that influence the rate of grain settling to varying extents include the density of fluid and/or grain, kinematic viscosity of fluid and also the grain size. Each of these parameters are also commonly incorporated into concentration formulae. The sediment characteristics are commonly included in concentration formulae in the form of sediment density (ρ_s) and average grain diameter (D_{50}). Van Rijn (1984; 2007) incorporated a dimensionless grain diameter (D^*). Including the grain diameter into reference concentration formulations is of particular importance when attempting to apply the proposed model to field locations with multiple sediment fractions – in this thesis only single sediment fractions are tested with average grain diameters in the range of $D_{50} = 0.22\text{-}0.25\text{mm}$ over different datasets (refer to Chapter 3.2. for details on used datasets).

Though not directly responsible for (or representative of) differences in cross-shore regions, or magnitude/variation of sediment entrainment and/or grain settling, the inclusion of the wave climate and fluid characteristics can also be important in the concentration models, as described in point 1) earlier in this section. One of the more commonly used parameters is the wave height, which is often used as a measure of the intensity of wave breaking and is loosely (inversely) correlated with the magnitude of SSC – this is discussed further in the following Chapter 2.3.1.2.

2.3.1.2. Key Parameters and Assumptions of L19 Model

Some key parameters and assumptions made in the derivation of the L19 model are presented herein. It should be noted that the L19 model was developed after the evaluation of existing models (presented in Chapter 3.3.1.) but the development process is described here to enable the reader to compare key parameters, assumptions and formulations of all models used in this thesis in one chapter. Hence, following descriptions include comments regarding the performance of the models that were described in Chapter 2.2.1. (the performance of the existing and newly proposed models is presented in Chapter 3.3.1.).

As discussed in Chapter 2.3.1.1., some of the greatest limitations of existing models is that the majority do not accurately reproduce the cross-shore variation in reference concentration (i.e. for different cross-shore zones) nor do they adeptly account for the localised high levels of SSC in the breaking zone (these limitations are thoroughly demonstrated in Chapter 3.3.). Of the

existing models covered in this thesis, results indicate that the model of vdZ et al. (2017c), referred to as the vdZ17 model in Chapter 3, best reproduces the cross-shore variation in C_0 over the shoaling, breaking and inner surf zones (see Fig. 17 in Chapter 3.3.1.6.). There are however numerous challenges (e.g. the accurate acquisition of TKE data required to drive the model) that limit the use of the vdZ17 model, particularly in morphodynamic models – refer Chapters 5.1.1.2. and 5.1.2. of this thesis for details.

Herein, a new and unique solution is proposed for representing the sand entraining/settling forces as well as the cross-shore variation in C_0 . When tested against monochromatic/regular and irregular waves, C_0 in the nearshore region (between the shoaling and breaking zones) was found to have a strong inverse relationship with the local water depth (d), up until the wave plunging point.

$$C_0 \propto 1/d$$

I.e. as the cross-shore measurements went in the shoreward direction from the shoaling zone to the breaking zone, local water depth decreased, and corresponding measured SSC increased (see Fig. 12 in Chapter 3.3.1.3.), indicating an inverse relationship between C_0 and d . In the vicinity of the breaking point (generally near the bar crest when a breaker bar is present) and the plunging point (generally near the bar trough) where water depths were lowest, the measured SSC was found to be highest. Assuming a strong causal relationship between TKE and SSC, this inverse relationship between C_0 and the local water depth is supported by the observations of De Serio & Mossa (2019) who reported time-averaged TKE declined as depth increased, and also Pang et al., (2020) who found that in the breaking zone where water depth decreased, TKE levels increased greatly compared to the shoaling zone. The (relative) water depth is commonly incorporated in reference concentration models, sometimes in combination with the wave height (H/d), as a measure of the wave breaking intensity and depth penetration of surface generated forces (e.g. Mocke & Smith, 1992). Similarly, it is proposed that by using the inverse water depth as a key driving parameter, the cross-shore distribution of the reference concentration can be modelled empirically.

Similar trends were observed between C_0 and the local wave height (H), suggesting that the inverse wave height ($1/H$) could potentially be used instead of the inverse water depth. There are however several benefits of using the inverse water depth over the inverse wave height. For example, the inverse water depth ($1/d$) takes into consideration the location of the breaker bar(s), the development of the bar (and/or other bathymetry) with time and the breaking/plunging

points which can often be estimated qualitatively from the bar profile – all of which can influence suspended sand transport patterns. Additionally, individual wave heights and SSC are not always well correlated, with multiple cases where high waves did not result in high SSC, and cases where low SSC was not associated with low wave heights. This is also consistent with vdZ et al. (2017c) who reported poor correlation between measured wave climate and reference concentration particularly in the breaking zone. Analysis of the regular breaking wave conditions showed that wave breaking generally occurred (more or less) in the same cross-shore location, making it easier to correlate the wave height with the breaker bar – i.e. wave breaking generally occurred at the bar crest and plunging (lowest wave heights) occurred at the bar trough. This trend however was not as consistent in the irregular breaker conditions – particularly in the accretive case where the waves often would not break and pass over the bars (this is discussed in more detail in Chapter 5.1.3.). For these reasons, it is proposed that the inverse water depth is the better-suited parameter for use in the proposed C_0 formula.

The wave height, period, length and celerity are incorporated in the proposed formula – some directly and others as constituent parameters in the roller energy dissipation (D_r) term of Nairn et al. (1990) that was used in the C_0 formulation of Spielmann et al., (2004; Chapter 2.2.1.3.). The roller energy dissipation (D_r) parameter is important both practically (in terms of its constituent parameters) and theoretically. Practically, the D_r formula incorporates many of the aforementioned parameters that are key drivers of SSC, including the wave climate (wave height and length) and also the fluid density. It is also a product of the surface shear stress (related to wave breaking) and the wave celerity, both of which influence sediment entrainment and transport. From a theoretical viewpoint, it is common knowledge that the wave energy dissipation due to bottom friction is dominant in the shoaling/pre-breaking region, but in the breaking zone the breaking-induced wave energy dissipation becomes the dominant dissipative mechanism (Thornton & Guza, 1983). Upon breaking, this wave energy is transferred through sea spray production, heat, sound, turbulent kinetic energy, bubble formation and buoyancy, mean current and sediment suspension (Carini et al., 2014). The largest of these is the dissipation through TKE in the form of turbulent vortices, with the dissipation via other means generally being considered relatively small and negligible. The roller energy dissipation rate is used in the L19 model to represent the effects of rapid wave energy dissipation on the reference concentration, which occurs in the transition zone between shoaling and inner surf zones, (c.f. Spielmann et al., 2004).

Another key parameter in the newly proposed model is the dimensionless grain diameter. The dimensionless grain diameter of van Rijn not only considers the average grain diameter of the local sediment, but also incorporates some of the key parameters discussed in Chapter 2.3.1.1, including settling forces (gravity) and fluid and sediment characteristics such as viscosity and density. As each of these said parameters are essential to incorporate into an SSC model (as described in Chapter 2.3.1.1.), the dimensionless grain diameter parameter of van Rijn is chosen over the average grain diameter D_{50} parameter.

2.3.1.3. Formulation & Calibration of Model

Model Formulation

Based on the key parameters and assumptions covered in Chapter 2.3.1.2. the following equation was formulated:

$$C_0 = D_* \cdot g \cdot \frac{1}{D_r} \cdot T \cdot \frac{1}{d} \quad (35)$$

The combination of inverse water depth parameter ($1/d$) and the other key parameters in Equation 35 succeeded in accurately reproducing key qualitative trends in the cross-shore variations of reference concentration (i.e. relatively low SSC in shoaling region, gradual increase towards breaker bar, localised increases in SSC at plunging point, relatively low SSC in inner surf zone). The values of predicted C_0 however were often up to an order of magnitude smaller than measurements in the different cross-shore zones. The tuning parameter Ω was therefore introduced to increase the overall magnitude of C_0 to the correct order, but also to empirically deal with the difference in trends between the shoaling/breaking zones and the inner surf zone. In other words, the main driving relationship between the inverse water depth ($1/d$) and C_0 was only valid in the shoaling and breaking zones, with a very different pattern seen in the inner surf zone. The simplest method of resolving this issue was to use a different value of Ω for the shoaling/breaking zones and the inner surf zone. Details on the calibration of the Omega constant (Ω) is provided later in this section.

Based on Eq. 35 and calibration of tuning parameters, the following formula was proposed for reference concentration in kg/m^3 at the reference level of $100D_{50}$:

$$C_0 = (\gamma D_*)^{-0.695} \cdot g \left[\left(\frac{\Omega}{D_r} \right)^{1.9} \right] \cdot \frac{T}{d} \quad (36)$$

where

$\gamma = 0.0464 = \text{constant}$

$\Omega = \text{constant related to cross-shore region}$

- For erosive cases:

$\Omega = 7.5\text{-}15.0$ for shoaling and breaking regions

$\Omega = 1.0\text{-}3.0$ for inner surf zone

- For accretive cases:

$\Omega = 1.5$ for breaking and shoaling zones

$\Omega = 0.6$ for inner surf zone

The Ω constants empirically account for different (combinations of) suspension mechanisms found in the different cross-shore zones. The values of Ω were derived empirically via a ‘best-fit’ method based on the computed vs. measured reference concentration using the SINBAD and LIP datasets only. Before applying these constants in Eq. 36, users must determine whether conditions are erosive – i.e. lead to erosion; which generally consist of relatively larger wave heights combined with shorter wave periods, or accretive – i.e. lead to accretion; which generally consist of relatively smaller wave heights combined with longer wave periods – c.f. Chapter 3.2. Further elaboration on the use of the Ω constant in morphodynamic models and field conditions is provided in Chapter 5.1.2.

Calibration of Omega Constant (Ω)

Each of the datasets used in this study (described in detail in Chapter 3.2.) comprised of multiple test ‘cases’ or ‘runs’, where each case or run refers to a set of measurements collected over a pre-determined period of time at a single cross-shore location. Rather than using every single run from both datasets for calibration, only a few representative runs were selected from two out of the four datasets (SINBAD and LIP datasets) to carry out calibration for the Ω constant. As there is not an abundance of data available and using the same runs for calibration and validation is meaningless, it was deemed necessary to use as few cases in the calibration stage and as many as possible in the validation stage of the model development. For both datasets, measurement cases were selected from each of the shoaling, breaking and inner-surf

zones, with more than one case being taken from the breaking zone only: one case covering pre-plunging and one post-plunging, where ‘plunging’ indicates the breaking wave plunging as described in Chapter 1.1.

The measurement cases used from the SINBAD experiments were all taken from the 00-15mins run (refer to Chapter 3.2. for details) where breaker bar development was minimal. Some key details regarding the test cases used are summarised below in Tables 1 & 2.

Table 1 – Experiment data cases used from SINBAD dataset in calibration of Ω constant

| Case Number | x-coordinate (m) | Local Wave Height - H (m) | Local Water Depth - d (m) | Wave Period - T (sec) | Wavelength - L (m) | Cross-shore Zone |
|-------------|------------------|---------------------------|---------------------------|-----------------------|--------------------|---------------------------|
| 1 | 51.0 | 0.79 | 1.14 | 4 | 14.35 | Shoaling |
| 67 | 53.0 | 0.73 | 0.89 | 4 | 14.56 | Breaking (Pre-plunging) |
| 13 | 55.5 | 0.53 | 0.71 | 4 | 15.64 | Breaking (Plunging point) |
| 31 | 59.0 | 0.42 | 1.28 | 4 | 14.81 | Inner-surf start |
| 55 | 63.0 | 0.41 | 1.24 | 4 | 14.76 | Inner-surf |

Table 2 - Experiment data cases used from LIP dataset in calibration of Ω constant

| Case Number | x-coordinate (m) | Local Wave Height - H (m) | Local Water Depth - d (m) | Wave Period - T (sec) | Wavelength - L (m) | Cross-shore Zone |
|-------------|------------------|---------------------------|---------------------------|-----------------------|--------------------|------------------|
| 1B0304 | 115 | 0.64 | 1.583 | 4.96 | 17.61 | Shoaling |
| 1B0405 | 130 | 0.57 | 1.25 | 4.97 | 16.94 | Breaking |
| 1B1706 | 138 | 0.46 | 0.827 | 5.02 | 12.76 | Plunging |
| 1B1010 | 170 | 0.26 | 0.381 | 5.02 | 9.45 | Inner-surf |
| 1C0204 | 115 | 0.45 | 1.62 | 7.97 | 31.64 | Shoaling |
| 1C0405 | 130 | 0.44 | 1.174 | 7.98 | 27.85 | Breaking |
| 1C0615 | 134 | 0.44 | 0.973 | 7.98 | 24.14 | Plunging |

| | | | | | | |
|--------|-----|------|------|------|-------|------------|
| 1C1110 | 170 | 0.24 | 0.41 | 7.97 | 16.01 | Inner-surf |
|--------|-----|------|------|------|-------|------------|

Note: The case numbers that start with 1B were from the erosive test cases in the LIP experiments and 1C were from the accretive test cases. Refer to Chapter 3.2. for details.

2.3.2. L19 Concentration Profile and Mixing Parameter

In Chapter 3.3.2., existing $C[z]$ models such as SR93 and JS07, which use the power function equation (Eq. 24), are found to over-predict concentration in the upper water column (where $z/d > 0.2$), even when agreement is good in the lower water column. This is because the magnitude of the computed dimensionless mixing parameter (M) is too small (generally < 0.5), causing the resulting concentration profile curves to be steep and quasi-uniform/linear on the log-scale (i.e. almost perpendicular to the x-axis). Herein, it is proposed that this issue can be resolved simply by multiplying the existing mixing parameter (M) by a dimensionless constant $B (>1)$ to increase the magnitude of M and thereby produce a concentration profile with more gradual variation in concentration per change in elevation above bed (resulting in a more parabolic curve on the log scale). Larger values of constant B produce larger values of M , which in turn leads to smaller values of $C[z]$ and more parabolic curves.

The implementation of constant B is suitable for all formulae that compute $C[z]$ using the power function equation (Eq. 24). It was tested on both the SR93 and JS07 models, but as described in Chapter 3.3.2.5., of the two formulae, the JS07 model produces marginally higher values of $C[z]$ in all cross-shore zones. As the initial issue was that the SR93 and JS07 models were overpredicting $C[z]$ in the upper water column, it was logical to implement the B constant into the formula that produced lower values of $C[z]$. Hence, the B constant was added to the existing mixing parameter of SR93 to form a modified SR93 $C[z]$ formula, which is simply referred to as the ‘L19 $C[z]$ ’ formula in this thesis. The same power function $C[z]$ formula (Eqs. 22-24) is used, but an alternative mixing parameter M is used as described above:

$$M = B \left(\frac{w_s}{\varepsilon_b} \right) \quad (37)$$

where B is a calibration constant (>1). Details of the implementation and calibration of the B constant are provided in Chapter 3.3.2. under the ‘Proposed Model’ sub-section. Further details on the constituent parameters and key assumptions made for the original SR93 $C[z]$ formulae are provided in Chapter 2.2.2.2. and are therefore not repeated here.

Chapter 3 – Validation of Reference Concentration and Concentration Profile Models

3.1. Introduction

The reference concentration is often used to compute the concentration profile, which in turn can be used to compute the (current-related) suspended load transport rate. As such, the performance (and improvement) of reference concentration and concentration profile models can have a direct impact on our ability to accurately reproduce sand transport rates and resulting morphodynamic changes. Small discrepancies between measured and computed suspended load can accumulate over time, leading to unrealistic predictions of resulting morphology, particularly in the medium- to long-term. The aim of the studies presented in this chapter therefore is to validate and evaluate the performance of 7 (6 existing and 1 newly proposed as detailed in Chapter 2.3.1. of this thesis) reference concentration models and 6 (5 existing and 1 newly modified as detailed in Chapter 2.3.2. of this thesis) concentration profile models against 4 recently published datasets that were collected under regular and irregular large-scale breaking waves.

Chapter 3.2. gives a detailed description of the test conditions and relevant information regarding the datasets used to validate the models in this chapter. The datasets used are from ‘LIP’ (refer to Roelvink & Reniers, 1995), ‘CROSSTEX’ (refer to Yoon & Cox, 2010), ‘SandT-Pro’ (refer to Ribberink et al., 2014) and ‘SINBAD’ (refer to vdZ et al. 2016) projects. Chapter 3.3. is separated into two parts: Chapter 3.3.1. covers the validation of the new and existing reference concentration models detailed in Chapter 2.2.1. and 2.3.1. The validation and analysis for the concentration profile models (detailed in Chapter 2.2.2. and 2.3.2.) is covered in Chapter 3.3.2. A summary of key findings from this chapter are provided in Chapter 3.4.

3.2. Overview of Experimental Datasets

In this section a brief description is given regarding the various experimental datasets used in this thesis for validation purposes. This section will cover the facility in which the data was collected, test conditions, instrumentation and profile evolution. As only a general description

of the data is presented in this section, readers are directed to the original works for more detailed descriptions of the datasets and experimental conditions. Note: the coordinate system in this thesis indicates x positive onshore and z positive upward from the bed – i.e. $x = 0$ is at wave paddle and $z = 0$ is at the bed.

LIP Experiments – Roelvink & Reniers (1995)

Facility and Test conditions

The LIP experiments were carried out in the Delta Flume at Delft Hydraulics. The Delta Flume has a length of 225m, width 5m and depth 7m. The bed profile consisted of sand with an average grain diameter of $D_{50} = 0.22\text{mm}$, with a measured average settling velocity of 0.029 m/s. Note: the LIP experiments consisted of two different types irregular breaking waves: 1) erosive conditions and 2) accretive conditions. Both were run using the same conditions except for the wave period and target significant wave height. For the erosive (accretive) case, the target peak wave period was 5s (8s) and the target significant wave height was 1.4m (0.6m).

During the LIP experiments, narrow-banded, random waves were generated by a wave paddle to produce a stable erosive and accretive beach consecutively. In total, 8 different experiments were run: Tests 1a-c and 2a-e. The initial bed profile was flat in test 1a. As the tests progressed, the final profile of 1a was used as the initial profile of Test 1b, the final profile of Test 1b as the initial profile of 1c and so on until the final test was completed. As mentioned above, the measurements in the LIP dataset were carried out under two types of irregular waves, leading to different morphological development in each of the observed cases. Only Test 1b and 1c are used in this thesis. Test 1b was carried out in erosive conditions and Test 1c in accretive conditions. Each test run had a duration of 60 minutes. With Test 1b consisting of 18 runs and 1c consisting of 13 runs, the total run times were 18hrs and 13hrs respectively. However, only 7 runs were used from the erosive case and 7 from the accretive case. Details of which runs were used are provided in the Tables below.

In the erosive case (Test 1b) the breaker bar developed throughout the duration of the runs, with the bar crest increasing in height and migrating in the offshore direction. In the accretive case, Test 1c, strong plunging breakers were predominant, with bar development seen to be more significant and bar migration occurring in the onshore direction. Though it is difficult to

set one particular cross-shore location as the breaking or plunging (spilling) point under irregular wave conditions, estimations were made for the purpose of comparison between measured and computed concentration. Based on hydrodynamics, profile evolution and corresponding sediment concentration measurements the breaking point was estimated to be at $x = 134\text{m}$ (136m) and plunging point at $x = 138\text{m}$ (145m) for the erosive (accretive) case. Based on these points, the shoaling zone is estimated to be around $120 < x \leq 125\text{m}$ ($130 < x \leq 134\text{m}$), breaking zone around $125 < x \leq 152\text{m}$ ($134 < x \leq 152\text{m}$) and inner-surf zone around $152 < x \leq 170\text{m}$ ($152 < x \leq 170\text{m}$) for the erosive (accretive) case.

Table 3 - Summary of experimental conditions for the LIP Experiments

| | |
|---|--|
| Flume | Delta Flume at Delft Hydraulics: L225m x W5m x D7m |
| Breaker bar | Yes. Erosive case: offshore bar migration, accretive case: onshore bar migration |
| Mobile sand bed | Yes: $D_{50} = 0.22\text{mm}$ |
| Measured settling velocity | Erosive case: 0.03m/s , accretive case: 0.028m/s |
| Regular or Irregular waves | Irregular (erosive and accretive) |
| Breaker types | Spilling and plunging |
| Offshore wave height (H_{m0}) | erosive case: 1.4m , accretive case: 0.6m |
| Offshore wave period (T) | erosive case: 5s , accretive case: 8s |
| Duration of runs and number of repeats | erosive case: $18 \times 1\text{hr}$ runs, accretive case: $13 \times 1\text{hr}$ runs |
| Number of cases used in present study | 7 erosive cases + 7 accretive cases = 14 cases |

Table 4 - Overview of Test 1B conditions used

| t (mins) | Run No. | x (m) | H (m) | Hb (m) | d (m) | T (s) | CS zone |
|-----------------|----------------|--------------|--------------|---------------|--------------|--------------|----------------|
| 00-60 | 1B0102 | 65 | 0.84 | 0.95 | 2.30 | 4.81 | SH |

| | | | | | | | |
|----------|--------|-----|------|------|------|------|----|
| 120-180 | 1B0304 | 115 | 0.64 | 0.73 | 1.58 | 4.96 | SH |
| 900-960 | 1B1605 | 130 | 0.59 | 0.67 | 1.21 | 5.02 | SH |
| 960-1020 | 1B1706 | 138 | 0.46 | 0.52 | 0.83 | 5.02 | BR |
| 360-420 | 1B0707 | 145 | 0.40 | 0.45 | 0.92 | 5.02 | BR |
| 420-480 | 1B0808 | 152 | 0.37 | 0.42 | 0.97 | 5.02 | IS |
| 540-600 | 1B1010 | 170 | 0.26 | 0.29 | 0.38 | 5.02 | IS |

Table 5 - Overview of Test 1C conditions used

| t (mins) | Run No. | x (m) | H (m) | Hb (m) | d (m) | T (s) | CS zone |
|-----------------|----------------|--------------|--------------|---------------|--------------|--------------|----------------|
| 00-60 | 1C0102 | 65 | 0.44 | 0.74 | 2.25 | 7.986 | SH |
| 60-120 | 1C0204 | 115 | 0.45 | 0.75 | 1.62 | 7.968 | SH |
| 180-240 | 1C0405 | 130 | 0.44 | 0.73 | 1.17 | 7.981 | SH |
| 300-360 | 1C0615 | 134 | 0.44 | 0.73 | 0.97 | 7.977 | BR |
| 480-540 | 1C0908 | 152 | 0.33 | 0.55 | 1.01 | 7.977 | BR |
| 540-600 | 1C1009 | 160 | 0.33 | 0.54 | 0.51 | 7.971 | IS |
| 600-660 | 1C1110 | 170 | 0.24 | 0.39 | 0.41 | 7.972 | IS |

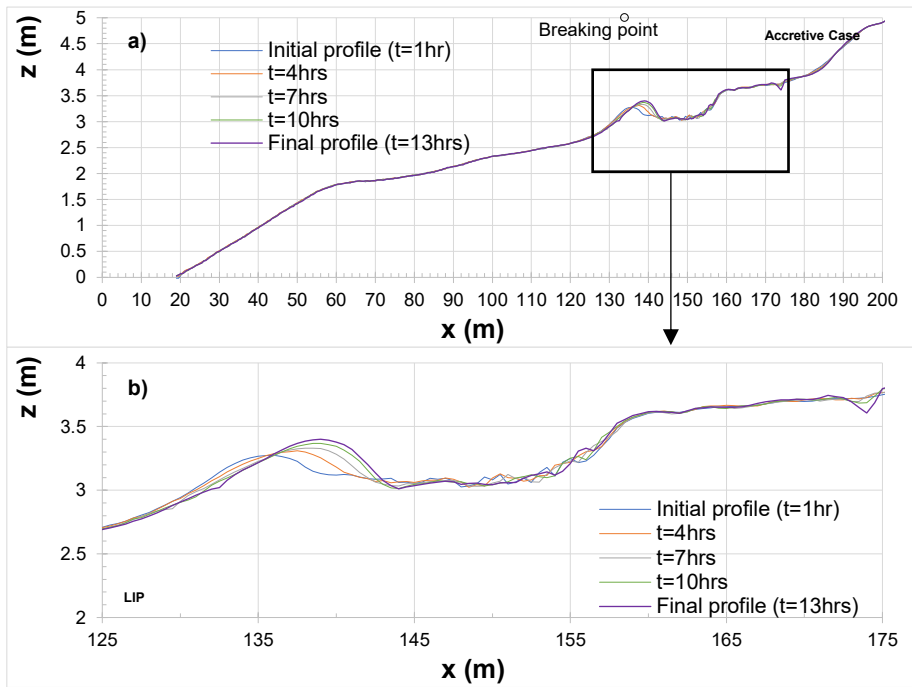


Figure 1 - Cross-shore profile evolution of LIP Experiments (Erosive case). a) shows whole cross-shore profile, b) shows zoom in of breaking zone

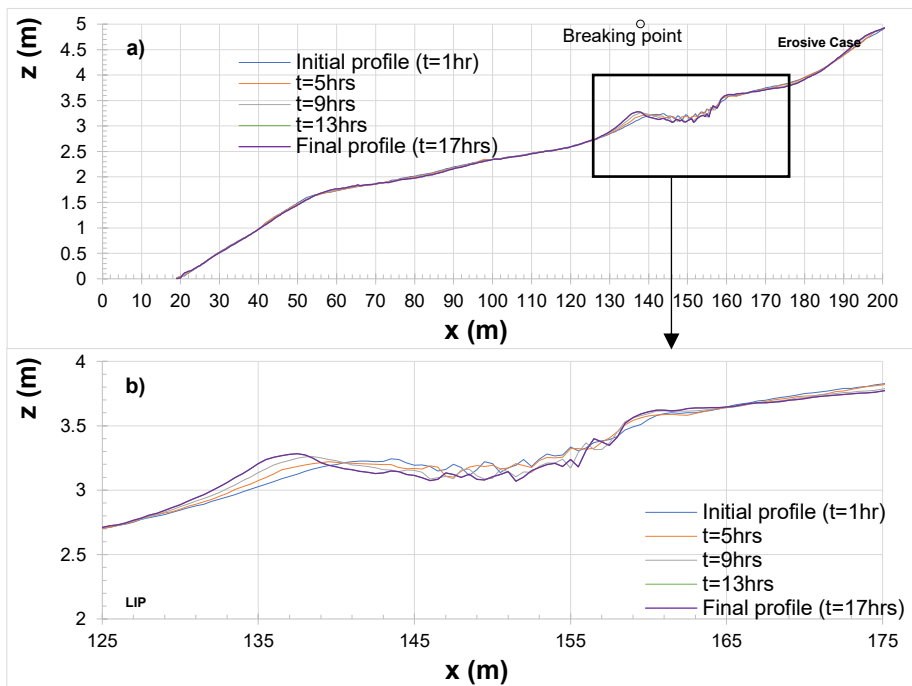


Figure 2 - Cross-shore profile evolution of LIP Experiments (Accretive case). a) shows whole cross-shore profile, b) shows zoom in of breaking zone

Instrumentation

Water surface elevations were taken using two surface-following wave gauges for regions outside of the breaking zone, but for the breaking zone, one Resistance Wave Gauge (RWG) was used. The PROVO (Profiel Volger: Dutch for Profile Follower) was used, providing a combination of echo sounding and rod displacement measurements to obtain the bottom profile measurements. The data from the echo sounder was used wherever possible, but where anomalous data was produced, the data from the wheel recording was used instead. A total of 3 profile transects were taken, one in the middle of the flume and two at distances of 0.85m from the flume walls (either side of the middle transect) and later averaged. The profile data was measured at a spatial resolution of 0.01m.

Electromagnetic field (EMF) current meters were used to measure the flow velocity in the water column. A total of 10 EMF current meters were used: 5 were positioned at an elevation equal to 1/3 of the local water depth, and the other 5 were mounted onto a mobile measurement carriage at elevations of 0.10m, 0.20m, 0.40m, 0.70m and 1.10m above the bed.

The mean suspended sand concentration was measured by transverse suction. A total of 10 suction samplers were deployed, each taking 10L samples of water-sediment. The content of sand present in the samples was determined by measuring the volume in pre-calibrated glass tubes. The velocity and sand concentration measurements were taken at numerous cross-shore locations between $x = 65$ -170m.

CROSSTEX Experiments – Yoon & Cox (2010)

Facility and Test conditions

The CROSSTEX dataset was measured in the O H Hinsdale Laboratory of Oregon State University. The flume is a large-scale flume with length 104m, width 3.7m and depth 4.6m. A bed profile was made consisting of sand with average grain diameter $D_{50} = 0.22$ mm with a computed settling velocity of 0.032 m/s. Note: just like the LIP dataset, the CROSSTEX experiments consisted of two different types irregular breaking waves: 1) erosive conditions and 2) accretive conditions. Both were run using the same conditions except for the wave period and target significant wave height. For the erosive (accretive) case, the target peak wave period was 4s (7s) and the target significant wave height was 0.6m (0.4m).

For the erosive case and accretive case, 11 runs (E1-E11) and 9 runs (A1-A9) were carried out respectively. Both spilling and plunging breakers were observed in the erosive and accretive cases, but spilling breakers were prevalent in the erosive case and plunging breakers prevalent in the accretive case. Each experimental run lasted around 15 minutes, with only a few runs in the accretive case running for 45 minutes. The total run time for the erosive and accretive cases were 180mins and 300mins respectively.

The initial bed profile for the erosive case was planar. Runs E1-E6 were carried out at the same cross-shore location, until a quasi-equilibrium was reached in the beach. The mobile measurement frame was then moved to 5 additional cross-shore locations for Runs E7-E11. Similarly, for accretive case, the mobile measurement frame was stationed at two different locations near the offshore end of the surf zone during Runs A1-A4. The frame was then moved to 5 other cross-shore locations where further velocity/concentration measurements were carried out for Runs A5-A9.

As mentioned above, the bed profile in the erosive case was initially planar. The formation of a sand bar was observed, with offshore bar migration in the erosive case. The accretive case saw the barred bed being restored to a planar bed, with onshore migration of the bar. Though the breaking/plunging points were not explicitly stated by Yoon & Cox (2010), the breaking point (breaking initiation) was estimated to be at around $x = 61\text{m}$ and the plunging point (for waves that plunged) was estimated to be at approximately $x = 63.7\text{m}$ for the erosive cases. For the accretive cases, the breaking point was estimated to be around $x = 63.7\text{m}$ and the plunging point at $x = 65.5\text{m}$. Although in the erosive case, breakers were predominantly spilling and in the accretive, predominantly plunging, for simplicity, the point at which the wave spills or plunges in erosive cases will also be referred to as the plunging point throughout this thesis. Based on these points, it is estimated that the shoaling zone is around $57 < x \leq 61\text{m}$ ($57 < x \leq 63\text{m}$), the breaking zone around $61 < x \leq 64\text{m}$ ($63 < x \leq 67\text{m}$) and the inner-surf zone around $64 < x \leq 72\text{m}$ ($67 < x \leq 75\text{m}$) for the erosive (accretive) cases.

Table 6 - Summary of experimental conditions for the CROSSTEX Experiments

| | |
|--------------|--|
| Flume | O H Hinsdale Laboratory, Oregon State University – L104m x W3.7m x D4.6m |
|--------------|--|

| | |
|--|--|
| Breaker bar | Yes: Erosive case – offshore bar migration, accretive case – onshore bar migration |
| Mobile sand bed | Yes: $D_{50} = 0.22\text{mm}$ |
| Measured settling velocity | N/A – computed settling velocity $\approx 0.032\text{m/s}$ |
| Regular or Irregular waves | Irregular (erosive and accretive) |
| Breaker types | Spilling and plunging |
| Offshore wave height (H_0) | erosive case: 0.6m, accretive case: 0.4m |
| Offshore wave period (T) | erosive case: 4s, accretive case: 7s |
| Duration of runs and number of repeats | 15-45min runs, erosive case: total 180mins, accretive case: total 300mins |
| Number of cases used in present study | 11 erosive cases + 9 accretive cases = 20 cases |

Table 7 - Overview of Erosive Test conditions

| t (mins) | Run No. | x (m) | H (m) | H_b (m) | d (m) | T (s) | CS zone |
|-----------------|----------------|--------------|--------------|--------------------------|--------------|--------------|----------------|
| 165-180 | E11 | 60.04 | 0.545 | 0.545 | 0.681 | 3.99 | SH |
| 00-15 | E1 | 63.7 | 0.4372 | 0.518 | 0.702 | 4.01 | BR |
| 15-30 | E2 | 63.7 | 0.4264 | 0.525 | 0.729 | 4.02 | BR |
| 30-45 | E3 | 63.7 | 0.4221 | 0.538 | 0.747 | 4.01 | BR |
| 45-60 | E4 | 63.7 | 0.4194 | 0.538 | 0.777 | 3.99 | BR |
| 60-75 | E5 | 63.7 | 0.4191 | 0.546 | 0.784 | 3.97 | BR |
| 75-90 | E6 | 63.7 | 0.4166 | 0.547 | 0.81 | 3.97 | BR |
| 150-165 | E10 | 63.7 | 0.4165 | 0.538 | 0.817 | 4.00 | BR |
| 90-105 | E7 | 65.54 | 0.3672 | 0.578 | 0.624 | 4.00 | IS |

| | | | | | | | |
|---------|-----------|-------|--------|-------|-------|------|----|
| 105-120 | E8 | 67.37 | 0.3216 | 0.591 | 0.612 | 4.00 | IS |
| 120-135 | E9 | 71.03 | 0.2765 | 0.584 | 0.556 | 4.00 | IS |

Table 8 - Overview of Accretive Test conditions

| t (mins) | Run No. | x (m) | H (m) | Hb (m) | d (m) | T (s) | CS zone |
|----------|-----------|-------|--------|--------|-------|-------|---------|
| 255-270 | A9 | 60.04 | 0.4518 | 0.452 | 0.738 | 7.27 | SH |
| 00-15 | A1 | 63.7 | 0.3515 | 0.455 | 0.644 | 7.28 | BR |
| 30-75 | A3 | 63.7 | 0.3723 | 0.45 | 0.636 | 7.27 | BR |
| 90-135 | A5 | 63.7 | 0.3808 | 0.46 | 0.634 | 7.25 | BR |
| 180-225 | A7 | 63.7 | 0.3362 | 0.436 | 0.607 | 7.23 | BR |
| 15-30 | A2 | 65.54 | 0.3402 | 0.455 | 0.753 | 7.24 | BR |
| 75-90 | A4 | 65.54 | 0.3486 | 0.444 | 0.752 | 7.23 | BR |
| 135-180 | A6 | 67.37 | 0.3617 | 0.437 | 0.731 | 7.24 | BR |
| 240-255 | A8 | 74.69 | 0.302 | 0.45 | 0.536 | 7.23 | IS |

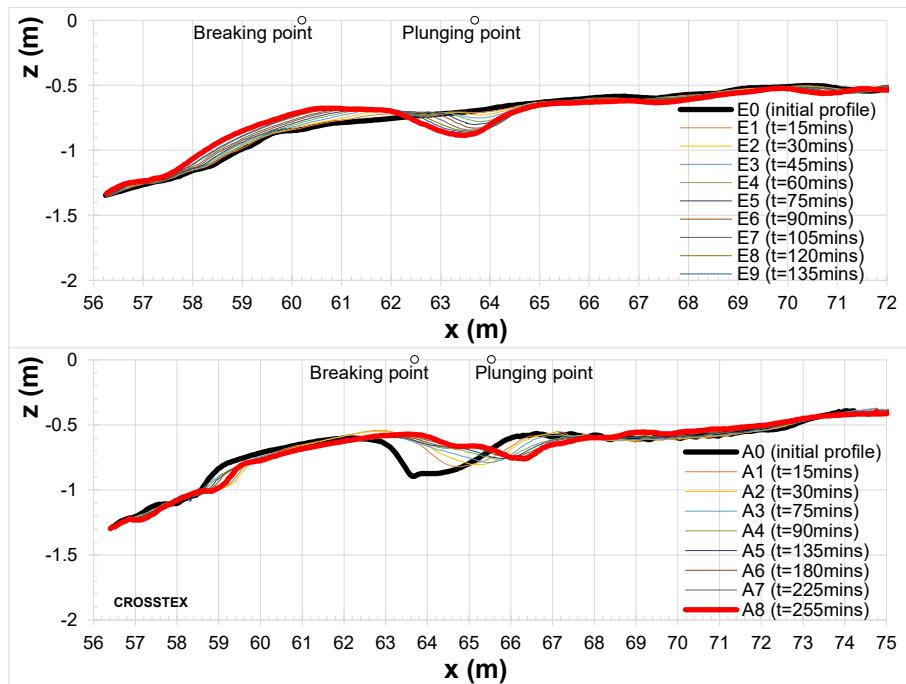


Figure 3 - Cross-shore profile evolution of CROSSTEX Experiments.
a) shows erosive case, b) shows accretive case

Instrumentation

Water surface elevations were measured using 10 Resistance Wave Gauges (RWGs) mounted on the walls of the wave flume. Between the shoaling and breaking zones where sharp increases in wave height were observed, 5/10 wave gauges were set up at approximately 3.65m intervals. The bottom profile was surveyed using a multiple transducer array. This array was mounted on the mobile measurement frame along with other instruments.

Flow velocities throughout the whole water column were measured using 6 Acoustic Doppler Velocimeters (ADV) which were deployed at 0.01m, 0.05m, 0.09m, 0.20m, 0.31m and 0.50m above the bed. The ADVs also simultaneously measured the suspended sediment concentration at the same elevations above bed. Additionally, Fibre-Optic Backscatter Sensors (FOBS) were deployed at 14 elevations ranging from 0.01m to 0.32m above the bed. The sampling rate for the FOBS was 10 Hz.

SandT-Pro Experiments – Ribberink et al. (2014)

Facility and Test conditions

The SandT-Pro dataset was measured in the Canal d'Investigació i Experimentació Marítima (CIEM) Flume in the Polytechnic University of Catalunya (UPC) Barcelona. The CIEM Flume is a large-scale flume with a length of 100m, width of 3m and depth of 4.5m. Note: Two different experiments were run: Regular Breaking 1 (RB1) and Regular Breaking 2 (RB2). Only the RB1 experiments are covered in this thesis, and henceforth all reference to the SandT-Pro dataset is referring to the RB1 experiments. A mobile bed (with offshore bed slope was 1:10) was made in the flume consisting of sand with an average grain diameter $D_{50} = 0.246\text{mm}$ with a measured settling velocity of 0.034 m/s.

As the name of the experiment suggests, the experiment consisted of regular plunging breaking waves (with offshore wave height = 0.85m and wave period = 4s), which ran over the mobile bed for 15-30 minute periods, after which the wave-paddle was stopped and the mobile measurement frame was moved to a different cross-shore location – covering the shoaling, breaker and inner surf zones. In between each test run, the bed profile was measured – details on the procedure for bed profile measurement is provided below. Altogether 13 runs, each lasting 15-30mins were run, with a total of 365mins running time. Although the initial bed

profile was flat – i.e. there was no breaker bar, the bed profile evolved from planar to a barred profile, with some onshore bar migration. After 365mins the bar had fully developed, with a length of approximately 7m and height 60cm, and trough length of approximately 5m with maximum depth of 25cm (Ribberink et al., 2014). Wave breaking initiated at approximately $x = 54\text{m}$, reported to be approximately 2m before the bar crest (Ribberink et al., 2014). The breaking waves plunged at $x = 57\text{m}$ (plunging point) just after the bar crest. The shoaling zone was located around approximately $51 < x \leq 54\text{m}$, the breaking zone around $54 < x \leq 59\text{m}$ and the inner-surf zone around $59 < x \leq 65\text{m}$.

Table 9 - Summary of experimental conditions for the SandT-Pro Experiments

| | |
|--|---|
| Flume | CIEM Flume at Polytechnic University of Catalunya, Barcelona: L100m x W3m x D4.5m |
| Breaker bar | Yes – onshore bar migration |
| Mobile sand bed | Yes: $D_{50} = 0.246\text{mm}$ |
| Measured settling velocity | 0.034m/s |
| Regular or Irregular waves | Regular monochromatic |
| Breaker types | Plunging |
| Offshore wave height (H_0) | 0.85m |
| Offshore wave period (T) | 4s |
| Water depth at wave paddle | 2.55m |
| Duration of runs and number of repeats | 13runs x 15-30mins = total run time of 365mins |
| Number of cases used in present study | Only RB1 test used = 11 cases |

Table 10 - Overview of Test RB1 conditions

| t (mins) | Run No. | x (m) | H (m) | Hb (m) | d (m) | T (s) | CS zone |
|----------|---------|-------|-------|--------|-------|-------|---------|
| 150-180 | 14 | 51 | 0.81 | 0.50 | 1.12 | 4.00 | SH |
| 225-275 | 18 | 53 | 0.82 | 0.43 | 0.91 | 4.00 | SH |
| 15-30 | 2 | 54.5 | 0.70 | 0.63 | 1.18 | 4.00 | BR |
| 30-45 | 4 | 54.6 | 0.71 | 0.61 | 1.06 | 4.00 | BR |
| 00-15 | 1 | 55.6 | 0.68 | 0.61 | 1.18 | 4.00 | BR |
| 30-45 | 3 | 55.6 | 0.70 | 0.62 | 1.12 | 4.00 | BR |
| 150-180 | 12 | 56.5 | 0.49 | 0.49 | 1.09 | 4.00 | BR |
| 45-60 | 5 | 58 | 0.57 | 0.61 | 1.15 | 4.00 | BR |
| 90-120 | 8 | 60 | 0.41 | 0.58 | 1.27 | 4.00 | IS |
| 180-225 | 16 | 60 | 0.34 | 0.47 | 1.36 | 4.00 | IS |
| 120-150 | 10 | 63 | 0.27 | 0.53 | 1.21 | 4.00 | IS |

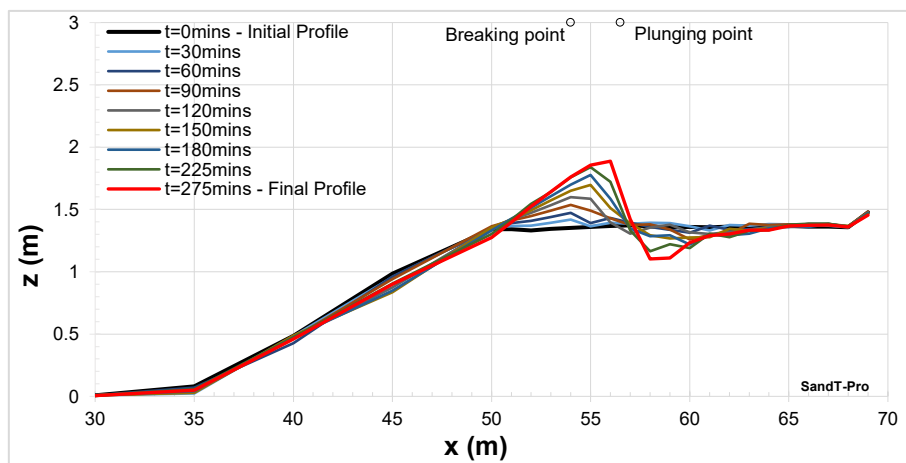


Figure 4 - Cross-shore profile evolution of SandT-Pro Experiments

Instrumentation

A Pressure Transducer (PT) was deployed from a mobile measurement frame to measure the local water surface elevations (i.e. surface elevation at the location of velocity/concentration measurements). An additional 13 Resistive Wave Gauges (RWGs) and 9 PTs were set out to

measure the surface water elevation. The 13 RWGs were spaced out along the flume, and the PTs were located at 1m intervals in the wave breaking region. The dynamic pressure from the PTs were converted to water surface elevation through linear wave theory. Bottom profile measurements were taken using echo sounders along two transects across the wave flume. The data from the two transects were cleaned (removed outliers) and gaps in data linearly interpolated.

In the outer-flow region (i.e. above the WBBL; $z > 0.10\text{m}$; where z = elevation above bed), Acoustic Doppler Velocimeters (ADV) were deployed to measure the flow velocities and/or concentration. In the near-bed region ($0.05\text{m} < z < 0.10\text{m}$), water-sediment velocities and sediment concentrations were measured simultaneously with a vertical resolution of 1.5mm using a High-Resolution Acoustic Concentration and Velocity Profiler (HR-ACVP). The time-averaged suspended sand concentration measurements were taken using a 7-nozzle Transverse Suction System (TSS). The suction samples were retrieved from the TSS, sieved and dry-weighted to obtain the time-averaged SSC.

SINBAD Experiments – van der Zanden et al. (2016)

Facility and Test conditions

The SINBAD dataset (vdZ et al., 2016) was measured in the CIEM Flume in the Polytechnic University of Catalunya (UPC) Barcelona. The CIEM Flume is a large-scale flume with a length of 100m, width of 3m and depth of 4.5m. A mobile bed (with offshore bed slope was 1:10) was made in the flume consisting of sand with an average grain diameter $D_{50} = 0.246\text{mm}$ ($D_{10} = 0.15\text{mm}$ and $D_{90} = 0.37\text{mm}$) with a measured settling velocity of 0.034 m/s.

Experimental tests were run for 90 minutes – six sets of 15-minute runs – during which regular plunging waves (with offshore wave height of 0.85m and wave period 4s) continually passed over the mobile bed and bed profile measurements were taken. After each 90-minute experimental test, the flume was drained, and the bed profile was restored to a pre-determined ‘reference’ profile. This process of running tests for 90 minutes, draining and restoring the profile was repeated 12 times – each time moving the mobile measurement frame to a different cross-shore location (i.e. 12 different cross-shore locations, 6 experimental runs at each location). In total there were 72 test cases. The test section (region where measurements were taken) was 18m long and 1.35m high ($x = 51\text{-}68\text{m}$; where x is the cross-shore coordinate), with

a breaker bar in the surf zone in the initial profile. Over the period of each 90-minute experiment, the bed profile developed, with the bar in particular growing in height and the bar trough deepening. This of course enhanced shoaling and plunging intensity over the course of the experiments (vdZ et al., 2016).

The 12 different cross-shore locations ranged over three cross-shore zones: the shoaling, breaking and inner-surf zones. The wave breaking initiation occurred at $x = 53\text{m}$ (breaking point) and plunged at $x = 55.5\text{m}$ (see Fig. 5) . The splash point was also identified to be at $x = 58.5\text{m}$, the point at which the water is pushed up from the plunge and transforms into a surf bore. Based on these cross-shore points, the shoaling region was defined to be $x \leq 53\text{m}$, the breaking region $53 < x \leq 58.5\text{m}$ and the inner surf zone $x > 58.5\text{m}$.

Table 11 - Summary of experimental conditions for SINBAD Experiments

| | |
|--|---|
| Flume | CIEM Flume at Polytechnic University of Catalunya, Barcelona: L100m x W3m x D4.5m |
| Breaker bar | Yes – onshore bar migration |
| Mobile sand bed | Yes: $D_{50} = 0.246\text{mm}$ |
| Measured settling velocity | 0.034m/s |
| Regular or Irregular waves | Regular monochromatic |
| Breaker types | Plunging |
| Offshore wave height (H_0) | 0.85m |
| Offshore wave period (T) | 4s |
| Water depth at wave paddle | 2.55m |
| Duration of runs and number of repeats | (6 runs x 15mins) x 12 repeats |
| Number of cases used in present study | 72 cases |

Table 12 - Overview of all Runs from t=30-45mins

| t (mins) | Run No. | x (m) | H (m) | Hb (m) | d (m) | T (s) | CS zone |
|----------|---------|-------|-------|--------|-------|-------|---------|
| 30-45 | 3 | 51.0 | 0.79 | 0.73 | 1.14 | 4 | SH |
| 30-45 | 69 | 53.0 | 0.73 | 0.73 | 0.89 | 4 | BR |
| 30-45 | 27 | 54.5 | 0.66 | 0.73 | 0.79 | 4 | BR |
| 30-45 | 63 | 55.0 | 0.65 | 0.73 | 0.76 | 4 | BR |
| 30-45 | 15 | 55.5 | 0.53 | 0.73 | 0.58 | 4 | BR |
| 30-45 | 39 | 56.0 | 0.41 | 0.73 | 0.97 | 4 | BR |
| 30-45 | 51 | 56.5 | 0.47 | 0.73 | 1.19 | 4 | BR |
| 30-45 | 21 | 57.0 | 0.45 | 0.73 | 1.38 | 4 | BR |
| 30-45 | 45 | 58.0 | 0.41 | 0.73 | 1.39 | 4 | BR |
| 30-45 | 33 | 59.0 | 0.41 | 0.73 | 1.31 | 4 | BR |
| 30-45 | 9 | 60.0 | 0.41 | 0.73 | 1.25 | 4 | IS |
| 30-45 | 57 | 63.0 | 0.41 | 0.73 | 1.24 | 4 | IS |

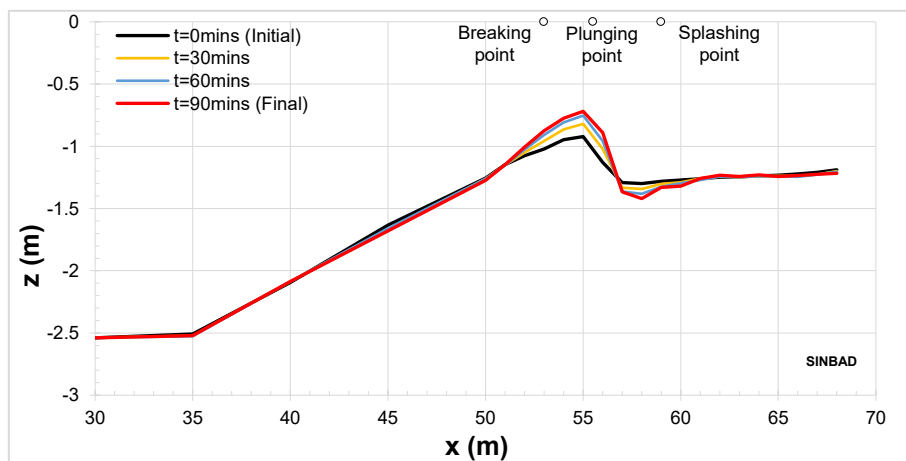


Figure 5 – Cross-shore profile evolution of SINBAD Experiments

Instrumentation

The water surface elevations were measured using Resistive Wave Gauges (RWGs) and Pressure Transducers (PTs) at 21 cross-shore locations. The water level at the measurement

location was taken by an additional PT attached to the mobile frame. The horizontal spatial resolution in the breaking zone was 1m, where PTs were used instead of RWGs due to the wave splash at plunging interfering with the quality of RWG measurements. Linear wave theory was used to convert the dynamic pressure measurements from the PT to water surface elevations.

The bed profile measurements were taken along two transects going across the test area. Echo sounders were deployed at a resolution of 2cm (estimated accuracy of +/- 1cm). The profile measurements from the two transects were averaged and taken to be the profile measurement.

The flow velocities in the outer region and the near-bed region were measured using different instruments, with greater resolution focused on the near-bed region. The outer-flow velocities ($z > 0.10$ m above bed) were measured using three Acoustic Doppler Velocimeters (ADVs) at three vertical elevations above bed, approximately 0.11m, 0.41m and 0.85m above the initial bed. Each ADV operated at an acoustic frequency of 10 MHz and provided cross-shore u , lateral v , and vertical w velocity measurements at a frequency of 100Hz. The near-bed velocities ($z < 0.10$ m above bed) were measured using a downward-facing High-Resolution Acoustic Concentration and Velocity Profiler (HR-ACVP). The HR-ACVP simultaneously measured the co-located vertical profiles of u & w and the sediment mass concentrations. The acoustic frequency for the HR-ACVP was set to 1 MHz – considerably lower than the ADVs.

The time-averaged suspended sand concentration was measured using a six-nozzle Transverse Suction System (TSS). The nozzle intake diameter of the TSS was 3mm and pump discharge was 1 L/min. The 30mm long nozzles were set parallel to the bed (i.e. perpendicular to wave direction).

3.3. Validation of Models

3.3.1 Reference Concentration (C_0) and Vertical Mixing (M)

It was found that the coefficient of determination (R^2) is strongly affected by the sample size (i.e. the size of the dataset). In the present study, as can be found in Chapter 3 of this report, the number of measured cases varies greatly between each dataset, with the SINBAD experiments having as many as 72 cases, and the SandT-Pro with only 11 cases used. Sample sizes too large produce very high values of R^2 as the coefficient of determination never decreases, but only increases with added data points. On the contrary, sample sizes too small

would also lead to unreliable (very small) values. It is for this reason the root-mean-square error (RMSE) has been used instead to quantitatively compare the performance of the different models. These RMSE values have not been normalised, and therefore are not intended for inter-comparison between datasets, but to compare the performance of the various models against the measured data, and against each other. These RMSE values are summarised in Table 13 in Chapter 3.3.1.7.

3.3.1.1. Mocke & Smith (1992) – MS92

LIP: Figure 6a shows that agreement between measured and computed C_0 is generally reasonable for the erosive case. Figure 7a indicates agreement is good in the shoaling (approx. $x = 115-130\text{m}$ for erosive case) and breaking zones (approx. $x = 135-165\text{m}$ for erosive case). Even at and around the plunging point ($x = 138\text{m}$), where MS92 is seen to under-predict C_0 significantly in other plots (e.g. see Figs. 7e-f), it shows good agreement with the measured data. The magnitude of measured concentration at the spilling/plunging point in Fig. 7a is consistent with that seen in Fig. 7c (approx. $4-5 \text{ kg/m}^3$), which was also measured under erosive irregular wave conditions (predominantly spilling breakers). It is speculated that the difference in observed performance (between Figs. 7a, c and Figs 7e-f) is due to the lower levels of breaking-generated TKE found under spilling breakers as the erosive cases consisted predominantly of spilling breakers. This suggests that the model of MS92 is reasonably adept in modelling reference concentration for non-breaking or spilling wave conditions, where there are lower levels of breaking-induced TKE.

In the accretive case (Fig. 7b), despite breakers being predominantly plunging, the cross-shore variability of measured C_0 is almost linear with steady low levels ($<1 \text{ kg/m}^3$) of SSC throughout all regions, even at the plunging point (approx. $x = 134\text{m}$). This trend is not consistent with the accretive case from the CROSSTEX experiments (Fig. 7d) where there are strong localised increases in measured C_0 at the plunging point ($x = 65.5-67.5\text{m}$). It is speculated that this inconsistency may be a result of some waves propagating over the breaker bar without breaking (further elaborated in Chapter 5.1.3.), inferring that the constant low levels of measured SSC observed in Fig. 7b are a result of bed shear or sediment remaining in suspension due to residual turbulence. Regardless, Fig. 7b shows that the low levels of C_0 in the shoaling zone (approx. $x = 115-132\text{m}$ for accretive case) and breaking zone (approx. $x = 132-165\text{m}$ for accretive case) are captured reasonably well. Though Fig. 6b indicates that all of the points lie outside of the

factor 2 region, the discrepancies are generally quite small (in the order of 10^0 kg/m^3) in the shoaling and breaking zones.

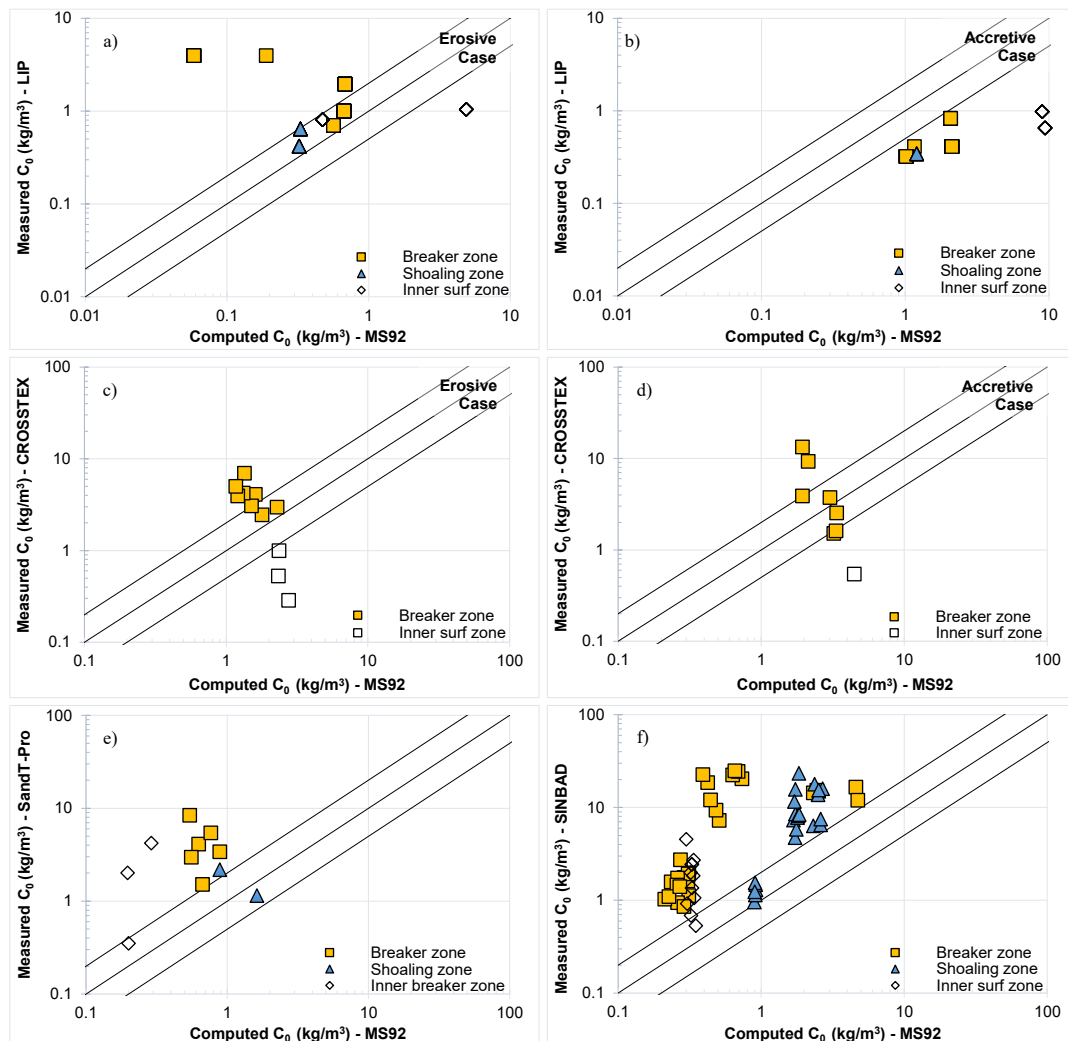


Figure 6 – Measured vs. Computed reference concentration: derived using the model of MS92.

Plot a-b) show the MS92 model validated against LIP erosive and accretive conditions respectively; c-d) show validation against CROSSTEX erosive and accretive conditions respectively; e-f) show validation against the SandT-Pro and SINBAD experiments respectively. The solid line indicates perfect agreement between measured and computed, dotted lines indicate computed values being a factor of 2 larger/smaller than the measured – this is referred to throughout this thesis as the “factor 2 region”.

CROSSTEX: Contrary to the performance against the LIP datasets, Figs. 7c-d show MS92 under-predicting in the breaking zone, in both the erosive ($x = 61\text{-}64\text{m}$) and accretive ($x = 63.7\text{-}67.5\text{m}$) cases. The level of discrepancy between measured and computed C_0 is not as high in the erosive case as the accretive case, with peak concentration levels considerably lower in the

erosive cases ($\approx 5 \text{ kg/m}^3$) than in the accretive cases (peak at $\approx 9.3 \text{ kg/m}^3$, shoreward of the plunging point). The difference in peak concentration is attributed to the predominant breaker types observed in different cases – although both plunging and spilling breakers were present in both test conditions, it was reported that spilling breakers were prevalent in the erosive and plunging breakers in the accretive cases. It is well established in literature that spilling breakers are less effective in entraining and mixing sediment (e.g. vdZ et al. 2017b) with TKE being spread more gradually upon breaking, in comparison to the rapid spreading of TKE induced by plunging breakers.

As briefly mentioned above, significant under-predicting is seen around the plunging point ($x = 65.5\text{-}67.5 \text{ m}$) in the accretive case (Fig. 7d). This is attributed to highly turbulent eddies, induced by wave plunging, invading the WBBL and enhancing bed-shear stresses and entraining sediment as described in Chapter 1.1.1. It is noted that the measured concentration does not peak at the plunging point, but shoreward of the plunging point ($x = 67.37\text{m}$). This is likely due to the effects of horizontal advection, as well as the large-scale eddies continuing to travel obliquely downwards and in the direction of wave propagation as described in Chapter 1. This observation is consistent with that seen in Fig. 7f.

SandT-Pro: Though a couple of the points in Fig. 6e are within the factor of 2 region, the majority indicate considerable under-prediction of C_0 . A quasi-linear computed C_0 variability is observed (Fig. 7e) over the various cross-shore zones with the model of MS92, with considerable under-predicting at almost every cross-shore location. This is especially the case at the plunging point ($x = 56.5\text{m}$) where the discrepancy between measured and computed C_0 is the largest – just over a factor of 12. This is consistent with observations from other datasets, indicating that the strong localised increase in measured C_0 observed at the plunging point is not adequately accounted for by the model of MS92. The level of discrepancy observed at the shoaling ($x = 51\text{-}53 \text{ m}$) and inner surf zones ($x = 60\text{-}63 \text{ m}$) is reasonable, indicating good agreement in these zones.

SINBAD: The 30-45mins test cases (of a total run time of 90mins) were considered in the SINBAD case. This is because there were many instances of data being removed as outliers in other test cases, especially in the highly aerated breaking region (vdZ et al., 2016). The 30-45mins test case did not have missing data in any of the measured regions. Also, it is between 1/3 to 1/2 way through the experiment runs, where the bottom profile and breaker bar have developed quite substantially.

The trends seen in Figs. 6f&7f are generally similar to Figs. 6e & 7e, mainly with respects to the large under-predicting in the breaking zone ($x = 54.5\text{-}59\text{m}$). Although the computed cross-shore variability of C_0 indicates some localised increase in concentration around the plunging point ($x = 55.5\text{m}$), it does not sufficiently reflect the high levels of SSC measured at this point. The computed C_0 at the plunging point was $\approx 4.6 \text{ kg/m}^3$, whereas the measured C_0 is almost four times greater ($\approx 16.5 \text{ kg/m}^3$).

Mixing parameter: The same mixing parameter was used for MS92, SP04, JS07, VR07 and vdZ17. The cross-shore distributions of the mixing parameter M can be seen in the top panels of Figs. 7a-f. The mixing parameter generally captured the localised increases in concentration found at the breaking and plunging points in all cases (M increases at these points). Particularly in Figs. 7a & 7f, the mixing parameter indicates increases in sediment mixing just shoreward of the plunging point. As mentioned in Chapter 1 of this thesis, the combination of trapped bubbles and breaking-generated vortices (generated at the plunging point) enhance sediment mixing throughout the water column. The mixing effects of these turbulent vortices would not be limited to only the plunging point, but also to neighbouring zones as the breaking-induced TKE is advected horizontally. Fernandez-Mora et al. (2016) reported that high in the water column, breaking-generated TKE is partly advected in the offshore direction by undertow and orbital velocities, and party advected in the shoreward direction by onshore velocities under a secondary wave; the remainder of the broken wave (vdZ et al., 2016).

Summary: The level of accuracy varies quite largely between each dataset and also each cross-shore region. The model of MS92 generally performs quite well in the shoaling region, and even in the breaking region, pre-plunging point, for regular waves and irregular erosive wave conditions. Post-plunging however, the MS92 model is not able to capture the strong localised increase in C_0 observed at the plunging point and immediately shoreward of the plunging point. In the accretive conditions, the model shows mixed results, showing poor agreement with the CROSSTEX dataset but reasonable agreement with the LIP dataset. Overall, the model of MS92 does not seem well suited for the breaker (inner-surf zone) where under-(over-)prediction is often observed (see Figs. 7b-d), and though it may perform reasonably well for spilling waves (e.g. erosive case), it is not adept for plunging breaker conditions.

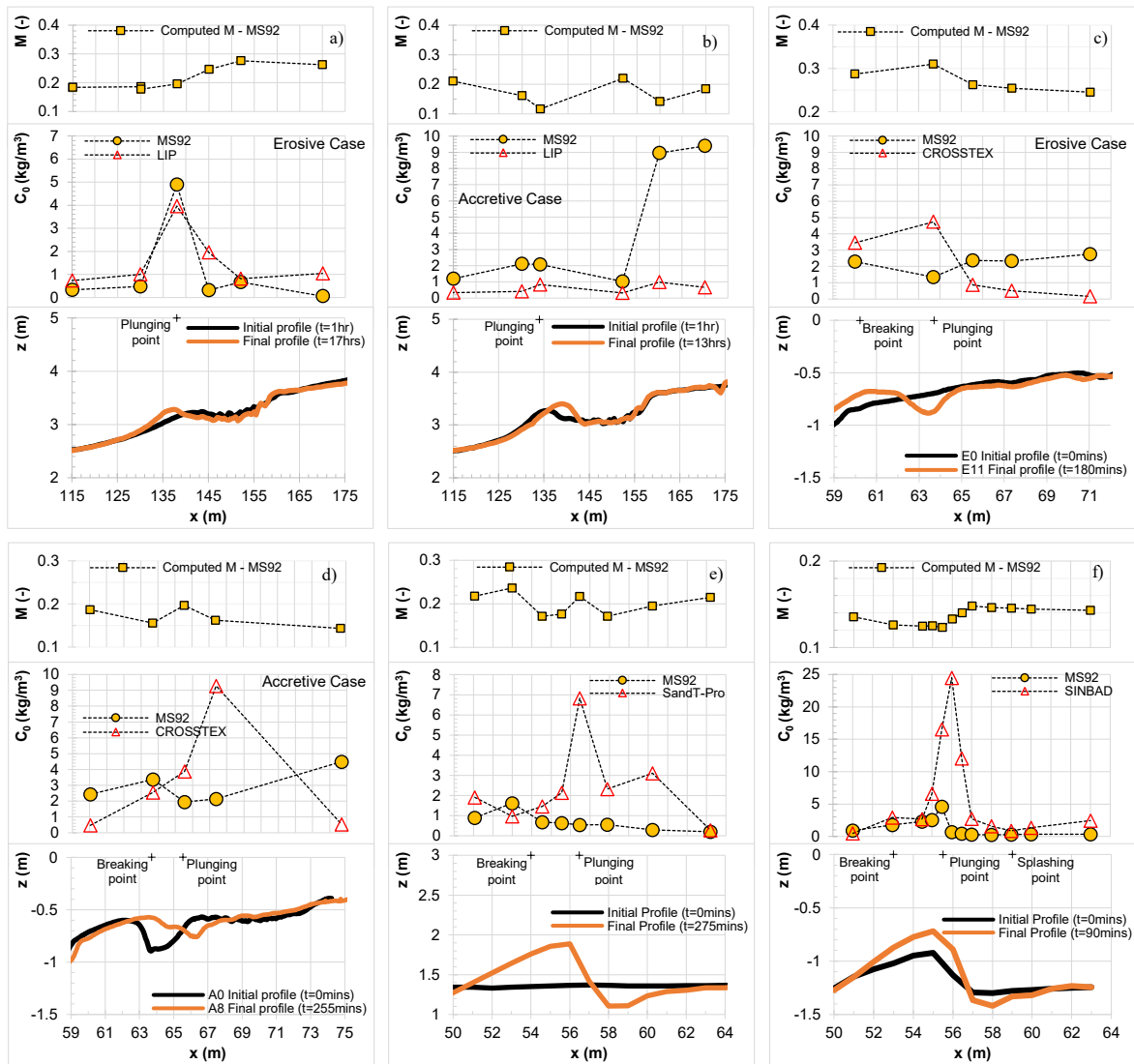


Figure 7 - Cross-shore distributions of mixing parameter (top panels), measured and computed reference concentration (middle panels) and bed profile evolution (lower panels).

Plots a-f) show the MS92 model validated against each of the datasets LIP erosive and accretive cases, CROSSTEX erosive and accretive cases, SandT-Pro and SINBAD respectively.

3.3.1.2. Shibayama & Rattanapitikon (1993) – SR93

LIP: SR93 generally shows poor agreement with measured data, with Figs. 8c-f showing considerable under-predicting in all cross-shore zones – both erosive and accretive, regular and irregular waves (note: 1 point is not shown in Fig. 8a and 1 point not shown in 8b as the discrepancies between measured and computed were too large to fit in the plot range). However, contrary to the trend observed against other datasets, Figs.8a-b indicate some over-predicting, particularly in the shoaling and inner surf zones (Fig. 9a-b). In the accretive case, over-

predicting occurs even at the plunging point ($x = 134\text{m}$), where the cross-shore variability of measured C_0 is constantly low ($<1 \text{ kg/m}^3$) (as seen in Fig.7b).

CROSSTEX & SandT-Pro & SINBAD: almost all of the breaker zone points lie outside of the factor 2 region of Figs.8c-f. Even in the erosive case of CROSSTEX (Fig. 9c) where breakers were a mixture of spilling and plunging waves, the model of SR93 is not able to account for the local increase in C_0 at the spilling/plunging point ($x = 61\text{-}64\text{m}$). This is observed to a greater extent in the accretive case, with larger discrepancies found at the plunging point ($x = 65.5\text{-}67.5\text{m}$). Figures 9e-f indicate that the cross-shore variability of computed C_0 are very similar to that observed in Fig. 7e; they are quasi-linear with largest discrepancies in the breaker zone (between $x = 55.5\text{-}59\text{m}$ for SandT-Pro, and $x = 54.5\text{-}57\text{m}$ for SINBAD) and also early in the inner surf zone (around $x = 60\text{m}$ for SandT-Pro). As seen with the MS92 model, discrepancies are especially large at the plunging point, where there are sharp increases in measured concentration. This localised increase in C_0 at the plunging point is not captured by the SR93 model, with computed C_0 being smaller than measured (Fig. 9e) by a factor of 14. The same is observed against the SINBAD experiments, with even larger discrepancies (see Fig.9f). This is not surprising as the SR93 formulation is driven mainly by the shear velocity and relies on the Shields Parameter to predict sediment pickup. vdZ et al. (2017b) reported that time-averaged reference concentrations showed poor correlation with periodic and time-averaged near-bed velocities, but significant correlation with near-bed time-averaged TKE. As such, the constant under-predicting of computed C_0 in the breaker zone suggests that the model is not adept for strong plunging conditions and needs to more effectively incorporate near-bed TKE to improve the formulation.

Summary: The model of SR93 generally performs reasonably in the shoaling and inner surf zones, with computed C_0 in the correct order of magnitude. It performs poorly in the breaker zone however, especially post-plunging. Instead of computed C_0 increasing (relative to the shoaling zone) at the plunging point as indicated by measured SSC, it decreases. This is due to the key driving parameters (e.g. the near-bottom velocity at the breaking point \hat{u}_b ; Eq.12), which correlate poorly with time-averaged reference concentration, and the Shields Parameter (Eq.4a) formulation which is dependent on the local wave height and water depth. This is discussed further in the validation of the model of SP04 below. Overall, the SR93 model

requires modification to account for the entraining and mixing effects of external breaking-induced TKE.

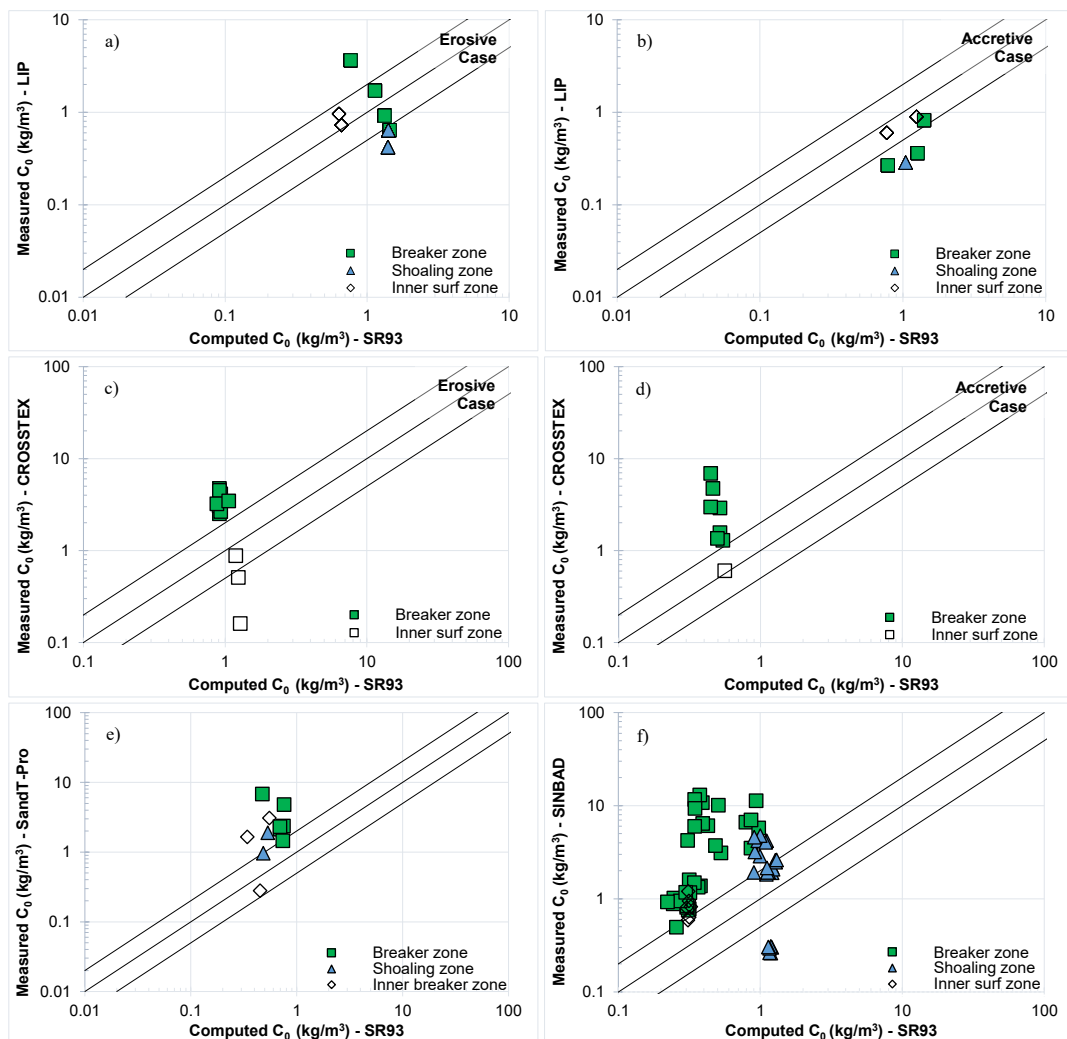


Figure 8 - Measured vs. Computed reference concentration – derived using the model of SR93.

Plot a-b) show the SR93 model validated against LIP erosive and accretive conditions respectively; c-d) show validation against CROSSTEX erosive and accretive conditions respectively; e-f) show validation against the SandT-Pro and SINBAD experiments respectively.

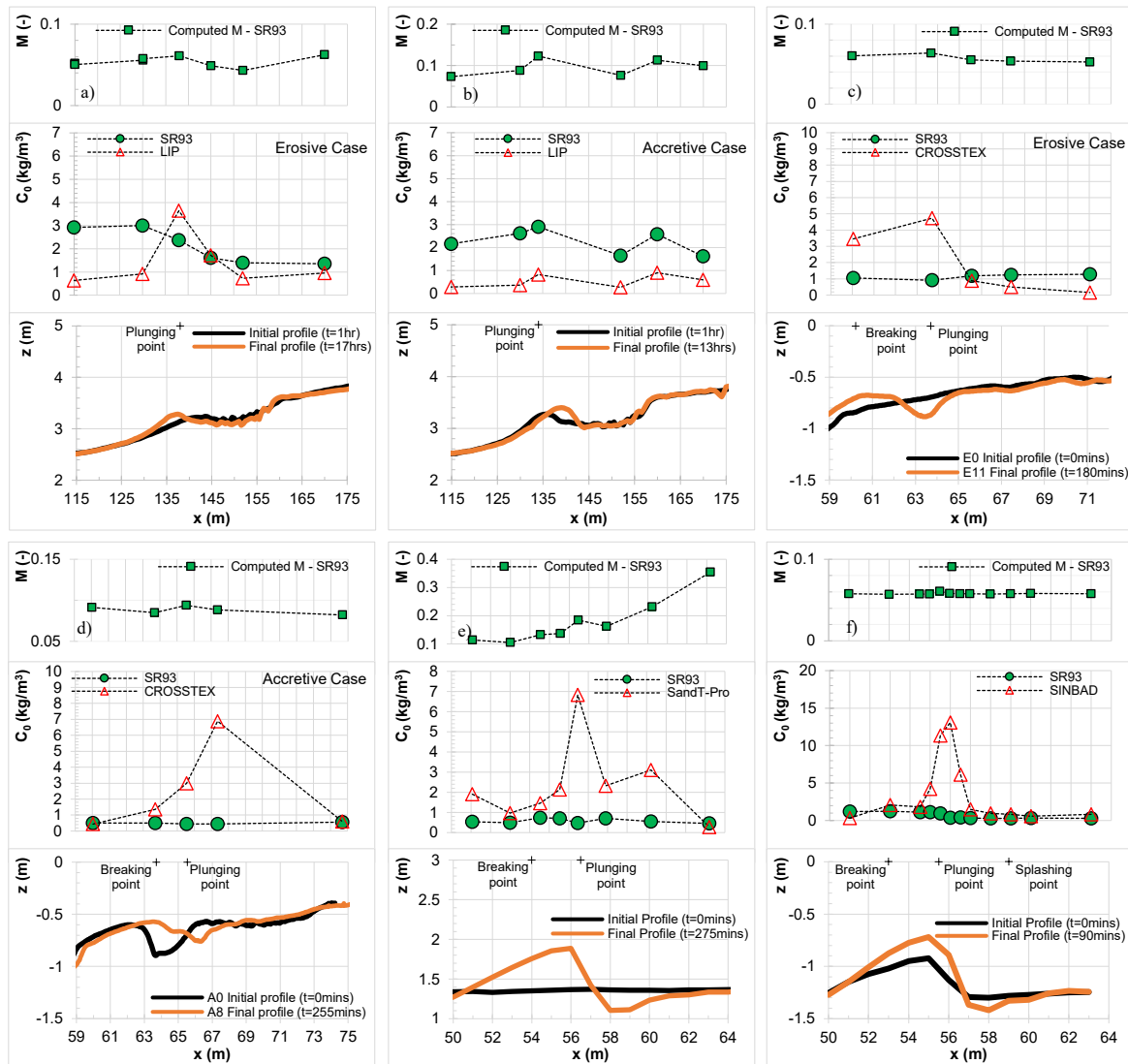


Figure 9 - Cross-shore distributions of mixing parameter (top panels), measured and computed reference concentration (middle panels) and bed profile (lower panels).

Plots a-f) show the SR93 model validated against each of the datasets LIP erosive and accretive cases, CROSSTEX erosive and accretive cases, SandT-Pro and SINBAD respectively.

3.3.1.3. Spielmann et al. (2004) – SP04

SandT-Pro: The model of SP04 shows poor agreement with measured data, with just less than half of the points lying within the factor 2 region in Fig.10e. The computations for the shoaling zone over-predict and those for the inner-surf zone under-predict substantially. Similar to the SR93 and VR07 models, the computed C_0 decreases (relative to the shoaling zone) at the plunging point instead of increasing. This common trend is attributed to the key driving parameters in the SR93, VR07 and SP04 formulations being a function of the local wave height

and water depth - which decline steeply at the plunging point. The wave heights (and water depth) are highest in the shoaling region as the waves shoal, and lowest at the plunging point (see Fig. 12). This trend is reflected in almost all of the cross-shore variability of C_0 for the SP04 model (see Figs. 11a, c-f).

One of the key parameters in the SP04 formulation is the roller energy dissipation term, which is a function of the roller energy term E_r . Different methods/formulae for modelling the roller energy term exist in literature (c.f. Nairn et al., 1990). The empirical method implemented in this study models the roller energy as a function of the local wave height (H) (refer to Eq.10). Considering the relationship between wave height and C_0 shown in Fig. 12, this explains the strong over-prediction of C_0 in the shoaling zone, and the gradual decrease in SSC in the shoreward direction throughout the cross-shore regions (i.e. cross-shore distribution of computed C_0 mirrors cross-shore distribution of measured H , with C_0 being largest in shoaling zone, gradually smaller in breaker zone and smallest in the inner surf zone). It should be noted that the performance of the SP04 model could vary depending on the method/formulation adopted for computation of the roller energy term. It is however beyond the scope of the present study to investigate the effects of different roller energy formulations on resulting reference concentration, and therefore the performance of the SP04 C_0 formula is only tested herein using the empirical method of Svendsen (1984) as specified in Chapter 2.1 (Eq. 10).

LIP & CROSSTEX (Accretive) & SINBAD: The same trend is observed in the LIP, CROSSTEX (accretive) and SINBAD experiments, with the cross-shore C_0 distribution gradually decreasing in the shoreward direction, from the shoaling to inner surf zones. This again is to be expected, as the cross-shore distribution of computed C_0 mirrors the cross-shore wave height variability, as seen in Fig. 12. In the LIP (erosive case), CROSSTEX (erosive and accretive cases) and SINBAD case (Figs. 11a, 11c-d, and 11f respectively), the discrepancy between measured and computed C_0 is highest at the plunging point and just shoreward of the plunging point. It is evident that SP04 is not able to account for the high levels of sediment entrainment induced by breaking-generated vortices post-plunging.

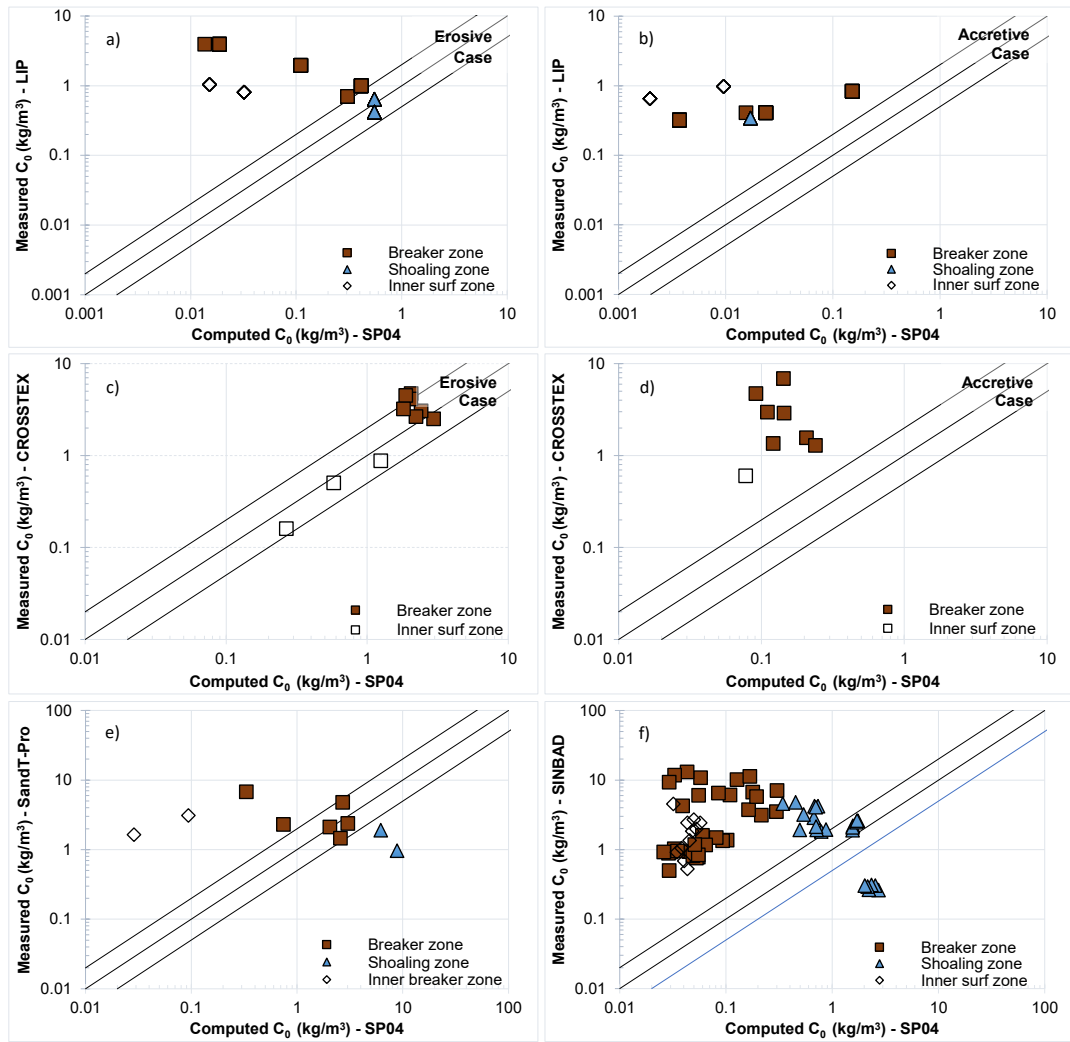


Figure 10 - Measured vs. Computed reference concentration – derived using model of SP04.

Plot a-b) show the SP04 model validated against LIP erosive and accretive conditions respectively; c-d) show validation against CROSSTEX erosive and accretive conditions respectively; e-f) show validation against the SandT-Pro and SINBAD experiments respectively.

Summary: Similar to the trend observed in the validation of SR93, some of the key driving parameters (e.g. roller energy dissipation term) of the SP04 model are strongly dependent on the local wave height. As a result, the SP04 model is highly sensitive to changes in the local wave height. Local wave height decreases at the plunging point (as seen in Fig. 12) and the corresponding computed C_0 also decreases at this point. This leads to large discrepancies between measured and computed C_0 , especially at the plunging point. Alternative formulations of modelling the roller area (see Eq. 10) may result in improved performance.

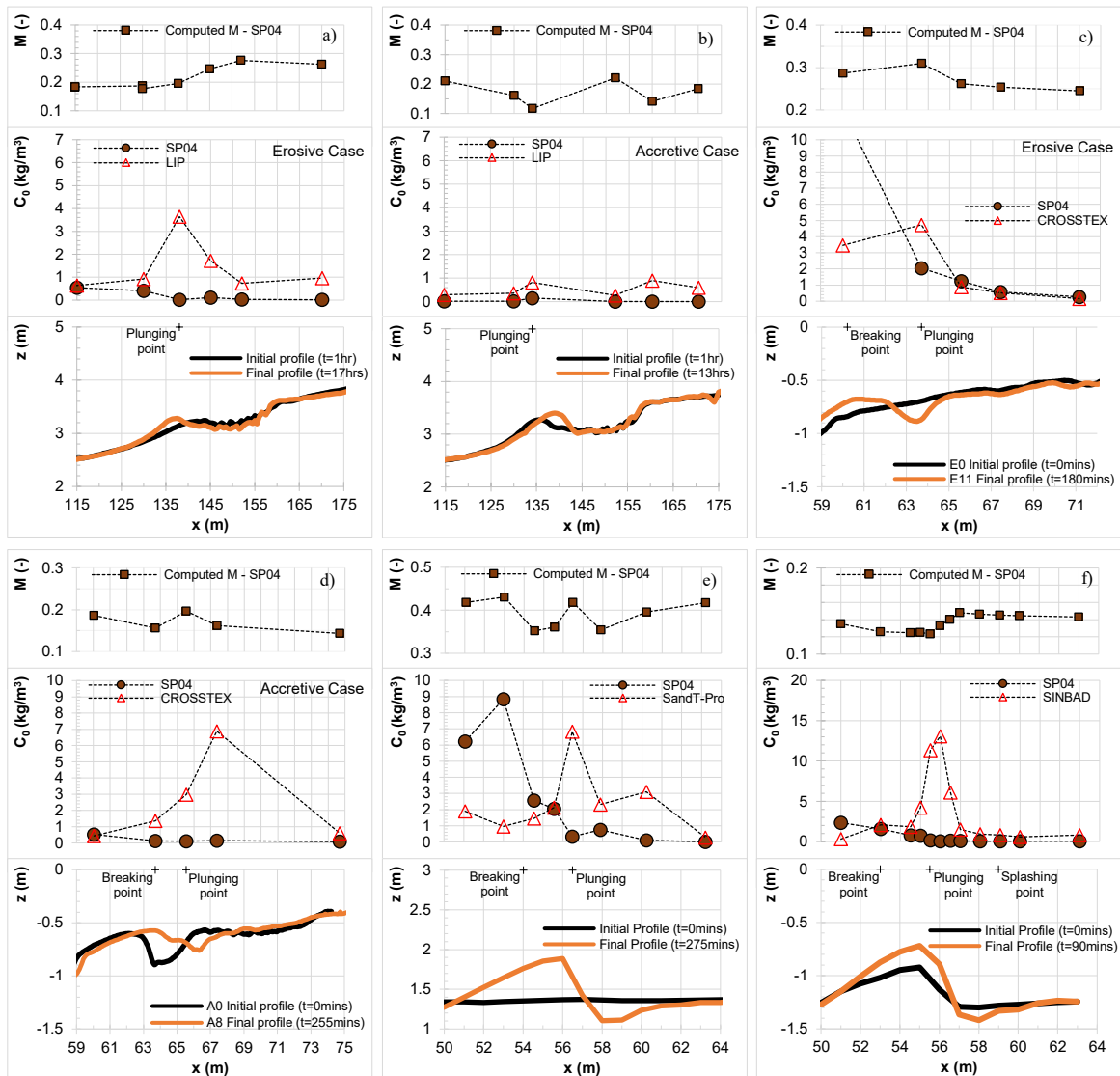


Figure 11 - Cross-shore distributions of mixing parameter (top panels), measured and computed reference concentration (middle panels) and bed profile (lower panels).

Plots a-f) show the SP04 model validated against each of the datasets LIP erosive and accretive cases, CROSSTEX erosive and accretive cases, SandT-Pro and SINBAD respectively.

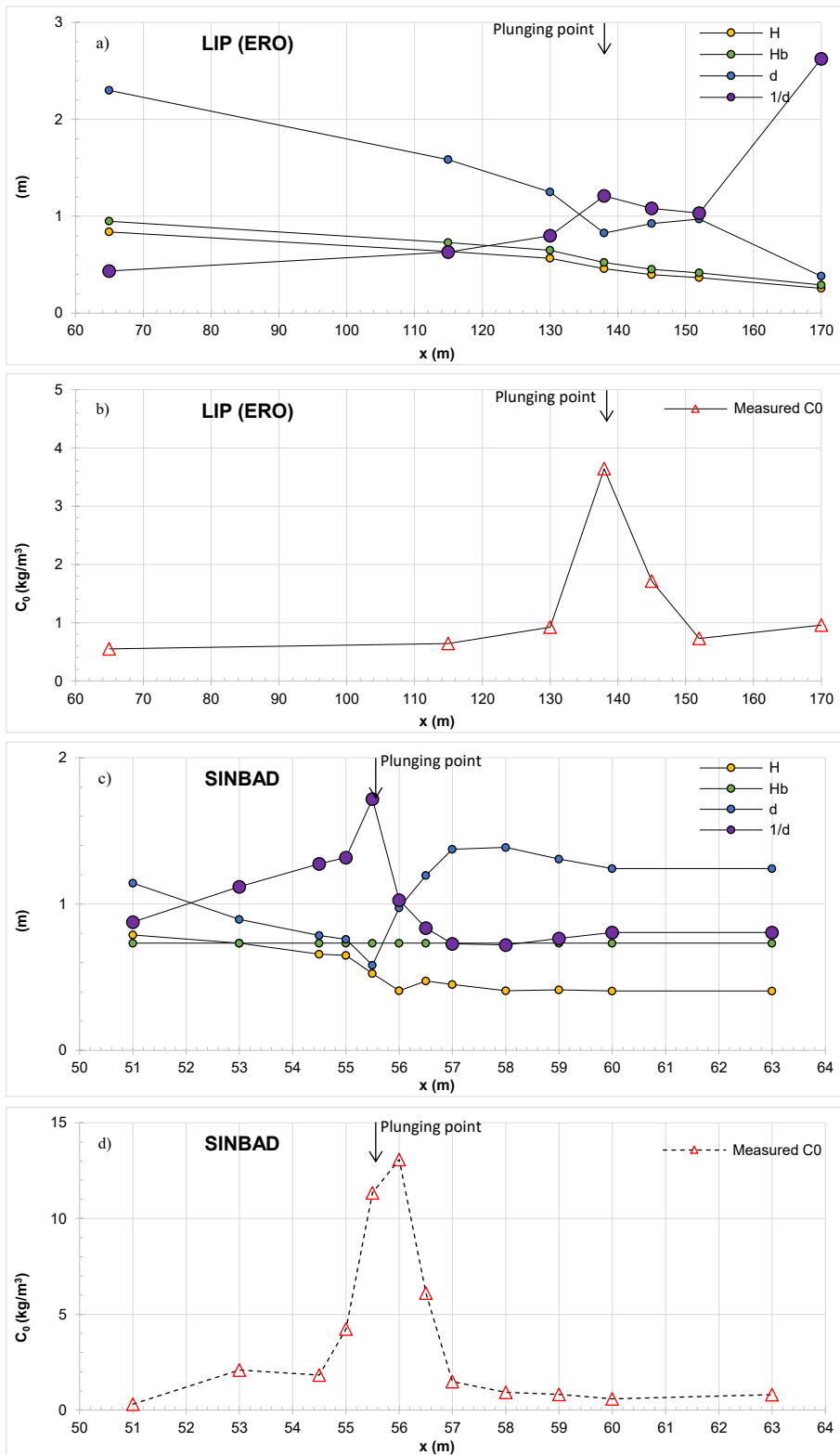


Figure 12 - Cross-shore distributions of local wave height (H), breaker height (H_b), local water depth (d), and inverse water depth (1/d) compared against cross-shore distribution of measured reference concentration (C_0)

Plots a) and c) show the cross-shore variability of wave climate and (inverse) water depth for LIP erosive case and SINBAD experiments respectively. Plots b) and d) show the cross-shore variability of measured reference concentration for LIP erosive case and SINBAD experiments respectively.

3.3.1.4. Jayaratne & Shibayama (2007) – JS07

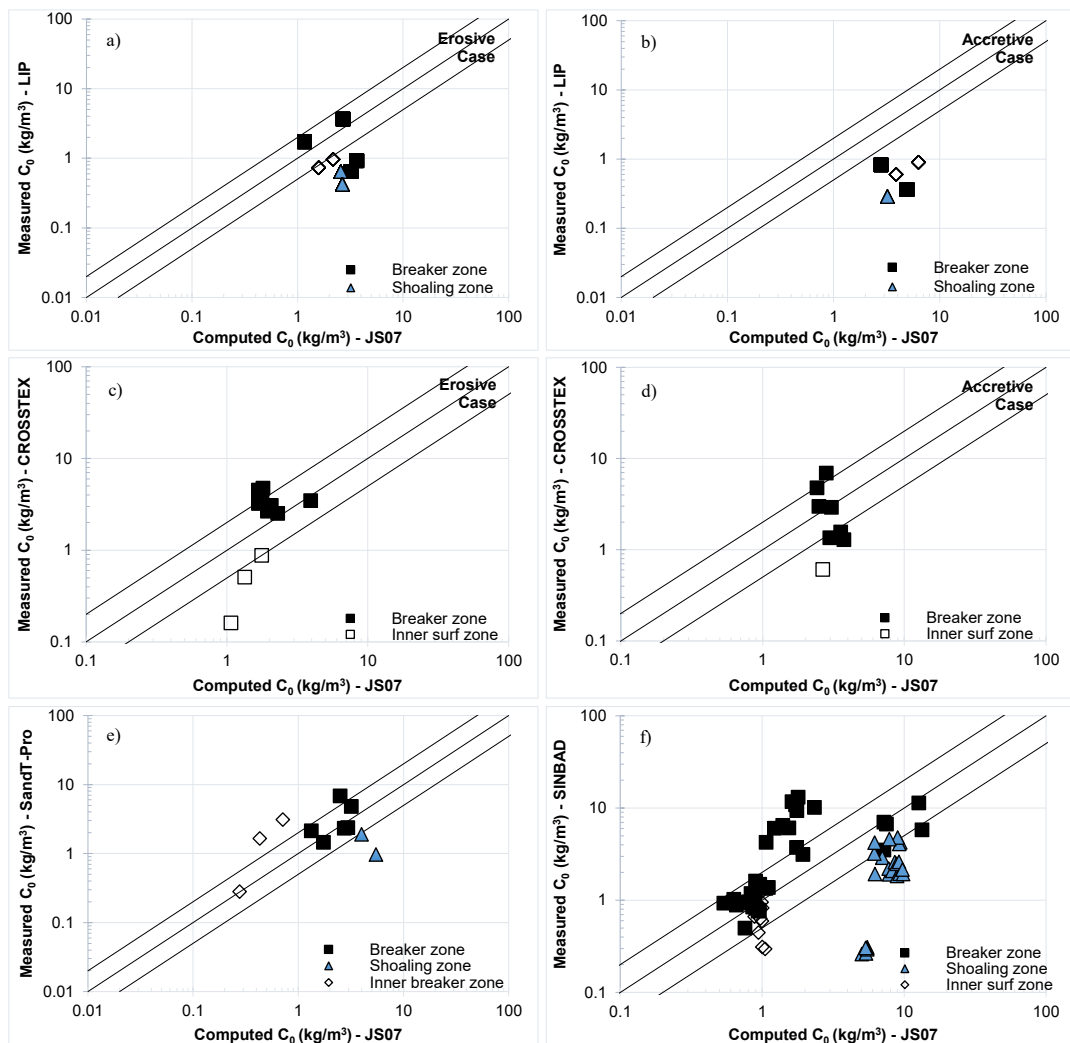


Figure 13 - Measured vs. Computed reference concentration – derived using the model of JS07.

Plot a-b show the JS07 model validated against LIP erosive and accretive conditions respectively; c-d show validation against CROSSTEX erosive and accretive conditions respectively; e-f show validation against the SandT-Pro and SINBAD experiments respectively.

LIP: JS07 shows poor agreement with measured data under the erosive case (Fig. 13a), with the majority of the points lying outside of the factor 2 region (note: 1 point is not shown in Fig. 13a and 2 points not shown in 13b as the discrepancies between measured and computed were too large to fit in the plot range). In Fig. 14 it is seen to over-predict C_0 substantially in the shoaling and inner surf zones. There is however some reasonable-good agreement at the breaking point. As mentioned previously in Chapter 2.1, the model of JS07 was only derived and validated for the breaking region, and as such was not designed to predict SSC in the shoaling and inner surf zones.

CROSSTEX: In Fig. 13c most of the computed vs measured C_0 values from the breaking zone fall within the factor of 2 margin, indicating good agreement with measured data, even at the plunging point for some test cases (e.g. Fig. 14d, $x = 65.5\text{m}$). There is however still discrepancy between measured and computed C_0 near the spilling/plunging point (Fig. 14c-d), both in the erosive (see $x = 63.7\text{m}$) and accretive (see $x = 67.5\text{m}$) cases. This discrepancy is seen to be larger in the accretive cases where breakers were predominantly plunging waves. Also, in the accretive case, large discrepancies are found in the shoaling region, as seen against the SandT-Pro (Fig. 14e) and SINBAD (Fig. 14f) datasets.

SandT-Pro: Figure 13e shows reasonable agreement between measured and computed reference concentration, with the points well-clustered around the 1:1 line, over half of points lying within the +/- factor 2 region. Similar to the models of SR93 and SP04, the model of JS07 is driven by parameters (such as near-bed shear velocity, \hat{u}_b) that are sensitive to local (or breaker) wave height. As a result, JS07 is generally shown to over-predict concentration in the shoaling zone (see Fig. 14a-b and 14d-f), with cases of concentration at the plunging point declining instead of increasing (e.g. Fig. 14e) as seen in the validation of SR93 and SP04. This indicates that the local wave height is a poor driving parameter for cross-shore reference concentration under plunging wave conditions.

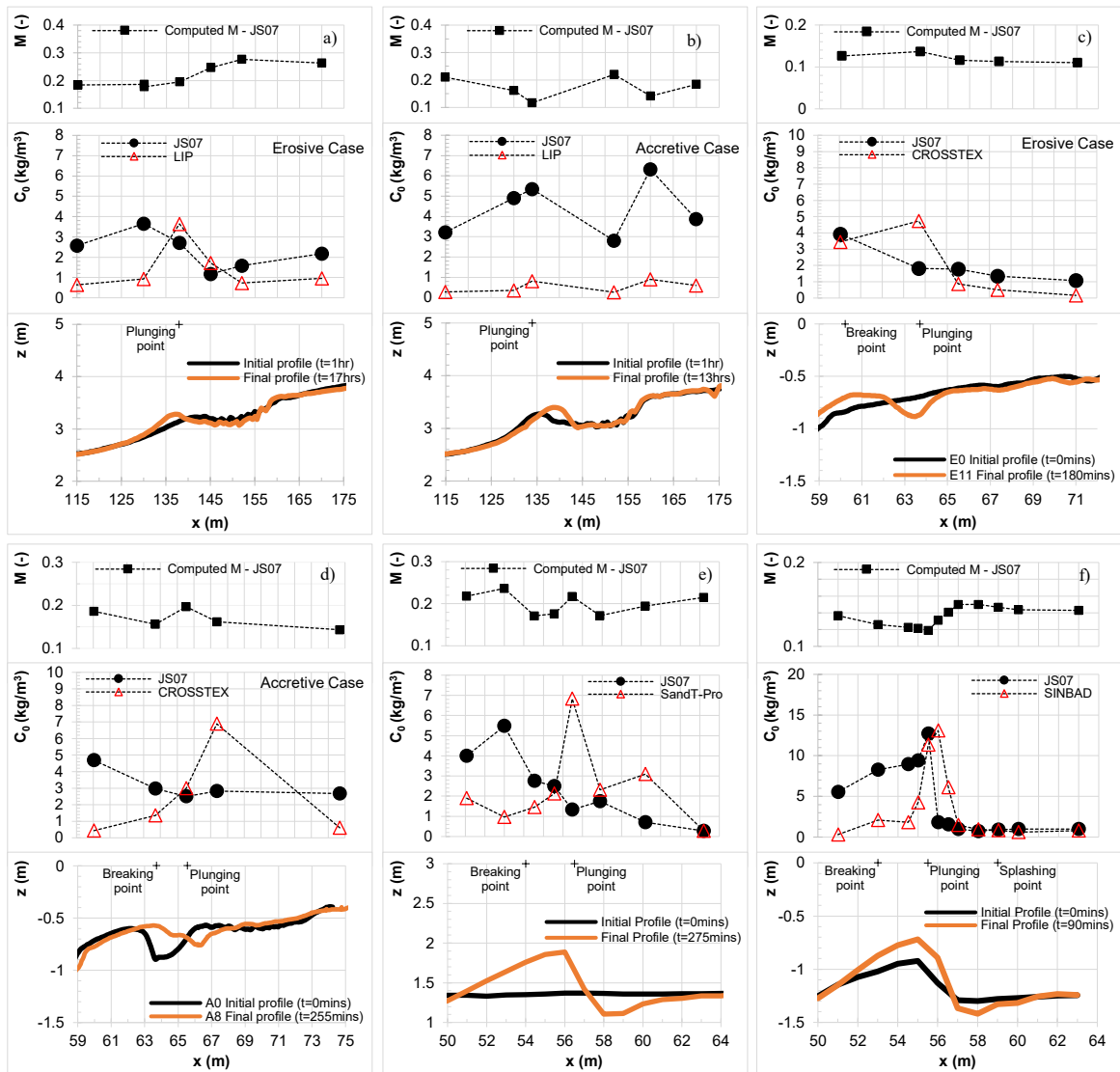


Figure 14 - Cross-shore distributions of mixing parameter (top panels), measured and computed reference concentration (middle panels) and bed profile (lower panels).

Plots a-f show the JS07 model validated against each of the datasets LIP erosive and accretive cases, CROSSTEX erosive and accretive cases, SandT-Pro and SINBAD respectively.

SINBAD: The general trend observed in Fig. 14f is quite good for the breaker and inner surf zones, but indicates some large over-predicting in the shoaling zone, as seen also against the SandT-Pro data (Fig. 14e). Contrary to the trend observed in Fig. 14e, the model of JS07 sufficiently captures the strong localised increase in measured C_0 at the plunging point ($x = 55.5\text{m}$), indicating very good agreement with measured C_0 . However, just after the plunging point ($x = 56\text{m}$) where measured C_0 peaks, there is seen to be a large discrepancy as computed C_0 suddenly drops drastically. This can be attributed to the drop in local wave height (H) after the wave plunging point. The agreement between measured and computed C_0 is very good in the outer breaker zone/inner surf zone (between $x = 57\text{-}63\text{m}$).

Summary: The model of JS07, originally derived only for use in the breaking zone, generally performs well throughout the breaking zone, sometimes even at the plunging point. There are however several instances of the model under-predicting at the plunging point (and just shoreward of the plunging point) where concentration is highest. Similar to the SR93 and SP04 models, the model of JS07 is sensitive to the local wave height, and therefore often over-predicts C_0 in the shoaling zone (where H is highest before breaking, see Fig. 12) and under-predicts at the plunging point (where H is lowest after breaking).

3.3.1.5. Van Rijn (2007) – VR07

SINBAD & CROSSTEX: The model of VR07 shows reasonable cluster around the 1:1 line (Fig. 15), with a fair percentage of points being within the factor 2 region. The computed C_0 measurements for the shoaling and inner surf zone are generally quite good, but as commonly seen in the previous models covered in this section, there is major under-predicting especially around the plunging point in all three plots of Fig. 16, where breaking-induced TKE invades the WBBL. Very similar to the trend observed with the models of MS92, SR93 and SP04, the local increase in C_0 at the plunging point is not captured by the model (Fig. 16) - instead of computed C_0 increasing at the plunging point, it is seen to fall. The validation in this section indicates that reference concentration models driven by bed shear (or Shields Parameter) are not adept for modelling C_0 under plunging breaker conditions, as the effects of surface-generated TKE are not incorporated into the formulations. Such models (e.g. MS92, SR93 and VR07) perform reasonably in non-breaking regions, e.g. shoaling zone. Also, as mentioned in the validation of SR93, vdZ et al. (2017b) reported poor correlations between time-averaged near-bed velocities and time-averaged reference concentration, but good agreement with near-bed TKE. It is thought therefore that VR07 could also be improved by accounting for the high levels of entrainment induced by external breaking-generated TKE, as proposed by vdZ et al. (2017b).

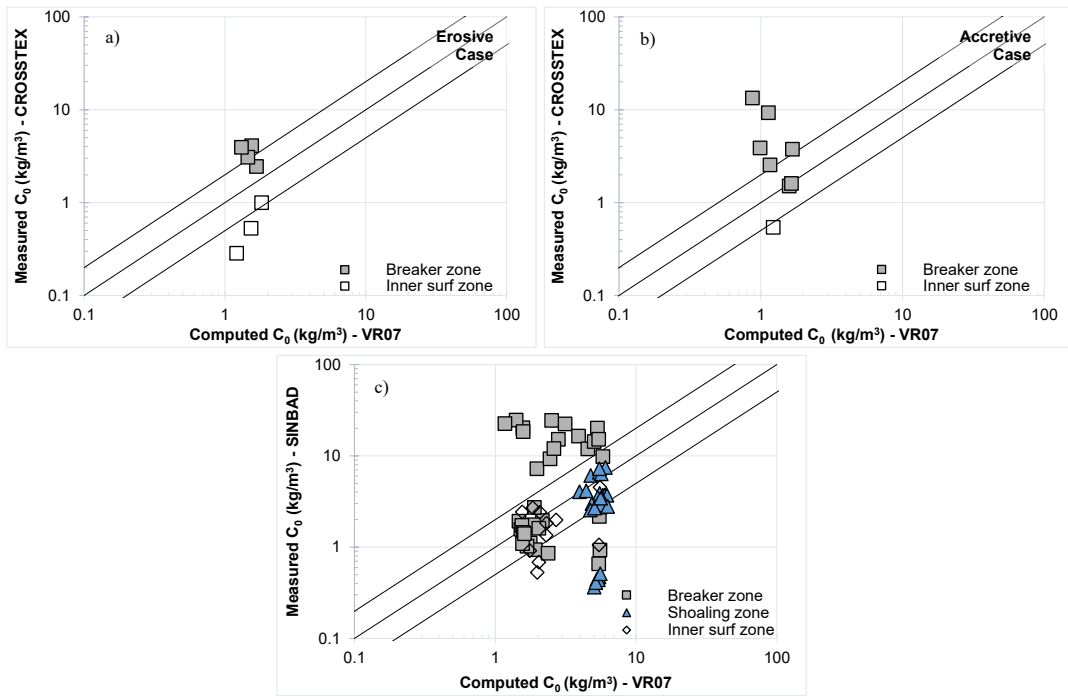


Figure 15 - Measured vs. Computed reference concentration – derived using the model of VR07.

Plot a-b) show the VR07 model validated against CROSSTEX erosive and accretive conditions respectively and Plot c) shows validation against the SINBAD experiments.

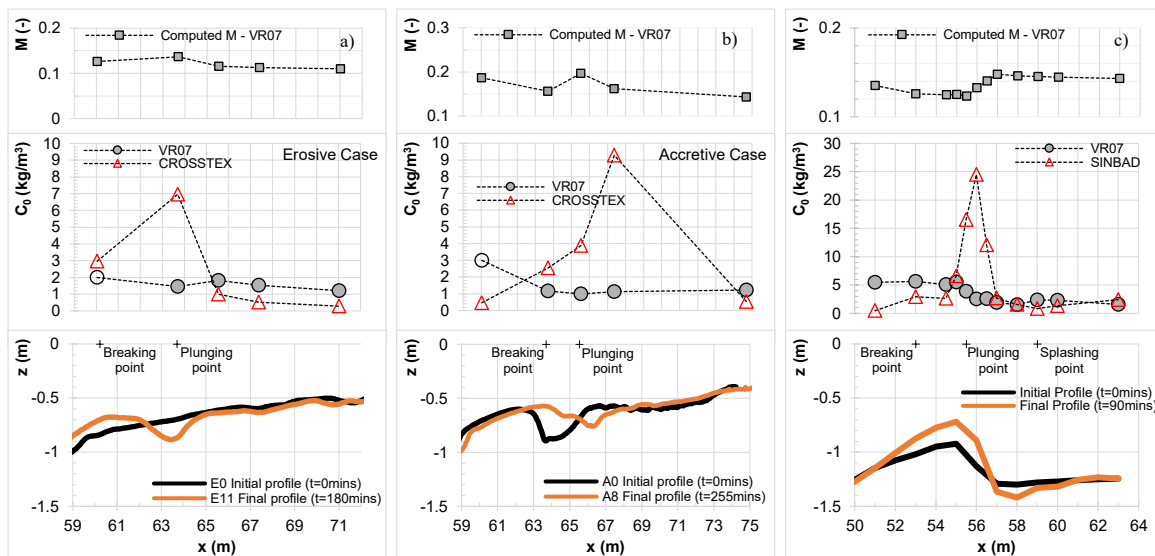


Figure 16 - Cross-shore distributions of mixing parameter (top panels), measured and computed reference concentration (middle panels) and bed profile (lower panels).

Plots a-b) show the VR07 model validated against CROSSTEX erosive and accretive cases respectively and Plot c) shows validation against SINBAD cases.

3.3.1.6. Van der Zanden et al. (2017c) – vdZ17

CROSSTEX: Despite the strong relationship between near-bed TKE and reference concentration reported in literature (e.g. vdZ et al., 2017b; Aagaard et al., 2018; Pang et al., 2020), the agreement with measured C_0 in the breaker zone is quite poor in the erosive case. All of the breaker zone points are outside the factor 2 region, indicating mild under-prediction. Almost all of the near-bed TKE (k_b) measurements at 1cm above the bed are missing for the accretive cases, making it difficult to effectively validate vdZ17 model with the CROSSTEX dataset for the accretive case.

SINBAD: Contrary to Figs. 17a-b, Fig. 17c indicates reasonable-good agreement between vdZ17 and measured data. The model's performance in the breaker zone is quite varied, with some cases of minor over- and under-predicting throughout. Though the strong local increase in C_0 around the plunging point is adeptly captured (with computed C_0 generally in the correct order of magnitude, see Fig. 18b), there is still some under-predicting (in varying extents) at this point.

Comparing the available k_b values between the CROSSTEX and SINBAD datasets has revealed that the values taken at 1cm above the bed at the plunging point differed by approximately a factor of 2. The measured k_b (at 1cm above bed) at the plunging point for the CROSSTEX erosive and accretive cases are very similar in magnitude and are between 0.003-0.006 m^2/s^2 . On the other hand, the measurements taken at the same point from the SINBAD experiments are between 0.006-0.01 m^2/s^2 . As k_b is one of the main driving parameters for the vdZ17 model, this difference in magnitude in measured k_b has a major effect on the performance of the model, hence the disparity in performance between Figs.18a and 18b. In this section, only the magnitude of k_b has been considered due to the affect it has on the reference concentration formula of vdZ et al. (2017c). Froude-scaled TKE values are compared and discussed in Chapter 5.1 of this thesis.

Summary: The model of vdZ et al. (2017c) shows varied performance between the different datasets. As k_b is the main driving parameter in the vdZ17 formulation, the magnitude of measured k_b has a large effect on its performance. The significant difference in magnitude of measured k_b between the two datasets will be discussed further in Chapter 5.1.

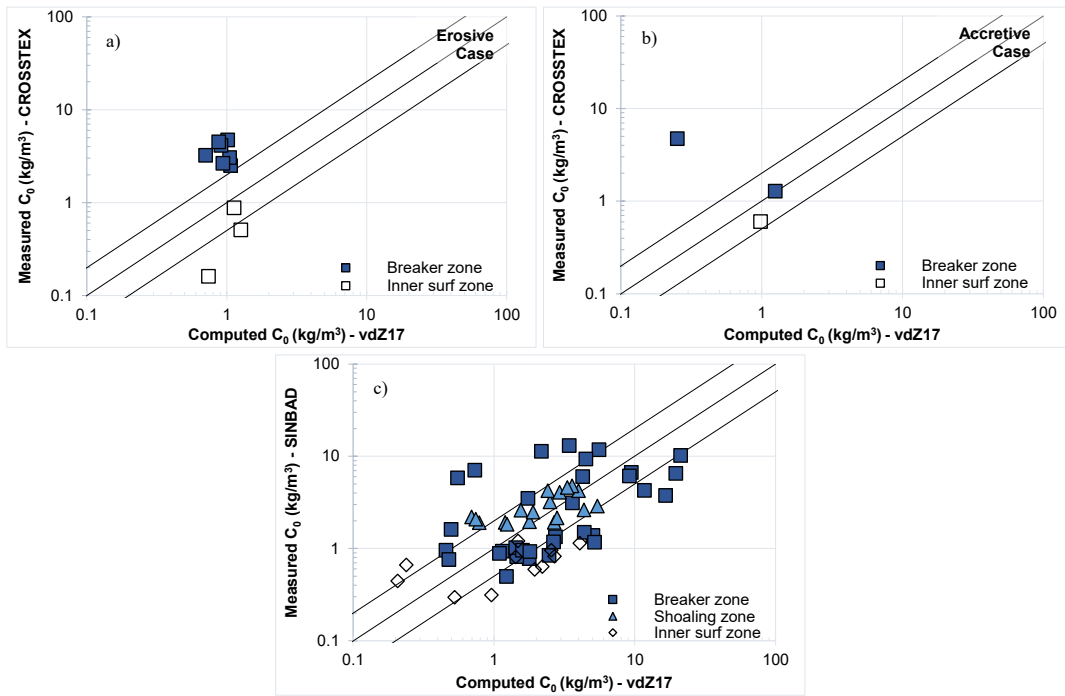


Figure 17 - Measured vs. Computed reference concentration – derived using the model of vdZ17.

Plot a-b) show the vdZ17 model validated against CROSSTEX erosive and accretive conditions respectively and Plot c) shows validation against the SINBAD experiments.

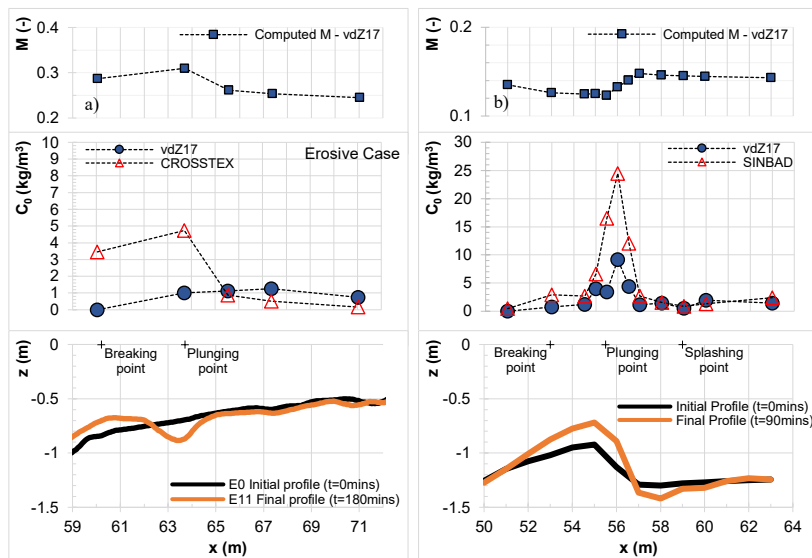


Figure 18 - Cross-shore distributions of mixing parameter (top panels), measured and computed reference concentration (middle panels) and bed profile (lower panels).

Plots a-b show the vdZ et al. (2017c) model validated against CROSSTEX erosive cases and SINBAD respectively.

3.3.1.7. Proposed model – L19

LIP & CROSS: The L19 model performs very well in all three regions, including the breaking region for the erosive and accretive cases (note: 1 point is not shown in Fig. 19b as it was an outlier located far outside the plot range). In the accretive case of CROSSTEX (Fig. 20d), L19 shows good agreement at the plunging point, but is seen to under-predict slightly immediately shoreward of the plunging point – as seen against the SINBAD dataset (Fig. 20f).

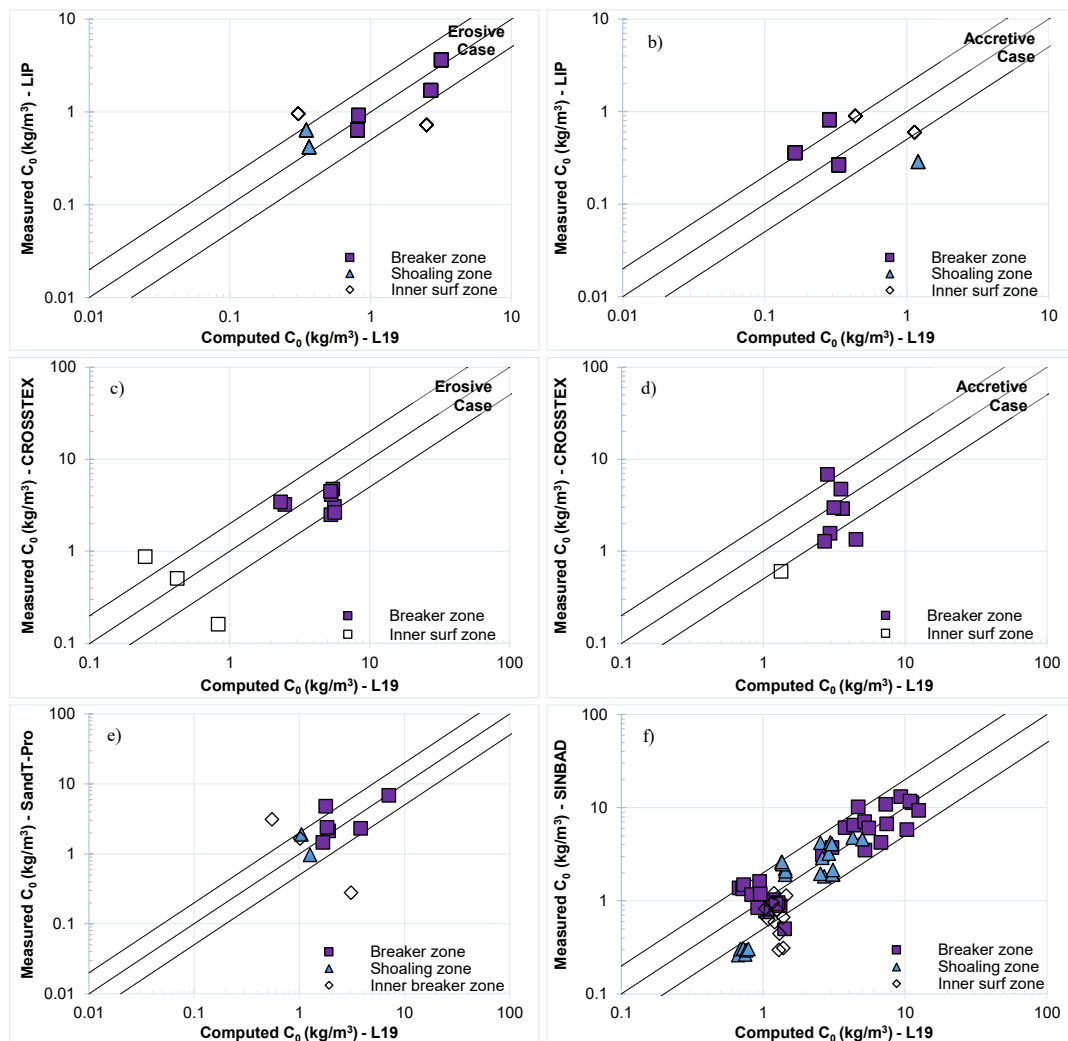


Figure 19 - Measured vs. Computed reference concentration – derived using the model of L19.

Plot a-b show the L19 model validated against LIP erosive and accretive conditions respectively; c-d show validation against CROSSTEX erosive and accretive conditions respectively; e-f show validation against the SandT-Pro and SINBAD experiments respectively.

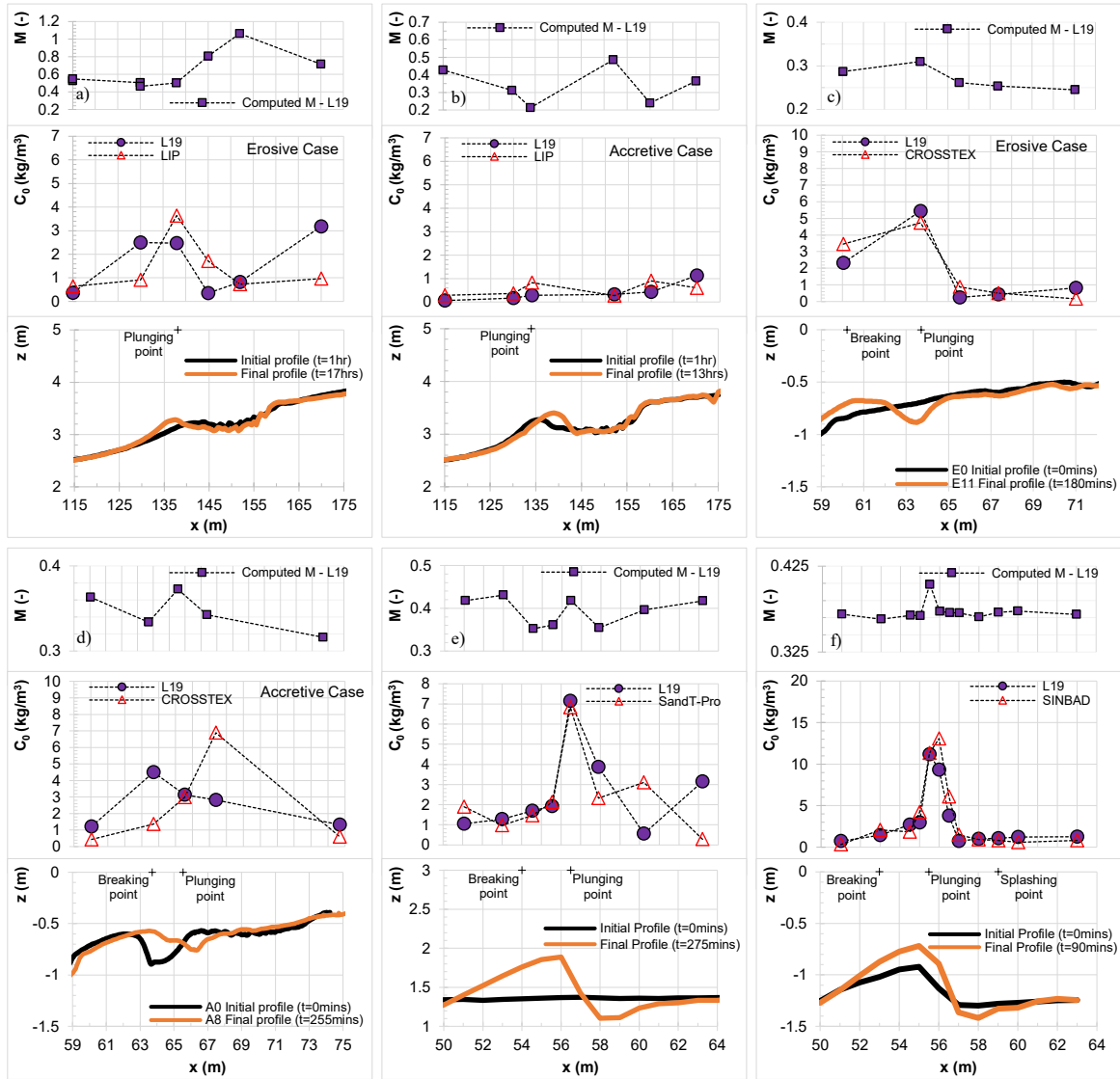


Figure 20 - Cross-shore distributions of mixing parameter (top panels), measured and computed reference concentration (middle panels) and bed profile (lower panels).

Plots a-f show the L19 model validated against each of the datasets LIP erosive and accretive cases, CROSSTEX erosive and accretive cases, SandT-Pro and SINBAD respectively.

SandT-Pro & SINBAD: L19 shows good agreement with the measured C_0 in the shoaling and breaker zones - considerably better agreement than other existing models - with $RMSE = 1.58\text{kg/m}^3$ for SandT-Pro (see Table 13). Figs. 19e-f show that almost all points are clustered around the 1:1 line and lie within the factor of 2 region. Even when the breaker bar is fully developed at $t=90\text{mins}$, the L19 model accurately captures the localised increase in C_0 at the plunging point, as well as maintaining good agreement with data in other zones. In Fig. 20f, there is some divergence just shoreward of the plunging point, between $x = 55\text{-}56\text{m}$. The bottom profile in Fig. 20e-f, shows that the bed level drops at this location. As the inverse of the water depth ($1/d$) is one of the main driving parameters of the L19 model, the fall in the

bottom profile between $x = 55\text{m}$ and $x = 56\text{m}$ is reflected in the corresponding computed C_0 , which also drops with the bed profile. The measured C_0 at this point however increases. This is attributed to the surface-generated TKE fully invading the WBBL at this point, entraining large amounts of sediment as well as enhancing vertical mixing. The L19 model does not account for the oblique downward movement or enhanced mixing effects of these turbulent eddies which continue to move towards the bed beyond the plunging point. The lag involved in the TKE travelling through the water column, as well as TKE being horizontally advected to/from adjacent regions is also not accounted for in the model. Instead it models the reference concentration empirically from the local water depth and roller dissipation rate. As a result, though L19 is adept for predicting C_0 at the plunging point, it is sometimes seen to under-predict immediately shoreward of the plunging point.

There are also some cases of noticeable over-predicting in the inner surf zone (particularly observed in Fig. 20a & 20e when validated against the LIP erosive and SandT-Pro datasets). As mentioned in Chapter 2 of this thesis, the observed inverse relationship between local water depth and corresponding C_0 is only applicable up until the plunging point ($x = 138\text{m}$ and $x = 56.5\text{m}$ for LIP and SandT-Pro datasets respectively). Figures 20a & 20e show that the agreement between computed and measured C_0 is very good up until this point, but afterwards there are some discrepancies.

Summary: The model of L19 generally performs very well in all three cross-shore regions, but especially in the shoaling and breaking zones. Unlike the other existing reference concentration models validated in this study, the L19 model is adept at capturing the strong localised increase in C_0 found at the plunging point. Immediately shoreward of the plunging point however, where SSC peaks due to the large-scale vortices fully invading the WBBL, the model is sometimes found to under-predict marginally. Overall, however, the model accurately reproduces the cross-shore variability of reference concentration under plunging breaker conditions.

Table 13 - Summary of RMSE for all reference concentration models tested against measured data.

| Model | SandT-Pro | SINBAD | Erosive | Accretive | Erosive | Accretive |
|-------|-------------|-------------|-------------|-------------|-------------|-------------|
| | | | CROSSTEX | CROSSTEX | LIP | LIP |
| MS92 | 3.41 | 8.08 | 2.75 | 4.54 | 1.89 | 4.57 |
| SR93 | 2.61 | 3.45 | 2.35 | 2.79 | 1.12 | 0.61 |
| SP04 | 3.61 | 4.13 | 1.47 | 3.81 | 1.44 | 0.52 |
| JS07 | 2.49 | 4.43 | 1.70 | 2.33 | 1.92 | 3.72 |
| VR07 | 2.85 | 7.43 | - | - | 3.28 | 10.47 |
| vdZ17 | - | 5.02 | 2.30 | 2.58 | - | - |
| L19 | 1.58 | 1.42 | 1.71 | 1.79 | 0.75 | 0.36 |

NB: Lowest RMSE (best agreement with measured data) in each dataset is highlighted in bold.

3.3.2. Concentration Profile (C[z])

The findings from this sub-chapter have been prepared for submission as a journal article for publication. The title of the paper is ‘Modelling the Suspended Sand Concentration Profile under Breaking Waves’.

The concentration profile $C[z]$ simply refers to the vertical distribution (as a function of elevation above bed, z) of the suspended sand concentration. In order to focus only on the differences in performance resulting from the variations in concentration profile $C[z]$ formulations used, all analysis carried out in this section is done using the same reference concentration C_0 model. As detailed in Chapter 2.2.2., the reference concentration (C_0) is one of the major parameters in computing the $C[z]$, and therefore it is essential that C_0 is accurately modelled in order to obtain accurate computed concentration profiles. As the formula of L19 (Eq. 36, Chapter 2.3.1.3.) showed very good agreement in the validation presented in section 3.3.1., it is used to compute C_0 for all cases shown herein, and the various concentration profile formulae described in Chapters 2.2.2. and 2.3.2. are used to compute $C[z]$.

In all plots presented in this sub-chapter, the left column of plots shows $C[z]$ in the shoaling zone (pre-breaking), the centre column of plots shows $C[z]$ in the breaking zone (around the plunging/spilling point), and the right column of plots shows $C[z]$ in the inner surf zone (post-plunging). The plots in this section follow the same design, showing the measured vs. computed concentration profiles. The measured profile is named after the dataset used in each plot, and the computed profile is named after the formulae used to compute it (e.g. concentration profile computed using the formulae of Shibayama and Rattanapitikon, 1993, is referred to as SR93 in plots). The y-axis has been normalised to allow for inter-comparison of trends between multiple datasets and transport models.

3.3.2.1. Measured Concentration Profiles

The different measured concentration profiles shown in Fig. 21 indicate a similar pattern over the cross-shore regions. Generally, prior to plunging (left column of plots: shoaling zone), concentration levels are relatively low, in the order of 10^{-1} kg/m^3 . The magnitude of sediment concentration declines substantially from the breaking to the inner surf zone, where in most cases the measured SSC is less than 1 kg/m^3 . Even still, the concentration profiles are quite steep (almost perpendicular to x-axis), indicating that concentration levels are quasi-uniform throughout the water column. This seems to be the case under both spilling and plunging breakers. Regardless of breaker type or cross-shore region, all concentration profiles seem to follow the same (mildly) concave shape.

Under spilling breakers (erosive cases), the concentration profile changes very little between shoaling, breaking and inner surf zones, with the shape of the profile of concentration remaining relatively constant throughout the whole water column (see Fig. 21a-c, g-i). Magnitude does vary slightly between different cross-shore zones, but they are not as drastic as those found under plunging breakers. Under plunging breakers, it is clear that wave breaking has a considerable effect on sediment pickup rates as well as the near-bed or reference concentration, which is evidently larger by one order of magnitude in the breaking zone than the shoaling zone (c.f. vdZ et al. 2017b; 2019). Assuming that the magnitude of near-bed TKE is directly correlated with the magnitude of sediment pickup rates, this is also consistent with the findings of De Serio & Mossa (2019) who found that time-averaged near-bed TKE was highest in the breaking zone and decreased with distance from the breaking region, and also

Scott et al. (2005) who reported that levels of near-bed TKE were an order of magnitude higher at the bar crest (generally where waves break) than in the shoaling and inner surf zones.

Under spilling/weakly-plunging waves (e.g. Fig. 21 b, e, h), the measured concentration profile indicates a quasi-uniform level of concentration (i.e. almost perpendicular to x-axis), but under strong plunging breakers (e.g. Fig. 21 k, n, q) the near-bed concentration is seen to rise drastically. Under plunging breakers, the concentration profiles show that suspended sand concentration doesn't only increase near the bed in the breaking zone but increases throughout the whole water column – with concentration in the upper water column in the breaking zone being as high or even higher than the concentration near-bed in the shoaling zone. Near the bottom, concentration reached almost 10 kg/m^3 . At this point, the measured profile increases exponentially near the bed ($z/d < 0.2$) but SSC in the upper water column (outer region) increases at a slower rate (i.e. the curve is more gradual) – measured concentration increased at a rate of up to 2.1 kg/m^3 per cm elevation at the bed, and gradually slowed down to an increase of around 0.02 kg/m^3 per cm elevation. This is most clearly shown in Fig. 21k.

vdZ et al. (2016) reported that TKE is almost depth-uniform in the vicinity of the plunging point, and this is reflected in the high concentration in the full water column (e.g. Figs. 21h, k, n, q). This phenomenon is attributed to strong vertical mixing by the breaking-generated turbulent vortices, rising air bubbles (as described in Chapter 1) and also upward advection by two-dimensional undertow circulation (Fernandez-Mora et al., 2016; vdZ et al. 2017b). This strong vertical mixing is most evident in Figs. 21n & 21q.

3.3.2.2. Rouse (1939) – R39

Unlike other $C[z]$ models covered in this thesis, the performance of the R39 model seems to be unaffected by the cross-shore region, or even the breaker type, but highly sensitive to the elevation above bed (z) at which the measurement is taken. Predicted $C[z]$ is generally in the correct order of magnitude in the near-bed region ($z/d < 0.1$), but there are very large discrepancies in the upper water column. This is the case, even when there is good agreement in the near-bed region (e.g. Fig. 21a, c, p, q), with discrepancies getting increasingly larger as z approaches the surface (where $z = d$). In the upper water column, the magnitude of computed $C[z]$ is frequently seen to be smaller than measured $C[z]$ by two orders of magnitude and in some cases even more. [Note: the x-axes in Fig. 21 are different to those in the remainder of

this section, as the Rouse equation produces very small values ($\approx 0 \text{ kg/m}^3$) in the upper water column].

It is clear that the limitations mentioned in Chapter 2.2.2. regarding the Rouse equation producing unrealistic values very close to the bed and the surface are indeed an issue. Based on the analysis carried out in this thesis however, it would seem that the issue is considerably greater in the near-surface region where $z \approx d$. In the near-bed region, where one could expect to see computed concentration being significantly greater than the measured, more often than not we see under-prediction of concentration. Of course, as measurements get closer and closer to the bed (i.e. $z \rightarrow 0$), concentration will increase exponentially. This however is less of an issue than at the surface, as measurements that close to the bed (below the reference level which is 0.02-0.025m for L19) are generally classified as bedload and are therefore modelled separately. Only in Figs. 21h, j, l, is there considerable over-prediction of concentration near the bed. All three of these cases were from the CROSSTEX dataset, where the lowest elevation at which measurements were taken was at $z = 0.01\text{m}$ (which is below the reference level). In all other plots, the measurements closest to the bed (i.e. lowest z) were taken between approx. $z = 0.02\text{-}0.05\text{m}$. From the analysis presented in here, it can be concluded that the Rouse equation is applicable to conditions of $d \gg z \geq 0.02\text{m}$.

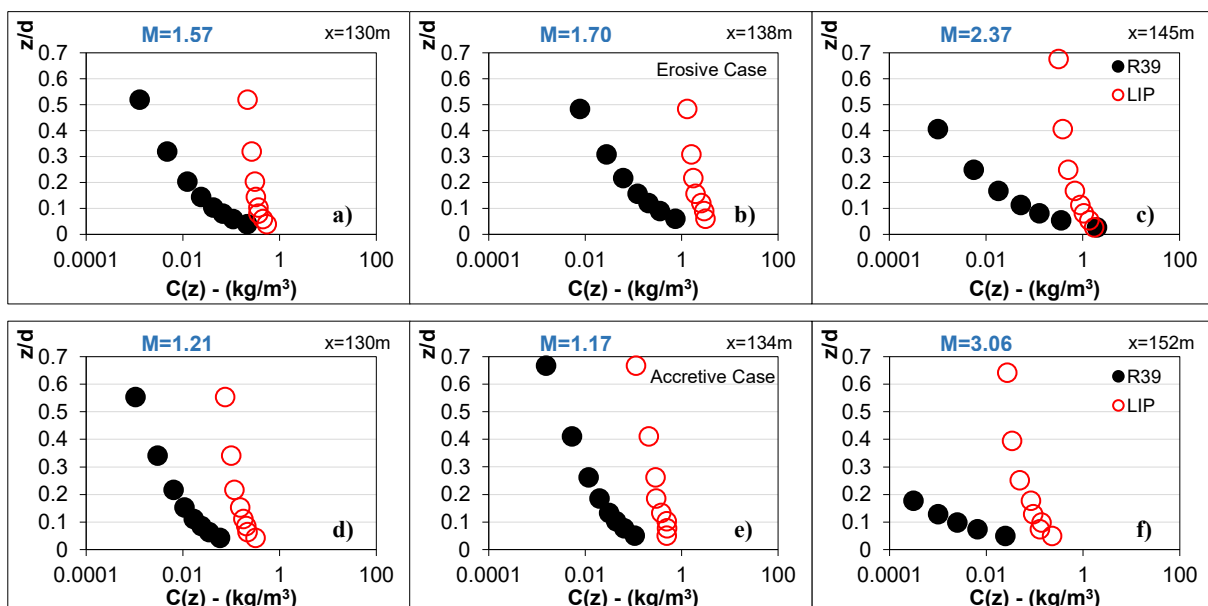
As mentioned earlier in this section, there are cases where the concentration in the upper water column is smaller than the measured by two or more orders of magnitude. Assuming that all computed concentration values lower than 0.01 kg/m^3 in Fig.21 are negligible ($=0$), the guidelines provided by van Rijn (2007) for the Rouse number (M) can be compared against modelled results. Note: The Rouse number is shown in blue at the top of each plot on Fig. 21. The guidelines provided by van Rin (2007) are repeated here for the reader's convenience:

1. $M=5$: suspended sediment in near-bed layer ($z < 0.1d$)
2. $M=2$: suspended sediment up to mid of water depth ($z < 0.5d$)
3. $M=1$: suspended sediment up to water surface ($z < d$)
4. $M=0.1$: suspended sediment almost uniformly distributed over water depth.

Most of the plots shown in Figure 21 indicate that the dimensionless Rouse Number (mixing parameter) has a value between 1-3, with a few cases being marginally larger or smaller. Figs. 21 a-b for example have values of $M=1.57$ and 1.70 respectively. Thus, they fall between the second and third categories from the van Rijn (2007) guidelines, indicating that they should have suspended sediment going up to a level between the water surface and the middle of the

water depth. Going back to the assumption that values of $C[z] < 0.01 \text{ kg/m}^3$ in Fig.21 being negligible, the prediction provided by the guideline is reasonable – with computed suspended sand concentration being $> 0.01 \text{ kg/m}^3$ up to the mid- to upper-water column. The van Rijn (2007) guidelines also adeptly describe the trend observed for values of $0.1 < M < 1$ (between third and fourth categories), e.g. Figs. 21g, h, i, where concentration is significant (i.e. not negligible) throughout the whole water column. However, the guidelines and the R39 model do not well-represent the measured $C[z]$, which indicates quasi-uniform distribution over the whole water column in numerous plots (e.g. Figs. 21a-i).

Evaluating the performance of the R39 model quantitatively, the RMSE values shown in Tables 15 & 16 at the end of Chapter 3.3.2.7. indicate that the discrepancies between computed and measured concentration seem to be marginal in term of magnitude. This is seen to be the case even in plots where performance is clearly poor from a qualitative standpoint. For example, in Figs 21a, b, c, despite the large discrepancies seen in the upper water column, the RMSE ranges between $0.29\text{-}1.89 \text{ kg/m}^3$, which seems quite small. It is important however to consider that the magnitude of measured concentration at these locations are also relatively small. E.g. in Fig. 21a the highest measured concentration is 0.546 kg/m^3 , and RMSE is 0.29 kg/m^3 , which is over 50% of the measured value. Thus, though the magnitude of the RMSE is relatively small, in comparison to the measured concentration it is still quite large. In Fig. 21k however, the RMSE is 1.09 kg/m^3 , which again is relatively small, but this time is only 15% of the maximum measured concentration at this location, indicating better performance. It is therefore important to consider both the qualitative and quantitative performance of these models when evaluating them.



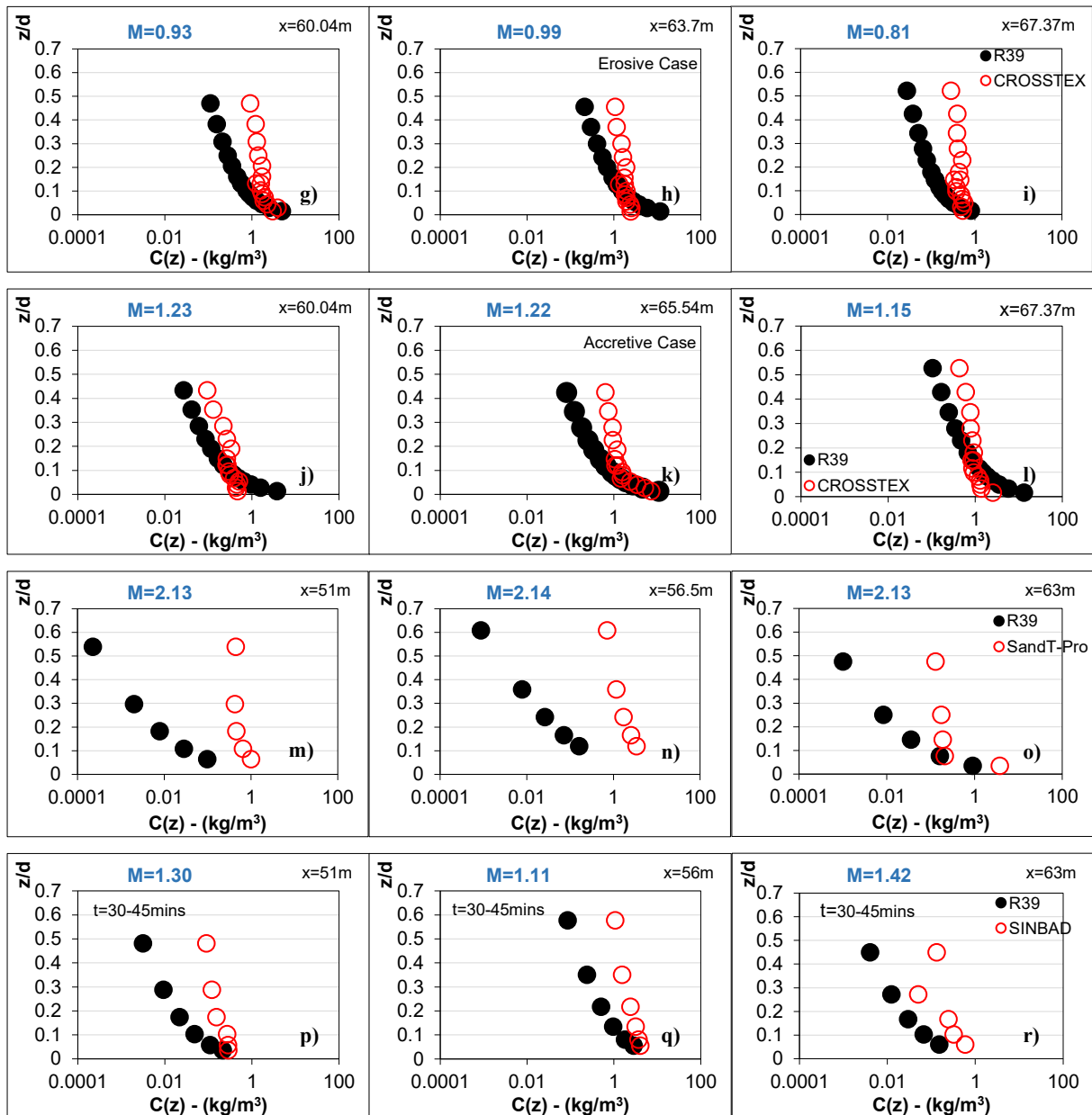


Figure 21 - Concentration profile ($C[z]$) of Measured (red circles) vs. computed (R39, black circles) concentration.

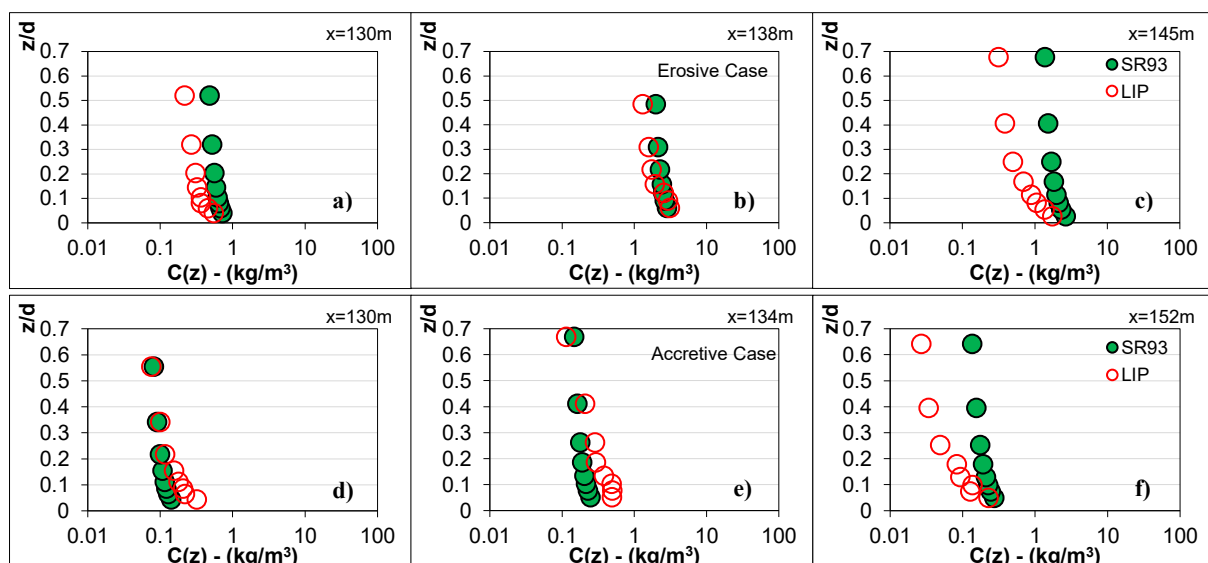
Plots a-c show LIP erosive and d-f show LIP accretive cases respectively; plots g-i show CROSSTEX erosive and j-l show CROSSTEX accretive cases respectively; plots m-o show are SandT-Pro and plots p-r are SINBAD. Each row of plots shows three different cross-shore locations: before the breaking point (left plots), at the breaking or plunging point (central plots) and onshore of the breaking point (right plots).

3.3.2.3. Shibayama & Rattanapitikon (1993) – SR93

In the shoaling zone, SR93 largely shows reasonable-good agreement with measured data throughout the whole water column (e.g. see Fig. 22a, d, g). This is also the case under spilling wave conditions and even under some weaker plunging waves (e.g. Fig. 22b, e), indicating that the $C[z]$ formulae of SR93 are fairly adept in replicating the concentration profile under breaking wave conditions. SR93 however does sometimes over-predict concentration in the upper water column ($z/d > 0.2$), despite agreement in the near-bed region being good. This indicates that the discrepancy between measured and computed profiles is not resulting from the reference concentration model, but the concentration profile model of SR93.

Throughout Fig. 22, the SR93 concentration profile is quite steep (almost perpendicular to the x-axis, particularly in the outer region, $z/d > 0.1$) indicating a quasi-uniform distribution of SSC in the whole water column. This steep curve is reasonably suitable for the shoaling zone where there is a constant, relatively low level of measured SSC in the whole water column. Even in the breaking zone, under spilling/irregular plunging breakers, the SR93 model is seen to perform reasonably well. Under the regular plunging breakers however discrepancies are found in the upper water column, indicating overprediction.

A similar pattern is found in the inner surf zone where the SR93 formulae tend to overpredict concentration, particularly in the upper water column ($z/d > 0.2$). Practically speaking, the reason for this issue is that the magnitude of the mixing parameter (M), which is used as the power function exponent in the SR93 and JS07 $C[z]$ formulae (Eq. 25), is too small (generally < 0.5). This causes the resulting curves to be steeper in their changes (appearing quasi-uniform/linear on the log scale).



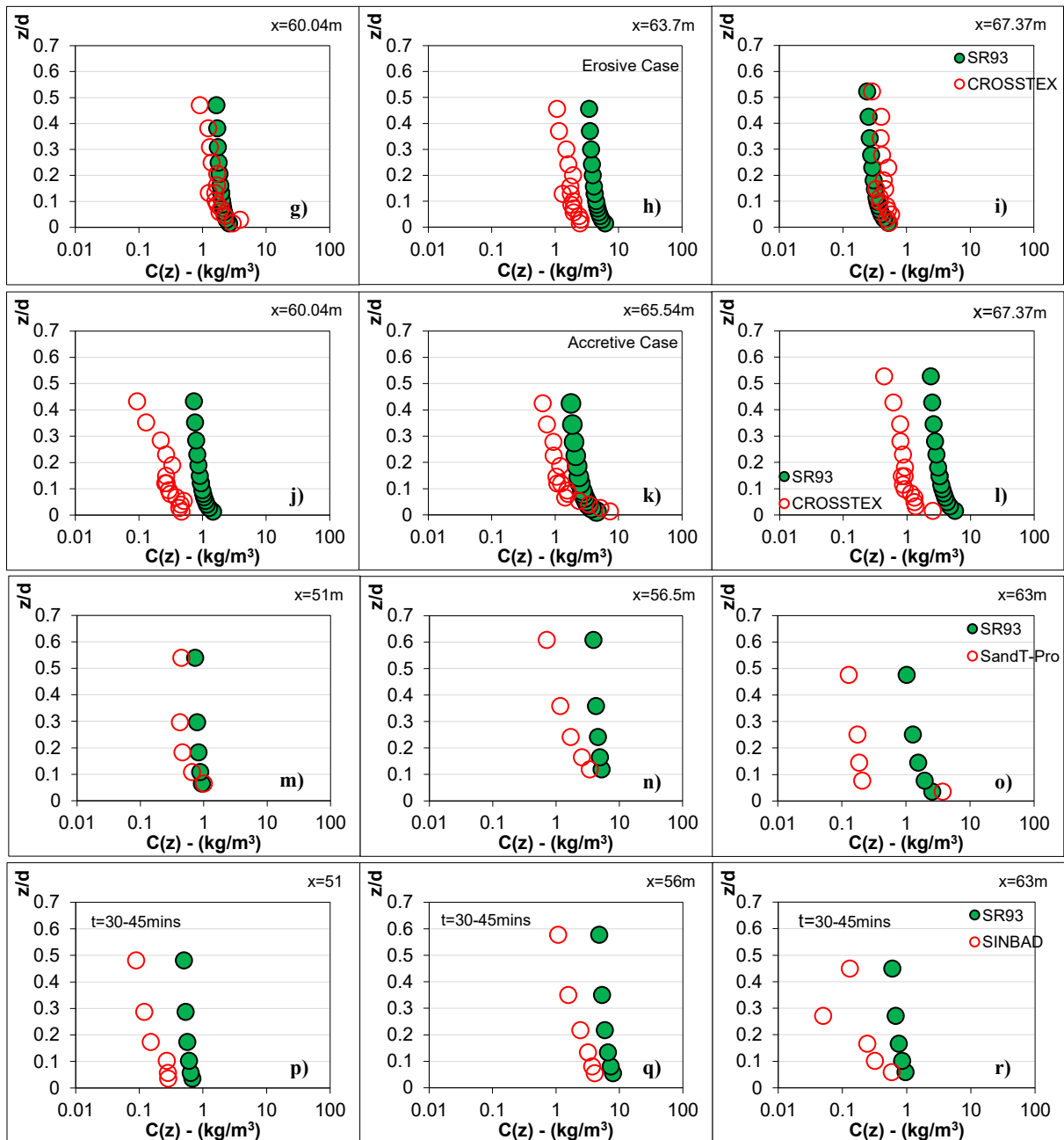


Figure 22 - Concentration profile ($C[z]$) of Measured (red circles) vs. computed (SR93, green circles) concentration.

Plots a-c show LIP erosive and d-f show LIP accretive cases respectively; plots g-i show CROSSTEX erosive and j-l show CROSSTEX accretive cases respectively; plots m-o show are SandT-Pro and plots p-r are SINBAD. Each row of plots shows three different cross-shore locations: before the breaking point (left plots), at the breaking or plunging point (central plots) and onshore of the breaking point (right plots).

3.3.2.4. Larson & Kraus (2001) – LK01

Wang et al. (2012) reported that for the spilling breaker case, the value of $k_d = 0.03$ (recommended by Larson & Kraus, 2001) resulted in concentration profiles that were too steep at most cross-shore locations, and that a value of $k_d = 0.01$ produced more gradual profiles that better fit the measured values. The only exceptions were reported at the secondary breaker line, where $k_d = 0.03$ produced a closer fit to measured concentration. For the plunging breaker case, Wang et al. (2012) reported that $k_d = 0.01$ produced better agreement in the mid-surf zone but $k_d = 0.03$ produced better agreement near the plunging point and near the secondary breaker line. These findings are not entirely consistent with the findings from the present study, which indicate that the recommended k_d value of 0.03 works best for all tested conditions, both under spilling and plunging breakers, and in all three cross-shore regions. It is possible that the reason for these differences is due to the difference in the scale of the experiments and/or characteristics of sediment (e.g. D_{50} and w_s) used in each of the experiments.

The measured concentration profiles in this study were generally steeper than those from the LSTF dataset (c.f. Wang et al., 2002; Wang et al., 2012), in both the spilling and plunging cases. This indicates that there were high levels of SSC not only near the bed, but in the upper water column also. Assuming that the high concentration in the upper water column indicates enhanced vertical sediment mixing, this suggests that vertical sediment mixing was more prominent in the datasets used in this thesis (refer to Chapter 3.2.) than in the LSTF dataset. The enhanced sediment mixing also points to higher levels of TKE present in datasets used in this thesis, which practically speaking would have the effect of a vertically extended concentration profile (Nielsen, 1992). It is speculated that this steepness in concentration profile may be related to the scale of the experimental conditions covered herein. All datasets used in this section were collected under large-scale wave flumes which were not only considerably longer (more than 3 times the length) than the flume used in the LSTF dataset, but also considerably deeper as well (refer to Chapter 3.2). Comparing the wave conditions from the LSTF dataset against those used in the present thesis indicate that the wave heights, wavelength, wave period and water depth were considerably smaller in the LSTF experiments (a brief summary of the LSTF test conditions can be found in Table 14 below).

Furthermore, the average grain diameter from the LSTF dataset was 0.15mm, which is considerably smaller (finer) than that used in this thesis, where D_{50} ranged between 0.22-0.25mm. The grain settling velocity of 0.018 m/s for LSTF was also much slower than those

from Chapter 3.2. which ranged between 0.030-0.034 m/s. Finer sediment generally takes longer to settle, hence the lower settling velocity, and also less resistance to entraining forces. One would therefore predict higher levels of SSC under the LSTF experiments, but this is contrary to what is seen in the data. Therefore, it is speculated that the difference was not due to the sand characteristics, but due to variations in turbulence structure observed under the relatively smaller-scale LSTF experiments.

Also, in the LSTF dataset, the high levels of vertical mixing that is induced by strong plunging breakers (e.g. by breaking-generated turbulent eddies) was only seen in close vicinity to the plunging point (c.f. Wang et al., 2012). Wang et al. (2002) reported that in the breaking zone under plunging breakers, at elevations of $z = 0.05\text{-}0.35\text{m}$ above bed, concentrations ranged between 1-3 g/l (where 1 g/l = 1 kg/m³). This is similar to the magnitude of SSC found at the same elevations in the SandT-Pro and CROSSTEX datasets, but considerably smaller than those found in the SINBAD dataset, where concentrations at the same elevations ranged between 1.2-9.0 kg/m³, with average values in the range of 1.4-5.7 kg/m³.

Though the magnitude of concentration in the breaking zone differed between the LSTF and SINBAD datasets, the shape of the concentration profiles seem to be similar. Further onshore however, in the inner-surf zone of LSTF, the SSC remained high only in the near-bed region ($z < 0.10\text{m}$), with very low concentration (as low as an order of 10⁻² g/l) in the mid/upper water column. This was not the case in the present study (e.g. see measured concentration profiles in Figs. 23i, l), where measured $C[z]$ remained considerably steeper in all test cases. Again, it is speculated that this is a result of the scale of the experiments. Regardless of the reasons for the differences between results reported by Wang et al. (2012) and those found in this section, the analysis carried out herein indicates that $k_d = 0.03$ provides better agreement with measured data, and therefore all analysis carried out with the LK01 and W12 models are done using $k_d = 0.03$.

Table 14 - Brief summary of LSTF dataset (c.f. Wang et al. 2002)

| | |
|-----------------------------------|-----------------------------------|
| Mobile sand bed | Yes: $D_{50} = 0.15\text{mm}$ |
| Computed settling velocity | 0.018m/s |
| Regular or Irregular waves | Irregular (erosive and accretive) |
| Breaker types | Spilling and plunging |

| | |
|--|--|
| Offshore wave height (H_0) | Spilling case: 0.25m, Plunging case: 0.23m |
| Offshore wave period (T) | Erosive case: 1.5s, Plunging case: 3.0s |

The model of LK01 generally performs well, with relatively good agreement with measured data in the shoaling and breaking zones, both in the WBBL (approx. $z/d < 0.2$) and in the outer region ($z/d > 0.2$). Agreement between measured and computed $C[z]$ is seen to be particularly good under spilling and weakly plunging breakers (e.g. Figs. 23a-i) but is sometimes quite poor under stronger plunging breakers (e.g. Figs. 23n & q). Figures 23n & q seem to indicate good agreement, but the magnitude of RMSE is relatively large at these cross-shore locations, with $RMSE = 2.03 \text{ kg/m}^3$ (60% of max. concentration) and 3.47 kg/m^3 (86% of max. concentration) respectively. Despite this overprediction in the breaking zone however, measured and computed profiles are still in the same order of magnitude. This indicates that the $C[z]$ formulae of LK01 satisfactorily accounts for the high levels of breaking-induced vertical sediment mixing and advection that occurs in the breaking zone. It also shows that exponential $C[z]$ formulae can be used in the modelling of the concentration profile under breaking wave conditions. As the profile is quasi-linear however, it cannot capture large contrasts between the near-bed concentration (which is can be very high) and outer region concentration (which is often relatively lower). An example of this can be found in Figs. 23k & 23r. As these discrepancies are sometimes quite high, it is possible that they could influence resulting transport rate computations. At this stage however, it is uncertain if such effects will be an issue or whether they will be negligible. Effects of the performance of $C[z]$ formulae on resulting transport rate computations is examined in Chapter 4 of this thesis.

Performance of the LK01 model is relatively poorer in the inner-surf zone, when compared against performance in shoaling and breaking zones. All plots tend to indicate discrepancies between measured and computed profiles in the inner surf zone, with computed $C[z]$ generally over-predicting. This trend is quite common in all concentration profiles evaluated in this chapter (i.e. SR93, LK01, JS07, W12 and L19). This seems somewhat acceptable however as the $C[z]$ formulae used in this thesis were derived and calibrated for use under breaking wave conditions and not for the inner-surf zone. Though some turbulent entraining forces remain in the inner surf zone in the form of bores, measured concentration levels in the inner-surf zone are lower than those found in the breaking zone, hence the over-predicting. Despite this

however, the discrepancies between measured and computed concentration are generally not very large and indicate that the exponential profile of LK01 is suitable for reproducing the measured profile in all three tested zones, despite the wave orbital velocity not being included into the formulation (Wang et al., 2012). As detailed in Chapter 2.2.2.5., Wang et al. (2012) argued that it was important to incorporate the influences of both wave-breaking turbulence and orbital motions on the suspended sediment concentration profile. The performance of this model is shown later in this chapter under the subsection titled ‘Wang et al. (2012) – W12.’

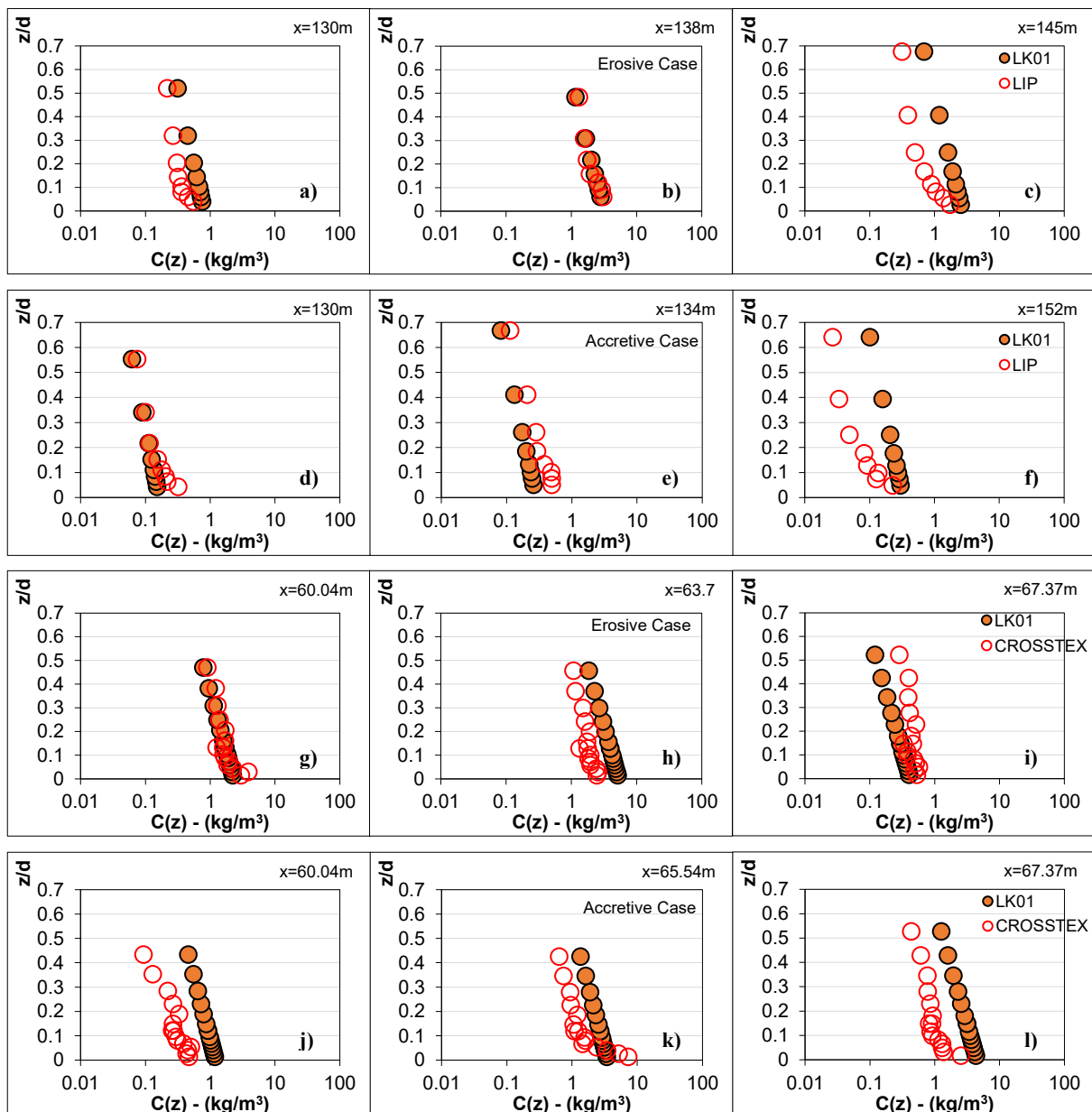


(Figure continued over page)

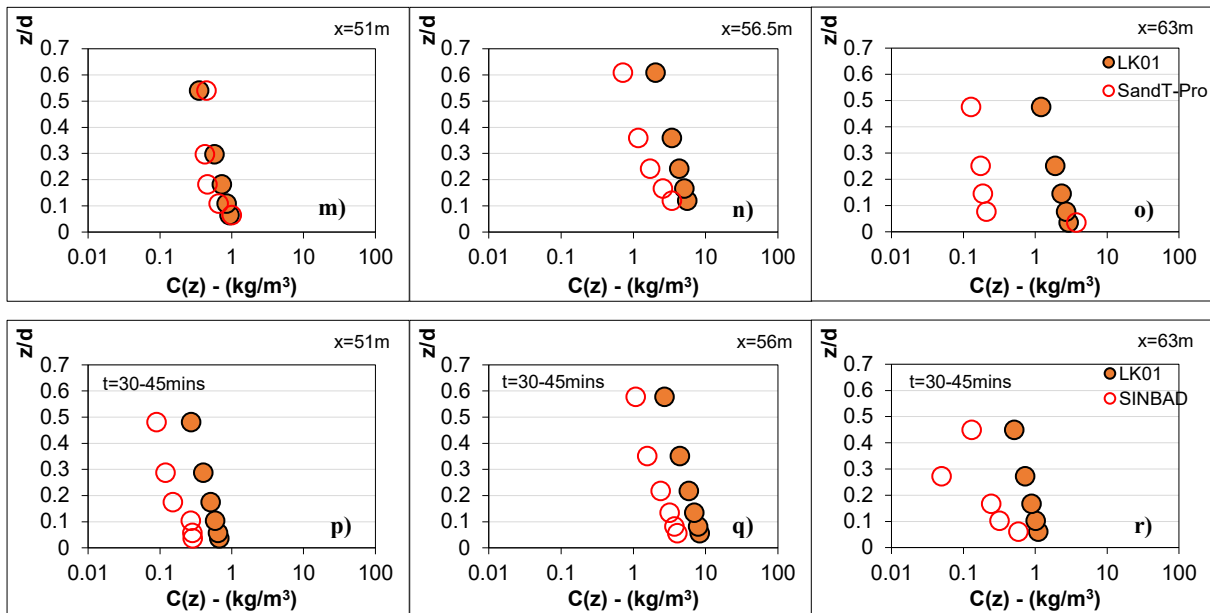


Figure 23 - Concentration profile ($C[z]$) of Measured (red circles) vs. computed (LK01, orange circles) concentration.

Plots a-c show LIP erosive and d-f show LIP accretive cases respectively; plots g-i show CROSSTEX erosive and j-l show CROSSTEX accretive cases respectively; plots m-o show are SandT-Pro and plots p-r are SINBAD. Each row of plots shows three different cross-shore locations: before the breaking point (left plots), at the breaking or plunging point (central plots) and onshore of the breaking point (right plots).

3.3.2.5. Jayaratne & Shibayama (2007) – JS07

The performance of the JS07 model is almost identical to that of the SR93 model – the shape of the profile is almost the same in all three cross-shore zones, with the computed values of JS07 being marginally higher than those of SR93. The two models were essentially modelled in the same way, with both using the same power function $C[z]$ model. The main differences between the two formulations however were the minor differences in values used for constants k_1 and k_2 in the computation of diffusion coefficient (ϵ_b), the use of the shear velocity under wave-current coexistent field instead of the shear velocity (refer to Chapters 2.2.1. & 2.2.2. to see differences between these parameters), and the different formulations implemented for computing the rate of wave energy dissipation (D_B). Of these, the difference in D_B formulation is the most major, with SR93 using the formulae of Thornton & Guza (1983), and JS07 using the formulae of Rattanapitikon and Shibayama (1998). Despite these noticeable differences however, the effects on the resulting concentration profiles could be considered negligible.

Just like the performance of the SR93 $C[z]$ model indicated over-prediction to varying extents in all three cross-shore zones, the same is seen of the JS07 $C[z]$ formulae, with relatively large discrepancies found in the upper water column (e.g. Fig. 24 k, n, q, where RMSE ranges between 1.5-4.71 kg/m^3). Discrepancies in the upper water column between JS07 and measured concentration were as large as 5.2 kg/m^3 which is almost 5 times larger than the corresponding measured concentration at that cross-shore location. These large discrepancies in the upper water column are largely related to the mixing parameter M which ranges between 0.1-0.2. Though the mixing parameter of JS07 is formulated differently to the Rouse profile, it can still be compared against the guidelines provided by van Rijn (2007) mentioned earlier in this section. According to the guidelines of van Rijn, $M = 0.1$ results in suspended sediment being almost uniformly distributed over the whole water depth. This is consistent with what can be observed in Fig. 24, in which JS07 predicts quasi-uniform concentration in the whole water column in all tested cases, regardless of cross-shore region. Therefore, it does not well-represent the commonly seen concave shape of the measured profiles, which indicate higher concentration near the bed and gradually lower concentration towards the surface. It is speculated that the introduction of a new constant or parameter to increase the magnitude of M will result in a more gradual and parabolic concentration profile that more closely mirrors the measured profile. This is further discussed under the “Proposed Model” section later in this chapter.

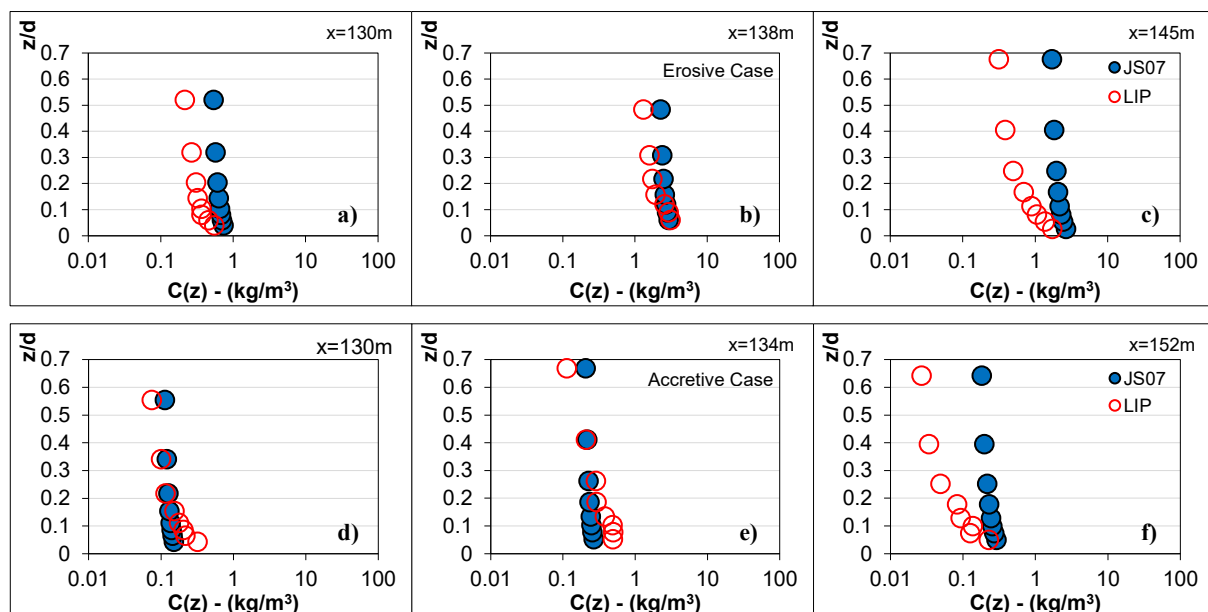


(Figure continued over page)

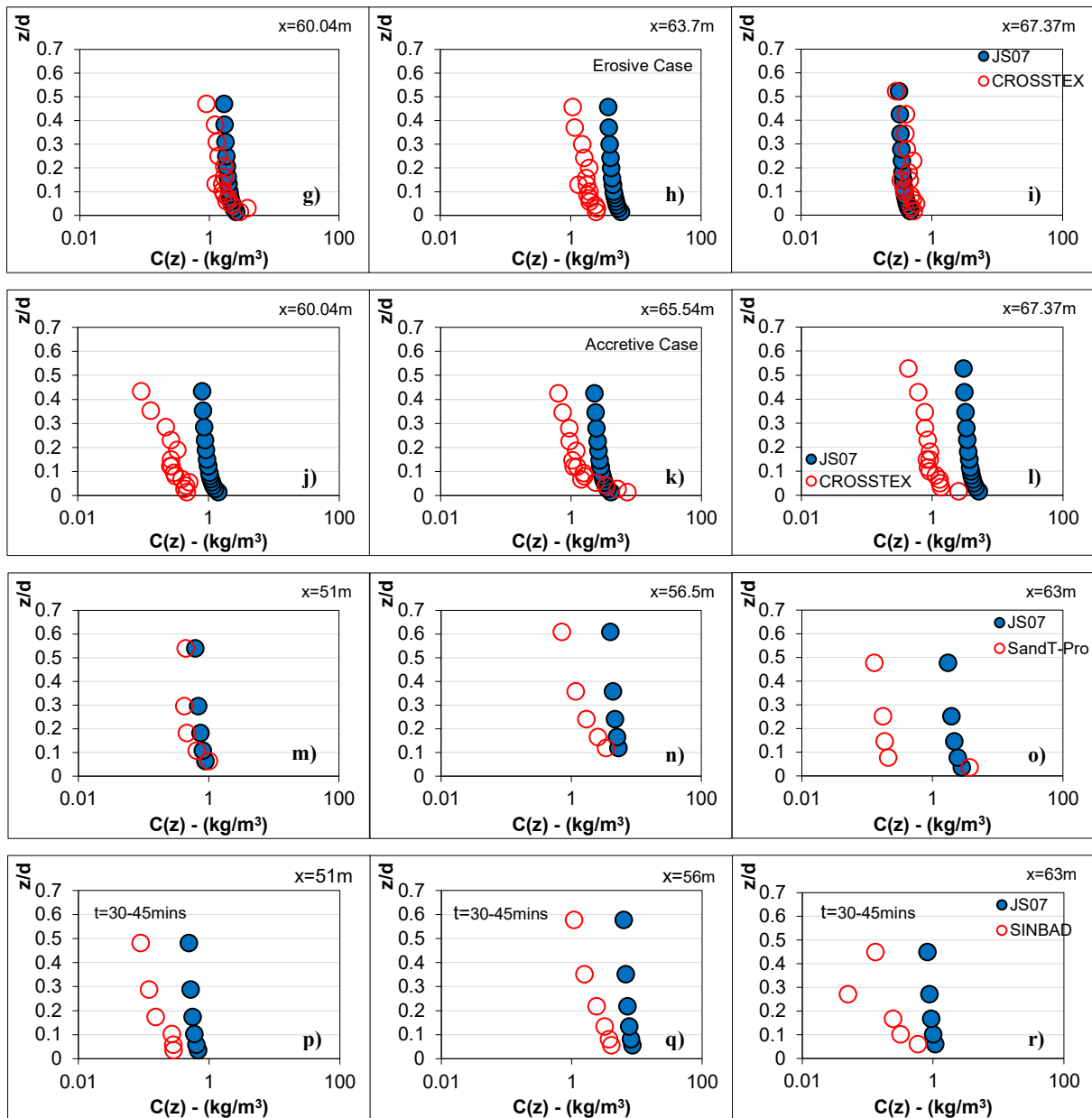


Figure 24 - Concentration profile ($C[z]$) of Measured (red circles) vs. computed (JS07, blue circles) concentration.

Plots a-c show LIP erosive and d-f show LIP accretive cases respectively; plots g-i show CROSSTEX erosive and j-l show CROSSTEX accretive cases respectively; plots m-o show are SandT-Pro and plots p-r are SINBAD. Each row of plots shows three different cross-shore locations: before the breaking point (left plots), at the breaking or plunging point (central plots) and onshore of the breaking point (right plots).

3.3.2.6. Wang et al. (2012) – W12

As mentioned in Chapter 2.2.2.5., the Larson-Kraus-Nielsen model is referred to here as Wang et al. (2012) or W12 for short, as Wang et al. (2012) integrated the Larson-Kraus model with the model of Nielsen to produce an improved $C[z]$ model for breaking wave conditions. Despite

the implementation of the intensity and length scale of wave orbital motion into the original formula of LK01, the resulting differences in performance appear to be quite small in Fig. 25.

Unlike the SR93 and JS07 concentration profile models, which produce (mildly) parabolic profiles, the models of LK01 and W12 produce profiles which appear to be linear on the log-scale. As such, the parabolic shape of the measured profiles is often not well-mirrored, with computed profiles serving more like a line of best-fit through the measured concentration points (e.g. Fig. 25k). This means that the performance of these formulae is relatively more dependent on the accurate prediction of the reference concentration, as the reference concentration essentially serves as the starting point on the best-fit line. Regardless however the model of W12 generally performs well, with relatively good agreement with measured data in all three zones, throughout the whole water column.

Generally, in comparison to the LK01 curve, the computed W12 curve has shifted slightly towards zero (concentration decreased) and has become marginally more gradual. The decreases in magnitude of concentration are non-uniform over the water column. In the upper water column, the W12 concentration is on average around 60-70% smaller than corresponding computed values of LK01, and in the lower water column the W12 concentration values are on average around 2-5% smaller than corresponding computed values of LK01. These result in better agreement with measured $C[z]$ overall (in 13/18 cases), as it was observed that there was mild over-prediction of $C[z]$ in almost all tested cases using the LK01 model. As the magnitude of computed values from the W12 model are smaller than those of the LK01, the performance is generally better – this is particularly seen in the breaking zone under strong plunging breakers (e.g. Figs. 25 k, n, q, where RMSE ranges between 1.02-2.47 kg/m^3) and in all cases for the inner-surf zone.

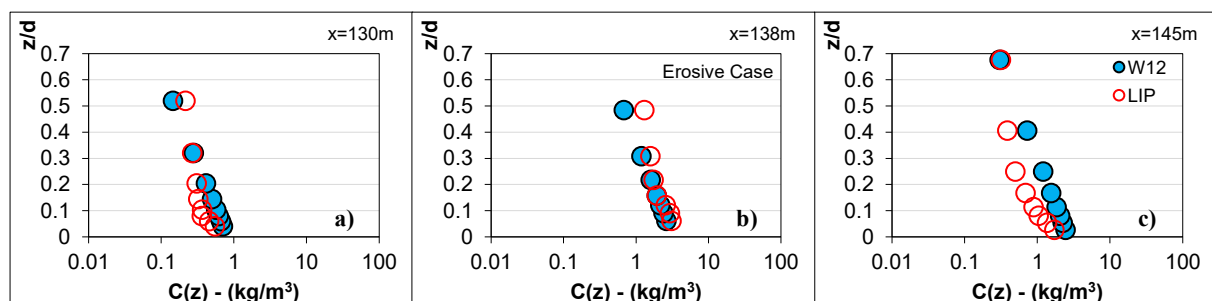


(Figure continued over page)

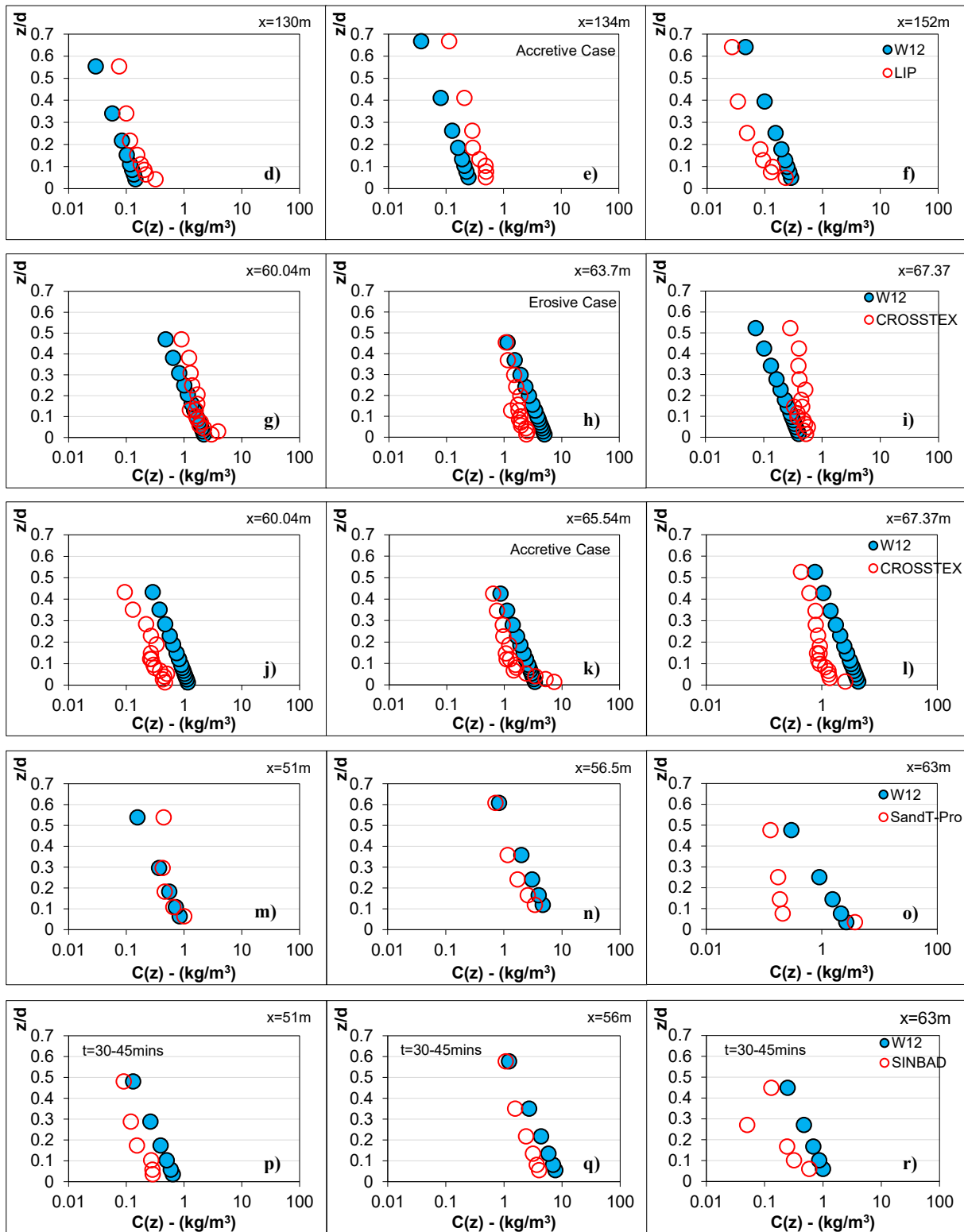


Figure 25 - Concentration profile ($C[z]$) of Measured (red circles) vs. computed (W12, light blue circles) concentration.

Plots a-c show LIP erosive and d-f show LIP accretive cases respectively; plots g-i show CROSSTEX erosive and j-l show CROSSTEX accretive cases respectively; plots m-o show are SandT-Pro and plots p-r are SINBAD. Each row of plots shows three different cross-

shore locations: before the breaking point (left plots), at the breaking or plunging point (central plots) and onshore of the breaking point (right plots).

3.3.2.7. Proposed Model – Lim et al. (2020) – L19

As the L19 $C[z]$ model is a modification of the SR93 formula (as described in Chapter 2.3.2.), a new value for the B constant is applied and compared herein against the original plots from SR93. Agreement between measured and computed $C[z]$ shown in Fig. 22f (from the subsection “Shibayama & Rattanapitikon, 1993”; where essentially $B = 1$) is improved significantly by multiplying the mixing parameter (M) by a constant $B = 3.3$. This value of B was determined based on some empirical analysis which was carried out on a couple of test cases. The test plots from the calibration analysis are shown in Fig. 26 below.

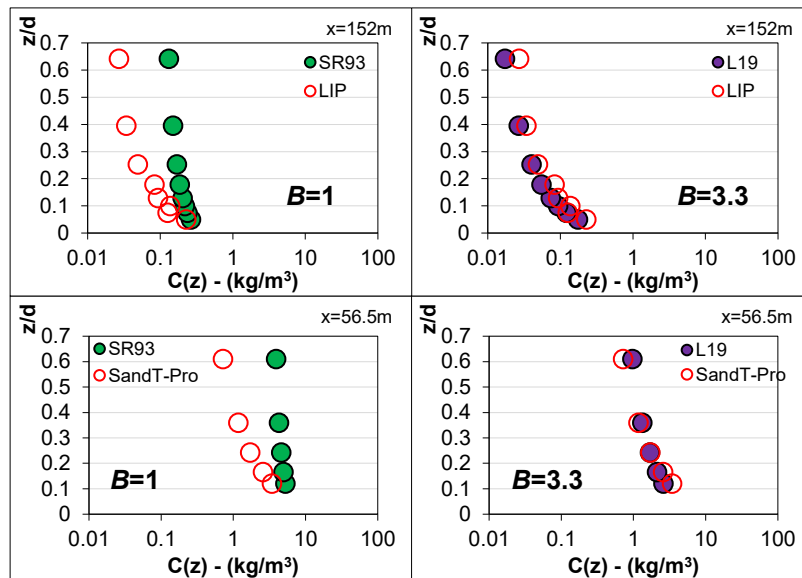


Figure 26 - Concentration profile ($C[z]$) of Measured vs. computed (SR93, green circles on left plots) vs. computed (L19, purple circles on right plots) concentration.

Left plots show original SR93 plots: top left plot from Fig. 22f (i.e. where constant $B = 1$) and bottom left plot from Fig. 22n. Right plots show the new L19 concentration profiles with constant $B = 3.3$, top right plot shows Fig. 22f with new B value and bottom right plot shows Fig. 22n with new B value.

Figure 26 shows that the simple incorporation of a constant (>1) changes the shape of the concentration profiles, and also deals with the overprediction found throughout the whole water column. Based on the improved predictions of the concentration profile observed in Fig. 26,

the constant value of $B = 3.3$ was applied to all plots. The new profiles (with $B = 3.3$) are shown in Figure 27 below.

Upon comparison between Figs. 22 and 27, it can clearly be seen that the incorporation of the dimensionless constant $B = 3.3$ has resulted in improved agreement between measured and computed $C[z]$ in the majority of plots, particularly in the breaking and inner surf zones (centre and right columns of Fig. 27 respectively). Just as it was seen in Fig. 26, the over-prediction seen in every plot of Fig. 22 (original SR93 formula) has been resolved, and also the shape of the concentration profile has been made more parabolic, better mirroring the measured profile. The better performance of the L19 model can also be seen in the RMSE values presented in Table 15 below, where L19 produces considerably smaller RMSE than the SR93 model in 14/18 cases over all 4 datasets (RMSE for SR93 ranged between 0.08-3.62 kg/m^3 with an average of 1.04 kg/m^3 ; RMSE for L19 ranged between 0.03-2.13 kg/m^3 with an average of 0.56 kg/m^3). As the modification of the mixing parameter was aimed at reducing the magnitude of the suspended sand concentration overall (as well as modifying the profile shape), there are now a couple of instances of under prediction seen in Fig. 27 d & e. Considering however that these discrepancies are not very large (within in the same order of magnitude, with $\text{RMSE} = 0.13$ and 0.27 kg/m^3 for Figs 27 d & e respectively), and the vast improvements seen in the majority of the plots in Fig. 27, it would seem that the implementation of the constant B was effective in improving the concentration profile formulae of SR93. As the JS07 concentration profile model uses the same formula to compute the concentration profile (Eq. 24), it suffers the same limitations as the original SR93 formula. Analysis (not shown) indicate that the implementation of the B constant can be used as a solution for the JS07 formula also.

Table 15 - RMSE for individual test cases of $C[z]$ models (kg/m^3).

| | | R39 | SR93 | LK01 | JS07 | W12 | L19 |
|------------------------------|------------|-------------|-------------|-------------|-------------|-------------|-------------|
| SINBAD | Shoaling | 0.14 | 0.39 | 0.32 | 0.38 | 0.24 | 0.19 |
| | Breaking | 1.64 | 3.62 | 3.47 | 4.71 | 2.47 | 0.61 |
| | Inner surf | 0.25 | 0.51 | 0.60 | 0.69 | 0.41 | 0.06 |
| SandT-Pro | Shoaling | 0.58 | 0.28 | 0.20 | 0.20 | 0.23 | 0.16 |
| | Breaking | 1.90 | 2.78 | 2.03 | 2.88 | 1.02 | 0.40 |
| | Inner surf | 1.16 | 1.22 | 1.63 | 1.71 | 1.11 | 0.89 |
| CROSSTEX EROSIVE | Shoaling | 1.07 | 0.55 | 0.52 | 0.56 | 0.58 | 0.47 |
| | Breaking | 2.66 | 2.55 | 2.09 | 2.71 | 1.74 | 2.13 |
| | Inner surf | 0.29 | 0.13 | 0.17 | 0.09 | 0.20 | 0.25 |
| CROSSTEX ACCRETIVE | Shoaling | 0.92 | 0.68 | 0.60 | 0.72 | 0.51 | 0.58 |
| | Breaking | 1.09 | 1.33 | 1.57 | 1.65 | 1.40 | 0.39 |

| | | | | | | | |
|------------|------------|------|------|-------------|-------------|-------------|-------------|
| | Inner surf | 3.03 | 2.48 | 2.11 | 2.79 | 1.81 | 2.30 |
| LIP | Shoaling | 0.29 | 0.24 | 0.24 | 0.29 | 0.16 | 0.05 |
| EROSIVE | Breaking | 1.89 | 0.49 | 0.26 | 0.67 | 0.47 | 0.85 |
| | Inner surf | 0.67 | 1.03 | 1.02 | 1.25 | 0.76 | 0.35 |
| LIP | Shoaling | 0.15 | 0.08 | 0.07 | 0.07 | 0.08 | 0.13 |
| ACCRETIVE | Breaking | 0.33 | 0.18 | 0.17 | 0.16 | 0.20 | 0.27 |
| | Inner surf | 0.11 | 0.10 | 0.14 | 0.14 | 0.10 | 0.03 |

Note: RMSE is averaged for each cross-shore location, shown in Figs. 21-25, 27. The lowest RMSE values are highlighted in blue for convenience.

Table 16 - RMSE for each model over all cross-shore regions for each dataset (kg/m^3).

| | | | EROSIVE | ACCRETIVE | EROSIVE | ACCRETIVE |
|-------------|-------------|-------------|-------------|-------------|-------------|-------------|
| | SINBAD | SandT-Pro | CROSSTEX | CROSSTEX | LIP | LIP |
| R39 | 0.99 | 1.33 | 1.66 | 1.93 | 1.15 | 0.22 |
| SR93 | 2.18 | 1.76 | 1.51 | 1.67 | 0.66 | 0.13 |
| LK01 | 2.10 | 1.51 | 1.25 | 1.56 | 0.61 | 0.13 |
| JS07 | 2.83 | 1.93 | 1.60 | 1.92 | 0.82 | 0.13 |
| W12 | 1.49 | 0.88 | 1.07 | 1.35 | 0.52 | 0.13 |
| L19 | 0.38 | 0.57 | 1.27 | 1.39 | 0.52 | 0.17 |

Note: RMSE was taken for all data points (regardless of test case or cross-shore location of measurement) for each dataset in Table 16, as opposed to taking RMSE for individual test cases/cross-shore locations in Table 15. The lowest RMSE values are highlighted in blue for convenience.

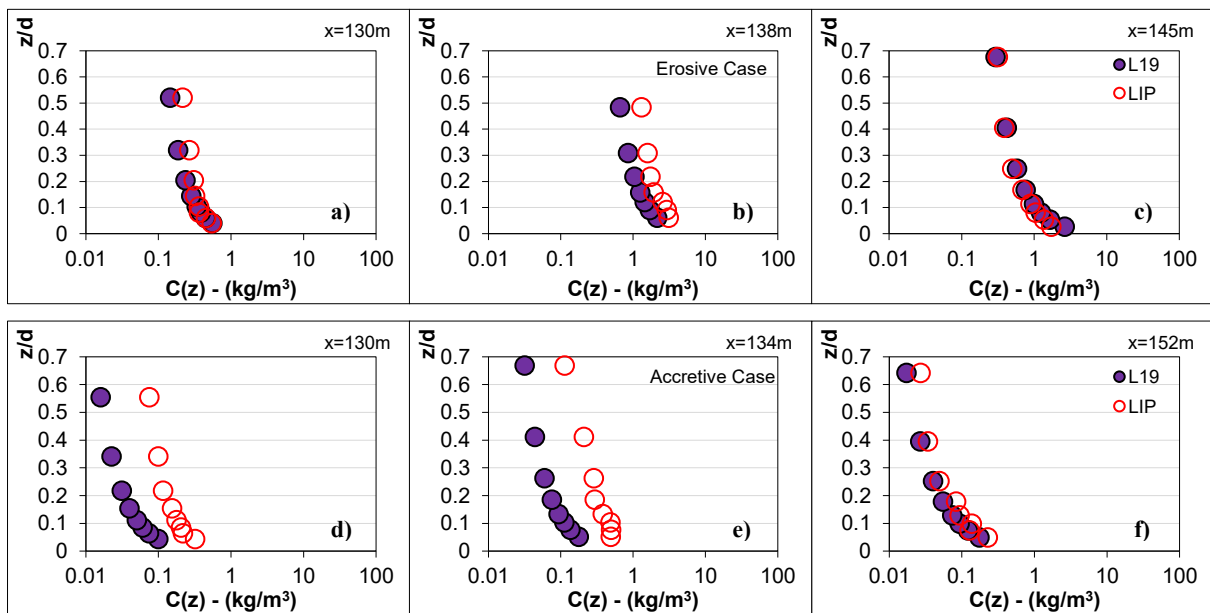


(Figure continued over page)

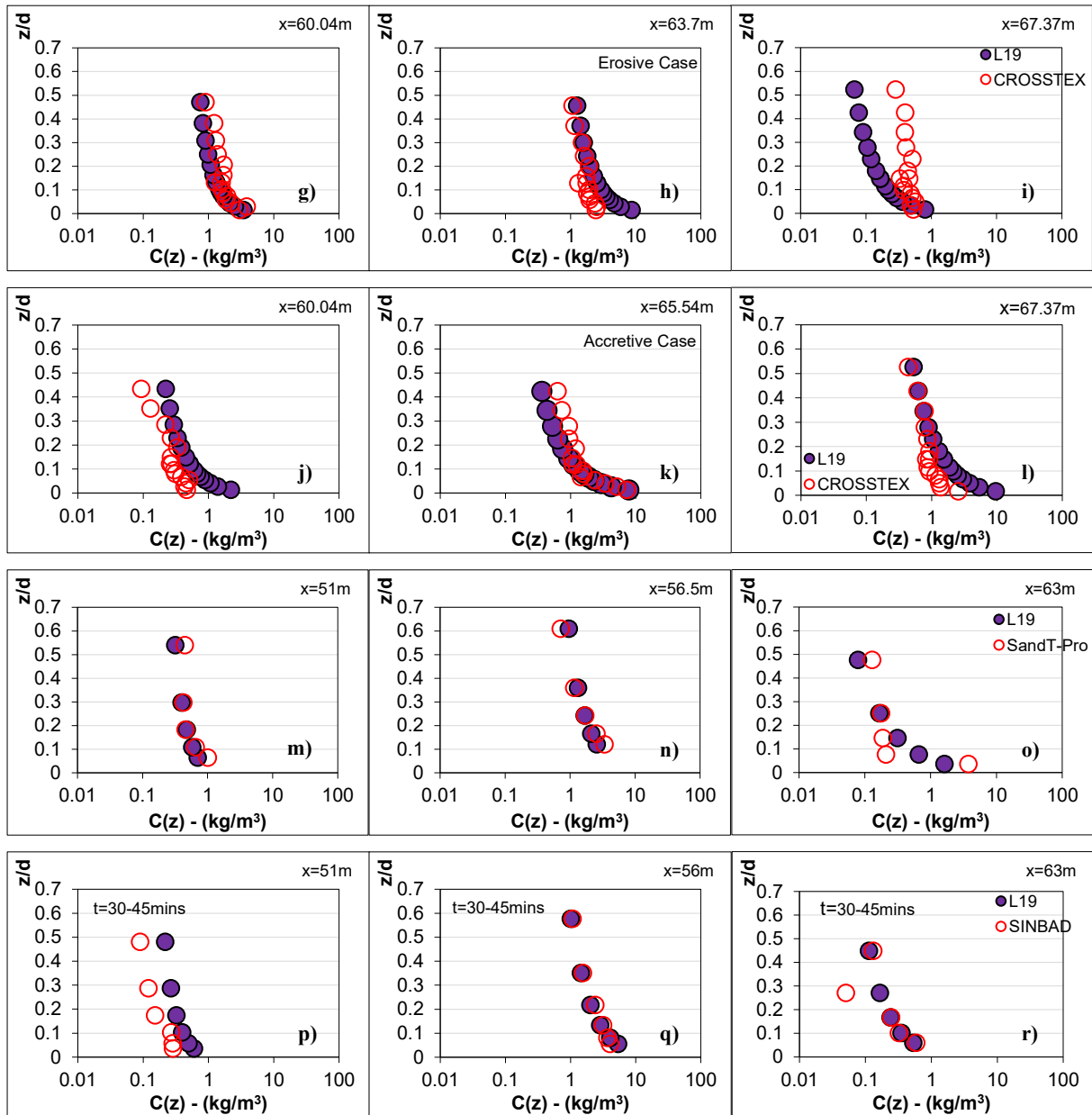


Figure 27 - Concentration profile ($C[z]$) of Measured vs. computed (L19) concentration with new constant $B = 3.3$; Eq.(33).

Plots a-c show LIP erosive and d-f show LIP accretive cases respectively; plots g-i show CROSSTEX erosive and j-l show CROSSTEX accretive cases respectively; plots m-o show are SandT-Pro and plots p-r are SINBAD. Each row of plots shows three different cross-shore locations: before the breaking point (left plots), at the breaking or plunging point (central plots) and onshore of the breaking point (right plots).

Reviewing the performance of all the models tested in this section, it can be seen that the L19 model produces the best results of the power function $C[z]$ models and the W12 model produces the best results of the exponential $C[z]$ formulae. Comparing the performance of the parabolic L19 concentration profile against the exponential $C[z]$ model of W12 in Fig. 28

shows that both models perform very well in almost all cases, with each of the models indicating some small discrepancies in different regions. When analysed qualitatively, it would seem that the parabolic L19 model generally better mirrors the curved measured concentration profile throughout the whole water column than the W12 model. This is also supported by the RMSE values shown in Table 15, where the L19 model has lower (better) RMSE than the W12 model in 11/18 test cases (RMSE for W12 ranged between 0.08-2.47 kg/m³, with an average of 0.75 kg/m³).

The W12 model also generally models the measured profile well, but there are some instances where the SSC at the top of the water column and nearest the bed is well-modelled, but not in the mid-water column – this is best demonstrated in Figs. 28 f, o, r. This is a result of the quasi-linear concentration profile that essentially serves as a line of best-fit, as discussed under the Larson & Kraus (2001) and Wang et al. (2012) subsections. Though these discrepancies in the mid-water column are found in most plots, the discrepancies are often negligible. Overall, however, it would seem that the L19 model is relatively simpler (computationally) and produces slightly better agreement with measured data based on the tests covered in this thesis. The implications of the better agreement in $C[z]$ on the resulting suspended sand transport rates will be investigated in Chapter 4 of this thesis.

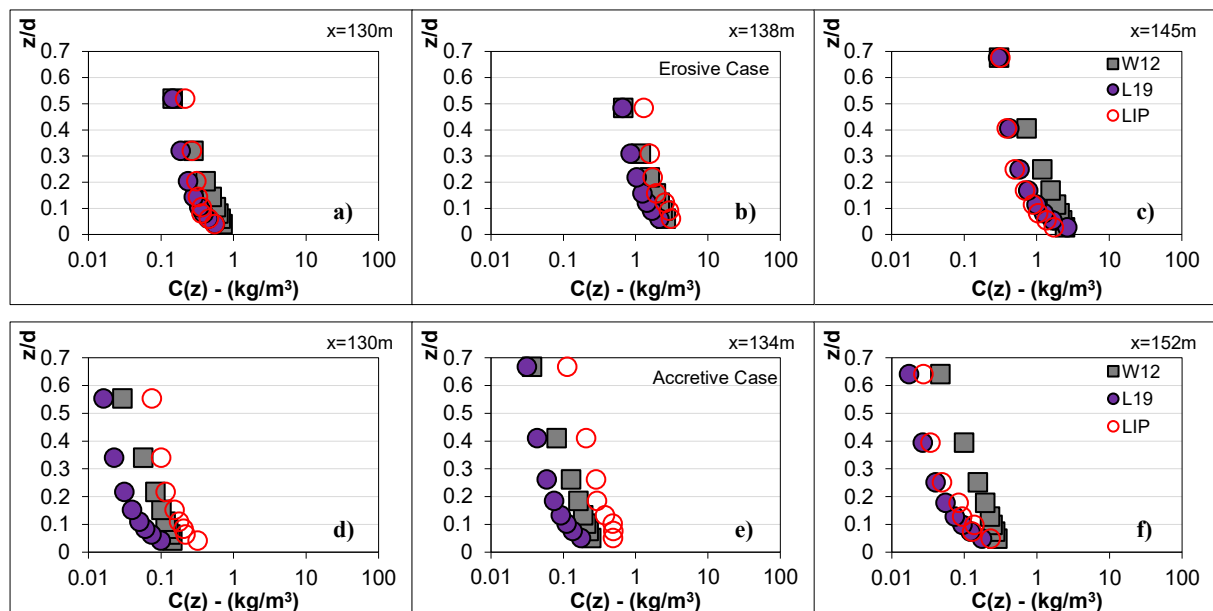


(Figure continued over page)

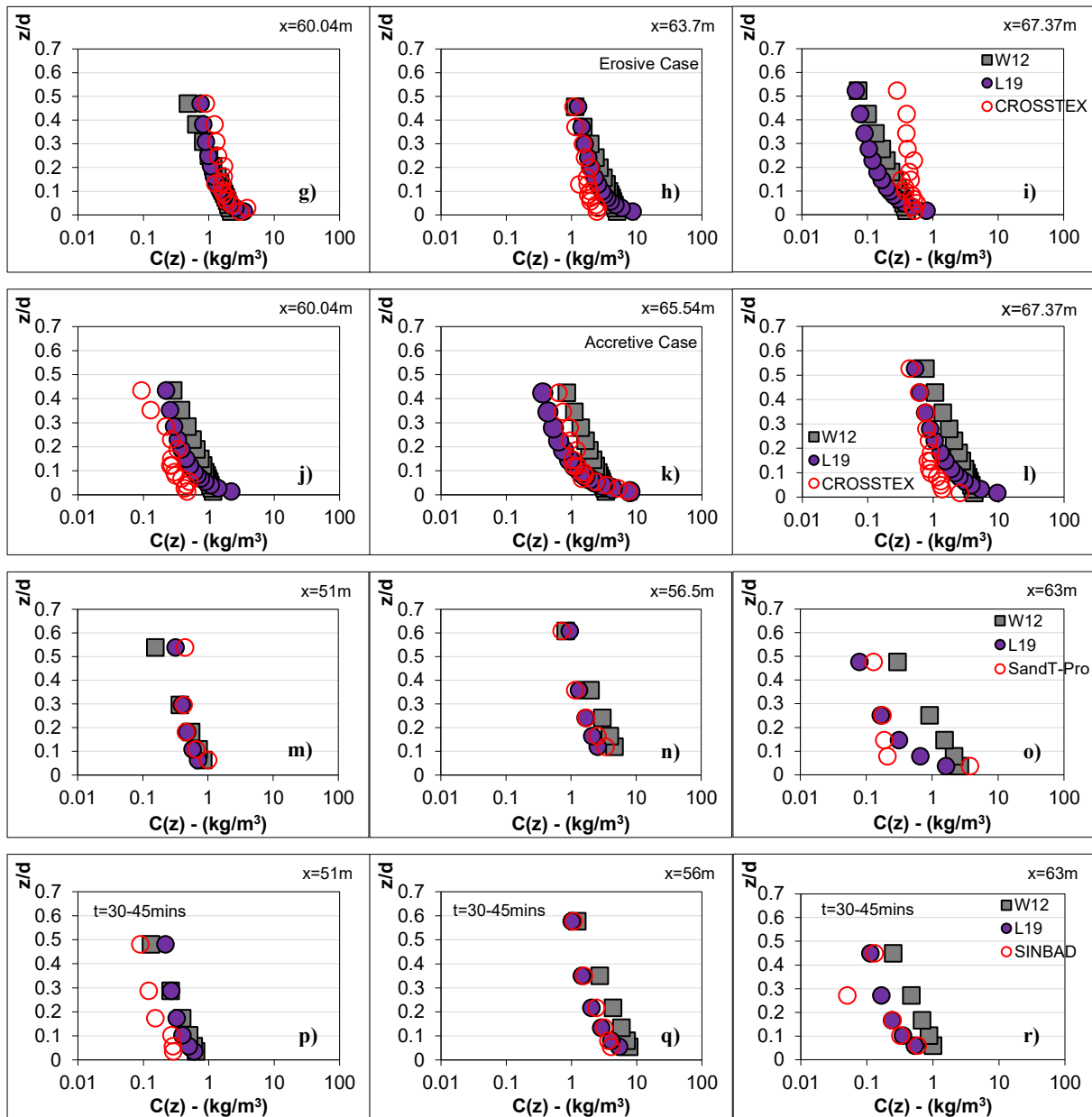


Figure 28 - Concentration profile ($C[z]$) of Measured (red circles) vs. computed (L19, purple circles; W12 grey squares).

Plots a-c show LIP erosive and d-f show LIP accretive cases respectively; plots g-i show CROSSTEX erosive and j-l show CROSSTEX accretive cases respectively; plots m-o show are SandT-Pro and plots p-r are SINBAD. Each row of plots shows three different cross-shore locations: before the breaking point (left plots), at the breaking or plunging point (central plots) and onshore of the breaking point (right plots).

3.4. Chapter Summary & Overview of Key Findings

A thorough evaluation study was carried out (Chapter 3.3.1.) for 6 existing reference concentration (C_0) formulae under field-scale regular and irregular breaking wave conditions,

identifying numerous limitations in the models studied. Common limitations observed in all existing C_0 models evaluated in this thesis could be largely put into two categories: 1) inapplicability to multiple cross-shore zones, and 2) inability to replicate the high levels of breaking-induced SSC found in the breaking zone. Models that are only applicable to one cross-shore zone (e.g. the breaking zone) are not very practical or widely applicable in morphodynamic models. If such models were to be incorporated into morphodynamic models, they would need to be adept in reproducing sediment concentration/transport patterns in multiple cross-shore zones. This is discussed in more detail in Chapter 5.1.2. of this thesis. Also, as SSC is highest in the breaking zone, under breaking conditions, large discrepancies between measured and predicted SSC in the breaking zone (which were observed to be up to an order of 10^1 kg/m^3) would likely result in unrealistic transport rates and resulting morphodynamic predictions. This is further examined in Chapter 4 of this thesis.

Several of the existing models related the C_0 to the sand pickup rate or Shields Parameter (i.e. assumed that sand pickup occurred when exerted bed shear exceeded critical bed shear). Such models were adept in reproducing measured SSC in the shoaling zone where there was no external (breaking-induced) turbulent kinetic energy (TKE), but performed poorly in the breaking zone, particularly around the plunging point, where breaking-induced TKE was highest. The poor performance of these models near the plunging point was a result of the implicit assumption that the sediment entrainment was only forced by local TKE generated by bed shear; neglecting the external TKE generated by strong breaking-induced vortices.

This limitation in models driven by the Shields parameter was addressed in more recent studies that incorporated the measured near-bed TKE (k_b) into the C_0 formulae, modifying the bed-shear-driven transport parameters to include the external TKE. Though latest studies (e.g. vdZ et al., 2017b) have indicated strong causal relationships between near-bed TKE and reference concentration/sediment pickup, there are also major limitations to using k_b to model the reference concentration. For example, such C_0 models were found to be highly sensitive to the accuracy and magnitude of measured or modelled k_b . This led to the k_b -driven models showing varied performance under different datasets.

A new practical model was developed to be able to adeptly tackle these commonly observed limitations. A unique and new method of modelling the cross-shore distribution of C_0 was proposed, driven in-part by a novel empirical relationship between the local water depth and reference concentration. It was proposed that by incorporating the inverse water depth ($1/d$)

into the proposed formula, the cross-shore distribution of C_0 could be captured well. The new C_0 model showed very good agreement with measured data (RMSE range 0.36-1.79 kg/m³) in the shoaling, breaking and inner surf zones, when validated against 119 tests cases from 4 high-resolution field-scale datasets. Even at the plunging point, where all other tested models were found to underpredict to varying degrees, the proposed model accurately replicated the measured reference concentration. This high level of accuracy in predictions was maintained even when the breaker bar was fully developed, where wave plunging intensity was highest.

There were however some discrepancies between measured and computed C_0 just after the plunging point where the bar trough was located. This was due to the model's sensitivity to the local water depth, which suddenly increases at the bar trough. This resulted in computed C_0 decreasing, whilst corresponding measured C_0 increased and peaked, leading to some discrepancies. It was speculated that under-prediction at this point was also partly related to the effects of horizontal advection of TKE and SSC, which is not incorporated in the simple L19 model. As not all concentration is locally generated, particularly in the breaking zone under strong plunging breakers, it is likely that some of the sediment in suspension was advected to/from adjacent regions. These effects were not incorporated into the L19 model, sometimes leading it to slightly under-predict immediately shoreward of the plunging point. These discrepancies were however relatively small, and the cross-shore distribution of C_0 was generally modelled very well. This is further discussed in Chapter 5.1.2.4. of this thesis. Overall, the new L19 model performs very well, with good applicability to shoaling, breaking and inner surf zones.

A second study was carried out (Chapter 3.3.2.), evaluating the performance of 5 existing and one newly modified concentration profile ($C[z]$) models against the same high-resolution datasets used for evaluating the reference concentration models. The existing $C[z]$ models were categorised generally as either power function or exponential, resulting in (mildly) parabolic and quasi-linear profiles respectively. The use of the well-known Rouse equation (which is a power function formula) is limited by its poor performance near the surface (where as $z \rightarrow d$, $SSC \rightarrow 0$) and also near the bed (where as $z \rightarrow 0$, $SSC \rightarrow \infty$). This resulted in unrealistic concentration profiles, and therefore it was suggested (both in literature and also in this thesis) that boundary conditions should be set for which the Rouse equation can be used. Based on the findings presented in Chapter 3, a condition of $d \gg z \geq 0.02m$ was suggested.

Both the SR93 and JS07 power function formulae were essentially modified from the Rouse equation to overcome the unrealistic predictions near the surface and bed. However, due to the small magnitude of the computed mixing parameter (M), all computed profiles were very steep, indicating quasi-uniform concentration over the whole water column, regardless of the cross-shore region. Contrarily, the measured concentration profiles were generally concave, indicating relatively higher SSC in the near-bed region and lower levels of SSC in the upper water column. Thus, there were often very large discrepancies between the measured and computed profiles, with the power function models (SR93 and JS07) overpredicting the concentration particularly in the upper water column. It was proposed that this issue could be resolved practically by incorporating a simple empirical constant to increase the value of the mixing parameter, and this theory was tested to produce a modified and improved $C[z]$ model.

The original SR93 model was modified and referred to as the L19 $C[z]$ model (not to be confused with the L19 C_0 model). The implementation of a new constant B into the existing mixing parameter of SR93 resulted in a more gradual (parabolic) curve that closely mirrored the measured profile. Not only did the L19 $C[z]$ model perform better than existing models qualitatively, but the RMSE of the L19 $C[z]$ model was considerably smaller than those of existing models, ranging between 0.03-2.3 kg/m^3 with an average of only 0.56 kg/m^3 (see Tables 15-16 above). The best alternative to the L19 model was the W12 model which also performed very well under most test cases. The main issue with the exponential type $C[z]$ models tested in this chapter (LK01 and W12 models) were that they produced quasi-linear concentration profiles that essentially worked like a line of best-fit through the measured concentration profile. This often resulted in good agreement between computed and measured $C[z]$ at the top and bottom of the water column but saw some discrepancies in the mid-water column. Though the performance of all $C[z]$ models is strongly dependent on the accurate estimation of the reference concentration, the exponential formulae seem to be more-so affected by the C_0 prediction, as the reference concentration practically serves as the starting point for the line of best-fit. Overall, it was found that the L19 $C[z]$ model best mirrored the measured concentration profile, both qualitatively and quantitatively in all cross-shore zones.

Chapter 4 – Validation for Cross-shore Suspended Transport Rates

The findings from this chapter have been prepared for submission as a journal article for publication in Coastal Engineering, Elsevier. The title of the paper is ‘Modelling the Suspended Sand Transport Rates under Breaking Waves’.

4.1. Introduction

The sediment transport rate, also known as the sediment discharge, can be defined as the mass (or volume or weight) of sediment – either dissolved or particulate – that is transported across a given cross-section of a given flow, per unit of time. Various methods have been developed over the years to predict the sediment transport rate, including graphical methods as well as mathematical and (semi-)empirical equations. Producing a single formula or a concise set of formulae to accurately model the sediment transport rate is a complex task, as there are numerous variables that affect and/or drive the transport rate that must first be defined for each individual case – e.g. the sediment concentration (bedload and suspended load; wave-related, current-related), the flow velocity (e.g. orbital, horizontal, vertical and turbulent), wave climate, particle size distribution, bathymetry, sediment settling velocity, local water depth and more. Not only so, but there are also several complex hydrodynamic forces acting at any one time – some of which are still poorly understood – along with resulting sediment-hydrodynamic and sediment-sediment interactions that need to be considered. Measuring sediment transport rates can also be quite challenging, as often any attempts to measure the transport rates will disturb the flow and therefore likely the measurements.

Despite the various obstacles, considerable success has been made in this endeavour over the last century, with transport rate formulae being developed and validated under certain pre-defined boundary conditions for both the bedload and suspended load – e.g. formulae that are applicable only to breaking (e.g. Jayaratne & Shibayama, 2007; Lim et al. 2020) or non-breaking waves (e.g. van der A et al., 2013), including (e.g. Bijker, 1971; van Rijn, 1993; 2007) or excluding waves (e.g. Meter-Peter-Muller, 1948; Engelund & Hansen, 1967; van Rijn, 1984), non-cohesive or cohesive sediment; for grain sizes within a certain range, etc. For such endeavours to continue to enhance our understanding, and therefore our ability to model such complex processes, there is an urgent need for more experimental studies collecting high spatial

(vertical and horizontal/cross-shore) and temporal resolution data in the field and in controlled laboratory settings: particularly (but not limited to) datasets consisting of co-located sediment concentration profiles and flow velocities, sediment settling velocities, bed profile evolution, direct measurements of sediment fluxes and/or transport rates and wave climate.

A recent example includes the large-scale laboratory experiments of the SINBAD project (vdZ et al., 2016) which consisted of thorough measurements of flow velocities, concentration profiles, grain size distributions and bed profile evolution, among other parameters that are key to gathering insights into transport processes and rates under plunging breaking conditions – some of which are documented in vdZ et al. (2017a&c). These measurements were carried out with particularly high spatial resolution in the wave bottom boundary layer WBBL (this is especially important as sediment transport in the near-bed region contributes largely to net sediment transport), allowing for more thorough development and validation of sediment concentration (e.g. concentration profile, reference concentration/sediment pickup models), velocity, turbulent kinetic energy (TKE), sediment flux and transport rate models. Similar data was collected in the field (e.g. Yu et al., 1993; Beach & Sternberg, 1996; Masselink et al., 2007; Miles & Thorpe, 2015; Brand et al., 2019), in large-scale laboratory settings with irregular breaking waves (e.g. Roelvink & Reniers, 1995; Yoon & Cox, 2010), and also for smaller scale experiments (e.g. Kobayashi et al., 2005). The majority of these studies however consisted of measurements of a relatively lower spatial resolution in the cross-shore and vertical directions. Depth-integrated sediment transport rates estimated from such datasets may be less reliable (not accurately representing true values), but the data can still be used for any studies investigating sediment fluxes and transport rates (e.g. Beach & Sternberg, 1996; Yoon & Cox, 2012; van der Werf et al., 2015) or concentration profiles within the water column (e.g. Yoon & Cox, 2015; Lim et al., 2020), and also to analyse the relative contributions of bedload and suspended load transport components, as well as the patterns of onshore/offshore transport (e.g. Masselink et al, 2007; Miles & Thorpe, 2015; Brand et al., 2019; 2020).

It is also essential to carry out complementary modelling studies that focus on the development of new formulae based on novel insights and trends discovered in the experimental studies. The level of robustness required in sediment transport models are still insufficient in computing medium- to long-term morphology via a process-based approach, often causing the modeller to have to rely on considerable calibration efforts to produce good results (as described in Chapter 1.1.1.).

One fundamental process that is often not well-accounted for in existing transport models is the influence of wave-breaking on resulting bedload and suspended load. It was demonstrated in Chapters 3.3.1. & 3.3.2. that many existing suspended sediment concentration models (that were developed for breaking wave conditions) were incapable of accounting for the strongly enhanced sediment pickup and vertical mixing induced by breaking-generated TKE under plunging breakers. It was predicted that such large discrepancies would inevitably result in unrealistic estimations of transport rates and therefore corresponding morphodynamic predictions. This chapter therefore aims to investigate the effects of improved suspended sediment concentration (SSC) models – reference concentration C_0 and concentration profile $C[z]$ models – on the prediction of cross-shore sediment transport rates. Chapter 4.2. provides an overview of the methodology and key formulae used in this chapter. Chapter 4.3. presents two different sets of analysis:

- 1) The new L19 C_0 and $C[z]$ models are used to compute the current-related suspended sand transport rates (q_{sc}). These computed values are then validated against measured transport rates and also against the default Delft3D sediment transport formulae of van Rijn (1993) as well as those of van Rijn (2007). The aim of this analysis is to examine the extent to which improvements in C_0 and $C[z]$ formulae (detailed in Chapter 3) affect the accuracy of resulting sediment transport rate computations.
- 2) A combination of tests is carried out to investigate the extent to which improvements in C_0 formulae alone and improvements in $C[z]$ formulae alone have on computed transport rates. The analysis also examines which of the aforementioned improvements have a greater effect on the accurate prediction of transport rates.

It should be noted that the computation of the wave-related suspended transport is not focused on in this thesis, but it is briefly covered in Chapters 4.3.2. and 5.1.6. as the wave-related component contributes towards the net suspended transport rate q_s . The main focus of Chapters 3 & 4 is on improving the modelling of the current-related suspended transport rate q_{sc} , under which the enhancing effects of breaking-generated vortices and strong undertow on SSC are included (refer to Chapter 4.2.). It should also be noted that when referring to “measured transport rates” herein, it is referring to the transport rates estimated using measured horizontal velocity (separated into time-averaged and oscillating components) and also the measured concentration profile, as opposed to “computed transport rates” which refer to transport rates estimated using measured horizontal velocity components and computed concentration profile.

4.2. Methodology and Formulae

The sediment transport rate is generally computed separately for the bedload and suspended load and use the sum of the two to find the total load – however there are some formulae that compute the total load directly (e.g. Meyer-Peter-Muller, 1948; Engelund & Hansen, 1967). Although in nature there is no clear division between the bedload and suspended load, it is often necessary to define a boundary layer that separates the two for practical reasons. Often this is done by specifying a reference level (z_0), considering all transport below this level to be bedload and above it as suspended load. The suspended sediment concentration (SSC) at this reference level is referred to as the reference concentration (C_0), which can be used to compute the concentration profile ($C[z]$) – as seen in Chapter 3.3 of this thesis. The reference concentration essentially serves as an indicator of how much sediment is in suspension at a given cross-shore location and the concentration profile specifies the vertical distribution of the concentration within the water column.

The cross-shore suspended transport rate (q_s) is generally split into an oscillatory wave-related component (q_{sw}) which is driven by wave asymmetry, and a mean current-related component (q_{sc}) driven by the undertow. The wave-related component refers to the sediment particles transported by oscillating fluid components (orbital motion) and the current-related component refers to the sediment transported by advective time-averaged, or mean, current velocities. Waves are able to generate net sand flux in the cross-shore direction due to the oscillating components of flow \tilde{u} and sand concentration \tilde{C} (van Rijn et al., 2013). The product of the oscillating (demeaned) flow velocities and sand concentration components are referred to as the wave-related sand flux and can be vertically (depth-)integrated to estimate the wave-related suspended transport rate:

$$q_{sw} = \int_{z_0}^{0.10} \langle \tilde{u}\tilde{C} \rangle dz \quad (38)$$

Where the $\langle \rangle$ indicates wave-averaging.

Net currents such as breaking-induced cross-shore and longshore currents are also induced by waves (van Rijn et al., 2013). These currents, as well as increased near-bed concentrations induced by the stirring action under (breaking) waves, are included in the current-related suspended transport rate (q_{sc}). The current-related horizontal sand flux is a product of the wave(time)-averaged horizontal velocity and the time-averaged sand concentration profile.

Coastal area models such as Delft3D obtain the time-averaged suspended sand concentration field by solving the wave-averaged flow and advection/diffusion equations (van Rijn et al., 2013). In this chapter the horizontal velocities measured from the SINBAD project will be used in conjunction with the SSC computed using the various formulae (detailed later in this section) to find the current-related suspended sand flux. The current-related suspended transport rate (q_{sc}) is estimated by taking a vertical integral of the current-related horizontal suspended transport flux, from the reference level to the surface:

$$q_{sc} = \int_{z_0}^d \overline{u(z)C(z)} dz \quad (39)$$

Where d is the local water depth and the overbar indicates time-averaging; $u[z]$ is the time-averaged horizontal fluid velocity profile and $C[z]$ is the time-averaged suspended sediment concentration profile. The lower limit of the integral must be precisely defined when computing q_{sc} and q_{sw} , as it is very important when determining suspended transport rates. It should be noted that the proposed L19 formulae have a different z_0 to the formulae of van Rijn (1993; 2007). Details of the different z_0 values used are detailed in Chapters 2.2.1. and 2.3. The net cross-shore suspended transport rate (q_s) is simply the sum of the mean (current-related) and oscillatory (wave-related) suspended transport rate components.

The SINBAD experiments (van der Zanden et al., 2016) [discussed in Chapter 3.2 of this thesis] measured sediment transport fluxes and rates: bedload transport rates and suspended transport rates (wave-related, current-related, and turbulence-related). As briefly mentioned in Chapter 4.1, the aim of this chapter is to test the improved time-averaged reference concentration and concentration profile formulae presented in Chapter 3 (c.f. Lim et al., 2020) in computing suspended sediment transport rates. This evaluation will be carried out systematically by running two sets of tests referred to throughout this chapter as Part 1 and Part 2.

- 1) The current-related suspended transport rates computed using the L19 C_0 and $C[z]$ formulae will be compared against those computed using the original (unmodified) suspended load models of VR93 and VR07. When computing the current-related sediment flux $uC[z]$, the $C[z]$ component of $uC[z]$ will be estimated using each of the L19, VR93 and VR07 transport models. Measured horizontal velocities are used for the $u[z]$ component of $uC[z]$ - these were measured using two different sets of instruments: the near-bed region ($z \leq 0.10m$) was measured using Acoustic Concentration and Velocity Profilers (ACVP) and the outer flow region ($0.10m < z$) was measured using

Acoustic Doppler Velocimeters (ADV) – further detailed provided in Chapter 3.2. of this thesis.

- 2) The extent to which improvements to C_0 and $C[z]$ formulae affect resulting transport rates will be investigated. By keeping the same C_0 formula and changing only the $C[z]$ formulae, it will be possible to observe the extent to which $C[z]$ formulae affect the transport rates. Similarly, by running standalone tests with different C_0 formulae combined with the same $C[z]$ formula, the extent to which the reference concentration has an effect on resulting transport rates will be investigated.

For Part 1, the VR07 formulae are detailed in Chapters 2.2.1. (Eqs. 14-16) and 2.2.2. (Eqs. 20-21; VR07 used the Rouse Equation to compute the concentration profile). The L19 formulae are detailed in Chapters 2.2.2., 2.3.1. and 2.3.2. (Eqs. 36-37; 22-24). The VR93 formulae are detailed below. For Part 2, the performance of the SR93 and W12 $C[z]$ (Chapter 2.2.2., Eqs. 22-25 and Eqs. 32-33 respectively) formulae are compared against the L19 $C[z]$ formula.

Van Rijn (1993) use the same reference concentration formula as van Rijn (2007), defining the reference concentration as a function of the dimensionless particle diameter and transport parameter T_Φ , and determining the magnitude of sediment transport based on applied shear stress exceeding the Shields critical shear stress as seen in Eq. 15 (Chapter 2.2.1.5.). The transport parameter T_Φ of VR93 however differs from that of VR07. Van Rijn (1993) defined the transport parameter as follows:

$$T_\Phi = [(\alpha_{cw} \mu_c \tau_c + \mu_{w,a} \tau_w) - \tau_{cr}] / \tau_{cr} \quad (40)$$

where:

α_{cw} = wave-current interaction coefficient

μ_c & $\mu_{w,a}$ = efficiency factor current & wave respectively

$\tau'_{b,c}$ & $\tau'_{b,w}$ = current-related bed-shear stress & wave-related bed-shear stress respectively

$\tau'_{b,cr}$ = Shields critical bed shear stress

Van Rijn (1993) also use the Rouse Equation to compute the concentration profile (Eqs. 20-21)

4.3. Validation

4.3.1. Current-related suspended transport (q_{sc})

4.3.1.1. Part A – L19 vs VR93 vs VR07

As seen in Chapter 3 of this thesis (e.g. Chapter 3.2.), three cross-shore zones are specified in the SINBAD dataset: the shoaling zone ($x = 51-53$ m), the breaking zone ($x = 53-58.5$ m) and the inner-surf zone ($x = 58.5-63$ m). Figure 29a shows that measured horizontal flow velocity profile $u[z]$ is lowest in the shoaling zone ($x = 51$ m), with relatively constant levels of offshore-directed $u[z]$ ranging between $-0.02-0.16$ m/s (negative sign indicates offshore-directed) throughout the water column, and an depth-averaged $u[z]$ of ≈ -0.147 m/s. However, in the breaking zone ($x = 53-58.5$ m) – particularly after the wave plunges (at $x = 55.5-56$ m; Figs. 29 d, g) there is a large decrease in orbital velocities and a sharp increase in the magnitude of offshore-directed $u[z]$ in the lower half of the column ($z/d < 0.5$) – by approximately a factor of 4 larger than those found in the shoaling zone. This large velocity skew in the cross-shore direction is attributed to strong plunging waves breaking over relatively low water depths, which induces a combination of onshore-directed mass flux increase and positive pressure gradients. Consequently, net currents compensate (undertow) for the onshore flux and pressure gradients, causing increases in the magnitude of offshore-directed horizontal velocity in the lower half of the water column (vdZ, 2016). This local increase in $u[z]$ continues past the plunging point (in the onshore direction) and peaks at $x = 57$ m (reaching as high as -0.55 m/s) before it begins to decline again in the inner surf zone. This spatial lag in undertow magnitude peaking at $x = 57$ m (0.5m after the plunging point) is consistent with observations from van der A et al. (2017) and vdZ et al. (2019). Nearest the bed ($z/d < 0.05$), the magnitude of offshore-directed horizontal velocities is generally slightly lower than in the lower-mid water column, particularly in the breaking zone (in the order of 10^{-1} m/s in the breaking zone). This is attributed to the velocities being reduced by bed friction forces that work in the opposite (onshore) direction (vdZ, 2016). Even still, the net horizontal velocity continues to be offshore-directed in the lower half of the water column in all three cross-shore zones. In the lower water column of the inner surf zone the velocities remain relatively high in comparison to the shoaling zone.

The vertical concentration profile varies considerably with elevation above bed, with relatively lower levels of suspended sand concentration (SSC) in the upper half of the water column and

increasingly higher concentrations in the lower water column towards the bed. Measured sediment concentration in the lower water column varies by one order of magnitude – in some instances even two orders of magnitude – between the shoaling zone (where SSC is in the order of 10^0 kg/m^3) and the breaking zone (in the order of 10^1 kg/m^3) – refer also to Chapter 3.3.2.1. Measured concentration levels in Fig. 29 are seen to peak at $x = 55.5\text{-}56\text{m}$ around the plunging point (see Figs. 29 e, h) as described in Lim et al. (2020) [Chapter 3.3.1.]. This sharp increase is very well modelled by the L19 ($C_0 + C[z]$) model throughout the whole water column (as further demonstrated in Chapter 3.3.2.7.) and reasonably well by VR93 model in the lower water column, near the bed. The VR07 model underpredicts the concentration by one order of magnitude throughout the whole water column at this cross-shore location. Analysis and evaluation of the performance of the L19 and VR07 reference concentration models are covered in-depth in the paper of Lim et al. (2020) [analysis presented in Chapter 3.3.1.].

Measured current-related suspended flux ($uC[z]$) is entirely offshore directed (negative values) in the lower water column (see right column of Fig. 29). The magnitude of measured $uC[z]$ is relatively small in the shoaling zone – in the order of $10^{-2} \text{ kg/m}^2\text{s}$ even in the WBBL but increases by one order of magnitude as it enters the breaking zone (at $x = 53\text{m}$). Similar to the measured reference concentration [Chapter 3.3.1.], concentration profile and even the horizontal flow velocity profile, there are large increases in measured $uC[z]$ in the lower water column (around $z/d = 0.2$) just shoreward of bar crest (plunging point) – at $x = 55.5\text{m}$ – with values in the order of $10^0 \text{ kg/m}^2\text{s}$, which is two orders of magnitude higher than those found in the shoaling zone. It was reported that the largest vertical flux between the bedload and the suspended load layers occurred in the breaking region ($54\text{m} < x < 58\text{m}$), with steep cross-shore gradients in SSC and transport rates in this region due to the strongly non-uniform cross-shore hydrodynamics which were induced by wave breaking and varying water depths (vdZ et al., 2017b).

As described in Chapter 1.1.1., dense clouds of sediment are thrust into suspension at the plunging point, as strong turbulent eddies are injected into the water column near the breaker bar crest, travelling through the water column towards the bed. Though suspended flux is always seen to be highest near the bed, even in the upper water column at the plunging point, the magnitude of suspended flux is larger than the flux in the WBBL of the shoaling zone – by approximately a factor of 10. This indicates that aside from the higher levels of entrainment caused by the surface-generated TKE, vertical sediment mixing is also enhanced considerably due to these turbulent eddies (Nielsen, 1984; Ogston and Sternberg, 2002; Aagaard & Hughes,

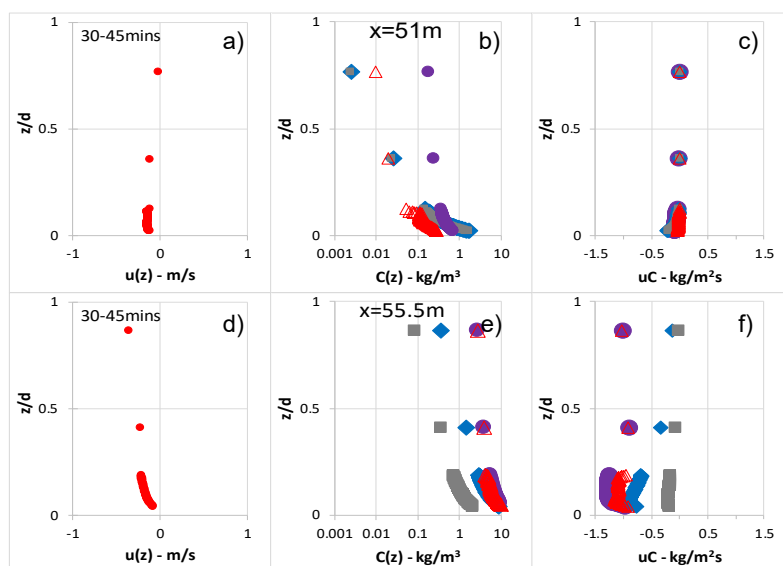
2010; Aagaard and Jensen, 2013; Yoon et al., 2015). This was also seen in the analysis of concentration profiles in Chapter 3.3.2. of this thesis.

Despite wave plunging occurring at $x = 55.5\text{m}$, the offshore directed sediment fluxes can be seen to peak near the bed at $x = 56\text{m}$ (Fig. 29 i) – which is in agreement with the trends observed in the cross-shore distribution of measured reference concentration and the concentration profile. This can be attributed to the turbulent eddies travelling not only downward towards the bed from the plunging point, but also obliquely in the direction of wave propagation (Nadaoka et al., 1989; Brinkkemper et al., 2016) – further entraining sand as it approaches the bed. This speculation is supported by the magnitude of measured $u_C[z]$ declining (settling) in the upper water column at $x = 56\text{-}56.5\text{m}$ whilst corresponding values increase and peak in the lower water column (see Figs. 29 i, l). This is contrary to the trend observed at $x = 55.5\text{m}$ where the sediment concentration and flux were constantly high throughout the whole water column (see Fig. 29 f). The decreases in upper water column and increases in the near-bed regions suggest that the turbulent eddies that were stirring sediment in the upper water column at $x = 55.5\text{m}$ have travelled towards the bed and in the direction of wave propagation, causing higher levels of pickup and mixing in the WBBL instead of in the outer flow (elevations outside of the WBBL). This is also supported by the corresponding $u[z]$ profiles at $x = 55.5\text{m}$ and $x = 56\text{m}$ which indicate increases in offshore velocities in the near-bed region whilst corresponding values are lower in the upper water column (refer to Fig. 29 d, g, j).

These dramatic changes in $u_C[z]$ between shoaling and breaking zones are well-modelled by L19 in both the vertical and cross-shore distribution of (depth-averaged) $u_C[z]$, even around the plunging point where horizontal sediment fluxes are highest. The suspended flux $u_C[z]$ computed using VR93 and VR07 models indicate reasonable agreement with measured flux in the shoaling and pre-plunging regions ($x < 55.5\text{m}$) but show varied degrees of underprediction in the breaking zone (between $x = 55.5\text{-}56.5\text{m}$). In this region, the discrepancies are greater in the VR07 model predictions, with computed $u_C[z]$ being very small ($\approx 0 \text{ kg/m}^2\text{s}$) over the whole water column at $x = 55.5\text{m}$ (plunging point) and at $x = 56\text{-}56.5\text{m}$ (where measured flux peaks). Only in the region nearest the bed ($z/d < 0.05$) does the VR07 model predict an increase in offshore-directed transport. This of course is contrary to the measured flux which indicates a steep exponential increase in horizontal flux at the corresponding cross-shore locations. A similar trend is observed with the VR93 model, but to a lesser extent (discrepancies are smaller but still considerable). Like the VR07 model, the VR93 model predicts very low (quasi-uniform) levels of horizontal flux from around $z/d \approx 0.08$ to the surface. Near-bed predictions of the

VR93 model are considerably larger than those of the VR07 model (by approximately a factor of 3 at $z/d \leq 0.1$) but are still significantly smaller in magnitude than the measured $uC[z]$ values (by 1 order of magnitude in some cases). These discrepancies observed in the VR07 and VR93 models are marginally smaller in the inner breaking zone ($x = 57\text{m}$; Fig. 29 o). The performance of the VR07 and VR93 models is relatively good in the inner surf zone, similar to that seen in the shoaling zone and breaking zone pre-plunging (Fig. 29 r).

The bed profile evolution from the initial run (00-15mins) to the final bed profile (75-90mins) are shown in plots c-d) of Fig. 30. As bar morphology is intrinsically linked to the transport rates – where the sediment transport affects bar morphology, and the subsequent bar morphology affects local hydrodynamics and therefore resulting sediment transport – it is essential to consider how the bed (particularly the breaker bar) evolves over the period of the experiments. Though detailed explanations of the bed profile evolution and related hydrodynamics can be found in vdZ et al. (2017c), some key points are described briefly herein for the readers’ convenience. As seen in plots c-d), the bar migrates marginally in the onshore direction, with both the onshore- and offshore-facing slopes of the bar becoming steeper as the experiment runs progress. At the same time, the bar crest increases in height, whilst the bar trough deepens. VdZ et al. (2017c) reported that the bar growth was a result of the accumulation of 1) primarily onshore-directed transport in the shoaling zone and 2) offshore-directed transport in the breaking and inner-surf zones. In this chapter, the reference is given to the initial (00-15mins) profile and final (75-90mins) profiles where necessary, but the main validation and analysis of transport rates are focused on tests/data from the midpoint of the experiments (30-45mins; as done in Chapter 3) where the breaker bar was sufficiently developed and data contained the least anomalies.



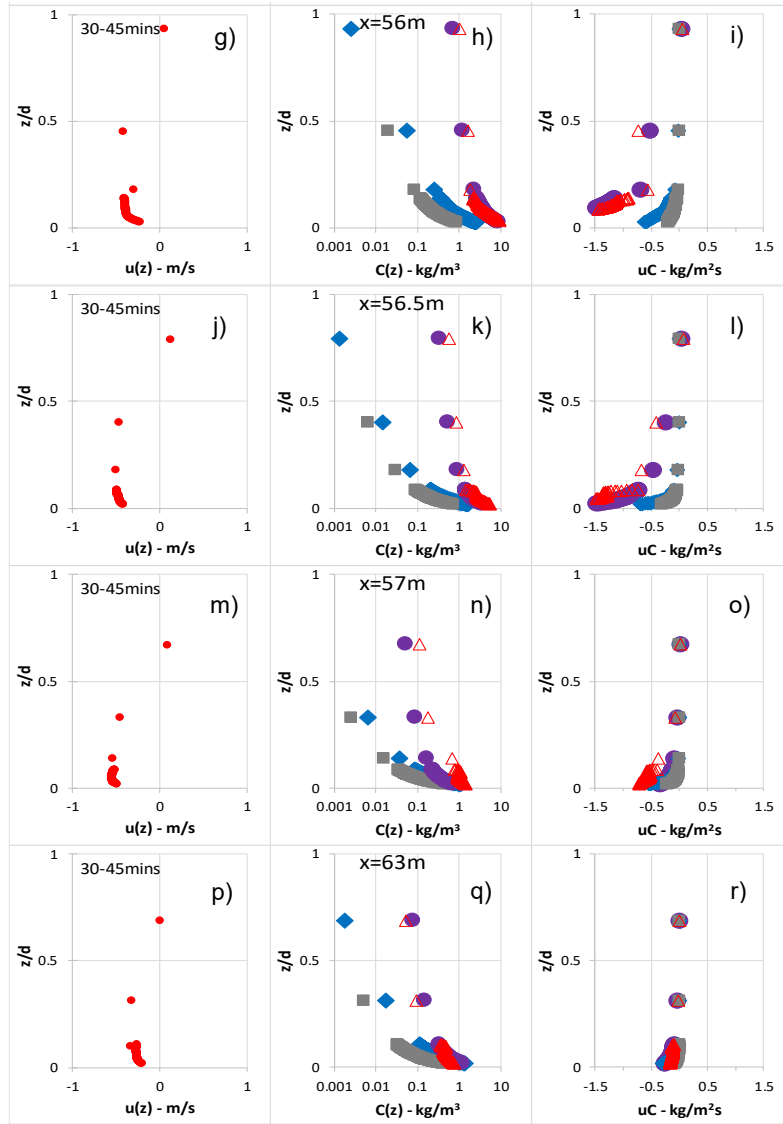


Figure 29 – Vertical profiles of computed $u[z]$, $C[z]$ and $uC[z]$ – L19 vs. VR93 vs. VR07.

Left column: horizontal velocity profile $u[z]$, middle column: concentration profile $C[z]$ and right column: horizontal suspended sediment flux – measured (red) vs. computed (purple: L19, blue: VR93, grey: VR07).

The measured wave-related transport rate (see Fig. 30) is almost entirely onshore-directed (positive), and dominant in only the shoaling region at $x = 51\text{m}$ (c.f. vdZ et al., 2017a). Note: q_{sc} is displayed in m^2/s which is the volumetric transport rate instead of mass transport which is displayed in $\text{kg}/\text{m}/\text{s}$. Simply multiplying the mass transport by sediment density = $2650 \text{ kg}/\text{m}^3$ gives the volumetric transport rate in m^2/s . Though it is marginally dominant in the shoaling region, the magnitude of q_{sw} is very small, in the order of $10^{-3} \text{ kg}/\text{m}/\text{s}$ (or $10^{-7} \text{ m}^2/\text{s}$). After wave breaking occurs at $x = 53\text{m}$, the current-related suspended transport becomes dominant and remains so throughout the breaker and inner surf zones. The measured current-

related suspended transport rate (q_{sc}) is entirely offshore directed (negative), with smallest levels of offshore transport in the shoaling zone (magnitude in the order of 10^{-3} kg/m/s) and peaking at approximately -0.69 kg/m/s in the vicinity of the plunging point. Just as the magnitude of reference concentration (concentration profile) was found to increase sharply at the plunging point in Chapter 3.3.1. (Chapter 3.3.2.), the magnitude of q_{sc} also increases sharply, indicating direct correlation between C_0 , $C[z]$ and q_{sc} . The current-related suspended transport rate gradually declines in magnitude between $x = 55.5$ m (after peaking) and $x = 59$ m, approximately where the inner-surf zone starts. The magnitude of q_{sc} in the inner surf zone remains at a steady level between ≈ 0.04 - 0.06 kg/m/s.

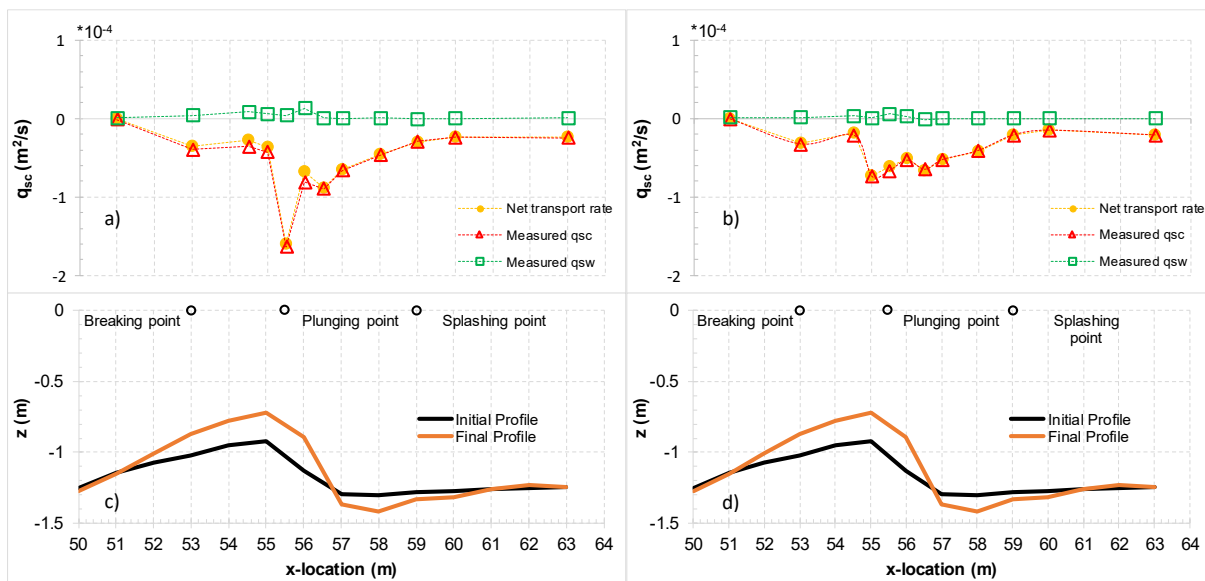


Figure 30 - Cross-shore distribution of measured volumetric q_{sc} .

Plots a-b) measured current-related (q_{sc}) & wave-related (q_{sw}) transport rates ($\cdot 10^{-4}$) and also the net transport rate ($\cdot 10^{-4}$). Plot a) is at $t=00$ - 30 mins and plot b) is at $t=75$ - 90 mins; c-d) bed profile evolution.

Figure 31 shows the cross-shore distributions of computed vs. measured q_{sc} . Fig. 31a displays the current-related transport rate computed using the newly proposed $C[z]$ formulation (purple circles). The shape of the cross-shore distribution of the measured q_{sc} is captured very well by the L19 formulae. This is consistent with the performance of the L19 reference concentration model shown in Chapter 3.3.1. and the concentration profile analysis presented in Chapter 3.3.2. of this thesis as well as Fig. 29. Even in the plunging region, the L19 model replicates the sharp increase in offshore-directed transport. Though small discrepancies were found between measured and computed C_0 immediately shoreward of the plunging point ($x = 56$ m) resulting

from horizontal advection and propagation of turbulent eddies (refer to Fig. 20, Chapter 3.3.1.7.), there seems to be little effect on the resulting q_{sc} , with marginal underprediction at different locations over the different cross-shore regions ($R^2 = 0.97$, RMSE = 0.06 kg/m/s; Table 17 below). This is also clearly illustrated in Fig. 32 where 75% of the L19 points lie within the \pm factor 2 region and 92% within a \pm factor 3 margin.

Similar to the trends observed with the concentration profile in Chapter 3.3.2., herein sensitivity analysis carried out in computing q_{sc} using different formulae (and/or values) for the mixing parameter M resulted in large variations in performance, indicating high sensitivity to the formulation (and/or value) used in estimating the mixing parameter in the concentration profile. I.e. small changes in the magnitude of the mixing parameter had relatively larger effects on the accuracy of resulting q_{sc} . Similar trends were observed for both VR93 and VR07, which indicate that the quality of predictions of q_{sc} is strongly dependant on the formulation of $C[z]$ that is applied. The (extent of) effects of different concentration profile and reference concentration formulae on resulting transport rates are further investigated in Parts B.1. and B.2. of Chapter 4.3.1.2. respectively.

Table 17 - R^2 and RMSE values between computed and measured q_{sc}

| | R^2 for t=30-45 (-) | RMSE 30-45 (kg/m/s) |
|---------------------------------|---|----------------------------|
| L19 q_{sc} | 0.97 | 0.06 |
| VR93 q_{sc} | 0.68 | 0.24 |
| VR07 q_{sc} | 0.36 | 0.62 |

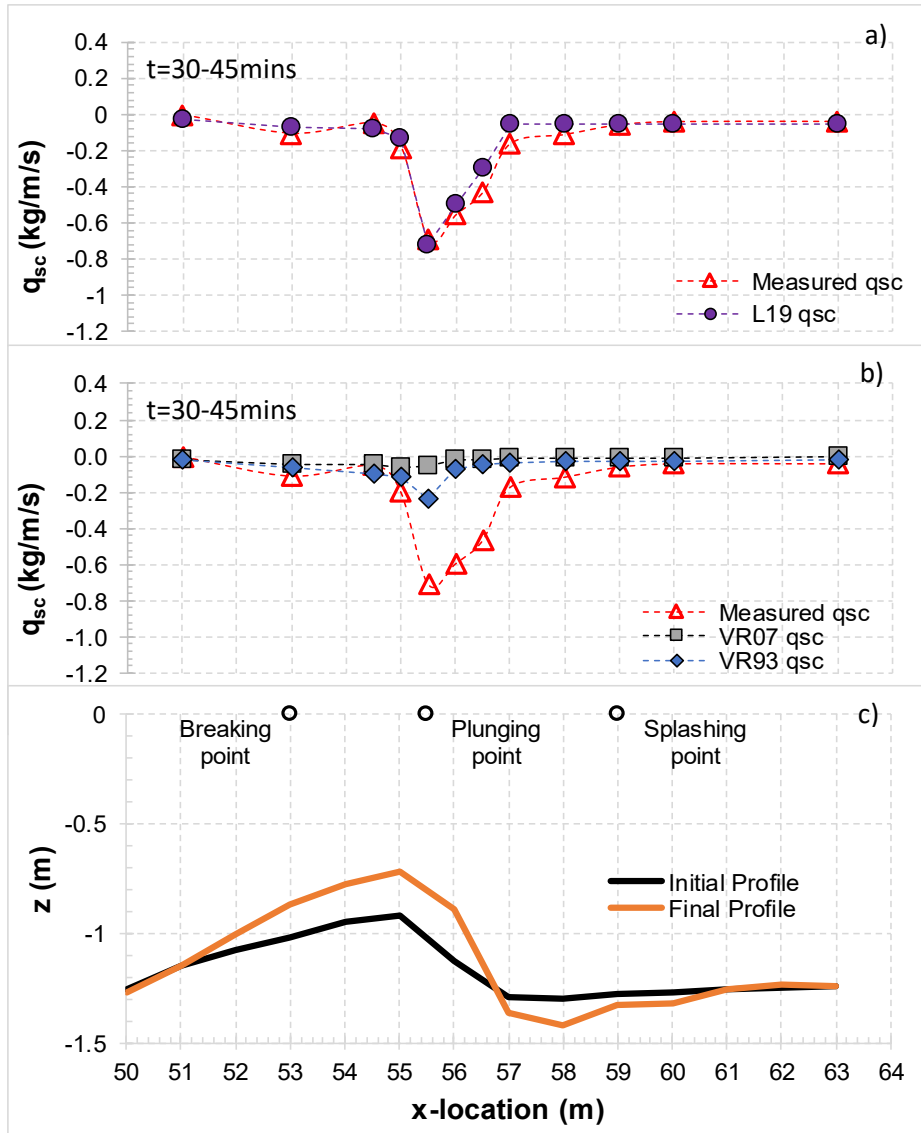


Figure 31 - Cross-shore distribution of q_{sc} : Computed (VR93, VR07) vs. Measured
 Plots a) L19 q_{sc} vs. measured, b) VR93 q_{sc} and VR07 q_{sc} vs. measured, c) bed profile evolution

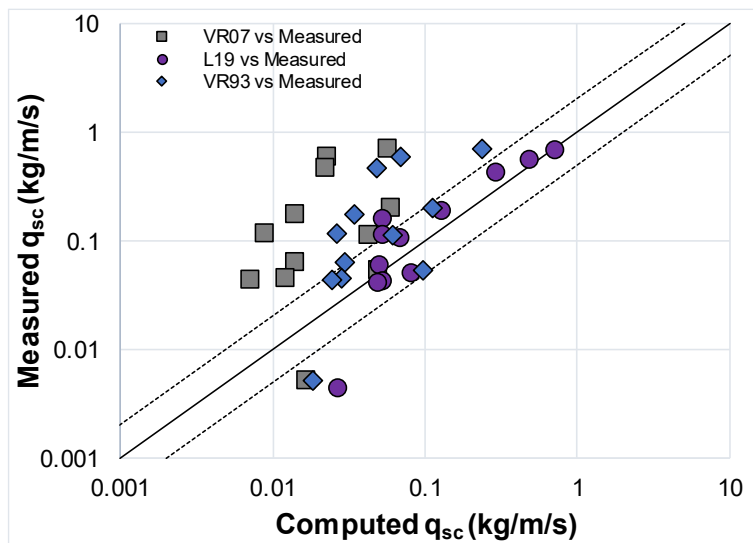


Figure 32 - computed vs. measured q_{sc} (scalars) – (kg/m/s).

L19 (Purple circles), VR07 (Grey squares) and VR93 (Blue diamonds). Solid line indicates 1:1 ($x=y$) and dotted lines indicate \pm factor 2 region.

Fig. 31b shows that the VR93 model produces quite good agreement with the measured data in the shoaling and inner surf zones, capturing the cross-shore distribution of q_{sc} to a satisfactory degree, but (as seen in Fig. 29 with $uC[z]$) large discrepancies are seen in the breaking zone – particularly between $x = 55-56.5m$ which is at the plunging point. In these regions, measured transport rates are larger than computed by up to a factor of 9.6 (at $x = 56m$), with measured q_{sc} being larger on average by a factor of 6.1 between $x = 55.5-58m$. In terms of magnitude, the greatest discrepancies are as large as 0.52 kg/m/s which is 88% of the magnitude of measured q_{sc} at that location ($x = 56m$). The largest discrepancies between measured q_{sc} and L19 at the same cross-shore location are marginal in comparison, ranging between $0.008-0.13 \text{ kg/m/s}$. The underprediction observed in the VR07 model is even greater than the VR93 model, with the magnitude of discrepancy being as large as 0.57 kg/m/s (96% of measured q_{sc} at that location).

In Fig. 32 only 8% of the VR07 points fall within a \pm factor of 2 margin, with significant underprediction in most cross-shore locations. Unlike the case for L19, the overall cross-shore distribution of q_{sc} is not well-captured by VR07 (Fig. 31 b), which instead indicates a quasi-uniform cross-shore distribution of q_{sc} , even at the wave plunging point. This is consistent with the findings of Lim et al. (2020; Chapter 3.3.1.) who found that the VR07 C_0 model predicts reference concentration well in the shoaling and inner-surf zones, but poorly in the breaking zone where externally generated breaking-induced TKE invades the wave bottom boundary layer (WBBL). This was attributed to the model of VR07 not sufficiently accounting for highly turbulent eddies generated by wave plunging, instead modelling the reference concentration as a function of locally generated (bed-shear induced) TKE only. As wave-breaking also induces strong undertow currents, the current-related suspended transport increases sharply around the plunging point ($x = 55.5-56.5m$). It was speculated in Chapter 3 that the large discrepancies observed between measured and computed suspended sediment concentration would have direct effects on the accuracy of resulting transport rates, producing unrealistic values. This is clearly the case as seen in Figs. 29-32.

It is worth considering whether the performance of the reference concentration model was the main cause of the poor performance seen in the VR93 and VR07 models, or if it was the concentration profile model – or even a combination of both. In the following sections, a

systematic analysis is carried out to investigate the (extent of) the influence different C_0 and $C[z]$ models have on the resulting transport rates.

4.3.1.2. Part B – Effects of Improvements to C_0 and $C[z]$ on Resulting Transport Rates

Part B.1. Fixed C_0 + Varied $C[z]$

Similar to the analysis carried out in Chapter 3.3.2., a single reference concentration formula is paired up with a number of different concentration profile formulae, but this time to determine how the accuracy/performance of different $C[z]$ models affects the accuracy of resulting computed transport rates. For example, whether the same trends observed in Chapters 3.3.1. and 3.3.2. (e.g. poor performance near the plunging point) are reflected in the computation of transport rates and to what extent, whether these trends are linear or not, etc. Among the reference concentration formulae tested in Chapter 3.3.1. of this thesis, the L19 C_0 model was demonstrated to perform the best under breaking wave conditions. Thus, it is used to compute C_0 in all tests presented in Part B.1. The following combinations will be tested in this section:

Table 18 - Combinations of C_0 and $C[z]$ formulae used for Part B.1

| Reference Concentration Formula (C_0) | Concentration Profile Formula ($C[z]$) |
|---|--|
| L19 – Eq. 9, 14, 36 | L19 – Eqs. 22-24, 37 |
| L19 – Eq. 9, 14, 36 | W12 – Eqs. 33-34 |
| L19 – Eq. 9, 14, 36 | SR93 – Eqs. 22-25 |

The reason the L19, W12 and SR93 $C[z]$ formulae were chosen to be tested is straightforward: the L19 and W12 $C[z]$ models indicated the best performance in the analysis presented in Chapter 3.3.2. Both models performed consistently well in the shoaling, breaking and inner-surf zones but indicated some minor discrepancies in varying areas. The W12 $C[z]$ formula showed some small discrepancies in the mid- and upper-water column, and the L19 $C[z]$ formula showed occasional underprediction in the shoaling and inner-surf zones. As the L19 and W12 models were the best performing of the power function type and exponential type

$C[z]$ formulae respectively, their performances are compared to see if they perform just as well in computing sand transport rates, and/or if there are any unexpected effects on computed transport rates resulting from the differences in formulae. The SR93 $C[z]$ model did not perform very well in Chapter 3.3.2. but was chosen as it was the base model which was modified to obtain the L19 $C[z]$ model. By comparing the difference in performance between the SR93 and L19 formulae, it will be possible to assess the impact that the small change (made to the mixing parameter) has on resulting transport rates.

Analysis:

Measured Transport Rates

The shape of the cross-shore distributions of measured suspended sand flux $uC[z]$ and measured current-related suspended sand transport rate q_{sc} appear to be the inverse of the cross-shore distribution of depth-averaged $C[z]$ – i.e. quasi-symmetrical across the x -axis, as seen in Figs. 33-35. There are however some small variations in the cross-shore location at which the breaking-generated TKE causes a peak in the respective parameters ($uC[z]$, $C[z]$ and q_{sc}). For example, the depth-averaged (d.a.) $C[z]$ and q_{sc} peak at $x = 55.5\text{m}$ (at the plunging point), whereas the $uC[z]$ peaks further onshore, at $x = 56\text{m}$. The cross-shore distribution of depth-averaged $C[z]$ is also very similar to the distribution of measured C_0 seen in Chapter 3.3.1. As seen throughout this thesis and clearly presented in Figs. 33-35, the effect that breaking-generated TKE has on sediment transport patterns in the breaking region is substantial and must be well-incorporated in transport models for breaking wave conditions.

Measured sand concentration, horizontal flux levels and transport rates are all relatively steady and low in the shoaling and inner surf zones (e.g. Fig. 33 b-d) but increase drastically in magnitude at the wave plunging point (which is at the breaker bar crest and where local water depth is lowest). This can also be seen in the cross-shore distribution of d.a. horizontal flow velocity \bar{u} (e.g. Fig. 33a), which indicates a sudden increase in magnitude (in the offshore direction) in the breaking zone, at the plunging point ($x = 55.5\text{m}$), and a peak around the bar trough at $x = 57\text{m}$, at which point the corresponding concentration and transport rates have already dropped significantly. This indicates considerable lag between the peak in \bar{u} and the peak in suspended sand transport parameters. The increase in horizontal velocity between $x = 55.5\text{-}57\text{m}$ may be a result of the breaking-generated TKE that is partly advected in the offshore

direction by the undertow and orbital velocities (Fernandez-Mora et al., 2016; vdZ et al., 2017b). The observed trend in \bar{u} suggests that using it as one of the main driving parameters to estimate the reference concentration and/or other transport related parameters may reflect this lag in the peak concentration and therefore result in underprediction of SSC near the plunging point and overprediction towards the inner-surf zone.

L19 C_0 + SR93 $C[z]$

Pre-breaking, at $x = 51-53\text{m}$, the depth-averaged $C[z]$ is relatively low ($< 2 \text{ kg/m}^3$) and corresponding flux $uC[z]$ and current-related transport rate q_{sc} are also close to zero. Suspended sand concentration levels remain low even after breaking initiation (at $x = 53\text{m}$) but begin to increase in magnitude at $x = 55\text{m}$ and peak at $x = 55.5\text{m}$ at the plunging point. As seen in the analysis presented in Chapter 3.3.2., the $C[z]$ formula of SR93 results in relatively good agreement in the shoaling and breaking zones pre-plunging point. However, all sand transport components are found to peak in magnitude once breaking induced TKE is injected into the water column, at which point SR93 overpredicts all transport components (this again is in line with the analysis presented in Chapters 3.3.1. and 3.3.2.). At this point, the computed transport components ($C[z]$, $uC[z]$ and q_{sc}) show large discrepancies when compared against the corresponding measured transport components – particularly between $x = 55.5-56\text{m}$ (around the plunging point; see Fig. 33).

Though the L19 C_0 formula used herein predicted the reference concentration to a high level of accuracy (refer to Chapter 3.3.1.), the plots in Fig. 33 indicate that values computed using the combination of L19 C_0 and SR93 $C[z]$ models are considerably larger in magnitude than the measured values around the bar crest. This indicates that the cause of the observed discrepancies is not the C_0 model, but the $C[z]$ model of SR93. As mentioned in Chapter 3.3.2.3., this overprediction is a result of the mixing parameter of SR93 over-compensating for the high levels of breaking induced vertical sediment mixing – i.e. predicted values of mixing parameter M are too small. This leads to an overprediction of $C[z]$ (as seen in Chapter 3.3.2.3.) and also in the subsequent $uC[z]$ and q_{sc} . Post-plunging, at $x = 57\text{m}$ where depth-averaged \bar{u} peaks, the transport parameters shown in Fig. 33 b, c, d, indicate good agreement with measured data, and agreement continues to be relatively good throughout the remainder of the inner-surf zone (from $x = 58-63\text{m}$).

As mentioned earlier in this section, the shape of the respective cross-shore distributions of the aforementioned parameters also indicate that $uC[z]$ and q_{sc} are almost identical inverted (quasi-symmetrical across the x-axis) of the depth-averaged (d.a.) $C[z]$ distribution. This is generally the case for all three $C[z]$ models tested in this section, indicating that the relationship between $C[z]$ and q_{sc} is quasi-linear and therefore that improvements to $C[z]$ formulae will also result in improvements to q_{sc} predictions. Though the relationship between $C[z]$ and resulting $uC[z]$ and q_{sc} is linear, it is not inversely proportional. For example, at $x = 55.5\text{m}$ the SR93 $C[z]$ overpredicts the d.a. SSC by a factor of approx. 1.5, but overpredicts the magnitude of $uC[z]$ and q_{sc} by a factor of 1.1 and 2.2 respectively. Regardless, based on the trends seen in Fig. 33-35, it would seem that even if the reference concentration is well modelled (in this case with the L19 formula), poor performance of the concentration profile formula still leads to considerable discrepancies in the resulting sediment flux and transport rate predictions. This suggests that making improvements to both C_0 and $C[z]$ models are essential to accurately modelling transport rates. The RMSE for the depth-averaged $C[z]$, $uC[z]$ and also the q_{sc} can be seen in Table 19.

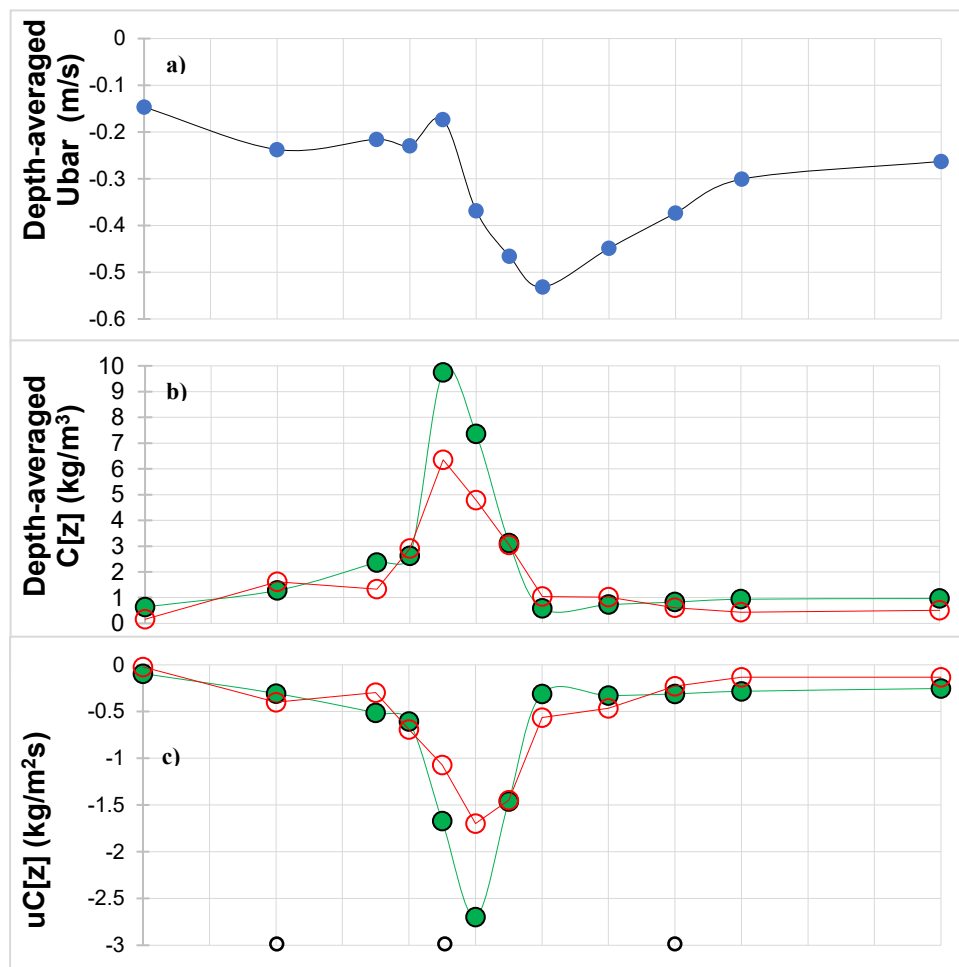


(Figure continued over page)

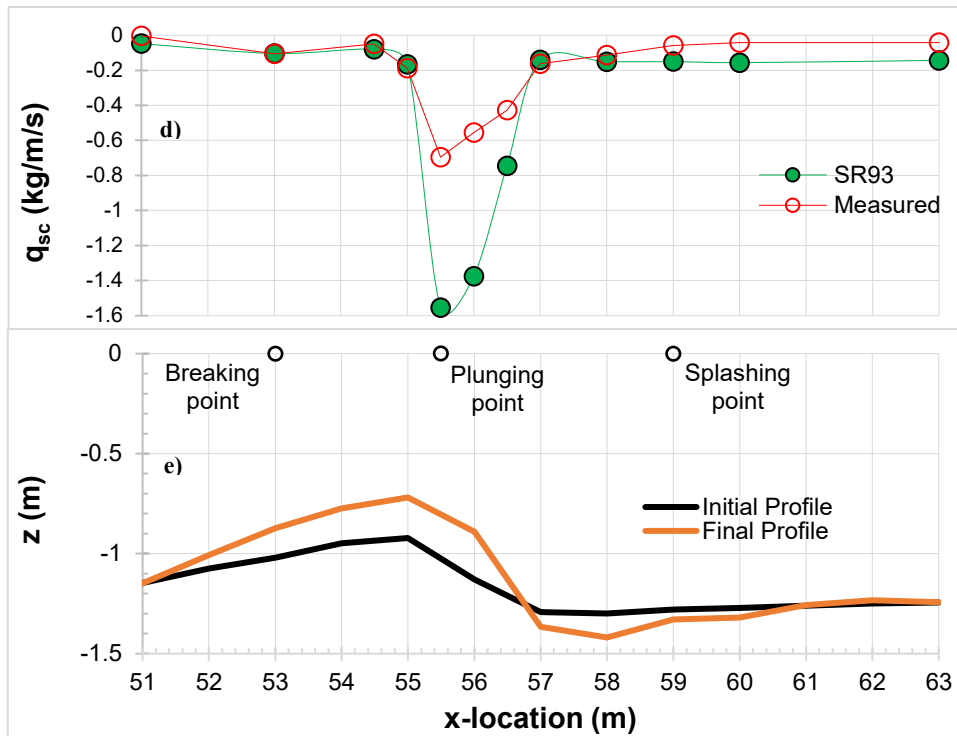


Figure 33 – depth-averaged u_{bar} , $C[z]$, $uC[z]$ and q_{sc} for SR93 in plots a-d) respectively.

In all plots, green filled circles are computed SR93 values, red empty circles are measured values. Plot e) shows the measured bed profile.

L19 C_0 + W12 $C[z]$

Similar to the L19+SR93 combination, the combination of L19 C_0 + W12 $C[z]$ shows good agreement in the shoaling and inner surf zones for all computed parameters shown in Fig. 34b, c, d, but some varied performance in the breaking zone, particularly at the plunging point and just shoreward of the plunging point ($x = 55.5m$ and $x = 56m$ respectively). This region seems to be the same region in which accurate prediction of all transport components tested in this thesis is most challenging.

As seen in Chapter 3.3.2., the combination of L19 C_0 and W12 $C[z]$ formulae generally replicate the concentration profile well, with the cross-shore distribution of d.a. $C[z]$ showing good agreement with measured data. Fig. 34b does however indicate that W12 overpredicts the SSC at $x = 56m$, which is just shoreward of the plunging point. This was also seen in Fig. 25q (at $x = 56m$) in Chapter 3.3.2.6. where W12 overpredicted the concentration throughout the whole water column, with largest discrepancies being near the bed. This relatively large overprediction of $C[z]$ in Fig. 34b is also reflected in the corresponding computed $uC[z]$ and

q_{sc} in Figs. 34c & d (at $x = 56m$, the L19+W12 overpredicts depth-averaged $C[z]$ by a factor of 1.7 and overpredicts q_{sc} by a factor of 1.5). As the magnitude of the transport parameters are relatively large in the breaking zone where discrepancies are highest, these errors described in terms of factors are more significant than where magnitudes are smaller. For example, 0.005 kg/m^3 is factor 2 larger than 0.0025 kg/m^3 , but in terms of difference in magnitude, the difference is very small, but 3.0 kg/m^3 being factor 2 larger than 1.5 kg/m^3 is quite significant. Although the discrepancies between measured and computed transport components in the wave plunging region are relatively large, they are not as large as those found in the SR93 predictions, with the RMSE between computed and measured transport parameters found in Table 19 for W12 being smaller than those from SR93. These discrepancies are however still reflected in the resulting transport rates, resulting in predicted offshore-directed transport rates being around 0.3 kg/m/s larger than measured. This is quite substantial, considering it is almost half the magnitude of the peak measured offshore transport rate of $\approx -0.7 \text{ kg/m/s}$ (peak transport rate measured at $x = 55.5m$).

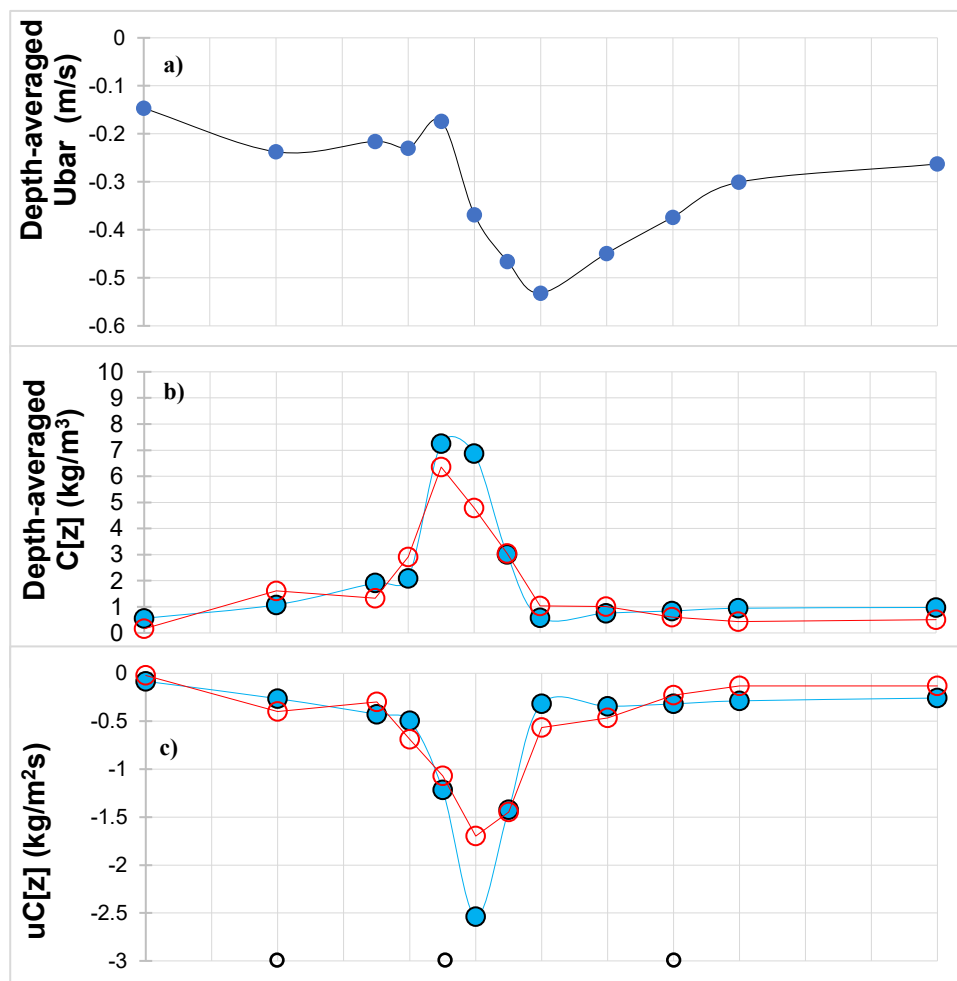


(Figure continued over page)

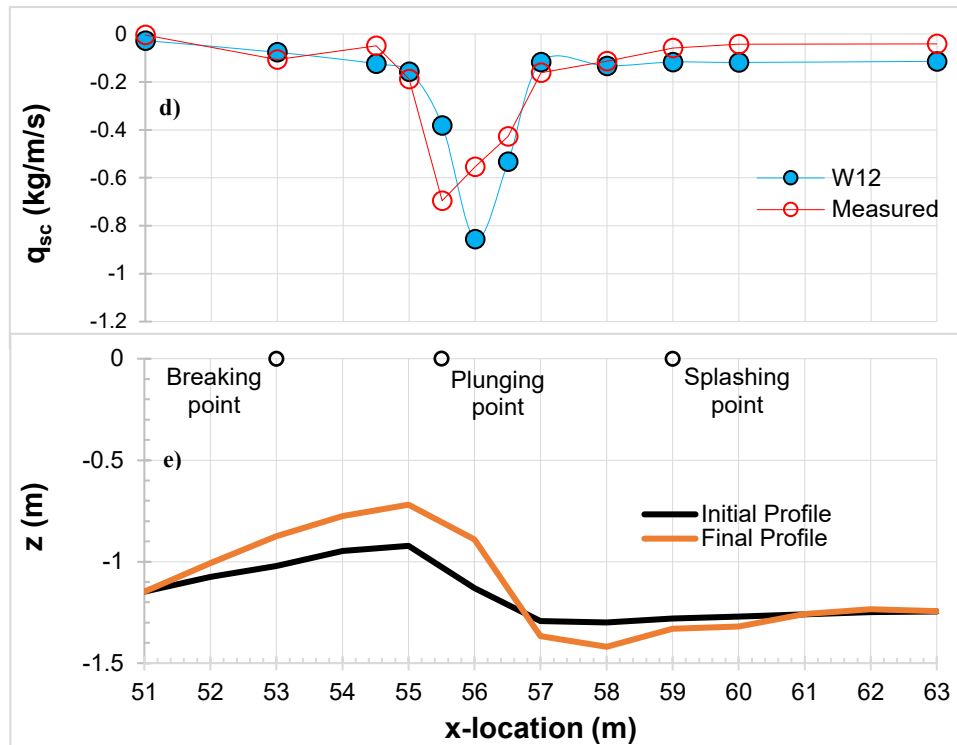


Figure 34 - depth-averaged u_{bar} , $C[z]$, $uC[z]$ and q_{sc} for W12 in plots a-d) respectively.

In all plots, light blue filled circles are computed W12 values, red empty circles are measured values. Plot e) shows the measured bed profile.

L19 C_0 + L19 $C[z]$

The good agreement between the L19 $C[z]$ computations and measured $C[z]$ seen in Chapter 3.3.2. is well reflected in the depth-averaged $C[z]$ in Fig. 35b with noticeably smaller (compared to SR93 and W12 $C[z]$ models) discrepancies between measured and computed values in all three cross-shore zones. Similar to the performance of the SR93 and W12 $C[z]$ models, agreement is good in the shoaling and inner surf zones, but especially in the inner surf zone ($x = 59-63m$) where the average error is only 0.1 kg/m^3 . Even at the plunging point, where other models were found to largely overpredict the d.a. $C[z]$, the L19 formulae only overpredict by a factor of 1.1 at $x = 55.5m$ and even less at $x = 56 \text{ m}$ indicating marginal underprediction with factor of only 1.06.

Underprediction of d.a. $C[z]$ is relatively larger towards the boundary between breaking and inner surf zones (between $x = 57-58m$) compared to other regions and also compared to the SR93 and W12 models. However, as the magnitude of discrepancy is relatively small in the area (e.g. in the order of 10^{-1} kg/m^3 in Fig. 35b), it is considered to be reasonable. This

discrepancy seems to be somewhat amplified in the suspended flux $uC[z]$ computation (Fig. 35c) at $x = 57-58\text{m}$, where the magnitude of error is between $0.29-0.35\text{ kg/m}^2\text{s}$, but the residual effects on the resulting current-related transport rate is marginal. This is reflected in the RMSE values in Table 19 which indicate that errors produced by the L19 $C[z]$ model are significantly smaller than those of the SR93 and W12 models. Overall, Fig. 35d indicates good agreement in all three cross-shore regions, with RMSE over all regions being only 0.06 kg/m/s , which is smaller than that of the SR93 model by a factor of 6. This indicates that the small improvement to the $C[z]$ model of SR93 (detailed in Chapter 3.3.2.7.) has substantial effects on resulting transport rate predictions.

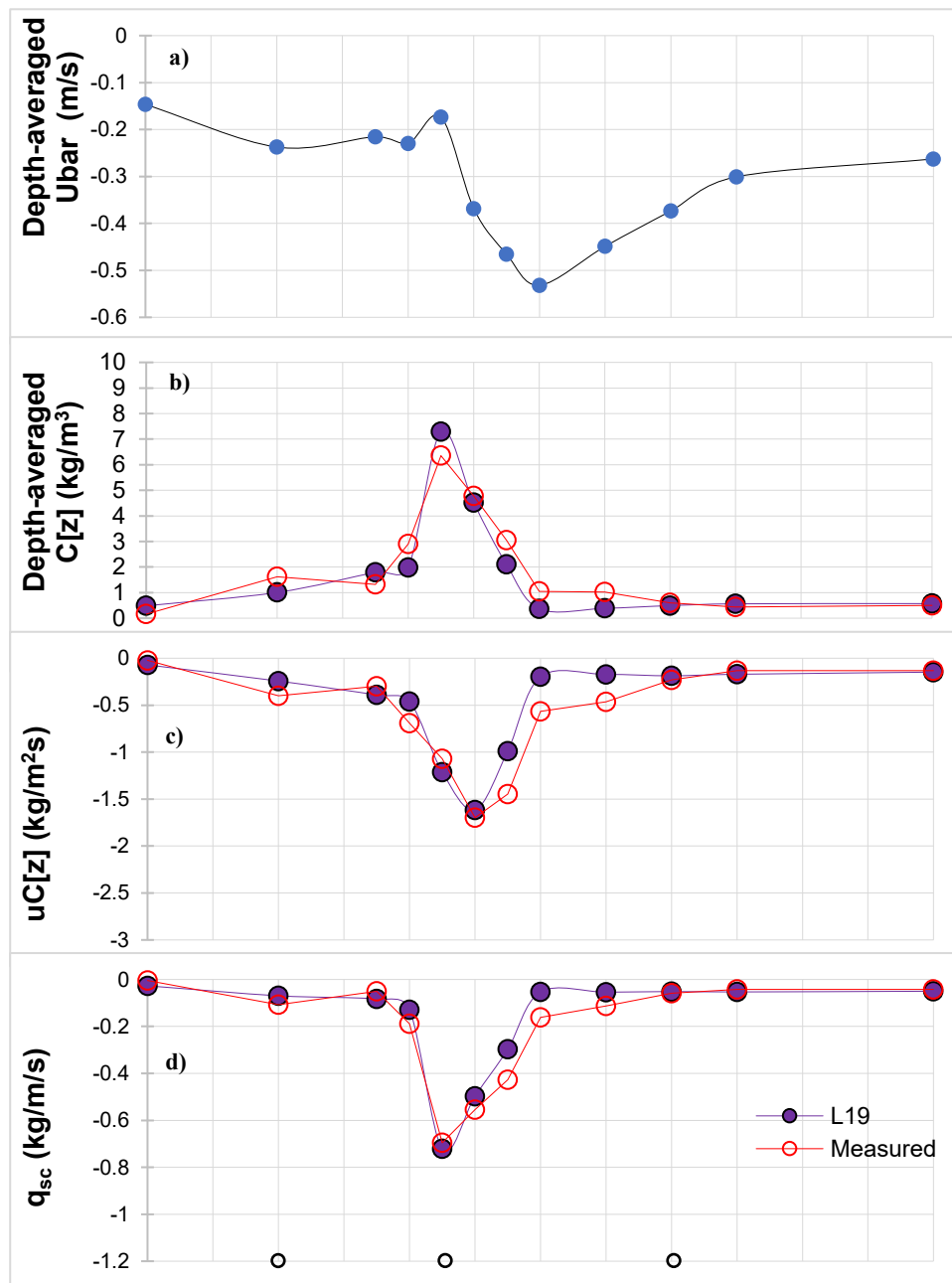


(Figure continued over page)

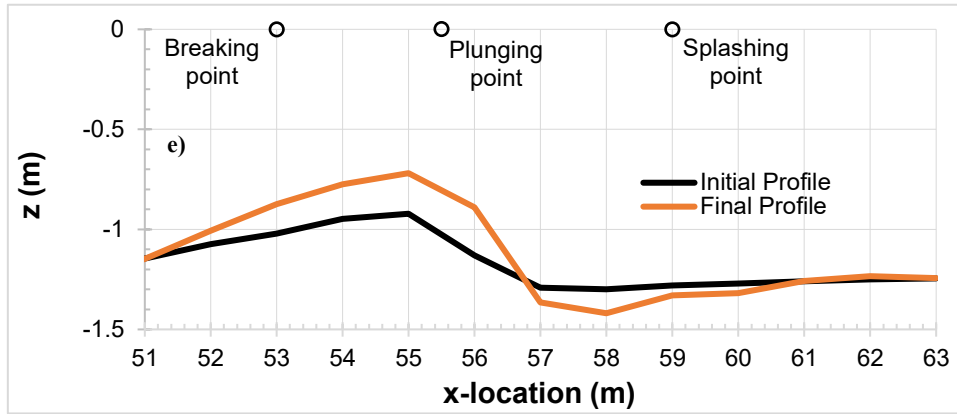


Figure 35 - depth-averaged u_{bar} , $C[z]$, $uC[z]$ and q_{sc} for L19 in plots a-d) respectively.

In all plots, purple filled circles are computed L19 values, red empty circles are measured values. Plot e) shows the measured bed profile.

Summary of comparison between different $C[z]$ formula

General:

The cross-shore distributions of $uC[z]$ and q_{sc} are almost identical inverts (quasi-symmetrical across the x-axis) of the d.a. $C[z]$ and C_0 cross-shore distributions. This is the case for all three model combinations tested in this section, suggesting that the relationship between $C[z]$ and q_{sc} is quasi-linear. This is further supported by the results which clearly show that improvements to $C[z]$ formulae are reflected in the resulting q_{sc} predictions. The relationship between the tested parameters ($C[z]$, $uC[z]$ and q_{sc}) is not however inversely proportional. I.e. increases in the magnitude of $C[z]$ does result in an increase in magnitude of $uC[z]$ and q_{sc} , but the resulting increases in $uC[z]$ and q_{sc} are not proportional to the increase in magnitude of $C[z]$. Also, results indicate that accurate prediction of both C_0 and $C[z]$ are essential in producing accurate estimations of $uC[z]$ and q_{sc} . The extent to which these improvements are important are further discussed in the discussion section of this thesis (Chapter 5.1.4.).

Specific:

All three models generally replicated the shape of the cross-shore distributions of $C[z]$, $uC[z]$ and q_{sc} well. The SR93 and W12 models produced good agreement in shoaling and breaking zones pre-plunging (as seen in Chapter 3.3.2) where $uC[z]$ and q_{sc} levels were very low (close to zero), but substantially overpredicted the SSC and resulting horizontal flux and transport

rates around the wave plunging point where breaking induced TKE and resulting sediment pickup and vertical mixing are highest. The same trend was observed in the modelling of the reference concentration, indicating that breaking-induced TKE has a substantial effect on all suspended sand transport related parameters in the plunging region.

Despite the C_0 being well predicted, the $C[z]$, $uC[z]$ and q_{sc} were overpredicted by SR93 and W12. This indicates that the error was with the SR93 and W12 $C[z]$ formulae. This is further supported by the performance of the L19 C_0 + L19 $C[z]$ combination which performed well in all regions, but particularly in the inner surf zone. Even in the plunging region, agreement was very good with measured data for all tested parameters. In the case of the SR93 $C[z]$ formulae, as mentioned in Chapter 3.3.2.3., the overprediction was a result of the mixing parameter of SR93 over-compensating for the high levels of breaking-induced vertical sediment mixing – i.e. the computed values of mixing parameter M were too small, leading to an overprediction of $C[z]$ (as seen in Chapter 3.3.2.3.) and also in the resulting $uC[z]$ and q_{sc} . Modifying the mixing parameter of SR93 to make values slightly higher vastly improves its performance in all three zones as shown by the L19 $C[z]$ model, which is a modified form of the SR93 model. The RMSE presented in Table 19 below also clearly illustrate the improvements made to the SR93 model as well as providing an overview of the performance of each of the tested models. Figure 36 also shows a side-by-side comparison of each of the tested models in predicting the suspended sand transport rates.

Table 19 - Part B.1. RMSE for depth-averaged $C[z]$, depth-averaged $uC[z]$ and q_{sc}

| | RMSE $C[z]$ kg/m^3 | RMSE $uC[z]$ kg/m^2s | RMSE q_{sc} $kg/m/s$ |
|-----------------|---|---|---|
| L19+SR93 | 1.31 | 0.36 | 0.36 |
| L19+W12 | 0.79 | 0.28 | 0.14 |
| L19+L19 | 0.60 | 0.21 | 0.06 |

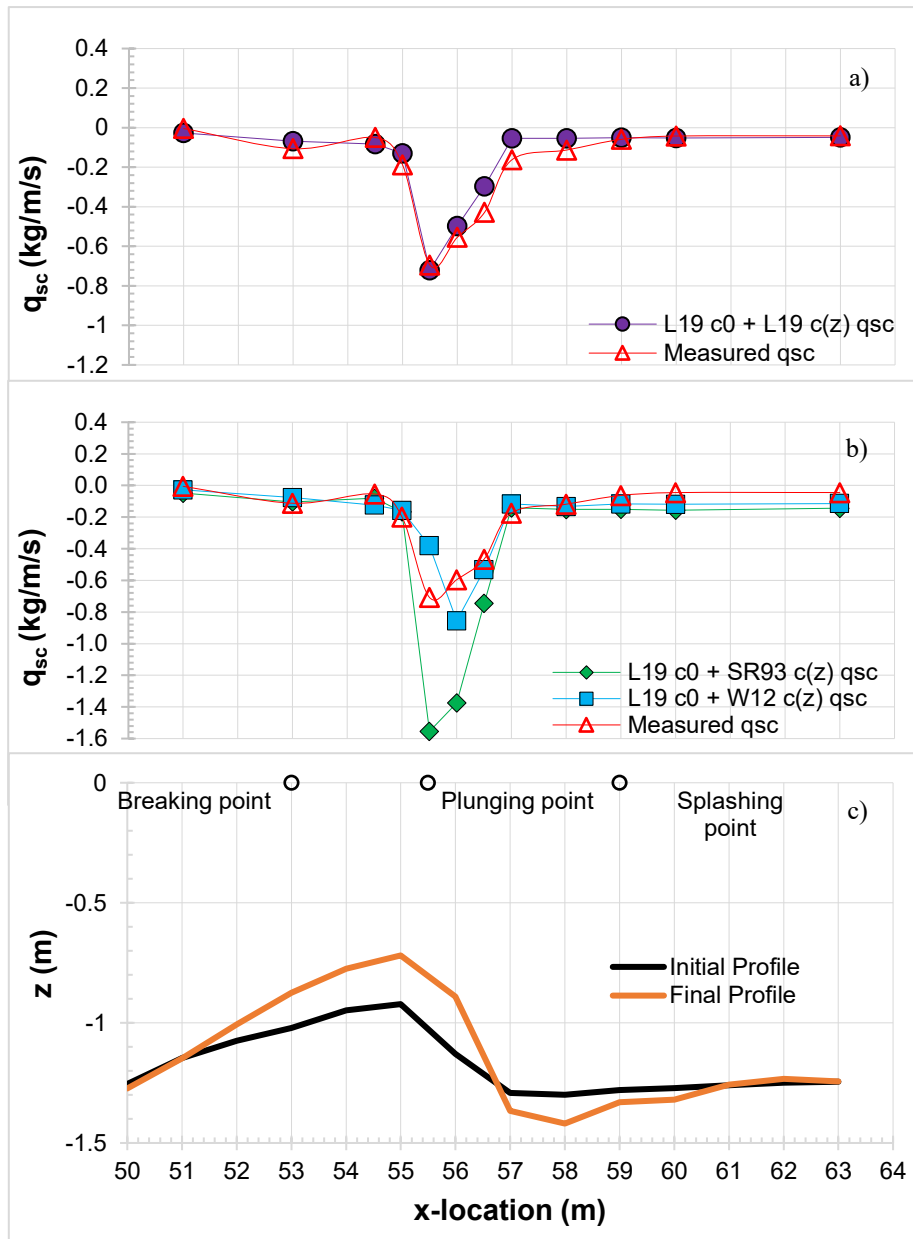


Figure 36 - q_{sc} for L19 vs. measured in plot a), q_{sc} for SR93 vs. W12 vs. measured in plots b). Plot c) shows the measured bed profile.

Part B.2. Fixed $C[z]$ + Varied C_0

As mentioned earlier in this chapter, this subsection further investigates the extent the performance of the reference concentration model has on resulting transport parameters by keeping a constant $C[z]$ model paired with different C_0 models. The different combinations of reference concentration and profile formulae are shown in Table 20 below.

Table 20 - Combination of C_0 and $C[z]$ formulae used for Part B.2

| Reference Concentration Formula (C_0) | Concentration Profile Formula ($C[z]$) |
|---|--|
| L19 – Eq. 9, 14, 36 | L19 – Eqs. 22-24, 37 |
| VR07 – Eqs. 14-16 | L19 – Eqs. 22-24, 37 |
| VR93 – Eqs. 14, 16, 40 | L19 – Eqs. 22-24, 37 |

Analysis:

VR93 C_0 + L19 $C[z]$

The cross-shore distributions of the respective depth-averaged concentration profile, flux and current-related suspended transport rate in Figs. 37-38 can immediately be seen to be less accurate (poor agreement with measured profiles) than those presented in Part B.1. of this chapter. In Part B.1., in all three tested model combinations, performance was generally good in regions with relatively lower concentration – i.e. in the shoaling, outer breaker (pre-plunging) and inner surf zones (see Figs. 33-35). This can be attributed to the reference concentration profile being accurately predicted and also the effects of vertical sediment mixing being minimal in these regions. In Figs. 33-35, considerable discrepancies between measured and computed transport parameters were only found near the plunging point where sediment pickup and vertical mixing levels were highest. In Figs. 37-38 however, significant discrepancies can be seen in *all* cross-shore regions, with large overprediction particularly seen in the shoaling and breaking zones.

Figure 37 indicates that the VR93 C_0 + L19 $C[z]$ model combination produced values of d.a. $C[z]$ that were greater than corresponding measured values by factors ranging between 3.5 – 26 in the shoaling region (average discrepancy between $x = 51$ - 53 m is 3.98 kg/m^3). This large overprediction of d.a. $C[z]$ continues into the breaking zone where computed values are 1.63 – 5 times larger than measured (average discrepancy between $x = 54.5$ - 55.5 m is 4.46 kg/m^3). The overprediction of d.a. $C[z]$ peaks at $x = 55.5$ m which is at the plunging point, or in terms of the bed profile is at the bar crest. After this point, the magnitude of (measured and computed) concentration parameters decreases substantially in the $C[z]$, $uC[z]$ and also q_{sc} . The reference concentration formula of VR93 was not evaluated in Chapter 3.3.1. of this thesis, nor is it

presented herein, but separate analysis showed that the cross-shore distribution of C_0 produced by VR93 is very similar to the distribution of d.a. $C[z]$ seen in Fig. 37b. This further supports the findings from Part B.1. which indicated that the performance of the reference concentration model plays a fundamental role in the accurate prediction of resulting concentration profile, sediment flux and transport rates. The large overprediction in the shoaling, early breaking and inner surf zones are also seen in the horizontal flux and transport rate computations. As these discrepancies are substantial (RMSE over all cross-shore regions shown in Table 21 in Summary at the end of Part B.2.), accumulation of such errors in medium- to long-term morphodynamic computations would likely produce unrealistic predictions.

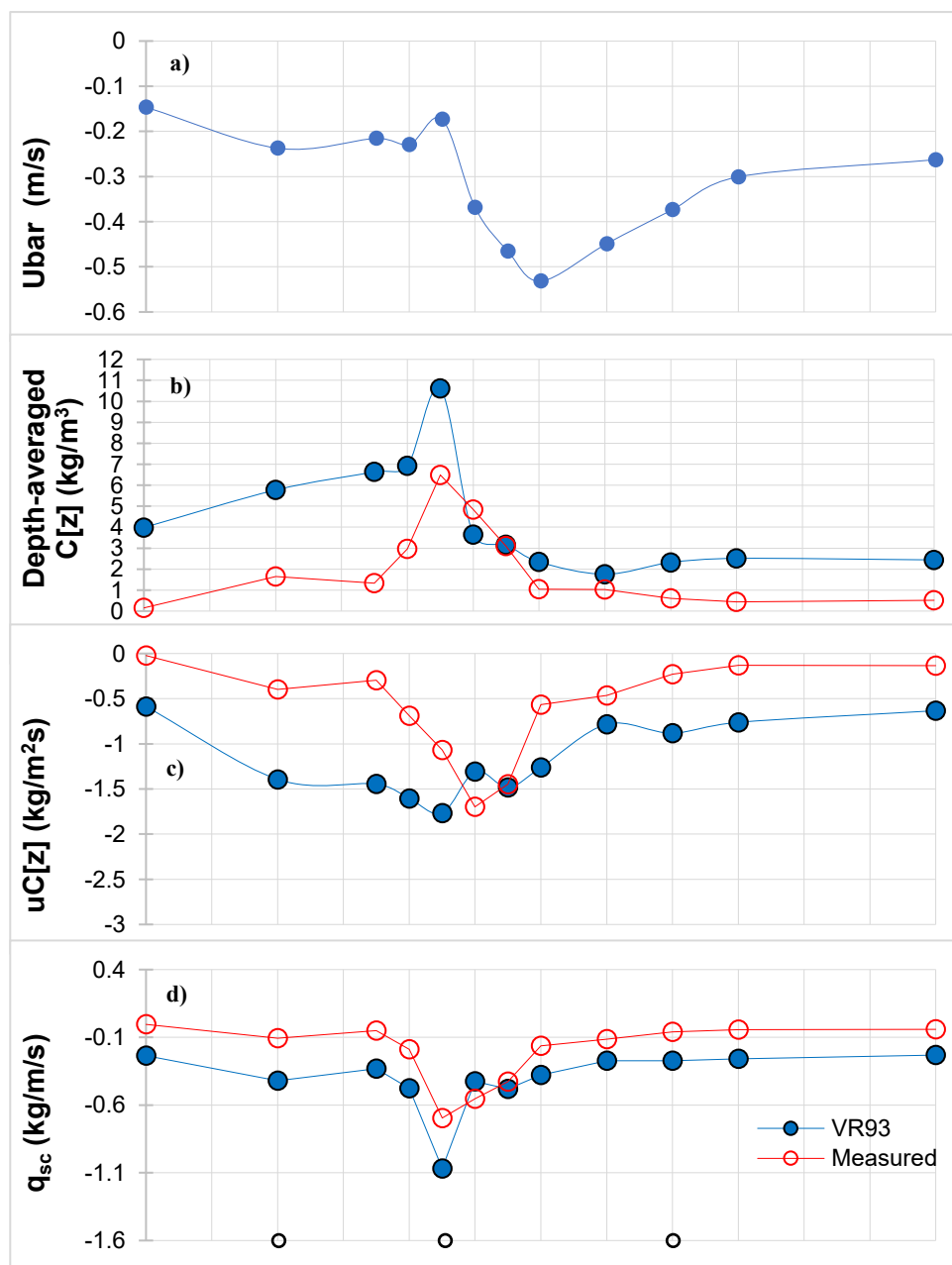


(Figure continued over page)

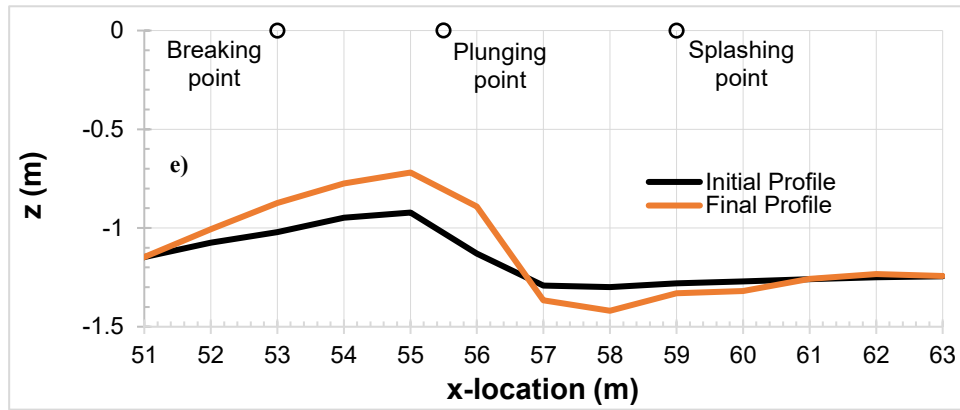


Figure 37 - depth-averaged \bar{u} , $C[z]$, $uC[z]$ and q_{sc} for VR93 in plots a-d) respectively.

In all plots, dark blue filled circles are computed VR93 values, red empty circles are measured values. Plot e) shows the measured bed profile.

VR07 $C_0 + L19 C[z]$

As seen with VR93, performance of VR07 model is relatively poor in the shoaling and breaking zones. This is consistent with the results from the analysis of the VR07 C_0 model presented in Chapter 3.3.1. The magnitude of values predicted using VR07 are generally smaller than those of VR93, indicating marginally better agreement than the VR93 model, particularly in the shoaling and inner surf zones. This is reflected in the RMSE values in Table 21 in the summary section below which shows that RMSE values were smaller for VR07 than VR93 in all three tested transport components by 11-14%.

Considering the VR93 and VR07 C_0 models are almost identical, with the only difference being the transport parameter (see Eq. 15 in Chapter 2.2.1.5. and Eq. 40 in Chapter 4.2.), the results are substantially different. The VR93 model predicts the reference concentration as a function of the bed-shear stress instead of bed-shear velocity (VR07 predicts C_0 as a function of bed-shear velocity) and better represents (qualitatively) the localised increase in suspended transport components that occur in the plunging region as a result of wave breaking. As seen in Chapter 3.3.1. and in Part B.1. of this chapter, Fig. 38 shows that the VR07 model greatly underpredicts all concentration parameters at the plunging point, predicting decreases in magnitude of concentration, flux and transport rates where the magnitude of measured parameters increases. In this regard, the of the VR07 and VR93 models, the VR93 model better captures the cross-shore distribution of d.a. $C[z]$ and q_{sc} in particular – showing relatively low

magnitudes of the respective parameters in the shoaling and inner surf zones, and localised increases post-plunging in the breaking zone.

In either case, discrepancies between measured and predicted transport parameters are quite large, not only in the breaking zone but also in the shoaling zone and in some cases the inner surf zone too. The RMSE values from this section are also much higher than those observed in Part B.1., reiterating that accurately modelling the reference concentration is essential. As the concentration profile is a function of the reference concentration, the accurate determination of the reference concentration essentially serves as the foundation upon which the concentration profile is predicted. Discussion regarding the relative importance of improvements to C_0 and $C[z]$ formulae and their influence on resulting transport rate predictions are covered in the discussion section in Chapter 5.1.4.

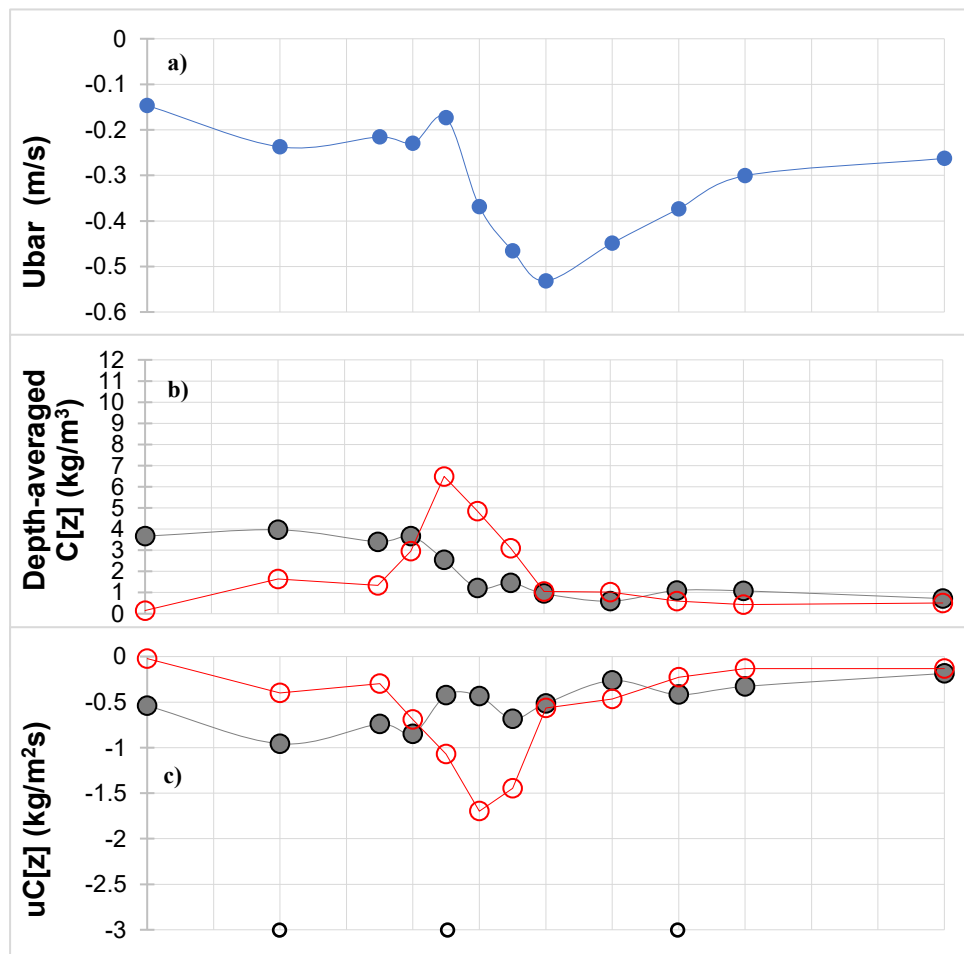


(Figure continued over page)

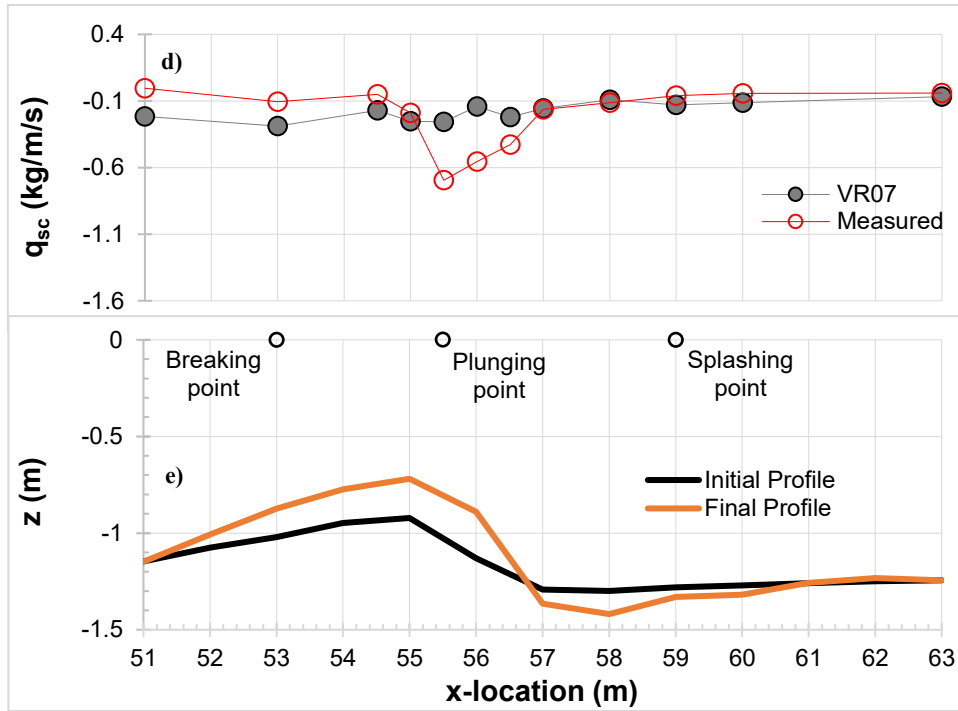


Figure 38 – depth-averaged u_{bar} , $C[z]$, $uC[z]$ and q_{sc} for VR07 in plots a-d) respectively.

In all plots, grey filled circles are computed VR07 values, red empty circles are measured values. Plot e) shows the measured bed profile.

Summary of comparison between different C_0 formula

General:

Cross-shore distributions of computed $uC[z]$ and q_{sc} are less accurate than those from Part B.1. – poor agreement with measured profiles. In Part B.1., agreement between computed and measured parameters was generally quite good in the shoaling/pre-breaking regions and also the inner surf zone. This was attributed to accurate predictions of the reference concentration. This was not the case in Part B.2. where very large discrepancies were not only found in the plunging region, but also in other areas of the breaking zone post-plunging, and also in the shoaling zone as well. RMSE is also significantly higher for the model combinations shown in Part B.2. Trends from Part B.1. also indicated that the cross-shore distributions of suspended flux and transport rates were almost identical inverts of the cross-shore distribution of depth-averaged concentration profile. This trend is seen to a lesser extent in Part B.2. but is still somewhat present. This can most clearly be seen for example in Figs. 37 b, d and also Figs. 38 b, c.

Specific:

Both the VR93 and VR07 models overpredicted all transport parameters in the shoaling zone. The magnitude of discrepancies (and RMSE; see Table 21) were higher in the VR93 model, but the VR93 model managed to qualitatively capture the localised increases in sand transport parameters observed around the plunging point. Even these values however were generally overpredicted, still indicating large discrepancies. The VR07 model on the other hand did not replicate the localised increases in transport parameters (around the plunging point) which occur as a result of wave plunging in the breaking zone. This was consistent with the findings in Chapter 3.3.1.5. of this thesis which showed similar patterns in the prediction of the reference concentration. It was predicted in Chapter 3.3.1.5. that these large discrepancies between computed and measured reference concentration would have residual effects on the resulting transport rate predictions. This was clearly seen to be the case in Part A of this chapter, as well as in this section. Despite the VR07 model not being able to replicate the transport patterns around the plunging point, performance in other regions are quite good, especially in the inner surf zone. It is uncertain whether the reasonable-good performance in the shoaling and inner surf zones alone will be sufficient in accurately modelling morphodynamic changes, as the magnitude of $C[z]$, $uC[z]$ and q_{sc} are relatively small in these zones and relatively large in the breaking zone where the model performs poorly.

The performance of the L19 models clearly showed significantly better results than both VR93 and VR07 models in predicting the $C[z]$, $uC[z]$ and q_{sc} , as seen in Part B.1. Table 21 shows the RMSE of each of the model combinations for each modelled parameter, and Fig. 39 below also shows a side-by-side comparison of the performances of all model combinations tested in Part B.2. Both indicate that the performance of the L19 C_0 and $C[z]$ model combination produces significantly better results than the alternative models, both qualitatively and quantitatively.

Table 21 - Part B.2. RMSE for depth-averaged $C[z]$, depth-averaged $uC[z]$ and q_{sc}

| | RMSE $C[z]$ kg/m^3 | RMSE $uC[z]$ $\text{kg/m}^2\text{s}$ | RMSE q_{sc} kg/m/s |
|-----------------|--|---|--|
| VR93+L19 | 2.99 | 0.69 | 0.24 |
| VR07+L19 | 2.14 | 0.54 | 0.21 |
| L19+L19 | 0.60 | 0.21 | 0.06 |

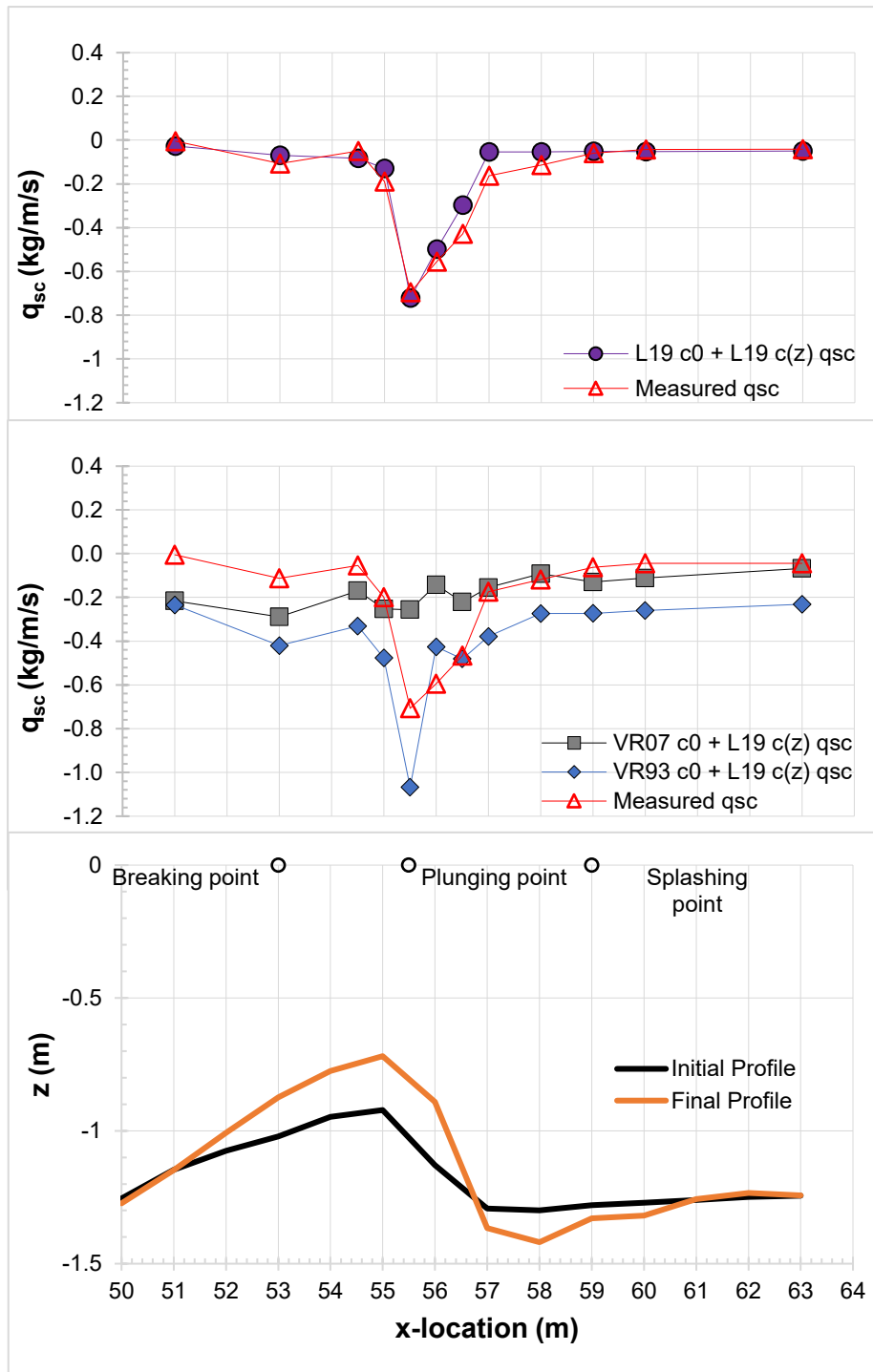


Figure 39 - q_{sc} for L19 vs. measured in plot a), q_{sc} for VR93 vs. VR07 vs. measured in plots b). Plot c) shows the measured bed profile.

4.3.2. Wave-related suspended transport (q_{sw})

As mentioned briefly in Chapter 4.3.1.1., the magnitude of wave-related suspended transport rate (q_{sw}) is onshore directed, but very small in comparison to the current-related suspended transport (see Fig. 30) – this is in agreement with the findings from the COAST3D field experiments (e.g. Grasmeyer, 2002; van Rijn, 2002) as documented by van Rijn et al. (2013). Even at $x = 55.5\text{m}$ where the magnitude of q_{sw} is largest, it is 0.035 kg/m/s which is only 16.3% of the magnitude of measured q_{sc} at the same cross-shore location. Thus, the performance of the L19 in making q_{sc} predictions shows good agreement with net suspended transport q_s despite not accounting for the wave-related transport component at all.

Though the results may be different when forced under different conditions – e.g. different breaker types, sediment diameter, stage of bed profile evolution, storm conditions, etc. – the results from this validation alone seem to indicate that the wave-related component of suspended transport is negligibly small and could perhaps even be omitted from practical sand transport models, so long as the current-related component is well-modelled. Evidently, there is still a level of uncertainty regarding the importance of q_{sw} under different breaker types and how to model and incorporate it into transport models (van Rijn et al., 2013). Wherever possible, sand transport models could be tested in modelling net transport rates with and without the inclusion of the wave-related component using high-resolution co-located sediment concentration and horizontal velocity measurements before more affirmative conclusions can be made regarding this matter. This is further discussed in the discussion section in Chapter 5.1.6. of this thesis.

Chapter 5 – Discussion

In Chapter 1.1.3. three research questions were posed, and along with them a series of objectives aimed at systematically answering the research questions. The thesis objectives are listed below once more for the reader's convenience:

-OB1: To identify key limitations of existing reference concentration and concentration profile models by qualitatively and quantitatively evaluating their performance against state-of-the-art measured datasets and latest process insights.

-OB2: To derive a new practical model that accurately predicts suspended sand transport patterns under breaking waves, and to validate it against existing models and measured data.

-OB3: To evaluate the applicability of the new and existing transport models to morphodynamic models and suggest methods of improvement.

-OB4: To investigate the extent to which the improvements to reference concentration and concentration profile models affect the prediction of cross-shore suspended sand transport rates.

The first objective answered the first research question, the second and third objectives answered the second research question and the fourth objective answered the third research question. The first three objectives were closely linked and were therefore not addressed in separate studies or chapters, but concurrently throughout Chapters 2-4. For this reason, the discussion of the findings and implications of the first three objectives are, to some extent, addressed simultaneously throughout Chapters 5.1.1. to 5.1.3. The sub-chapter 5.1.1. focuses mainly on the first objective, discussing the various limitations of the existing reference concentration models. Chapters 5.1.2. and 5.1.3. both address the second and third objectives, concentrating on the applicability of the newly proposed L19 C_0 formula, as well as other existing sand transport formulae, to morphodynamic models. Chapters 5.1.4. through to 5.1.6. address the fourth objective (third research question), but also discuss further implications on morphodynamic modelling (objective 3). The discussions regarding morphodynamic modelling provided in Chapters 5.1.4 to 5.1.6 differ from those in 5.1.2., as the former is focused more on the concentration profile, suspended flux and sand transport rates. Finally, a section discussing some of the important limitations of the used datasets is provided in Chapter 5.2.

5.1. Limitations and Improvements to Suspended Sand Concentration Models

REFERENCE CONCENTRATION

5.1.1. General limitations of existing C_0 models

5.1.1.1. Local wave climate and water depth

As mentioned briefly in Chapters 1.1.1. and 2.1., accurately predicting the reference concentration under breaking wave conditions has been the focus of numerous studies in the last few decades. The analysis carried out in Chapter 3 provided some insights into the various strengths and weaknesses of previous endeavours, as they were validated against four datasets measured under large-scale wave breaking conditions. One of the most commonly observed limitations was found in models (e.g. MS92, SR93, SP04 and JS07) that were dependant on, or driven by, the wave height (H), breaker height (H_b) and/or local water depth (d). As identified throughout Chapter 3.3.1. (refer to Fig. 12 in Chapter 3.3.1.3.), the cross-shore distributions of measured H , H_b and d did not correlate well with the cross-shore distribution of reference concentration, especially around the plunging point where these parameters were often seen to decline in magnitude whilst corresponding measured C_0 sharply increased. This finding is in agreement with those of vdZ et al. (2017b) and Pang et al. (2020) who reported poor correlation between the local wave climate and the strong localised increases in concentration observed in the breaking zone, particularly at the plunging point. The models of MS92 and SR93 which were largely driven by H and d , produced cross-shore C_0 distributions that mirrored the cross-shore distributions of H and d , with computed C_0 declining at the plunging point. Consequently, these models were not able to capture the high increases in C_0 post-plunging (see Figs. 7, 9, 11 & 14 in Chapter 3.3.1.) and were generally found to under-predict throughout the breaking region.

The MS92 and SR93 models were however adept in predicting the reference concentration in the shoaling and inner surf zones. The model validation in Chapter 3.3.1. has indicated that models that have related the reference concentration with the sediment pickup rate (formulations that depend on local bed shear levels exceeding critical bed shear for entrainment; formulations driven by the Shields Parameter) are quite capable of modelling reference concentration in regions and/or conditions that are predominantly influenced by local TKE induced by bed shear (e.g. the shoaling region or non-breaking conditions). These formulations

however are often based on the implicit assumption that sediment entrainment is only affected by the local TKE induced by bed shear (e.g. the models of van Rijn, 1984; 2007). Though this assumption is applicable to non-breaking conditions or in the shoaling zone, as reported by vdZ et al. (2017c), this assumption is no longer valid when the external breaking induced TKE invades the WBBL (c.f. Chapter 2.3.1.1.). This is consistent with Aagaard et al. (2018) who inferred that sediment concentration, or sediment pickup models based on bed shear stress derived from horizontal velocities would be unsuitable for breaking wave conditions. In response, vdZ et al. (2017c) proposed an adapted transport parameter that considers the near-bed TKE (k_b) induced by both internal (local) and external (surface/breaking-generated) TKE (refer to the vdZ17 model shown in Chapters 2.2.1.6. and 3.3.1.6.). This formulation was derived based on the causal relationships observed between k_b and C_0 , suggesting that when k_b exceeded the critical bed shear level, sediment would be entrained. An advantage of using near-bed TKE to drive sediment concentration and pick-up rate models is that it allows the model to account for breaking-induced turbulence which spreads through advection and diffusion processes, both vertically and horizontally (vdZ et al. 2016; 2017a,b). It could be important to incorporate such processes in concentration formulae as they are responsible for increased levels of k_b and sediment entrainment not only in the breaking region, but also in neighbouring locations (vdZ et al. 2017b). Such advection and diffusion processes are accounted for in models driven by k_b , but not in the other existing models covered in this thesis. The incorporation of advection in transport models is further discussed in Chapter 5.1.2.4.

5.1.1.2. Near-bed TKE

As seen in Fig. 18 (Chapter 3.3.1.6.), the C_0 model of vdZ17 shows varied performance when validated against the different datasets. In Chapter 3.3.1.6., it was briefly mentioned that the near-bed TKE measurements (at 1 cm above bed) varied in magnitude between the CROSSTEX and SINBAD experiments. For further comparison of the measured TKE values between the two experiments, the Froude-scaled TKE $(k/gh)^{1/2}$ was computed. The $(k/gh)^{1/2}$ levels found at ≈ 1 cm above the bed in the spilling/plunging region, in both the erosive and accretive cases of the CROSSTEX experiments, were found to be between 0.021-0.032, whereas in the SINBAD experiments, they were between 0.027-0.035. It is speculated that the differences in the magnitude of TKE measurements could be a result of several factors. VdZ et al. (2016) used a Reynolds decomposition based on the ensemble-averaging method, and Yoon & Cox (2010)

used a differencing method to separate the wave-related components from the turbulence-related components of velocity measurements. Scott et al. (2005) carried out analysis on three methods of extracting TKE from the velocity data (high-pass filtering, ensemble-averaging and differencing method) and reported that the different methods yield different estimates of TKE. For regular waves, the TKE estimates from the differencing method were larger than the estimates from the ensemble-averaging method by approximately 26% (Scott et al., 2005). This is inconsistent with the trend observed in Fig. 40 which shows that the ensemble-averaging method (SINBAD) yields higher values of $(k/gh)^{1/2}$. Assuming that the small difference in offshore conditions of the experiments are negligible (see Chapter 3.2. for details on offshore conditions), this suggests that the difference in magnitude of measured TKE is not a result of the method of extracting turbulence measurements.

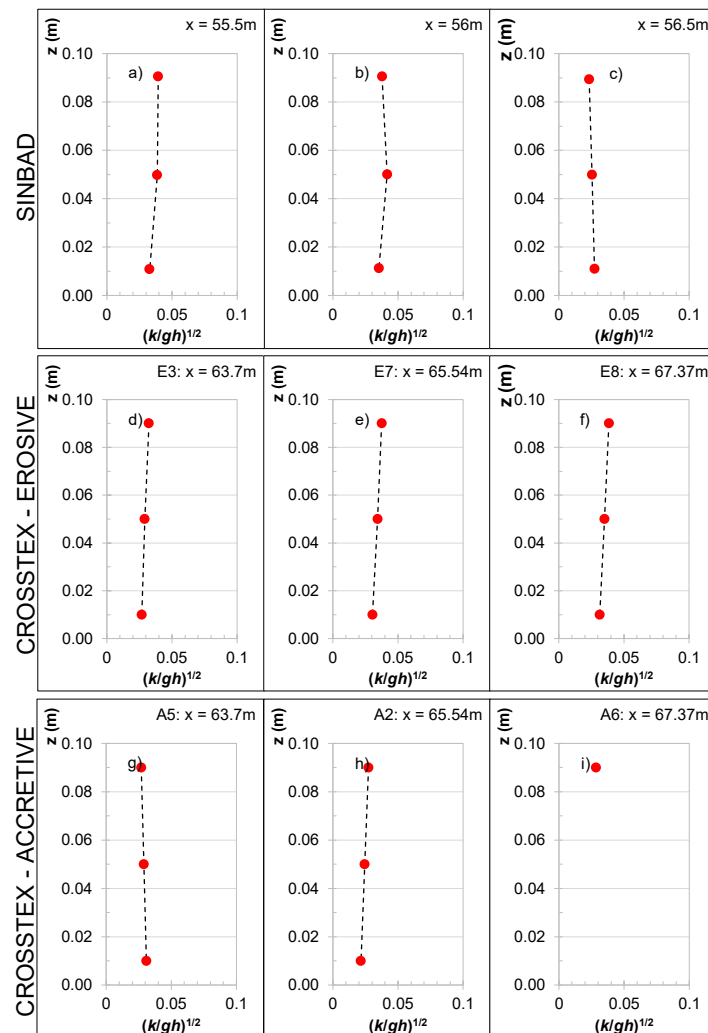


Figure 40 – Vertical profile of Froude-scaled TKE at 1 cm above the bed from the SINBAD and CROSSTEX datasets.

Plots a-c) show TKE at three cross-shore locations, at the breaking point, at the plunging point and onshore of the plunging point. Plots d-f) and plots g-i) show TKE at three cross-shore

locations, at the breaking point, at the plunging point and onshore of the plunging point, for erosive and accretive conditions respectively.

On the other hand, though the turbulence structure was reported to be the same in both the regular and irregular wave conditions, the magnitude of TKE was considerably smaller in the irregular/random cases – up to a factor of 5 (Scott et al., 2005) despite similar offshore wave conditions. This finding is more consistent with the trends observed in Chapter 3.3.1. As described by Scott et al. (2005), the vertical turbulence structure observed in Fig. 40 between the two experiments are similar despite the difference in wave conditions. Also, the Froude-scaled TKE measurements from the CROSSTEX experiments (irregular waves) are smaller by approximately a factor of 1.1-1.3. This suggests that the difference in trends observed between the two experiments could be a result of the wave conditions as the SINBAD experiments were carried out in regular, and the CROSSTEX in irregular wave conditions (c.f. vdZ et al., 2019). There were also differences in bottom profile and breaker bar development between the two experiments, which could also have influenced the difference in magnitudes of k_b and $(k/gh)^{1/2}$ between the two experiments.

Though a strong relationship between near-bed TKE and reference concentration is well validated (e.g. vdZ et al., 2017b, Pang et al., 2020), it can clearly be seen that there are some challenges in using k_b as the primary driving parameter for reference concentration models. These challenges range from choosing the best method of extracting turbulence from data, to the effects of the wave conditions (e.g. regular/irregular) and the bottom profile on the magnitude of TKE. It is also reported that there are numerous difficulties in the accurate modelling of the spatial trends and magnitude of near-bed TKE (vdZ et al., 2019), even with high-resolution state-of-the-art computational fluid dynamics (CFD) models (vdZ et al. 2017c, Fernandez-Mora et al., 2016).

With regards to magnitude of TKE, both k_b and $(k/gh)^{1/2}$, the deviation between values from the different datasets is smaller in the Froude-scaled turbulence. This suggests that $(k/gh)^{1/2}$ may serve as a better driver for reference concentration models than k_b , which fluctuates more between datasets. This is supported by Aagaard et al. (2018) who reported that for intense suspension events (such as those found under the plunging breakers observed in this thesis) Froude-scaled instantaneous TKE shows good agreement with instantaneous sediment concentration, for both plunging and spilling breakers.

5.1.2. Applicability to morphodynamic models

One of the issues in using process-based morphodynamic models (such as Delft3D, MIKE21 and Telemac) for long-term modelling is the lack of accuracy and/or robustness of constituent sediment transport models. This problem stems from limited understanding and insights into sediment transport processes and how they interact with complex hydrodynamic forcing – e.g. under breaking wave conditions. Therefore, until further insights and detailed understanding is obtained and implemented into more process-based models, even in the aforementioned state-of-the-art process-based morphodynamic modelling suites it is often necessary to rely on engineering or ‘practical’ models which incorporate relatively simpler physics with (semi-)empirical parameterisations. The various models covered in this thesis, including the L19 model can more or less be categorised as practical models. These practical models are not only useful but somewhat necessary in reducing computation times whilst maintaining modelling accuracy – benefits that are particularly valuable in modelling sediment transport and morphodynamics for medium- to long-term periods. Such benefits can also help researchers to obtain insights into poorly understood phenomena and processes by carrying out much needed (sensitivity) analysis to identify key parameters and causal relationships between physical processes.

Systematic validation (and development) of existing and new practical transport models using latest observational insights and data (as done in the Chapters 3 & 4) is essential in understanding the limitations of existing models and improving them for use in morphodynamic modelling. For example, many of the existing models in the present thesis (e.g. the van Rijn, 2007 formulae which are widely used in existing morphodynamic models) were found to under-predict the suspended load considerably, particularly in the breaking zone (see Chapters 3.3. and 4). Such under-prediction of the suspended load can lead to imbalances between the suspended load transport and bedload transport (which often occur in opposite directions), resulting in unrealistic net transport rates. Even if these errors are relatively small and negligible in the short-term, they can accumulate over the long-term to produce inaccurate predictions of morphological changes. As such, it is important to implement improved suspended load models and methods that are robust and accurate into morphodynamic models.

5.1.2.1. Applicability to multiple cross-shore zones

The practical reference concentration models evaluated in this thesis can be put into two categories regarding applicability to multiple cross-shore zones: 1) models that do not require additional formulae or changes in parameters/constants for implementation to multiple cross-shore regions, and 2) models that do require additional formulae or changes. For example, models that utilise a transport parameter that is based on the Shields Parameter or sediment pick-up rate (e.g. refer to MS92, SR93, VR07 and vdZ17 C_0 models in Chapter 2.2.1. and 3.3.) do not need to be able to distinguish which cross-shore zone they are being applied to. I.e. the parameters or constants used in the formulations do not change based on the cross-shore region (category 1). Models such as JS07 and the proposed L19 C_0 models fall into category 2 and are affected by the cross-shore region, requiring different formulae/parameters depending on the regions they are applied to.

The reference concentration models in category 1 were often found to perform quite poorly in this thesis when applied to the different cross-shore regions, generally only being adept for one or two cross-shore regions at most. Analysis from Chapter 3.3.1. showed that the tested models performed particularly poorly in the breaking zone under strong plunging breakers. It is suggested that the inclusion of additional/different formulae or (tuning-)parameters to the models in category 1 could help to improve their overall performance in all cross-shore zones. For example, a model that is adept for performance in the shoaling and inner surf zones but performs poorly in the breaking zone could include a tuning (or additional) parameter or alternative formulae to improve agreement with measured data in the breaking zone. If performance is already good in the shoaling and inner surf zones, the value of the tuning-parameter can be set to =1 in those cross-shore zones and set to a different number in the breaking zone. Examples of using different formulae/parameter values can be found in the work of Jayaratne & Shibayama (2007) and also the newly proposed L19 C_0 formulae.

As mentioned in Chapter 3.3.1.4., the JS07 model was derived for predicting SSC under breaking agitation only. Because the original C_0 formulation of JS07 was derived for use in the breaking zone only, parameters such as H_b , d_b and L_b were used, where the subscript b denotes 'at the breaking point'. However, from a practical point of view, there are limited uses for a reference concentration model that can only be used (adeptly) for the breaking zone. For this reason, in order to test the model's applicability to other cross-shore regions, the validation in Chapter 3.3.1.4. was carried out using local wave height (H) instead of breaker height (H_b),

local wavelength (L) instead of breaker length (L_b) and local water depth (d) instead of the water depth at the breaking point (d_b). Despite being derived for the breaking zone only, the JS07 model often performed reasonably when driven by local measurements, especially in the inner-surf zone and in some cases in the breaking zone also. Jayaratne & Shibayama (2007) also derived separate C_0 models for the various suspension mechanisms observed in breaking and non-breaking wave conditions. Three models were produced for each of the following mechanisms: 1) suspension due to rippled-bed, 2) due to sheet-flow and 3) due to wave breaking agitation (JS07 model covered in this thesis). When the models of Jayaratne & Shibayama (2007) are applied to the shoaling zone where sheet-flow conditions are prevalent (Ribberink et al., 2014; vdZ et al. 2018; Fromant et al. 2019), the reference concentration formula for sheet-flow conditions should be applied, and in the breaking zone the model for breaking agitation should be applied and in the inner surf zone where vortex ripples are present (e.g. vdZ et al., 2016), the model for rippled bed conditions could be applied. They also derived formulae to predict the reference concentration under the combined effects of ripples and breaking agitation – two suspension mechanisms that often occur in the same phase, as in some regions multiple suspension mechanisms will coexist.

Alternatively, the L19 C_0 model implemented a simple tuning parameter Ω (see Eq. 36 in Chapter 2.3.1.3.) which empirically accounts for the combined effects of the different suspension mechanisms present in the various cross-shore regions (e.g. sheet-flow in the shoaling zone, entrainment resulting from wave breaking in the breaking zone). The L19 C_0 model has generally shown very good agreement with measured data in the shoaling and breaking zones but requires a different value of the constant Ω to be implemented for the inner surf zone. By implementing the multiple-formulae method of Jayaratne & Shibayama (2007), or the tuning-parameter method of Lim et al. (2020), the suspended load can accurately be modelled in all cross-shore regions by applying the ideal model(s)/parameter value to each region.

One thing that has not been tested in this thesis is the performance of the L19 model in the swash zone. All validation and evaluation carried out in Chapters 3 & 4 were focused on the shoaling, breaking and inner surf zones, and therefore it is uncertain how the L19 model will perform when implemented into a morphodynamic modelling suite for all near-shore regions (i.e. including the swash zone). As one of the key drivers in the L19 C_0 formula is $1/d$, L19 may overpredict C_0 considerably in the swash region where water depths are very small. Not only so, but the swash zone is also a highly turbulent region that is relatively difficult to model.

As such, it may be necessary to combine a separate swash zone concentration model with the L19 model when applying to the swash zone also (like the C_0 models of Jayaratne & Shibayama, 2007). Alternatively, it may be possible to use different values of the Ω constant in the swash zone. Future studies could focus on the applicability of the L19 model to the swash zone and whether it could be used simply by changing the value of Ω or by introducing additional formulae.

5.1.2.2. Differentiating between different cross-shore zones

In cases where the boundaries for the cross-shore regions have been clearly established (e.g. breaking zone at $53\text{m} < x \leq 57\text{m}$), it is possible to manually (or by programming) implement the new Ω value for the shoaling zone, for example when running morphodynamic modelling simulations. When only computing the reference concentration for short-term laboratory experiments or micro-scale morphology (e.g. temporal scale of minutes to hours; spatial scale of metres), manually implementing the desired formula or constant (such as Ω) for the different cross-shore zones is straightforward. However, when such formulae are integrated into morphodynamic models for medium- to long-term simulations, it could be necessary to set explicit boundary conditions based on measured or modelled parameters to differentiate between the different zones. A simple and perhaps crude method of doing this could be for example to assume that local water depth $d = 2\text{m}$ at the boundary between breaking and inner surf zones: when $d \geq 2\text{m}$ then $\Omega = 7.5$ and when $d < 2\text{m}$, $\Omega = 1.0$ (refer to Chapter 2.3.1.3. for different values of Ω). Programming some form of boundary conditions for the application of different formulae or parameter values would ensure smoother simulations and be more efficient, especially in tests involving large amounts of data (e.g. medium- to long-term large-scale morphology). This is further discussed in Chapter 5.1.2.3.

In cases where the cross-shore regions have not been explicitly distinguished, implementing the different Ω values for different cross-shore zones could be more challenging. In the work of vdZ et al. (2016), the different cross-shore regions were identified by examining the phase-averaged measurements of the water surface elevation. Based on these observations, and the work of Svendsen et al. (1978), the three cross-shore zones were distinguished. Where surface elevation measurements are available, such analysis can be carried out to establish the various cross-shore regions. In cases where there is a breaker bar, the boundary between the breaking and inner surf zones also seems to be qualitatively distinguishable in terms of the wave climate

(e.g. local wave height) or the local water depth in the datasets described in Chapter 3.2. of this thesis (see also Fig. 12 and cross-shore profile evolution in Figs. 1-5). The experimental datasets described in Chapter 3.2. show that the cross-shore distribution of wave height (H) and water depth (d) decline from the shoaling region to the breaking region. vdZ et al. (2016) reported that the wave energy dissipation in the SINBAD experiments started at the breaking point, and continued through the breaking zone, with local wave height declining by 50% between the shoaling and inner surf zone. This is somewhat consistent with observations in the other datasets which indicate that H continues to fall until the plunging point, after which it increases marginally before falling again. It is speculated that this momentary marginal increase in H indicates the small wedge of water pushed up by the plunging jet which then forms a secondary wave (vdZ et al., 2016). Alternatively, the water depth gradually declines from the shoaling zone to the plunging point, where the breaker trough is located. At this point d begins to gradually rise again, before declining once more as the inner surf zone gives way to the swash zone. From these observations of H and d , and/or observations of the water surface level, as described by vdZ et al. (2016), the various cross-shore regions can be identified. These methods, among others, suggest that models such as JS07 or L19, that require the distinguishing of cross-shore zones, are applicable to morphodynamic models.

It should be noted however that the present observations are based on controlled prototype scale laboratory experiments and may differ from observations in the field. As such, the distinguishing of cross-shore zones may require more detailed examination of the interactions between hydrodynamic processes and sediments. The scope of the present study does not extend into the distinguishing cross-shore zones. It is speculated however that such research could be invaluable in the integrating of more accurate SSC models into morphodynamic models and would recommend a more detailed analysis of the sediment/hydrodynamic interactions and processes observed in the different cross-shore regions in future studies. Chapter 3.3. of this thesis has clearly indicated that the existing SSC models are not perfectly adept for use in all (multiple) cross-shore zones and transport mechanisms and thus, the recommended research could allow for separate (or a combination of) models or parameters that are idealised for specific cross-shore zones or sediment transport mechanisms (similar to the approach of Jayaratne & Shibayama, 2007) to be used in conjunction, rather than a one-size-fits-all model that is used for all cases.

5.1.2.3. Application of different Omega (Ω) constants to field-conditions

The biggest challenge with the use of the L19 formulae is the application of the different Ω constant values to the transport formulae of morphodynamic suites. As discussed in the previous sub-chapter, differentiating the various cross-shore regions is generally relatively straightforward. Having identified the different cross-shore regions however, applying the corresponding Ω constant to those cross-shore regions is more challenging. The issue that makes this endeavour troublesome is that in morphodynamic modelling suites, such as the Delft3D-FLOW module, there is often no built-in parameter/method of selecting cells in a grid that correspond to a specific cross-shore zone or range.

For example, in Fig. 41 below, there is a screenshot of a morphodynamic model grid, made using Delft3D-FLOW for a study site at Perranporth Beach, UK. Fig. 41 shows that the inner surf/swash zones are in the first 0.4 km from the shore, and from the seaward end of the inner surf zone is the breaking/shoaling and offshore region (breaking region at approximately $x = 450-600\text{m}$). Based on the values of Ω provided for erosive conditions in Chapter 2.3.1., a value of $\Omega = 7.5-15$ should be applied to all grid cells between $600 \leq x \leq 1200\text{m}$ and $\Omega = 1.0-3.0$ for $x < 600\text{m}$. As mentioned above however, the Delft3D-FLOW module does not have a built-in function that allows users to select all grid cells between $600 \leq x \leq 1200\text{m}$ or all grid cells $x < 600\text{m}$. Applying the Ω constant as a function of the cross-shore coordinate therefore requires additional code to be implemented into the transport module of Delft3D, to allow users to select specific cells in the grid and to apply specific values to only those pre-defined cells. Alternatively, one could define the cross-shore regions by more accessible parameters (such as wave climate and/or water depth, or even bed levels), as suggested in Chapter 5.1.2.2.

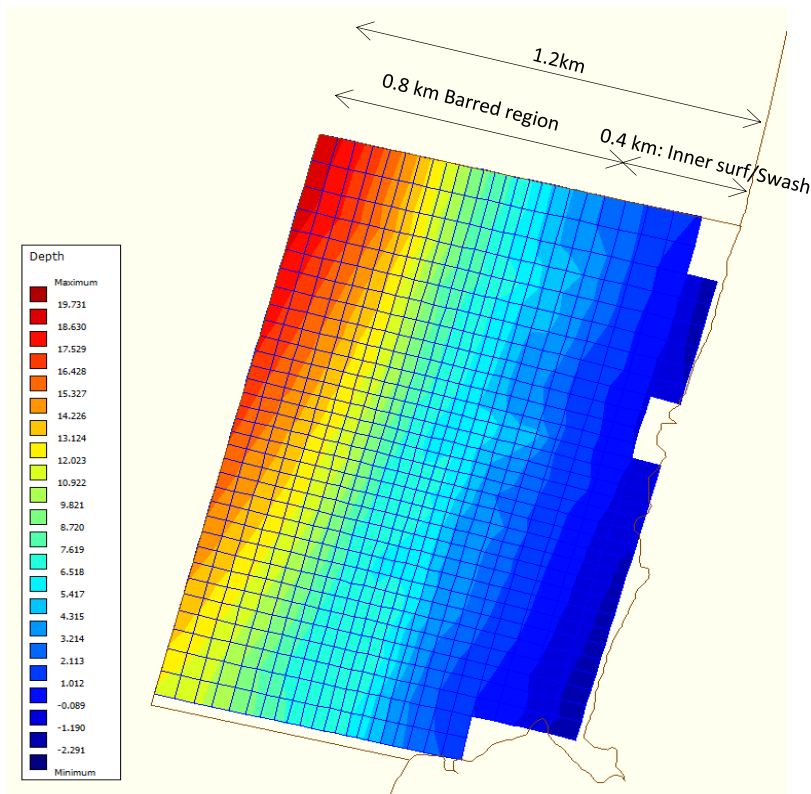


Figure 41 - Delft3D-FLOW model domain: grid and bathymetry for Perranporth Beach, UK.

One thing that should be considered however is that the local water depth (measured from the water level) fluctuates over time due to the presence of tides in field conditions. This is something that was not accounted for in the development of the L19 C_0 formula. Particularly at beaches such as Perranporth Beach, UK, which is a macro-tidal beach where the tidal range is large, the effects of varying water depth could be even greater. The presence of tides and how they affect model performance can be tested by the implementation of the L19 model into morphodynamic suites such as Delft3D, where the water depth can be input in two different ways. 1) Firstly, the water depth from a set datum (e.g. the mean sea level, MSL) could be used. This method would ensure that the level from which the water depth is measured from is constant, as found in the laboratory experiments by which the L19 model was developed and validated. Though this parameter (depth from MSL) is not computed by the Delft3D-FLOW module, it can be found by loading a parse file containing the MSL data into the software environment and then calling in the real-time bed level data from the running simulation to reconstruct the depth below reference level (which would be the MSL in this case). This method is plausible but is quite complex and would likely require high computational costs to run these simulations. 2) The second, alternative method is to use the varying water depth as it is. E.g.

for Perranporth Beach, having determined the shoaling and breaking regions, the initial bed level (depth measured from datum, ODN) at the shoreward limit of the breaking region was found to be approximately -2m ODN. Following on from the assumption that wave shoaling and breaking occur between the offshore boundary of the domain ($x = 1200\text{m}$; where bed level was approx. -20m ODN) and the shoreward limit of the breaking region ($x = 400\text{m}$; approx. -2m ODN) the following conditions could be used to define the Ω constant:

For erosive (high energy) cases:

$$\Omega = \begin{cases} 7.5 - 15.0 & \text{for } 20\text{m} > d \geq 2\text{m} \\ 1.0 - 3.0 & \text{for } d < 2\text{m} \end{cases}$$

For accretive (low energy) cases:

$$\Omega = \begin{cases} 1.5 & \text{for } 20\text{m} > d \geq 2\text{m} \\ 0.6 & \text{for } d < 2\text{m} \end{cases}$$

Whereas the breaking/plunging point was more or less constantly in the same cross-shore location in the laboratory datasets in Chapter 3.2., in the field the breaking point would essentially just alternate between the onshore/offshore direction. Also, the L19 formulae do not depend on wave breaking related parameters (such as enhanced turbulent kinetic energy or horizontal velocities) to predict suspended sediment concentration. Thus, regardless of the cross-shore region it is applied to, the predicted concentration will increase, or decrease based on the water depth (among other parameters).

As seen in Chapter 3.3.1., the L19 C_0 model produced accurate predictions of the reference concentration under a wide range of different conditions: plunging and spilling breakers, erosive and accretive, low and high energy conditions, on barred and planar beds. Therefore, it is thought that the performance of the L19 model will not be strongly affected by the change in water level (and water depth). By assuming that any region where the water depth is, say $\geq 2\text{m}$, is part of the offshore or shoaling/breaking zone, and any depth $< 2\text{m}$ is the inner-surf/swash zone, the corresponding Ω constant can be applied. As the water depth increases in the offshore direction, computed C_0 approaches zero, just as one would expect in real life conditions, therefore the value of Ω set in the deep-water regions is considered to be relatively unimportant. The region between $x = 400\text{m}$ and the shore in Fig. 41 can be assumed to be the inner-surf/swash zone, having an Ω value of 3(0.6) applied for high(low) energy conditions.

For whatever reason, the situation may require the user to use a one-size-fits-all formula or constant (like those in category 1 from Chapter 5.1.2.1.). The L19 model generally performed very well in all cases when using a varying Ω parameter, but there were some (often quite large) discrepancies found in the inner surf zone. If a constant value of Ω was to be used in all cross-shore regions, the level of accuracy could be forfeited (albeit marginally) for gain in computational efficiency. Depending on the constant value of Ω selected, the accuracy of the model can vary considerably. Using $\Omega = 7.5-15$ (recommended values for shoaling/breaking zones in erosive cases, refer to Chapter 2.3.1.) in all three zones would ensure good agreement in the shoaling and breaking zones, as observed in Chapter 3, but result in over-prediction in the inner-surf zone. Through sensitivity analysis, this over-prediction in the inner-surf zone was found to be as little as $\approx 1.5 \text{ kg/m}^3$ (still in the correct order of magnitude) and as large as $\approx 18 \text{ kg/m}^3$ (one order of magnitude higher than measured). Using $\Omega = 1.0-3.0$ (recommended values for inner surf zone in erosive case, suggested in Chapter 2.3.1) for all zones will ensure good agreement with data in the inner-surf zone, but substantial under-prediction in the shoaling and breaker zones. If a constant value of Ω is to be used for all zones, it is recommended that a value of $\Omega = 7.5-15$ for erosive cases and $\Omega = 1.5$ for accretive cases, based on the results of the sensitivity analysis (not shown).

Determining whether to use the Ω values for the erosive or accretive case is another issue to be considered in morphodynamic modelling. When predicting morphology for short-term (e.g. hours or days), it is possible to distinguish whether the conditions are erosive or accretive with relative ease. However, when applying the L19 model to longer periods, e.g. months or years or even decades, there will inevitably be both erosive and accretive conditions present, and often alternating randomly. Comparison between erosive and accretive conditions in the datasets in Chapter 3.2. indicate that the key differences between the two conditions is the wave period (T) and the offshore wave height (H_0). A simple but crude method of addressing this issue would be calibrating the L19 model for the given location using previous wave climate and sediment transport measurements. Such data could be used to set some pre-defined conditions, e.g. if $T > x$, use $\Omega = 7.5$, if $T \leq x$ use $\Omega = 1.5$. These boundary conditions could be combined with those for the water depth for different cross-shore zones. E.g. using the example for Perranporth Beach above, when $20\text{m} > d \geq 2\text{m}$, and if $T > 5\text{s}$ then use $\Omega = 7.5$, if $T \leq 5\text{s}$ then use $\Omega = 1.5$.

5.1.2.4. Incorporation of horizontal advection

It was briefly mentioned in Chapters 3.3.2. and 3.4. that not all suspended sand concentration observed in cross-shore measurements is produced locally but can also be advected horizontally to and from adjacent regions. In recent studies (e.g. vdZ et al., 2017b), horizontal advection of breaking-induced TKE and suspended sediment was quantified and evaluated, indicating that the effects are not trivial. As such, it is worth considering if and how horizontal advection could be incorporated into reference concentration models. As mentioned in Chapter 5.1.1.1., using the near-bed TKE or Froude-scaled TKE, either measured or computed, seems to be an ideal method as it not only accounts for the advection of TKE, but also of SSC (as the two are related). I.e. the near-bed TKE k_b has a strong causal relationship with SSC, and therefore would not need to be an additional parameter, but a single parameter that drives the C_0 model in predicting the SSC at a reference level, as well as modelling the advection of the TKE and suspended sediment. It would seem however that at present, our inability to accurately measure or model near-bed TKE under breaking wave conditions limits the possibility of this method (as mentioned in Chapter 5.1.1.1.). As the measuring and modelling of near-bed TKE becomes more accessible in the near future, it will enable further comprehensive studies to be carried out in using k_b or $(k/gh)^{1/2}$ to model suspended sand concentration and horizontal advection patterns in relation to TKE.

The L19 model does not explicitly account for the effects of horizontal advection, instead empirically modelling the reference concentration as a function of local conditions (e.g. sediment, bathymetry, wave conditions). I.e. as it does not account for advection, it implicitly assumes that the computed SSC is entirely locally produced. Despite not accounting for the advection processes however, the L19 C_0 model performs well, particularly in the shoaling and breaking zones (refer to Chapter 3.3.1.7.). It may be that the effects of advection could have a greater effect on model performance, but in considering the cross-shore distribution of reference concentration alone, the L19 model indicates good agreement with measured data. Considering that the existing models tested herein did not adequately account for the effects of breaking-induced turbulence on resulting SSC, let alone the effects of horizontal advection, the L19 model still represents a significant improvement. Future efforts will be focused on studying and developing feasible methods of including the horizontal advection into the L19 model, whilst attempting to maintain a balance between practical/computational efficiency and adequately accounting for all essential physical phenomena. By doing so, the newly developed

models will not be entirely empirical, relying solely on calibration efforts, but be robust and based on physical process insights wherever possible.

5.1.3. Applicability to irregular wave conditions

Though the new L19 C_0 model has been proven to perform very well under regular waves in controlled laboratory experiments (e.g. against the SINBAD and SandT-Pro datasets), it is also necessary to evaluate its applicability to field-scale random or irregular waves if the model is to be used practically in the field. As mentioned in Chapter 5.1.1., though there are considerable differences in the magnitude of measured k_b and in relative contributions to net cross-shore TKE. For example, the relative contribution of wave-related TKE transport was greater under irregular conditions than under regular conditions. I.e. the current-related TKE contributed more to net cross-shore TKE transport under regular breaking waves than under irregular breaking waves - this was partially attributed to regular waves producing stronger undertow currents which drive the current-related TKE transport (vdZ et al., 2019). Despite such differences, the general TKE structure and hydrodynamics remain similar between regular and irregular wave conditions (e.g. Scott et al., 2005; Brinkkemper et al., 2016). This is reflected in the performance of the existing models evaluated in this thesis which show similar skill in both regular and irregular conditions, with substantial under-predicting found at the breaking/plunging points for all tested parameters (C_0 , $C[z]$, $uC[z]$ and q_{sc}). It should be noted however that the random waves break over a wider cross-shore area than in regular wave conditions, making it difficult to pin-point one location as the breaking or plunging point. This is supported by the findings of Scott et al., (2005) who reported that the surf zone created under irregular waves was broader than that found under regular cases, with a larger percentage of waves not breaking over the bar but propagating over the bar without breaking. It is speculated that these waves could have broken further onshore. This is consistent with Yoon & Cox (2010) who reported that waves generally broke at the bar crest, but as time progressed in the accretive runs, the bar decayed, and more waves passed over the bar, breaking later in the surf zone. As such, the points labelled ‘breaking point’ and ‘plunging point’ in the CROSSTEX and LIP datasets are only estimations based on bottom profile evolution, measured TKE observations and the reports of the authors who collected and published the datasets. Based on the consistency of observed trends between computed and measured suspended sand transport parameters and also measured TKE however, these estimations of breaking and plunging points seem reasonable.

Despite the irregular wave conditions, the L19 C_0 model agreement is generally very good. As the L19 C_0 model is not driven by the local wave- or current-related velocity or near-bed TKE (k_b), it is not majorly affected by the differences in hydrodynamics between regular and irregular wave conditions. As it can be seen in Fig. 12 of Chapter 3.3.1., the proposed empirical relationship between the inverse water depth ($1/d$) shows good agreement with measured reference concentration throughout the shoaling and breaking zones for both regular and irregular wave conditions. Generally, the reference concentration models covered in this thesis performed better under irregular erosive conditions than accretive conditions. Accretive conditions are associated with low- to moderate-wave energy conditions with relatively long wave periods (Aagaard & Hughes, 2010). This suggests that the tested models are more adept for erosive, medium- to high-energy wave conditions with shorter wave periods.

CONCENTRATION PROFILE AND TRANSPORT RATES

5.1.4. Implications of improvements to C_0 & $C[z]$ models on resulting transport rates

The analysis presented in Chapters 3 and 4 clearly demonstrate that there is lack of robust suspended transport models adept for predicting the magnitude and transport patterns of sand suspended under breaking wave conditions. Throughout this thesis, existing reference concentration (C_0) and concentration profile ($C[z]$) models have systematically shown poor performance in predicting not only C_0 and $C[z]$, but also the suspended flux ($uC[z]$) and current-related transport rates (q_{sc}) which are functions of the reference concentration and profile. This poor performance was particularly observed in the breaking/plunging zone, with clear indications that breaking-generated TKE has quasi-linear effects on not only sediment pickup and mixing, but also on flux and current-related transport rates. Thus, the results presented in Chapters 3 and 4 indicate an urgent need for improved C_0 and $C[z]$ models in order to accurately predict sand transport patterns and resulting morphodynamics under breaking wave conditions.

Based on comparison between C_0 plots from Chapter 3.3.1., $C[z]$ formulations from Chapter 3.3.2., and those found in Chapter 4.3.1., it is clear that the accurate prediction of C_0 is essential in the prediction of $C[z]$, and therefore in the prediction of $uC[z]$ and q_{sc} also. As the reference concentration practically serves as a starting point for the estimation of the concentration profile, poor prediction of C_0 would inevitably result in relatively poor predictions of the

concentration profile. Part B.1. of Chapter 4.3.1.2 showed that in the breaking region, despite good prediction of C_0 , corresponding $C[z]$ was overpredicted considerably by SR93 and W12, resulting in relatively poor predictions of $uC[z]$ and q_{sc} . Part B.2. of Chapter 4.3.1.2. further provided evidence of the importance of accurately predicting C_0 , showing very large discrepancies not only in the wave plunging region, but also in the shoaling zone and pre-plunging regions of the breaking zone as well. It is clear that both the improvements to both reference concentration and concentration profile formulae are necessary in order to produce accurate transport rates.

Though the accurate prediction of both parameters is essential, it would seem that the accurate estimation of $C[z]$ is relatively less important in the shoaling ($x = 51-53m$) and inner surf zones ($x = 58-63m$), as well as the pre-plunging region of the breaking zone ($x = 54.5-55m$), where sediment pickup and vertical mixing levels are comparatively low. This can clearly be seen in Figs. 33-35 (see Part B.1. of Chapter 4.3.1.2.), which indicate that there is very little difference between magnitude of values (of all three parameters) computed using the SR93, W12 and L19 models in the shoaling and inner surf zones and breaking zone pre-plunging, despite being predicted using different $C[z]$ formulae. On the contrary, in regions where the concentration levels are higher – i.e. in the plunging region – the accurate estimation of the concentration profile becomes relatively more important, with large differences between the computed values of SR93, W12 and L19 models despite having the same C_0 value (see Fig. 36). This makes sense, as one of the key parameters in the $C[z]$ formulae is the mixing parameter, and vertical sediment mixing is most prevalent in the plunging region (as explained in Chapter 1.1.1. of this thesis).

The concentration profile can be seen to be very sensitive to the magnitude of the mixing parameter (M). For example, as presented in Chapter 3.3.2. (c.f. Chapter 2.3.2.), the only difference between the SR93 and L19 $C[z]$ formula is the introduction of the constant $B = 3.3$ in the L19 formulae. Despite the relatively small change to the original mixing parameter, the difference in results is clearly significant (refer to Figs. 33, 35, 36), particularly in the plunging region where the accuracy of the $C[z]$ formula is arguably most important. At this point, the magnitude of $C[z]$, $uC[z]$ and q_{sc} computed using SR93 are larger than the corresponding values computed using L19 by factors of 1.33, 2.16 and 1.38 respectively. The differences in RMSE between SR93 and L19 are also considerable, as presented in Table 19 in the summary section of Part B.1. of Chapter 4.3.1.2. This demonstrates that the performance of the commonly used power function $C[z]$ formulae (Eq. 24) can be calibrated if necessary, by means of the simple

B constant introduced in Chapter 3.3.2. Though the analysis carried out in this thesis indicates that the value of $B = 3.3$ works well for all tested conditions (including regular and irregular, spilling and plunging large-scale breaking waves), future studies could focus tests on a wider range of test conditions – e.g. different grain diameters, and/or with data collected in the field. Alternatively, a more robust method of estimating the mixing parameter and concentration profile could be developed in future studies. It is thought that the implications of such research would be particularly important for breaking wave conditions where strong vertical mixing is induced by breaking-related TKE.

Based on the findings from Parts B.1. and B.2. alone, one could argue that the improvements to reference concentration models has a greater influence on the resulting transport rates than improvements to concentration profile models. This argument may require more test cases (e.g. more C_0 and $C[z]$ model combinations, more data, different test conditions, etc.) and validation before it could be taken as fact. Due to the lack of datasets that comprises of co-located cross-shore sand transport rates and velocity measurements however, it is difficult to further quantitatively validate the implications of C_0 and $C[z]$ improvements and to what extent these improvements affect resulting transport rate (and morphodynamic) predictions. Regardless, qualitatively it can clearly be seen that even small modifications in constituent models (both C_0 and $C[z]$) can have considerable effects on resulting transport rate computations. This was seen with the modification of the SR93 $C[z]$ model and also, with the W12 and L19 models which showed that despite performance of both W12 and L19 being quite similar in predicting $C[z]$ (with regards to RMSE, see Chapter 3.3.2. of this thesis), the underpredictions of $C[z]$ produced by the W12 model had relatively larger effects on resulting transport rates than L19. This is consistent with the findings from Chapter 3.3.2. which indicated that though the performance of all $C[z]$ models was strongly dependent on the accurate estimation of the reference concentration, the exponential formulae (e.g. W12) were more-so affected by the C_0 prediction than the power function formulae (e.g. L19).

The extent to which the proposed improvements in sediment transport formulations will affect long-term morphodynamics is yet unclear due to the non-linear nature of coastal morphodynamics and uncertainties regarding which processes drive it in the long-term. It is theorised however, that the magnitude of impact will be dependent on various factors such as: modelling approach (e.g. 2D/3D), level of abstraction (e.g. low abstraction: process-based or high abstraction: data-driven/behaviour-oriented), coastal region (e.g. near-shore/offshore) and dominant driving processes in the region (e.g. wave-dominant/tidal dominant) to name a few.

Systematic studies investigating the limitations of existing transport models and how they can be improved could serve as the first step in investigating the different effects short-term sediment transport models have on long-term morphodynamics. Such research could shed valuable insights and help to improve morphodynamic models to more adeptly model long-term evolution.

5.1.5. Applicability to field conditions

Though experimental datasets collected in laboratories under regular wave conditions provide numerous benefits, such as controlled, designed and consistent test conditions – allowing more detailed analysis of processes – in nature waves are irregular and subject to various other processes and factors that are either simplified, reduced, isolated or unaccounted for in laboratory conditions. Therefore, any formulations developed under regular wave laboratory conditions should, if possible, be validated using data collected in the field (e.g. Russell, 1993; Yu et al., 1993; Birkemeier & Thornton, 1994; Beach & Sternberg, 1996; Grasmeyer, 2002; Masselink et al., 2007; Miles & Thorpe, 2015), or at least under field-scale irregular wave conditions (e.g. Roelvink & Reniers, 1995; Yoon & Cox, 2010). Nevertheless, field(-scale) experiments that have collected co-located measurements of concentration profiles and horizontal velocities with high enough (and consistent enough) spatial (especially vertical) resolution over different cross-shore locations to predict accurate transport rates are difficult to find. For example, the CROSSTEX dataset (Yoon & Cox, 2010) measured concentration profiles and horizontal (among other) flow velocities. However, the horizontal velocity profile measurements were only taken at 6 vertical elevations above the bed (compared to the SINBAD dataset which had co-located measurements at between 50-100 vertical elevations above bed per cross-shore location). As the current-related transport rates are computed by depth-integrating the product of the concentration and horizontal velocity profiles, predictions of the transport rates would benefit from greater spatial resolution of measurements/computations. Sediment transport rates computed from relatively lower-resolution measurements have not been individually validated against higher-resolution measurements, and it is therefore difficult to say whether or not they are accurate and to what extent. However, though transport rates computed from lower-resolution measurements may not be ideal in predicting, say, long-term morphodynamics which requires optimal accuracy, they can still help to identify relative contributions and patterns of different transport components to morphological changes (e.g. the magnitude and directions of current- and wave-related suspended load and also bedload).

Field experiments that focused on the collection of the concentration and horizontal velocity profiles under shoaling and breaking wave conditions include the works of Beach & Sternberg, (1996), Masselink et al. (2007) and Miles & Thorpe (2015) among others (refer to Chapter 4.1.). The study of Masselink et al. (2007) had the relatively higher vertical spatial resolution of the three mentioned experiments – with measurements of the suspended sand concentration profile being taken at 12 vertical locations above the bed in the near-bed region (between - 0.02m to 0.19m above bed with 1cm resolution from bottom to 0.06m). The flow velocity measurements were taken with relatively lower spatial (vertical) resolution than the SSC measurements, only being measured at 6 vertical locations. Though the flow and concentration measurements were not co-located, it was still possible to compute transport fluxes and rates by carrying out some interpolation to estimate any gaps in the concentration and flow measurements.

Masselink et al. (2007) found that the wave-related (oscillatory) component of suspended transport rates was dominant in the shoaling zone, which is consistent with the trends observed in this thesis and those found by vdZ et al. (2017b) – note: only the “energetic/high-waves” case of Masselink et al. (2007) is considered in this section. Contrary to the findings in Chapter 4.3.1.1. of this thesis however, the findings of Masselink et al. (2007) indicate that the magnitude of the onshore-directed oscillatory (wave-related) component of suspended transport rates are considerably higher (approximately a factor of 4) than the magnitude of offshore-directed mean (current-related) component in the breaking zone for high wave conditions ($H_s > 0.75\text{m}$). The reason for this difference is not certain, but it is speculated that it is related to a number of reasons. 1) Firstly, though there is mention of the presence of plunging breakers, it does not specify whether or not they were the dominant breaker type. As reported in Lim et al. (2020) and also in numerous studies (e.g. Yoon & Cox, 2010; Brinkkemper et al., 2016; Aagard et al., 2018; vdZ et al., 2019), the breaking-induced turbulence structure is very different under different breaker types, with sediment concentration being substantially higher under plunging breakers than spilling breakers. It is speculated that depending on the breaker types observed in the experimental conditions, the resulting suspended sediment concentration and the magnitude of corresponding suspended transport rate could vary significantly. 2) Secondly, there is no mention of the breaking and/or plunging point(s) or whether the sediment transport rates were measured at, before or after this cross-shore point(s). Analysis of measured transport rates in Chapter 4.3.1.1. showed that the magnitude of the offshore-directed current-related suspended transport rate increased sharply

and peaked at the wave plunging point. It was then seen to quickly fall again within a distance of 50 cm from the plunging point (onshore from $x = 55.5\text{m}$ to $x = 56\text{m}$; see Fig. 29, Chapter 4.3.1.1.), indicating that the magnitude of q_{sc} is strongly dependent on the cross-shore location at which it is measured. 3) Thirdly, there was a considerable difference in the average grain diameter at Sennen Beach, UK (Masselink et al., 2007), with a $D_{50} = 0.6 - 0.69\text{ mm}$. Though it was found by vdZ et al. (2017a) that sediment pickup and vertical mixing in the breaking region are grain size-indifferent (contrary to other cross-shore regions where sediment pickup and mixing were size-dependent, with more finer particles being suspended) it is thought that the amount of sediment entrained would be somewhat sensitive to the grain diameter – i.e. one would predict there to be lower SSC for a uniform bed of coarse grain than a uniform bed of fine grain given the same forcing conditions. 4) Fourthly, the boundaries defining the various cross-shore regions were determined by Masselink et al. (2007) using the relative water depth H/h , referring to the region of $H/h < 0.4$ as the shoaling zone, $H/h = 0.4-0.5$ as the breaker zone and $H/h > 0.5$ as the saturated surf zone. These definitions of the shoaling, breaker and saturated surf zone are not applicable to the SINBAD dataset, where the H/h value is highest in the shoaling zone and declines in the shoreward direction. As such, it is difficult to say whether or not the regions referred to as the “breaker zone” and “saturated surf zone” in Masselink et al. (2007) correspond to their namesake in the SINBAD dataset. 5) Finally, there was a difference in the bed slope, with $\tan(\beta) = 0.03$ at Sennen Beach, UK and $\tan(\beta) = 0.1$ in the SINBAD experiments. The slope was considerably steeper in the SINBAD experiments, leading to enhanced wave shoaling effects and strong plunging breakers in the breaking zone. As the wave-breaking induced velocities and sediment concentration contribute towards the current-related transport component q_{sc} , it is thought that the strong plunging breakers found in the SINBAD experiments may be responsible for the higher magnitudes of q_{sc} observed.

Miles & Thorpe (2015) found that offshore-directed current-related suspended transport (q_{sc}) was dominant over the onshore-directed wave-related component (q_{sw}), with q_{sc} reaching a peak of -0.18 kg/m/s in the mid-surf zone. This trend is more consistent with the findings of presented in Chapter 4.3.1.1. and of those vdZ et al. (2017a), as the magnitude of the peak q_{sc} is in the same order as those measured and computed in Chapter 4.3. Despite Perranporth Beach (location of study of Miles & Thorpe, 2015) having an even more gradual bed slope than that seen at Sennen Beach, UK ($\tan[\beta] = 0.0125$) a similar pattern of offshore/onshore-directed suspended transport was observed. This suggests that the fundamental differences between the outcomes of this thesis and those of Masselink et al. (2007) are more to do with the cross-shore

boundary definitions (i.e. which region is referred to as the breaking and surf zones) than the difference in beach slope. Assuming that this is the case, this indicates that the magnitude of offshore directed q_{sc} found in breaker/mid-surf zone of the SINBAD experiments is in the same order of magnitude as those found by Masselink et al. (2007) and Miles & Thorpe (2015). This also indicates that the cross-shore transport patterns predicted by the L19 model in Chapter 4.3.1. are in good agreement with those observed at Sennen and Perranporth Beaches.

Though these explanations may help to justify the relatively small q_{sc} values measured by Masselink et al. (2007), they do not however explain the large magnitude of the onshore-directed oscillatory (wave-related) suspended transport component q_{sw} , which is seen to be > 0.2 kg/m/s, which is one order of magnitude larger than those observed in the SINBAD experiments. In a related study, Austin et al. (2009) reported that the strong onshore-directed suspended fluxes observed at Sennen Beach, UK, were related to the onshore-directed flow accelerations found under the steep front faces of asymmetric waves, identifying strong correlations between this flow acceleration and sediment entrainment. It is also speculated that there may be some (albeit marginal) level of variance incurred by the different methods used to separate the mean and oscillatory components of the measured velocities. Masselink et al. (2007) and also Miles & Thorpe (2015) used the method of Jaffe et al. (1984), whereas a different method was adopted for the SINBAD project (refer to Chapter 3.2. and/or vdZ et al., 2016). The extent to which these different methods would influence the resulting data is however unknown, and beyond the scope of this study. The modelling of the onshore-directed q_{sw} is discussed further in Chapter 5.1.6.

An alternative method of testing the applicability of the L19, and other suspended transport formulae, in field conditions is to implement them directly into morphodynamic models as discussed thoroughly in Chapter 5.1.2. When implemented into morphodynamic suites, though the performance of the individual sediment transport model would not be validated directly in an isolated standalone evaluation, the model could still be verified indirectly by using it to compute bed changes and comparing the resulting morphology against measured bed changes (assuming that the input hydrodynamic and/or forcing conditions are accurate). The analysis carried out Chapter 3 and continued in Chapter 4 clearly show that there are strong links between the C_0 and/or $C[z]$ and the current-related suspended transport rate (q_{sc}). As the reference concentration and concentration profile models of L19 were thoroughly validated and found to perform well for: initially barred beds, initially planar beds, with regular and irregular breaking waves, spilling and plunging breakers (see Chapters 3 & 4; c.f. Lim et al.,

2020), there is ample reason to suggest that it would also perform reasonably in predicting q_{sc} under field conditions. There may of course be physical phenomena, differing conditions and/or forcing that occurs in the field that have not been observed in laboratory experiments (or observed to smaller extents and overlooked), and therefore are unaccounted for in the numerical models. For example, vdZ et al. (2017a) noted that the breaker bar in the SINBAD experiments was separated from the sloping beach by an elongated inner-surf zone to isolate the breaking zone morphodynamics from the effects of beach processes. In reality, the bar trough would likely be closer to the inner-surf/swash processes, and therefore be influenced by them to a greater extent (vdZ et al., 2017a). Though no major problems were identified when qualitatively comparing the performance of L19 against the field data of Masselink et al. (2007) and Miles & Thorpe (2015), higher resolution measurements could help to identify the presence of such poorly understood processes, particularly in the breaking and swash zones. Until such phenomena can be extensively measured, analysed and sufficiently understood, it seems that modellers would be forced to rely on empirical parameterisations and model calibration efforts to account for these unresolved processes. However, considering that there are relatively abundant amounts of datasets measuring morphodynamic changes, ranging from small- to large-scale (10^1 to 10^2 km) and short- to long-term (days to decades), it is thought that direct implementation of the L19 formulae to morphodynamic models could help to shed novel insights into the performance and potential limitations of the model, as well as improve our understanding of poorly modelled morphological processes.

5.1.6. Inclusion of the wave-related component

Analysis carried out in Chapters 4.3.1.1. and 4.3.2. have shown that the depth-averaged onshore- directed wave-related suspended transport rate (q_{sw}) is generally relatively small in magnitude when compared against the magnitude of the corresponding current-related transport component (q_{sc}) at the same cross-shore locations – this was found to be the case in the shoaling, breaking and inner-surf zones. These findings are consistent with Beach & Sternberg (1996) who found that the fluctuating (wave-related) component of suspended flux was generally small in most cross-shore locations. There was however substantial wave-related suspended transport above the shoreward bar slope where near-bed TKE was found to be highest (vdZ et al., 2017b). It was found in Chapter 4.3.1. that the difference between the measured q_{sc} and net suspended transport (q_s) was marginal, with the L19 model accurately

reproducing q_s despite not accounting for the wave-related suspended transport component (q_{sw}) – i.e. computed $q_{sc} \approx$ measured q_s . One cannot however determine whether or not the wave-related suspended transport rate component contributes significantly to modelling net suspended transport from these findings alone. As seen in Chapter 5.1.5., as well as in existing literature (e.g. Ruessink et al., 1998; Grasmeyer, 2002), previous studies have identified large contributions of the onshore directed q_{sw} component to net suspended transport, indicating that it must be adequately accounted for in sediment transport models. There is however still a considerable lack of process understanding regarding the wave-related suspended transport component. For example, there are still knowledge gaps in our understanding of the complex near-bed interactions between the flow and the entrained sediments (van Rijn et al., 2013), the relative importance of the wave-related fluxes under different breaker types, whether it is the breaking-induced turbulence or wave asymmetry (or both; to what extent) that is responsible for enhanced q_{sw} under plunging breakers, whether it is essential to include the wave-related suspended transport component into sediment transport models and how best to go about doing so. Even the method of separating the mean and oscillatory components of flow and suspended sediment measurements is not universally agreed upon, suggesting that there is room for comparison/evaluation studies comparing and validating the various methods.

The Delft3D coastal area modelling suite (Deltares) solves the shallow water equations and the advection-diffusion equation to obtain the mean flow and concentration profiles, which are then used to find the current-related suspended transport (q_{sc}). The turbulent and intra-wave timescales of flow and sediment transport processes are not resolved, instead relying on empirical parameterisations (e.g. van Rijn, 2007) to compute the wave-related transport as well as wave effects on the mean flow (van der Werf et al., 2015). The default sediment transport formulae for the Delft3D suite are those of van Rijn (1993), which was compared for performance against the L19 model in Chapter 4.3. As the systematic analysis in Chapter 4.3. indicated that the L19 model performed better than that of van Rijn (1993), it is proposed that by including the new L19 C_0 and $C[z]$ formulae into Delft3D (replacing the default reference concentration and concentration profile formulae), the overall predictions of q_{sc} could be improved, as demonstrated in this thesis. Keeping the default parameterisations that currently compute q_{sw} in Delft3D (and using them in conjunction, with the new L19 formulae to find q_{sc}) the net suspended transport rate (q_s) can be computed. The q_{sw} formulae of van Rijn (2007) is a function of the onshore/offshore-directed peak orbital velocity, based on the method of Isobe & Horikawa (1982). As such, the performance of the model of Isobe & Horikawa (1982) would

likely have a considerable impact on the performance of the q_{sw} model of van Rijn (2007). Hence, it may be necessary to carry out some calibration efforts to ensure that the L19 model is compatible with the model of van Rijn (2007), before implementing the L19 model into morphodynamic suites such as Delft3D.

5.2. Limitations of Datasets Used

5.2.1. Availability and limitations of data

One major limitation that was found at every turn throughout the entirety of the present thesis was the lack of high-resolution data needed to calibrate/validate models. The various datasets analysed, processed and used in Chapters 3 & 4 of this thesis took great efforts (and time) to obtain, waiting for embargo periods to expire and liaising with numerous researchers to find suitable data and converting the data into usable formats. Though not presented in the present thesis, morphological data was also collected for the purpose of implementing the L19 model into morphodynamic suites. When collecting such data for morphological studies, it was found that regions such as Perranporth where wave, wind, bathymetric and topographic data have been collected over long periods of time are ideal for verifying morphodynamic models, but often lack high-resolution sediment transport and bed change data which is needed to carry out quantitative analysis of these models. Many existing morphodynamic models are only validated against bed changes, with little regard to the accuracy of sediment transport predictions. As such, these models are often used much like empirical models that are calibrated using various parameters and data. This increases the risk of ‘over-calibrating’ models to specific study locations. In order for the weak links in morphodynamic models to be identified (not just qualitatively but also quantitatively) such sediment transport data is essential. Van Rijn et al. (2013) suggested in their vision paper that future efforts needed to be focused on the development of more practical and more process-based sediment transport models with concurrent efforts being made to collect more data that can be made available in collective repositories open to the research community. In particular, high-resolution (particularly in the WBBL) field measurements of cross-shore sediment transport processes collected in the surf zone under breaking wave conditions are needed to improve our current understanding of the complex phenomena, as well as breaking related hydrodynamics and resulting sediment transport mechanisms. Though such field data lacks the control, accuracy(resolution) and even detail found in laboratory datasets (van Rijn et al., 2013), they

provide measurements of full-scale processes that are controlled by many processes that are often neglected or simplified in laboratory experiments.

All validation carried out in this thesis has been done using data collected in controlled laboratory conditions with mobile beds consisting of medium sand with average grain diameter ranging between 0.22-0.25mm. Evidently, the datasets used do not cover a wide range of different sand diameters. The performance of each of the models could vary depending on the grain diameter, as magnitudes of suspended transport will be greater for finer sands than coarser sands, assuming all forcing and other conditions are the same. The effects of different grain diameters and how they affect the performance of the tested models however has not been tested herein and could be the subject of future studies. It is uncertain of how much of an effect differences in grain diameter will have on trends and conclusions made in this thesis, if any. The calibration of the Ω -constant for the L19 C_0 model may also vary with the average grain diameter, with different values of Ω being used for different sediment types and/or mixtures.

Another limitation in the datasets used is the inconsistency in spatial resolution of velocity and concentration measurements. Of the datasets used in this thesis, the SINBAD dataset had the highest spatial resolution, both in the horizontal (cross-shore) direction and in the vertical direction. However, the high vertical resolution of the SINBAD dataset was focused mainly in the near-bed region where $z \leq 10\text{cm}$, with resolution in the upper water column (outer-flow) above the WBBL being relatively low. The other three datasets had significantly lower resolution in the near-bed region but slightly higher resolution in the outer-flow region. The vertical resolution of velocity and concentration measurements are particularly important in the computing of depth-integrated transport parameters such as the suspended sand flux and current-related transport rate. As such, analysis of these parameters would benefit considerably from higher spatial resolution of measurements taken in the upper water column.

5.2.2. Instruments used and implications

It could be said that practical or (semi-)empirical models are only as good as the data with which they were calibrated and validated against, for if the data does not accurately represent reality, then the models developed using the data will be the same. For this reason, it is very important to consider the validity of all data used in modelling studies. Of course, all datasets

used herein were from published and often very extensively used datasets and experimental projects, but even still some important points are raised herein for consideration.

With regards to measurement accuracy/reliability, the accurate collection of flow velocity and particularly concentration measurements in the highly aerated breaking zone is difficult as the air bubbles interfere with acoustic and optical equipment. For example, the SINBAD dataset collected the time-averaged concentration measurements using the TSS, but also time-varying measurements using an Acoustic Backscatter System (ABS). The ABS data was however discarded entirely due to the contamination of air bubbles (vdZ, 2016). Not only the ABS data, but some data collected using Optical Backscatter Sensors (OBS) were discarded for the same reason as the ABS data. Cácares et al. (2020) carried out an extensive study on the effects of air bubbles on OBS measurements under breaking waves, concluding that they have a significant impact on the OBS signal. vdZ (2016) proposed that any acoustic or optical sand concentration measurements being collected in the highly aerated breaking region should ideally be compared against reference measurements that are insensitive to air bubble contamination. He stressed the importance of comparing acoustically measured concentration measurements (e.g. ABS) against reference measurements (e.g. TSS) as the work on acoustic scattering theory is still ongoing. (Note: the LIP experiments collected SSC measurements using suction samplers like TSS).

In the CROSSTEX experiments, the flow velocity and suspended sand concentration measurements were taken using Acoustic Doppler Velocimeters (ADV) and Fibre Optic Backscatter Sensors (FOBS) as described in Chapter 3.2. For the treatment of ADV data, a signal-to-noise ratio (SNR) threshold, in addition to the 3D phase-space threshold method of Mori et al. (2007) were used to identify spike noises in the data. Identified spikes were removed and linear interpolation, or a running mean, was used to replace the removed data. Yoon & Cox (2012) do not explicitly mention whether these spikes in the data were resulting from the interference of bubbles in the highly aerated breaking region, but it is assumed that the spikes refer to all interferences, including those caused by bubbles as the 3D phase-space threshold method of Mori et al. (2007) was developed to eliminate spike noises caused by bubbles. The tests of Mori et al. (2007) were however conducted in a small circular tank with an air bubble generator, not in a field-scale wave flume with strong breaking waves. Even still, they concluded that low correlation or SNR methods were not adequate for bubbly flows, and that the 3D phase-space threshold was most effective in removing spike noises of ADV velocity measurements. The method was not tested with the presence of suspended sediment and it is

uncertain if the effectiveness of the 3D phase-space threshold method would be the same under larger-scale conditions with strong plunging breaking waves that induce dense clouds of bubbles. Other studies over the years have focused on the removal of noise contamination from ADV measurements (e.g. Durgesh et al., 2014; Zhong et al., 2020) and also Acoustic Doppler Current Profiler (ADCP) measurements (e.g. Razaz & Kawanisi, 2011) in both laboratory and field settings, but to the author's knowledge no studies have been focused on the removal and validation of spike removal in acoustic instruments under field-scale breaking waves. Regardless, even if such studies have been carried out, it would seem the safest option to compare/validate any acoustic or optical measurements against reference measurements from instruments that are not sensitive to the presence of air bubbles, as recommended by vdZ (2016).

The FOBS from the CROSSTEX experiments were calibrated using a racetrack flume by adding known weights of sand and water to the flume. This calibration was done by using a propeller that was attached to the flume to circulate the sediment in the water and thereby simulate suspended sediment transported by currents (Yoon & Cox, 2012). The interference of breaking-generated bubble clouds on the optical instruments would not have been accounted for by the propeller in the racetrack flume. The FOBS data were also further filtered using a median filter. Whether any other precautions were taken to compare and validate the FOBS measurements against other measurements is not mentioned. Judging by the similar magnitudes of SSC between the CROSSTEX and SandT-Pro datasets (which used the same instrumentation as SINBAD experiments), it would seem that FOBS measurements are reliable. Considering the many similarities in transport patterns and cross-shore distributions of measured SSC over the 4 different datasets, it would seem that the various data treatment procedures carried out in the individual data collection campaigns were effective and that the reliability of the datasets used herein is also satisfactory.

Chapter 6 – Conclusions and Recommendations for Further Study

6.1. Conclusions

The research questions posed in Chapter 1.1.3. were answered through a systematic qualitative and quantitative evaluation of existing suspended sand transport formulae under breaking wave conditions. The aim of this thesis was to improve the accuracy and applicability of suspended transport models for breaking wave conditions, for implementation into morphodynamic modelling studies. This was done by investigating the key limitations of existing suspended sand transport formulae for breaking wave conditions and understanding how they could be improved for better implementation into future morphodynamic modelling studies. In particular, existing reference concentration (C_0) models and concentration profile ($C[z]$) models were evaluated and compared through standalone analysis, and by investigating the influence their performance had on resulting suspended flux and sand transport rate computations. Through this systematic study, key limitations to existing models were identified, with in-depth discussions on how they could be addressed to produce more accurate and robust models that could be implemented into morphodynamic models. A new and improved transport model was developed and thoroughly validated against measured data and evaluated against the performance of existing models. In this section, the main conclusions from each of the individual research questions are presented. This section follows the same pattern throughout: first the research question is posed, then the main conclusions are presented under each of the objectives that correspond to the posed research question.

RQ1) What are the key limitations of existing suspended sand transport formulae for breaking wave conditions?

-OB1: To identify key limitations of existing reference concentration and concentration profile models by qualitatively and quantitatively evaluating their performance against state-of-the-art measured datasets and latest process insights.

A total of 6 existing reference concentration (C_0) models were validated against 119 test cases from 4 recently published datasets collected under the *LIP*, *CROSSTEX*, *SandT-Pro* and

SINBAD experimental studies. These models were evaluated for performance in different cross-shore regions: the shoaling zone, breaking (outer surf) zone and inner surf zone, under regular and irregular field-scale breaking wave conditions. The most common limitations observed in existing C_0 models fall into two categories: 1) inapplicability to multiple cross-shore zones, and 2) inability to account for the high localised increases in suspended sand concentration (SSC) found in the breaking (plunging) zone. Many of the C_0 models developed in the last few decades were calibrated and validated against datasets that had measurements from only one (or two) cross-shore zones, e.g. the breaking zone only. Consequently, many of these models had not been validated for performance in multiple cross-shore zones where different transport patterns and mechanisms are present – as would be the case when being used for morphodynamic modelling. A concentration model that is only applicable to one cross-shore zone would have very limited uses in morphodynamic modelling studies.

In almost all existing C_0 models, substantial under-prediction was found particularly around the wave plunging point (point within breaking zone at which breaking wave plunges and surface generated turbulent kinetic energy, TKE, is injected into the water column) where strong localised increases in C_0 were observed. This sharp increase in concentration was attributed to strong plunging in regions of relatively low water depth (between bar crest and trough) which generated large-scale turbulent eddies invading the wave bottom boundary layer (WBBL) and entraining dense clouds of sediment near the plunging point. Reference concentration models that related C_0 to the local wave climate such as the local wave height (H), breaker height (H_b) or the local water depth (d) were generally not well suited for use in multiple cross-shore zones, as the cross-shore distribution of these parameters did not correlate well with the cross-shore distribution of C_0 . They were generally found to be adept for one or two tested near-shore regions at best, showing large discrepancies in alternative zones and requiring additional formulae or calibration constants for use in multiple regions. Alternatively, models that related C_0 to the sand pickup rate or Shields Parameter (i.e. depending on exerted bed shear exceeding critical bed shear for entrainment) were better suited for use in multiple cross-shore zones without additional formulae or constants, better capturing the cross-shore distribution of C_0 . Such models however failed to replicate the high levels of SSC found in the breaking zone. This is because these formulations were based on the implicit assumption that sediment entrainment is only induced by the local TKE generated by bed shear; not taking surface-generated breaking-induced TKE into account. This assumption was addressed in more recent literature, by including breaking-induced TKE into sediment pickup rate or reference

concentration formulations. Though latest studies have shown promising relationships between near-bed TKE (k_b) and reference concentration/sediment pickup, such formulations also face various limitations. These formulations are highly dependent on the accuracy of measured or modelled k_b and are also sensitive to the magnitude of k_b . For example, the magnitude of measured k_b was found to vary by a factor of 1.1-1.3 between regular and irregular wave conditions, with k_b being smaller under irregular wave conditions. This resulted in varied performance between datasets in k_b -driven reference concentration formulations. The Froude-scaled TKE produced smaller deviations in magnitude of TKE between datasets, suggesting that it may be a more suitable driving parameter for reference concentration models than k_b .

In a different study, 5 existing concentration profile ($C[z]$) models were validated against the same datasets used for the C_0 model validation. Existing $C[z]$ models were generally separated into exponential models and power function models. The exponential $C[z]$ models produced quasi-linear profiles on the log-scale, practically serving as a line-of-best-fit through the measured concentration profile. As measured profiles were generally parabolic (concave upward shaped), the quasi-linear profiles of the exponential models often did not accurately replicate the shape of the measured concentration profile, instead indicating relatively good agreement in the upper and lower water columns (top and bottom of concentration profile respectively) but showing significant discrepancies in the mid-water column. As suspended flux and transport rate computations are depth-averaged, large discrepancies in the mid-water column can lead to inaccurate estimations of the flux and transport rates. This is a greater issue when the reference concentration was poorly estimated, as $C[z]$ is a function of C_0 . Though all $C[z]$ formulae are highly sensitive to the performance of C_0 models, the exponential models were more so, as the reference concentration practically serves as the starting point for the line-of-best-fit. Analysis of the various existing $C[z]$ formulations were carried out with the base C_0 estimation being made using the newly proposed L19 C_0 model, which indicated best agreement with measured data (further discussed under Objective 2 below). Consequently, the aforementioned discrepancies found in the mid-water column for the exponential $C[z]$ models were relatively small and residual effects on subsequent suspended sand flux and transport rate computations were marginal.

The power function $C[z]$ formulae produced parabolic concentration profiles that better reflected the measured profiles. However, the power function formulae were found to be especially sensitive to the magnitude of the dimensionless mixing parameter M , which is a function of the balance between sediment entraining and settling forces. Both power function

$C[z]$ models tested in this thesis produced very steep (quasi-linear; vertical) concentration profiles, indicating good agreement in the lower water column (where lower water column agreement was dependent on the reference concentration estimation) but poor agreement in the upper water column. Again, the reference concentration was estimated with the L19 C_0 model which produced best agreement with measured C_0 . Had the estimation of C_0 been poor, the power function models would have shown poor agreement not only in the upper water column, but to a lesser extent in the lower water column also. The steep profiles produced by the power function formulae was attributed to the magnitude of M being too small. It was proposed that by increasing the overall magnitude of the mixing parameter, a smoother parabolic concentration profile shape could be obtained to better represent the measured profile. This hypothesis was tested in the modified $C[z]$ model (referred to as L19 $C[z]$ model), by increasing the magnitude of M , resulting in significantly improved performance in almost all tested cases. The drastic improvement and consistency of good agreement over the majority of test cases suggests that the physical processes accounted for in the power function formulae well-represent the forces in nature. Further details of the modified $C[z]$ formula is described under Objective 2.

RQ2) How can these limitations be addressed to produce more robust and accurate transport formulae for future use in morphodynamic modelling studies?

-OB2: To derive a new practical model that accurately predicts suspended sand transport patterns under breaking waves, and to validate it against existing models and measured data.

Based on the findings from OB1, it was concluded that future reference concentration models needed to be developed to be able to adequately predict the cross-shore suspended transport patterns for multiple cross-shore regions, especially in the breaking zone where SSC levels are highest. In response to the aforementioned limitations, a new practical reference concentration model was developed, incorporating key process understanding of sediment entrainment and settling forces, as well as a novel empirical relationship found between the reference concentration and the inverse of the local water depth. Additionally, a simple, yet unique method of increasing applicability of the newly proposed and existing reference concentration models to multiple cross-shore zones was provided by the implementation of the Omega (Ω) constant. This constant allows C_0 models that would otherwise only be adept for one or two

cross-shore zones (e.g. shoaling and inner surf zones) to be applied to any and all cross-shore zones by simply adjusting the value of Ω depending on the zone it is applied to.

The newly proposed L19 C_0 model was validated against the same state-of-the-art measured laboratory datasets that were used to validate the 6 existing reference concentration models, but validation was carried out using 106 test cases instead of 119, with 13 test cases being used for model calibration. Validation against the same datasets made it possible to directly compare and analyse the performance of the L19 model against alternative models. The L19 C_0 model showed good agreement with measured C_0 (with RMSE ranging between 0.36-1.79 kg/m³ over the different datasets), even at the plunging point where SSC was highest. The performance of the L19 C_0 model was better than all tested existing models, both qualitatively and quantitatively for all cross-shore regions, under regular and irregular breaking wave conditions, proving its robustness and applicability to multiple conditions.

The proposed L19 $C[z]$ model was a modification of the concentration profile model of Shibayama & Rattanapitikon (1993). As mentioned above, the existing power function $C[z]$ formulae produced very steep, quasi-linear profiles that indicated large discrepancies particularly in the upper water column. The existing model was modified by incorporating a constant (B) to the dimensionless mixing parameter (M). The B constant was calibrated against a few test cases from the aforementioned datasets. The small addition of the constant improved the performance of the $C[z]$ model drastically, indicating that the concentration profile was highly sensitive to mixing parameter (which is usually modelled after the well-known Rouse Number). The modified $C[z]$ formula combined with the newly proposed L19 reference concentration model were together referred to as the 'L19 model' and tested against 5 existing concentration profile models. Again, the modified $C[z]$ formula produced significantly improved predictions of the concentration profile, compared to both the original (unmodified) $C[z]$ model and also the alternative existing $C[z]$ models. The L19 concentration profile was more gradual than the original (unmodified) $C[z]$ model, showing good agreement with measured $C[z]$ throughout the whole water column in all cross-shore zones.

-OB3: To evaluate the applicability of the new and existing transport models to morphodynamic models and suggest methods of improvement.

As established under Objective 1, many of the existing transport models were not adept for use in multiple cross-shore zones. Unless a morphodynamic study is to be focused on a relatively

small region, limited to one cross-shore zone (e.g. only the barred region in the surf zone), many of the tested models would not be well suited for use in morphodynamic models. Most of the existing models also failed to adequately replicate the transport patterns (e.g. magnitude of SSC) in the breaking zone, leading to substantial discrepancies in subsequent flux and transport rate computations (refer to Objective 4 below). As the sand transport and morphodynamics are functions of the suspended sand flux and transport rates, such large discrepancies in the breaking zone must be addressed and accounted for in order to produce accurate estimations of morphological changes, particularly in the long-term.

Even if the magnitude of predicted SSC was corrected for the breaking zone, the bigger challenge lies in accounting for the different suspension mechanisms and transport patterns found in each of the cross-shore regions. Some effective methods of making models more applicable to multiple cross-shore regions are the ‘multiple formulae’ method (using more than one transport model, e.g. one for the shoaling zone and one for the surf zone) or the incorporation of measured or modelled near-bed TKE. Both methods have limitations that must be overcome before they can be implemented into morphodynamic models. The use of the simple Omega (Ω) constant (described under Objective 2 above) provides an immediate and practical method for use in accurately predicting suspended sand transport patterns under breaking waves, until more robust or process-based methods are developed.

The newly proposed L19 model accurately replicated the sand transport patterns for all tested cross-shore zones and conditions with the use of the Ω constant. The only (minor) challenges lie in the actual incorporation of the L19 model into morphodynamic models. Firstly, the implementation of different values of Ω require the user to determine the different cross-shore regions present at the study location, and secondly the user must decide whether the different values of Ω will be implemented manually (e.g. for each test run and/or time-step) or by programming. Determining the different cross-shore zones can be done quantitatively or qualitatively via numerous methods, ranging from crude methods of estimation based on bed profile or wave climate measurements, to more sophisticated quantitative methods involving the examination of wave surface elevation measurements. Implementing different values of Ω by programming is far more efficient and therefore recommended, particularly for morphodynamic studies covering medium- to long-term scales.

RQ3) To what extent do improvements to reference concentration and concentration profile models affect resulting computations of horizontal suspended flux and cross-shore transport rates?

-OB4: To investigate the extent to which the improvements to reference concentration and concentration profile models affect the prediction of cross-shore suspended sand transport rates.

The (extent of the) influence the improvements to C_0 and $C[z]$ models had on resulting horizontal suspended sand flux ($uC[z]$) and current-related suspended transport rate (q_{sc}) were investigated through a systematic evaluation divided into 3 parts. Part A focused on the performance of the L19 ($C_0 + C[z]$) model and its ability to accurately reproduce the measured q_{sc} . The L19 model was also tested against two existing models which are widely used in the field for sand transport and morphodynamic modelling. Part B focused on investigating the influence individual improvements to C_0 and $C[z]$ models had on resulting transport rate predictions, i.e. which of the components had a greater influence on the accurate prediction of transport rates.

Findings from Part A confirmed that improvements to C_0 and $C[z]$ models had significant effects on resulting computations of q_{sc} , with existing widely used models (that produced poor estimations of C_0 and/or $C[z]$) substantially underpredicting the current-related transport rate, particularly in the breaking zone where C_0 and $C[z]$ were also underpredicted. More thorough analysis in Part B showed that the cross-shore distributions of $uC[z]$ and q_{sc} were almost symmetrical across the x-axis to the cross-shore distributions of C_0 and the depth-averaged $C[z]$. This was the case (to varying extents) for all tested model combinations, suggesting that the relationship between C_0 , $C[z]$ and q_{sc} is quasi-linear. The relationship between these parameters is not inversely proportional however as differences in magnitude between the parameters differed. I.e. increases (decreases) in magnitude of $C[z]$ generally resulted in increases (decreases) in magnitude of $uC[z]$ and q_{sc} , but the increases (decreases) in magnitude of each of the parameters were not proportional. Regardless, it can be concluded that accuracy in the estimation of C_0 and/or $C[z]$ have direct effects on the computation of $uC[z]$ and q_{sc} .

Accurate predictions of both C_0 and $C[z]$ are essential to producing realistic estimations of the transport rate. When combining the widely used (less accurate) existing reference concentration models with the L19 $C[z]$ model (which produced the best agreement with measured data), resulting cross-shore distributions of depth-averaged $C[z]$, $uC[z]$ and q_{sc}

showed little resemblance to the measured profiles. This demonstrated that regardless of how well the vertical mixing and concentration profile is estimated, without an accurate estimation of C_0 the resulting flux and transport rate computations are inaccurate and unrealistic. Contrarily, when the L19 C_0 model (which produced best correlation with measured C_0) was combined with existing (less accurate) $C[z]$ models, resulting computations of suspended sand flux and transport rates closely resembled the measured values, with significant discrepancies only being found in the breaking zone. This suggested that the importance of improvements to $C[z]$ models were somewhat limited to the breaking zone where breaking-enhanced vertical mixing is highest. This was demonstrated by the L19 $C[z]$ model which showed much stronger agreement with measured data in the breaking zone than alternative models, but the difference in performance between the models was negligible in the shoaling and inner surf zones where vertical mixing levels are comparatively lower.

From these findings it is concluded that though improvements to both C_0 and $C[z]$ models are fundamental to enhancing the performance of current sediment transport and morphodynamic models, the development of C_0 models generally has a greater influence on the accurate estimation of all resulting parameters (e.g. $C[z]$, $uC[z]$ and q_{sc}) which are functions of the reference concentration. This affirms the significance of the development of transport models presented in this thesis, but in particular the newly developed L19 reference concentration model which resulted in improved estimations of not only C_0 , but also $C[z]$, $uC[z]$ and q_{sc} .

6.2. Recommendations for Further Study

Herein, some recommendations for further study are provided for the continual improvement of suspended sediment transport models for use in morphodynamic models.

- **Performance of models under different grain diameters:**

All sediment transport modelling carried out and presented in this thesis were focused on laboratory conditions that only consisted of medium sand with average grain diameter ranging between 0.22-0.25mm. As mentioned in the discussion section of this thesis, how the newly proposed L19 model and existing models perform with different grain diameters could be investigated.

- **Performance of models under wave groups:**

Another thing to be considered is the presence of wave groups and the effect they have on sediment transport processes, as in natural beaches waves will often approach in groups. All datasets used in this thesis consisted of single waves as opposed to wave groups, and the velocities and suspended sand concentration measurements from these single waves were time-averaged. There is however the concept of ‘intensification’ of sand suspension which occurs under groups of large waves. When multiple large waves pass over a certain location, the SSC can increase as there is sediment still in suspension when the subsequent wave comes. This occurs in single waves also, but more so under wave groups. Kosyan et al. (2007) reported that values of SSC under waves were several times larger in waves at the end of a wave group than corresponding values in similar waves at the beginning of the wave group. They also found that waves with the same wave height could have different concentration profiles depending on the wave position in the group. The performance of the L19 model and existing transport models could be tested under conditions with wave groups to examine the influence they have on SSC modelling.

- **Swash zone modelling:**

The analysis carried out in this thesis was focused on the nearshore region between the shoaling and inner-surf zones. How these models perform in the swash zone and whether or not they need modifications/additional models for use in the swash zone has not been investigated. In particular, if the L19 model is to be incorporated into morphodynamic models to predict nearshore change, it will have to incorporate the swash zone also. As the swash zone is highly turbulent, modelling sediment transport patterns within the swash zone remain challenging. Future efforts could be focused on extending the applicability of the L19 model (or alternative models) to be adept for use in all nearshore zones, including the shoaling, breaking, inner-surf and swash zones.

- **Implementation into morphodynamic models:**

Results from this thesis have indicated that the improvements of C_0 and $C[z]$ models are essential to producing realistic estimations of suspended flux and transport rate patterns. The extent to which they influence consequent morphodynamic predictions however is yet untested. As the nature of morphological change is non-linear and vastly complex, it would be beneficial to see just how much improvements to constituent sediment transport models influence

morphodynamic modelling, in the short-, medium- and long-term. This will help future researchers to make more informed decisions on whether it is worthwhile (and how much so) to invest more time in continuing to improve sediment transport models, or if it would be better to invest time and resources into the development of alternative areas of morphodynamic modelling.

Acknowledgements

First and foremost, I would like that give all thanks and glory to my Lord, Jesus Christ, without whom I would not have even considered embarking on this journey in academia, let alone completing a PhD. The last four years have been nothing short of an adventure, with periods of great joy and breakthroughs, but also times of difficulty and stress. But by the grace of God I have grown not only as a researcher, but as a person; learning not only about the field of coastal engineering, but also important lessons and skills that will stay with me the rest of my life.

I would like to thank Dr. Ravindra Jayaratne, my Director of Studies. He helped me to obtain funding for the first three years of my PhD. He also served as a mentor, guiding me through the academia path and helping me to find clear direction when I was swamped with information. A special thanks is given to Dr. John Walsh of UEL. Though not an official supervisor for my PhD, he has been there every step of the way, freely providing helpful comments and advice over the years. Thank you both for all the time and effort you have put in to help me get to where I am today. Gratitude is expressed to Dr. David Tann and Dr. Carlos de Luna who helped over the years to obtain funding for software packages, as well as oversea applications for conferences.

I gratefully acknowledge Professor Tomoya Shibayama of Waseda University as he has helped to co-author papers and shared comments, data and resources with me over the years. A special thanks is also given to Dr. Joep van der Zanden of the Maritime Research Institute Netherlands who freely shared his data, research, ideas and concerns with me over the years. His comments and suggestions were greatly helpful in the producing of my first journal paper and his clear and concisely written research papers have been of great benefit for me in understanding complex processes over the years. My gratitude is also extended to Professor Harshinie Karunarathna of Swansea University, whose comments and suggestions were very helpful in refining and improving my thesis and journal paper.

I cannot forget my family, my girlfriend, and my brothers and sisters in Christ who have supported me every step of the way. Your prayers and moral support have helped to keep me going when I was going through periods of doubt and difficulty. Truly, I could not have done it without your help. Thank you all so very much!

References

- Aagaard, T. and Hughes M.G., 2010. Breaker turbulence and sediment suspension in the surf zone. *Marine Geology* 271, 250-259.
- Aagaard, T. and Jensen, S.G., 2013. Sediment concentration and vertical mixing under breaking waves. *Marine Geology* 336, 146-159.
- Aagaard, T., Hughes, M.G. and Ruessink, G., 2018. Field observations of turbulence, sand suspension and cross-shore transport under spilling and plunging breakers. *Journal of Geophysical Research: Earth Surface*.
- Austin, M.J., Masselink, G., O'Hare, T.J. and Russel, P.E., 2009. Onshore sediment transport on a sandy beach under varied wave conditions: Flow velocity skewness, wave asymmetry or bed ventilation? *Marine Geology*, 259, 86-101.
- Barbaro, G., Malara, G., Martino, M.C., and Arena, F., 2010. Analytical development of a one-line model for the analysis of shoreline change by wind generated waves. *The Open Ocean Engineering Journal*, 3, 108-115.
- Beach, R.A. and Sternberg, R.W., 1996. Suspended-sediment transport in the surf zone: Response to breaking waves. *Continental Shelf Research* 16(15), 1989-2003.
- Benedet, L., Dobrochinski, J.P.F., Walstra, D.J.R., Klein, A.H.F. and Ranasinghe, R., (2016). A morphological modeling study to compare different methods of wave climate schematization and evaluate strategies to reduce erosion losses from a beach nourishment project. *Coastal Engineering*, 112, 69-86.
- Bijker, E. W., 1967. Some considerations about scales for coastal models with moveable bed. Tech. Rep. 50, WL | Delft Hydraulics, Delft, The Netherlands.
- Birkemeier, W.A., and Thornton, E.B., 1994. The DUCK94 nearshore field experiment. *Proceedings of Coastal Dynamics Conference*, 815-821.
- Brand, E., De Sloover, L., De Wulf, A., Montreuil, A.L., Vos, S. and Chen, M., 2019. Cross-Shore Suspended Sediment Transport in Relation to Topographic Changes in the Intertidal Zone of a Macro-Tidal Beach (Mariakerke, Belgium). *Journal of Marine Science and Engineering*, 7(6), 172.

Brand, E., Montreuil, A.L., Houthuys, R., and Chen, M., 2020. Relating hydrodynamic forcing and topographic response for tide-dominated sandy beaches. *Journal of Marine Science and Engineering*, 8, 151.

Brinkkemper, J.A., Lanckriett, T., Grasso, F., Puleo, J.A. and Ruessink, B.G., 2016. Observations of turbulence within the surf and swash zone of a field-scale sandy laboratory beach. *Coastal Engineering* 113, 62-72.

Brown, J. and Davies, A.G, 2009. Methods for medium-term prediction of the net sediment transport by waves and currents in complex coastal regions. *Continental Shelf Research*, 29, 1502-1514.

Cáceres, I., Alsina, J.M., Van der Zanden, J., Van der A, D.A., Ribberink, J.S., and Sánchez-Arcilla, A., 2020. The effect of air bubbles on optical backscatter sensor measurements under plunging breaking waves. *Coastal Engineering* 159, 103721.

Camenen, B. and Larson, M., 2008. A general formula for non-cohesive suspended sediment transport. *Journal of Coastal Research* 24(3), 615-627.

Carini, R.J., Chickadel, C.C., Jessup, A.T., and Thomson, J., 2015. Estimating wave energy dissipation in the surf zone using thermal infrared imagery. *Journal of Geophysical Research Oceans*, 120.

Christensen, D.F., Brinkkemper, J., Ruessink, G. and Aagaard, T., 2019. Field observations of intra-wave sediment suspension and transport in the intertidal and shallow subtidal zones. *Marine Geology* 413, Elsevier, 10-26.

Cox, D. T. and Kobayashi, N., 2000. Identification of intense, intermittent coherent motions under shoaling and breaking waves. *Journal of Geophysical Research-Oceans* 105(C6): 14223-14236.

Dabees, M., and Kamphuis, J.W., 1998. Online, a numerical model for shoreline change. *Proceedings of 26th International Conference on Coastal Engineering*, 2668-2681.

Dally, W.R., Dean, R.G., Dalrymple, R.A., 1985. Wave height variation across beaches of arbitrary profile. *Journal of Geophysical Research, Oceans*, 90.

- Dam, G., van der Wegen, M., Labeur, R.J., and Roelvink, D., 2016. Modeling centuries of estuarine morphodynamics in the Western Scheldt estuary, *Geophysical Research Letters*, 43, 3839–3847,
- Dastgheib, A., 2012. Long-term process-based morphological modeling of large tidal basins. Ph.D. Thesis, IHE Delft and Delft University of Technology, Delft, The Netherlands.
- De Serio, F. and Mossa, M., 2019. Experimental observations of turbulent events in the surfzone. *Journal of Marine Science and Engineering*, 7, 332.
- De Vriend, H., Capobianco, M., Cheshier, T., De Swart, H.D., Latteux, B., Stive, M., 1993. Approaches to long-term modelling of coastal morphology: a review. *Coastal Engineering* 21.
- Dean, R.G., 1977. Equilibrium beach profiles: U.S. Atlantic and Gulf Coasts. Ocean Engineering Report No. 12, Department of Civil Engineering, University of Delaware, Newark, DE.
- Deigaard, R., Fredsoe, J., 1989. Shear stress distribution in dissipative water waves. *Coastal Engineering* 13, 357–378.
- Deigaard, R., Fredsoe, J., and Broker-Hedegaard, I., 1986. Suspended sediment in the surf zone. *Journal of Water, Port, Coastal and Ocean Engineering*, 112(1).
- Dronen, N., and Deigaard, R., 2007. Quasi-three-dimensional modelling of the morphology of longshore bars. *Coastal Engineering* 54, 197-215.
- Durgesh, V., Thomson, J., Richmond, M.C., and Polagye, B.L., 2014. Noise correction of turbulent spectra obtained from acoustic doppler velocimeters. *Flow Measurement and Instrumentation* 37, 29-41.
- Elias, E., Teske, R., van der Spek, A. and Lazar, M., 2015. Modelling tidal-inlet morphodynamics on medium time scales. *Proceedings of the Coastal Sediments 2015*, San Diego, California, USA.
- Engelund, F. and E. Hansen, 1967. A monograph on Sediment Transport in Alluvial Streams. Teknisk Forlag, Copenhagen.

Fernandez-Mora, A., Ribberink, J.S., van der Zanden, J., van der Werf, J.J., and Jacobsen, N.G., 2016. RANS-VOF modelling of hydrodynamics and sand transport under full-scale non-breaking and breaking waves. Proceedings of the 35th Conference on Coastal Engineering. Antalya, Turkey.

Fromant, G., Hurther, D., van der Zanden, J., Van der A, D.A., Cáceres, I., O'Donoghue, T., and Ribberink, J.S., 2019. Wave boundary layer hydrodynamics and sheet flow properties under large-scale plunging-type breaking waves. *Journal of Geophysical Research: Oceans*, 124.

Grasmeijer, B., 2002. Process-based cross-shore modelling of barred beaches. Ph.D Thesis. Department of Physical Geography, University of Utrecht, The Netherlands.

Grasso, F., Castelle, B. and Ruessink, G., 2012. Turbulence dissipation under breaking waves and bores in a natural surf zone. *Continental Shelf Research* 43, 133-141.

Grunnet, N.M, Walstra, D.J.R and Ruessink, B.G., 2004. Process-based modelling of a shoreface nourishment. *Coastal Engineering* 51, 581–607.

Hanson, H., Aarninkhof, S., Capobianco, M., Jimenez, J.A., Larson, M., Nicholls, R.J., Plant, N.G., Southgate, H.N., Steetzel, H. J., Stive, M.J.F. and de Vriend, H.J., (2003). Modelling of Coastal Evolution on Yearly to Decadal Time Scales. *Journal of Coastal Research*, 19(4).

Hanson, H., and Kraus, N.C., 2004. Advancements in One-Line Modeling of T-Head Groins: GENESIS-T. *Journal of Coastal Research, Special Issue* 33, 315-323

Hsu, T.J., and Liu, P.L.F., 2004. Toward modelling turbulent suspension of sand in the nearshore. *Journal of Geophysical Research: Oceans*, 109(C6).

Hsu, W.Y., Huang, Z.C., Na, B., Chang, K.A., Chuang, W.L., Yang., R.Y., 2019. Laboratory observation of turbulence and wave shear stresses under large scale breaking waves over a mild slope. *Journal of Geophysical Research: Oceans*, 124(4).

Isobe, M. and K. Horikawa, 1982. Study on water particle velocities of shoaling and breaking waves. *Coastal Engineering in Japan*, 25: 109–123.

Jaffe, B.E., Sternberg, R.W., Sallenger, A.H., 1984. The role of suspended sediment in shore normal beach profile changes. Proceedings 19th International Conference on Coastal Engineering, 1983-1996.

Jayarathne, M.P.R. and Shibayama, T., 2007. Suspended sediment concentration on beaches under three different mechanisms. Coastal Engineering Journal, 49(04), 357-392.

Jayarathne, R., Takayama, Y. and Shibayama, T., 2012. Applicability of suspended sediment concentration formulae to large-scale beach morphological changes. Proceedings of 33rd International Conference on Coastal Engineering, 1(33).

Jones, O.P., Petersen, O.S. and Kofoed-Hansen, H., 2007. Modelling of complex coastal environments: Some considerations for best practise. Coastal Engineering 54, 717–733.

Kana, T.W., 1978. Surf zone measurements of suspended sediment. Proceedings of 16th Conference on Coastal Engineering, Hamburg, Germany, 1725-1743.

Kana, T.W., 1979. Suspended sediment in breaking waves; Technical Report No. 18-CRD. University of South Carolina, Columbia, 153.

Karunaratna, H., Horrillo-Caraballo, J.M. and Reeve, D.E., 2012. Prediction of cross-shore beach profile evolution using a diffusion type model. Continental Shelf Research, 48, 157-166.

Karunaratna, H., Horrillo-Caraballo, J.M., Burningham, H., Pan, S., and Reeve, D.E., 2016. Two-dimensional reduced-physics model to describe historic morphodynamic behaviour of an estuary inlet. Marine Geology 382, 200-209.

Karunaratna, H., Horrillo-Caraballo, J.M., Spivack, M., and Reeve, D.E., 2011. Analysis of key parameters in a diffusion type beach profile evolution model. Continental Shelf Research, 31, 98-107.

Karunaratna, H., Reeve, D.E. and Spivack, M., 2009. Beach profile evolution as an inverse problem. Continental Shelf Research, 29, 2234-2239.

Klonaris, G.T., Memos, C.D., Drønen, N.K. and Deigaard, R., 2018. Simulating 2DH coastal morphodynamics with a Boussinesq-type model, Coastal Engineering Journal.

Kobayashi, N., Zhao, H., and Tega, Y., 2005. Suspended sand transport in surf zones. *Journal of Geophysical Research*, 110, C12009.

Kos'yan, R.D., Krylenko, M.V., and Vincent, C.E., 2007. Fluctuations of instantaneous vertical distribution of suspended sediment in the surf zone. *Proceedings of 30th International Conference on Coastal Engineering*, 2524-2536.

Kriebel, D.L., Kraus, N.C., and Larson, M., 1991. Engineering methods for predicting beach profile response. *Proceedings of Coastal Sediments '91*, Reston, VA, 557-571

Larson, M., Kraus, N.C., 2001. Estimation of suspended sediment trapping ratio for channel infilling and bypassing. *Coastal Engineering Technical Note CETN-IV-34*. U.S. Army Engineer Research and Development Center, Vicksburg, Mississippi, 9.

Latteux, B., 1995. Techniques for long-term morphological simulation under tidal action. *Marine Geology* 126, 129-141.

Lesser, G., 2009. An approach to medium-term coastal morphological modelling. Ph.D Thesis, IHE Delft and Delft University of Technology, Delft, The Netherlands.

Lesser, G.R., Roelvink, J.A., van Kester, J.A.T.M., Stelling, G.S., 2004. Development and validation of a three-dimensional morphological model. *Coastal Engineering* 51 (8-9), 883-915.

Li, M., Fernando, P.T., Pan, S., O'Connor, B.A. and Chen, D., 2007. Development of a quasi-3d numerical model for sediment transport prediction in the coastal region. *Journal of Hydro-environment Research* 1, 143-156.

Lim, G., Jayaratne, R. and Shibayama, T. (2020): Suspended Sand Concentration Models under Breaking Waves: Evaluation of New and Existing Formulations. *Marine Geology* 426, 106197.

Liu, J.H., Yang, S.L., Zhu, Q., and Zhang, J., 2014. Controls on suspended sediment concentration profiles in the shallow and turbid Yangtze Estuary. *Continental Shelf Research*, 90, 96-108.

Luijendijk, A.P., de Schipper, M.A. and Ranasinghe, R., 2019. Morphodynamic acceleration techniques for multi-timescale predictions of complex sandy interventions. *Journal of Marine Science and Engineering*, 7, 78.

Luijendijk, A.P., Ranasinghe, R., de Schipper, M.A., Huisman, B.A., Swinkels, C.M., Walstra, D.J. and Stive, M.J., 2017. The initial morphological response of the Sand Engine: A process-based modelling study. *Coastal Engineering*, 119, 1–14,

Masselink, G., Austin, M.J., O'Hare, T.J. and Russell, P.E., 2007. Geometry and dynamics of wave ripples in the nearshore zone of a coarse sandy beach. *Journal of Geophysical Research: Oceans*, 112(C10).

Meyer-Peter, E. and R. Müller, 1948. Formulas for bed load transport. *Proceedings of the 2nd Congress IAHR, Stockholm*, 2, 39–64.

Miles, J. and Thorpe, A., 2015. Bedform contributions to cross-shore sediment transport on a dissipative beach. *Coastal Engineering*, 98, 65-77.

Mocke, G.P., and Smith, G.G., 1992. Wave breaker turbulence as a mechanism for sediment suspension. *Proceedings of the 23rd International Conference on Coastal Engineering, Venice, Italy*.

Mori, N., Suzuki, T., and Kakuno S., 2007, Experimental study of air bubbles and turbulence characteristics in the surf zone. *Journal of Geophysical Research: Oceans*, 112.

Nadaoka, K., Hino, M. and Koyano, Y., 1989. Structure of the turbulent-flow field under breaking waves in the surf zone. *Journal of Fluid Mechanics* 204, 359-387.

Nairn, R.B., Roelvink, J.A., Southgate, H.N., 1990. Transition zone width and implications for modelling surf-zone hydrodynamics. *Proceedings of 22nd Conference on Coastal Engineering, Delft, The Netherlands*, 68–81.

Nielsen, P., 1984. Field-Measurements of Time-Averaged Suspended Sediment Concentrations under Waves. *Coastal Engineering*, 8(1), 51-72.

Nielsen, P., 1986. Suspended Sediment Concentrations under Waves. *Coastal Engineering*, 10(1), 23-31.

- Nielsen, P., 1992. Coastal Bottom Boundary Layers and Sediment Transport. Singapore: World Scientific, 324.
- Ogston, A.S. and Sternberg, R.W., 2002. Effect of wave breaking on sediment eddy diffusivity, suspended-sediment and longshore sediment flux profiles in the surf zone. *Continental Shelf Research* 22(4): 633-655.
- Okayasu, A., 1989. Characteristics of Turbulence Structure and Undertow in Surf Zone, Ph.D Dissertation, University of Tokyo, 53-112.
- Okayasu, A., Fujii, K., & Isobe, M. 2010. Effect of external turbulence on sediment pickup rate. *Proceedings of the 32nd International Conference on Coastal Engineering*.
- Otsuka, J., Saruwatari, A., Watanabe, Y., 2017. Vortex-induced suspension of sediment in the surf zone. *Advances in Water Resources*, 110, 59-76.
- Pang, W., Dai, Z., Ma, B., Wang, J., Huang, H., and Li, S., 2020. Linkage between turbulent kinetic energy, waves and suspended sediment concentrations in the nearshore zone. *Marine Geology*, 425, 106190.
- Peregrine, D.H. and Svendsen, I.A., 1978. Spilling breakers, bores and hydraulic jumps, *Proceedings of 16th Conference on Coastal Engineering* 1, 540-550.
- Putzar, B. and Malcherek, A., 2014. Modelling of Sediment Transport and Morphodynamics. *Die Kuste* 81, 89-106.
- Ranasinghe, R., Swinkels, C.M., Lujendijk, A.P., Roelvink, J.A., Bosboom, J., Stive, M.J.F. and Walstra, D.J.R., 2011. Morphodynamic upscaling with the MORFAC approach: Dependencies and sensitivities. *Coastal Engineering*, 58, 806–811.
- Rattanapitikon, W., and Shibayama, T., 1998. Energy dissipation model for regular and irregular breaking waves, *Coastal Engineering Journal*, 40(4), 327–346.
- Razaz, M., and Kawanisi, K., 2011. Despiking high-resolution ADCP data. *Journal of Japan Society of Civil Engineers, Series B1 (Hydraulic Engineering)*, 67(4), 217-222.

Reeve, D.E., Karunaratna, H., Pan, S., Horrillo-Caraballo, J.M., Różyński, G., and Ranasinghe, R., 2016. Data-driven and hybrid coastal morphological prediction methods for mesoscale forecasting. *Geomorphology* 256, 49-67.

Ribberink, J., Van der A, D., Van der Zanden, J., O'Donoghue, T., Hurther, D., Cáceres, I. and Thorne, P., 2014. Sandt-Pro: Sediment transport measurements under irregular and breaking waves, *Proceedings of 34th Conference on Coastal Engineering*, 1(34).

Roelvink, J.A., Reniers, A.J.H.M., 1995. LIP 11D Delta Flume experiments, A data set for profile model validation. Report H2130, Delft Hydraulics, The Netherlands.

Rouse, H., 1939. Experiments on the Mechanics of Sediment Suspension. *Proceedings of the 5th International Congress for Applied Mechanics*. New York, 550-554.

Ruessink, B. G., K. T. Houwman, and P. Hoekstra (1998), The systematic contribution of transporting mechanisms to the cross-shore sediment transport in water depths of 3 to 9 m, *Marine Geology*, 152, 295–324.

Russell, P.E., 1993. Mechanisms for beach erosion during storms. *Continental Shelf Research*, 13, 1243–1266.

Sanchez, A., Brown, M., Beck, T., Styles, R. and Li, H., 2015. Long-term morphological modeling at Coastal inlets. *Proceedings of the Coastal Sediments 2015*, San Diego, California, USA.

Sato, S., Homma, K. and Shibayama, T., 1990. Laboratory study on sand suspension due breaking waves. *Coastal Engineering in Japan*, 33(2), 219–231.

Scott, C. P., Cox, D.T., Maddux, T.B. and Long, J.W., 2005. Large-scale laboratory observations of turbulence on a fixed barred beach. *Measurement Science and Technology* 16(10): 1903-1912.

Shibayama, T., and Rattanapitikon, W., 1993. Vertical distribution of suspended sediment concentration in and outside surf zone. *Coastal Engineering in Japan*, 36(1), 49–65.

Smith, G.G., & Mocke, G.P. 1993. Sediment suspension by turbulence in the surf zone. *Proceeding of Euromech 1993*, Le Havre, France.

- Spielmann, K., Astruc, D., & Thual, O. 2004. Analysis of some key parametrizations in a beach profile morphodynamical model. *Coastal Engineering*, 51(10), 1021-1049.
- Sumer, B.M., Guner, H.A.A., Hansen, N.M., Fuhrman, D.R. and Fredsøe, J., 2013. Laboratory observations of flow and sediment transport induced by plunging regular waves. *Journal of Geophysical Research: Oceans* 118(11): 6161-6182.
- Sun, Z., Zheng, H., Xu, D., Hu, C., and Zhang, C., 2020. Vertical concentration profile of non-uniform sediment. *International Journal of Sediment Research*.
- Svendsen, I.A. 1984. Wave Heights and Setup in a Surf-zone. *Coastal Engineering* 8, 303-329.
- Svendsen, I.A., Madsen, P.A. and Buhr Hansen, J., 1978. Wave characteristics in the surf zone. *Proceedings of 16th Conference on Coastal Engineering*, 520-539
- Swart, D.H., 1974. Offshore sediment transport and equilibrium beach profiles. Delft Hydraulic Lab., The Netherlands, 131, 1–244.
- Thornton, E.B. and Guza, R.T. 1983. Transformation of wave height distribution. *Journal of Geophysical Research* 88(C10), 5925.
- Ting, F.C.K. and Kirby, J.T., 1994. Observation of Undertow and Turbulence in a Laboratory Surf Zone. *Coastal Engineering* 24(1-2): 51-80.
- Ting, F.C.K. and Kirby, J.T., 1995. Dynamics of surf-zone turbulence in a strong plunging breaker. *Coastal Engineering* 24(3-4), 177-204.
- van der A, D. A., van der Zanden, J., O'Donoghue, T., Hurther, D., Cáceres, I., McLelland, S.J. and Ribberink, J.S., 2017. Large-scale laboratory study of breaking wave hydrodynamics over a fixed bar. *Journal of Geophysical Research: Oceans*, 122, 3287–3310.
- Van der A, D.A., Ribberink, J.S., Van der Werf, J.J., O'Donoghue, T., Buijsrogge, R.H., Kranenburg, W.M., 2013. Practical sand transport formula for non-breaking waves and currents. *Coastal Engineering*, 76, 26–42.

van der Wegen, M., and Roelvink, J.A., 2008. Long-term morphodynamic evolution of a tidal embayment using a two-dimensional, process-based model, *Journal of Geophysical Research: Oceans*, 113, C03016.

van der Werf, J. J., van Veen, R., Ribberink, J. S., & van der Zanden, J. 2015. Testing of the new SANTOSS transport formula in the Delft3D morphological modelling system. *Proceedings of the Coastal Sediments 2015*, San Diego, USA (1-14).

van der Zanden, J., 2016. Sand transport processes in the surf and swash zones. Ph.D Thesis, University of Twente, Netherlands.

Van der Zanden, J., Fernandez-Mora, A., Van der A, D.A., Hurther, D., Cáceres, I., O'Donoghue, T., and Ribberink, J.S., 2017c. Inclusion of wave breaking turbulence in reference concentration models. *Proceedings of Coastal Dynamics 2017*. Helsingor, Denmark. 14, 629-641.

van der Zanden, J., van der A, D.A., Cáceres, I., Hurther, D., McLelland, S.J., Ribberink, J.S. and O'Donoghue, T., 2018. Near-bed turbulent kinetic energy budget under a large-scale plunging breaking wave over a fixed bar. *Journal of Geophysical Research: Oceans*, 123,

van der Zanden, J., van der A, D.A., Cáceres, I., Larsen, B.E., Fromant, G., Petrotta, C., Scandura, P., and Li, M., 2019. Spatial and temporal distributions of turbulence under bichromatic breaking waves. *Coastal Engineering*, 146, 65-80.

van der Zanden, J., van der A, D.A., Hurther, D., Cáceres, I., O'Donoghue, T., and Ribberink, J.S., 2016. Near-bed hydrodynamics and turbulence below a large-scale plunging breaking wave over a mobile barred bed profile. *Journal of Geophysical Research: Oceans*, 121(8), 6482-6506.

van der Zanden, J., van der A, D.A., Hurther, D., Cáceres, I., O'Donoghue, T., Hulscher, S.J.M.H. and Ribberink, J.S., 2017a. Bedload and suspended load contributions to breaker bar morphodynamics. *Coastal Engineering*, 129, 74–92.

van der Zanden, J., van der A, D.A., Hurther, D., Cáceres, I., O'Donoghue, T., and Ribberink, J.S. 2017b. Suspended sediment transport around a large-scale laboratory breaker bar. *Coastal Engineering*, 125, 51–69.

van Rijn, L. C., 1993. Principles of sediment transport in rivers, estuaries and coastal seas. The Netherlands: Aqua Publications, 831.

van Rijn, L.C., 1984. Sediment Transport, Part II: Suspended Load Transport. *Journal of Hydraulic Engineering*, 110(11), 1613-1641.

van Rijn, L.C., 1993. Principles of Sediment Transport in Rivers, Estuaries and Coastal Seas. Aqua Publications, The Netherlands.

van Rijn, L.C., 2007. Unified View of Sediment Transport by Currents and Waves. II: Suspended Transport. *Journal of Hydraulic Engineering*, 133(6), 668-689.

van Rijn, L.C., Ribberink, J.S., van der Werf, J., and Walstra, D.J.R., 2013. Coastal sediment dynamics: recent advances and future research needs. *Journal of Hydraulic Research* 51(5): 475-493.

van Rijn, L.C., Ruessink, B.G. and Mulder, J.P.M., 2002. Coast3DEgmond; the behaviour of a straight sandy coast on the time scale of storms and seasons. Deltares, Delft, The Netherlands.

Voulgaris, G. and Collins, M.B., 2000. Sediment resuspension on beaches: response to breaking waves. *Marine Geology* 167, 167-187.

Walstra, D.J., Hoekstra, R., Tonnon, P. and Ruessink, G., 2013. Input reduction for long-term morphodynamic simulations in wave-dominated coastal settings. *Coastal Engineering*, 77, 57-70.

Wang, L., Zimmermann, N., Trouw, K., de Maerschalck, B. and Vanlede, J., 2014. Numerical modelling of long-term morphology in the surf zone of the Belgian coast. *Proceedings of the International Conference on Coastal Engineering*, 1(34).

Wang, P., Yuan, W., Min, L., 2012. Measuring and modelling suspended sediment concentration profiles in the surf zone. *Journal of Palaeogeography*, 1(2), 172-193.

Wang, P., Smith, E. R., Ebersole, B. A., 2002. Large-scale laboratory measurements of longshore sediment transport under spilling and plunging breakers. *Journal of Coastal Research*, 18: 118-135.

Williams, B.G., 2016. On the Medium-Term Simulation of Sediment Transport and Morphological Evolution in Complex Coastal Areas. Ph.D Thesis, Plymouth University, UK.

Yoon, H.D. and Cox, D.T., 2010. Large-scale laboratory observations of wave breaking turbulence over an evolving beach. *Journal of Geophysical Research: Oceans* 115(C10).

Yoon, H.D. and Cox, D.T., 2012. Cross-shore variation of intermittent sediment suspension and turbulence induced by depth-limited wave breaking. *Continental Shelf Research*.

Yoon, H.D., Cox, D.T. and Mori, N., 2015. Parameterization of time-averaged suspended sediment concentration in the nearshore. *Water* 7(11), 6228-6243.

Yu, Y., Sternberg, R.W. and Beach, R.A., 1993. Kinematics of breaking waves and associated suspended sediment in the nearshore zone. *Continental Shelf Research*, 13(11), 1219-1242.

Zhong, C., Yin, F., Zhang, J., Zhang, S., Wan, R., and Kitazawa, D., 2020. Optimized Algorithm for Processing Outlier of Water Current Data Measured by Acoustic Doppler Velocimeter. *Journal of Marine Science and Engineering* 8(9):655.

Appendix A

Herein some additional information is provided regarding the modelling of long-term morphodynamics and recent advancements in overcoming previous practical limitations.

Morphological Acceleration & Input Reduction Techniques

One of the biggest limitations regarding process-based medium- to long-term beach morphological predictions is the high computational costs (both CPU power and simulation run times) involved in running such simulations. Significant bed evolution often occurs over months, years, decades or even centuries and accurately modelling these morphological changes requires realistic simulations of the flow and sediment transport field as well as flow perturbations resulting from bed changes (Latteux, 1995). The morphological changes of interest however often occur over timescales that are several orders of magnitude larger than that of the fluctuations in hydrodynamic forces that drive the morphological changes (Lesser, 2009). This difference in temporal scales increases the computational costs – this is further explained under the sub-section Morphological Acceleration Factor (morfac), later in this section. Reducing the computational costs of such simulations has been the focus of many research projects (e.g. Latteux, 1995; Grunnet et al., 2004; Jones et al., 2007; Lesser et al., 2009; Brown & Davies, 2009; Ranasinghe et al., 2011; Walstra et al., 2013; Benedet et al., 2016; Luijendijk et al., 2017; 2019). There have been studies overviewing various strategies for reducing computational costs in long-term morphological simulations (e.g. de Vriend, 1993; Latteux, 1995; Lesser, 2009). The most commonly used and well-validated methods of reducing computational times in recent literature involve 1) increasing abstraction – e.g. model or input reduction and/or the use of 2) morphological acceleration factors (morfac) to bridge the gap in temporal scales between hydrodynamic forcing and resulting morphological changes. This section gives descriptions of various methodologies for reducing computational costs, with focus on input reduction methods and also the use of morphological acceleration factors.

Input Reduction

Input reduction techniques are methods used to produce a reduced or limited set of optimized, representative forcing conditions which are capable of reproducing the morphodynamic changes predicted using the original (full) time-series (de Vriend et al., 1993; Walstra et al., 2013). There are a range of different techniques that can be applied to different forcing conditions. These techniques are commonly used in reduction of wave, wind and tidal forcing

conditions. The input data can be schematized using various methods to produce representative forcing conditions – some of these methods are described below for predominant driving forces that are known to drive long-term morphology. The overall outcome and quality of predictions can be influenced by the method of input reduction applied. Therefore, it is important to verify all simulations (that are run using input reduction techniques) against an accurate benchmark (e.g. ‘Brute Force’) simulation that has had input reduction methods implemented.

Tidal Input Reduction

The astronomical tide is deterministic – meaning the global climate of tidal currents, as well as its evolution in time, can be predicted with a relatively high level of precision (Latteux, 1995). This simplifies the task of tidal input reduction considerably, as it does not require the use of any past measurements or analysis, unlike wave or wind data. There are however large fluctuations in the tidal levels and therefore in the resulting currents. Computing the complex current field, residual sediment transport and morphological change for all tidal measurements in a given study time period can be computationally expensive. The objective of tidal input reduction, therefore, is to reduce the time-series of tidal data to just one or a few representative tide(s). The representative tide(s) should be carefully selected so that it would produce residual sediment transport and morphological change patterns as close to the full data range as possible. Latteux (1995) reported that in cases with simple bed and coastal topography, a single representative tide could be applied, working in a similar way to the average effect of the full set of tidal data. However, in more complex scenarios, Latteux (1995) recommended using two (or three) representative tides – e.g. one around mean or neap tidal range and one around spring (Lesser, 2009). One other thing that must be considered when selecting the representative tide(s) is whether or not there is any non-random phasing between tides and other driving forces such as waves and/or wind. If there is such non-random phasing, this must be taken into consideration when implementing input reduction techniques and selecting representative forcing values (Lesser, 2009). For example, tidal forcing could have an indirect, residual influence on the wave climate that is visible in the simulations. Therefore, in such cases, this phasing would need to be incorporated into the respective input reduction processes. When a suitable representative tide (also sometime referred to as a ‘morphological tide’ in literature, e.g. Grunnet et al., 2004) has been found, harmonic analysis is carried out and the harmonic components are applied to the water level boundaries.

Wave Input Reduction

Wave input reduction, similar to tidal input reduction, aims to reduce the full wave climate into a set of representative wave conditions. Different methods of reducing the input conditions produce different numbers of representative conditions. The total weight applied to each condition can also vary depending on the applied method. Some wave input reduction techniques include using the energy flux method, weighted mean (e.g. Brown & Davies, 2009; Walstra et al., 2013), the OPTI-routine method (e.g. Lesser, 2009; Benedet et al., 2016), the OPTI-wave method (Williams, 2016), etc. The majority of the wave input reduction techniques are generally based on the characteristics of the wave climate (e.g. mean, frequency of occurrence), but some studies use methods that are based on sediment transport calculations and patterns (e.g. Grunnet et al., 2004). The latter of these categories obtain a set of representative conditions that can accurately model the sediment transport patterns computed from the full data set – similar to that seen in the tidal input reduction section. Some notable studies in wave input reduction are the studies of Benedet et al., (2016) who present findings from a comparison study of the performance of 5 commonly used wave schematisation methods, and Walstra et al. (2013) who investigated the effects of aggregation level, bin size, wave chronology, varying morfac, etc.

One important factor to consider, regardless of the method of wave schematization, is the extent of the effects of wave chronology. For example, Walstra et al., (2013) carried out some tests using two sets of schematized wave input data: 1) the first was a reconstructed (or aggregate) time-series which kept the original wave chronology (c.f. Brown & Davies, 2009) and 2) and the second was a synthetic time-series where wave chronology is ignored (e.g. Grunnet et al., 2004). Both options provide advantages and disadvantages, for example the synthetic time-series allows for varying morfac values to be applied, which could further reduce computational times. It was recommended however that careful investigations are carried out to identify the extent to which wave chronology has an effect on the chosen test location before attempting to use a synthetic time-series. Lesser (2009) also found that aside from the daily (or shorter-term) wave chronology, the effects of annual and seasonal wave chronology were considerable to varying extents.

Wind Input Reduction

In coastal area modelling suites such as Delft3D, the effects of wind forcing on sediment transport or resulting morphology are not directly incorporated, rather the effects of wind

forcing on waves and currents are considered (i.e. indirect forcing). As the wave climate in particular is affected by (partially forced by) the wind, it is likely that any schematising carried out on the wind data will have an effect on the wave forcing. The key challenge in schematising the wind data therefore is to do it in a way that correlates the wave and wind data schematisation, thereby avoiding any errors arising from incompatibility of the applied input reduction techniques (c.f. Lesser, 2009). Lesser (2009) describe a simple, commonly used method to overcome this problem.

Morphological Acceleration Factor (morfac)

The morphological acceleration factors (morfac) is a widely used and simple technique that bridges the gap between hydrodynamic and morphodynamic timescales. The hydrodynamic forces that drive morphology occur on relatively shorter timescales than the resulting changes in morphology. Multiplying the bed level changes that occur throughout the duration of one hydrodynamic time-step by a morfac value means that the morphodynamic updating does not need to be computed for each and every hydrodynamic step (Jones et al., 2007; Reeve et al., 2016). i.e. after a simulation over a hydrodynamic period (T), the morphological changes are computed for a period of $\text{morfac} \cdot T$ (Walstra et al., 2013).

Combinations of input reduction techniques and morfac can significantly reduce computational times. Processes of optimisation (e.g. mesh/domain and model optimisation; see Jones et al., 2007) can also help to bring down simulation run times to reasonable lengths. This combination of input reduction and morfac was referred to as the Brute Force Filtered Compressed (BFFC) technique by Luijendijk et al., (2019), and is suitable for implementation to the time-series of waves, surges and wind conditions. In cases where the wave time-series is compressed (i.e. morfac applied), it is applied over a non-compressed (no morfac) tidal time-series, assuming the timescales of waves and morphology can be separated from the tidal time scale (Luijendijk et al., 2019).

There are however limits to the morfac value that can be applied to any given simulation. These limits are determined by the characteristics of the location under consideration and therefore require careful assessment, judgement, calibration and sensitivity analysis (e.g. Jones et al., 2007; Lesser, 2009). For example, in low energy environments where the evolution of morphology is driven by constant forcing, the morphodynamic changes are gradual and linear. In such cases, higher values of morfac are applicable. In high energy conditions, however,

where there is strong non-linear forcing (e.g. storms), there is more ambiguity in the feedback between hydrodynamic forcing and resulting bed level changes (Jones et al., 2007). In such cases lower values of morfac are recommended. As such, as reported by Walstra et al., (2013), the maximum allowable morfac value is governed by the high-energy events in the time-series, suggesting that a morfac value of 10-20 can be applied to high-energy (storm) conditions, but morfac values in the order of 100 can be applied to moderate conditions without the overall quality of simulations deteriorating. Numerous different test simulations can be run for a given location, experimenting with different morfac values and comparing them against the benchmark brute force simulation (e.g. Jones et al., 2007; Lesser, 2009) to identify optimal values.